Synthesis of Hybrid Nanomaterials based on Defective Nanocarbons and Their Applications

Yuri Choi

Department of Energy Engineering

Graduate School of UNIST

2016

Synthesis of Hybrid Nanomaterials based on Defective Nanocarbons and Their Applications

Yuri Choi

Department of Energy Engineering

Graduate School of UNIST

Synthesis of Hybrid Nanomaterials based on Defective Nanocarbons and Their Applications

A thesis submitted to the Graduate School of UNIST
in partial fulfillment of the requirements
for the degree of Doctor of Philosophy

Yuri Choi

7. 11. 2016

Approved by

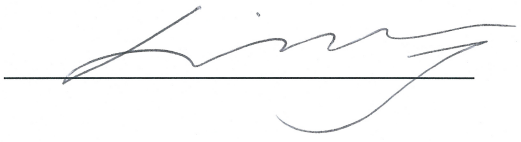

Advisor
Byeong-Su Kim

Synthesis of Hybrid Nanomaterials based on Defective Nanocarbons and Their Applications

Yuri Choi

This certifies that the thesis/dissertation of Yuri Choi is approved.

7. 11. 2016

Advisor: Byeong-Su Kim

Jin Young Kim: Thesis Committee Member #1

Tae-Hyuk Kwon: Thesis Committee Member #2

Oh-Hoon Kwon: Thesis Committee Member #3

Wonoh Lee: Thesis Committee Member #4

Abstract

Development of hybrid nanomaterials has attracted the intensive interest because of their synergetic effect from the advantages of each nanomaterial in various application. The hybrid nanomaterials based on graphene oxide (GO) and carbon nanoparticles (CDs) have been developed due to their abundant functional groups, large surface area and high conductivity. These nanomaterials is applied for a wide range of applications such as bioimaging, therapy, photocatalyst, electrocatalyst, sensor, and photovoltaic devices. However, tremendous efforts are necessary to develop homogeneous and controlled hybrid nanostructure coupled with the study of the unexpected behavior for the excellent efficiency in various fields. In this regard, this thesis describes the approaches to develop new types of hybrid nanomaterials based on GO and CDs functionalized with organic or inorganic materials.

This thesis divides into three parts; (1) hybrid nanomaterials based on GO, (2) hybrid nanomaterials based on CDs, and (3) origin of photoluminescence (PL) of nanocarbons.

The first part introduces the synthesis of gold (Au) and GO nanocomposite for the reduction of nitroarenes and methanol oxidation. In organic catalyst, GO play an important role as supporting and conducting materials, which results in high concentration of Au nanoparticles loaded on GO and thus high catalytic efficiency. In electrocatalyst, layer-by-layer assembly help to develop the controlled thickness of Au-GO film, which exhibits the excellent electron transfer properties.

The second part presents CDs functionalized with organic molecules and metal nanoparticles. CDs have the unique optical and electron transfer properties. When conjugated with polymer and targeting molecules, not only PL intensity but also the targeting efficiency is increased, leading to simultaneously targeted bioimaging and photodynamic therapy. Furthermore, heterodimeric silver-CDs nanostructures are developed by photo-reduction, which possess different interfaces, PL intensity, and SPR effects with respect to the amount of additives.

Finally, besides the synthesis of hybrid nanomaterials, origin of PL properties of nanocarbons is demonstrated to extend the applications. First, high PL intensity of dual heteroatom doped CDs is synthesized. To elucidate the origin of the unique properties, the structure analysis, photophysical properties, DFT calculations, and single molecule spectroscopy is carried out. Based on these studies, we found that high PL of CDs is achieved from graphitic structure as well as less oxygen groups and nitrogen traps. Furthermore, hybrid carbon nanosheets show solvent-dependent PL emission in accordance with polarity, because of different energy level by shape-tunable behavior.

Contents

List of Figures

and (e) 150 ˚C samples measured in 0.10 M KOH with 1.0 M CH_3OH. (c, f) Linear sweep voltammetry (LSV) of $(Au/GO)_n$ thin films thermal treated at (c) 100 ˚C and (f) 150 ˚C measured in 0.10 M KOH with 1.0 M CH_3OH. The insets in all images show the current density plot as a function of number of bilayer (BL). All measurements were carried out in a saturated N_2 at a scan rate of 20 mV/s.

Figure 2.3.9. Cyclic voltammetry of $(Au/GO)_6$ thin films thermal treated at 150 ˚C samples measured in 0.10 M KOH with 1.0 M CH_3OH in a saturated N_2 with various scan rates. The inset represents the linear response of current density with respect to the square root of scan rates.

Figure 2.3.10. Cyclic voltammograms of $(GO/GO)_6$ and $(Au/GO)_6$ thin films thermal treated at 100 ˚C, 150 ˚C, and 300 ˚C measured in 0.10 M KOH with 1.0 M CH_3OH in a saturated N_2 at a scan rate of 20 mV/s. Note that the plain ITO-glass substrate and $(GO/GO)_6$ thin film do not contribute to the catalytic activity toward methanol oxidation.

Figure 2.3.11. Schematic representation of the possible mechanism of electrocatalytic activity of $(Au/GO)_n$ toward methanol oxidation depending on the number of bilayers (BL). Two factors such as methanol diffusion into the electrode and electron and mass transfer from the electrode govern the fine balance of multilayered hybrid electrode in the observed electrocatalytic activity.

Figure 2.3.12. Cyclic voltammetry stability test of (a) $(Au/GO)_6$ thin film thermal treated at 150 ˚C samples, (b) DMAP-Au NPs on a glassy carbon electrode. Both samples were measured in 0.10 M KOH with 1.0 M CH_3OH in a saturated N_2 at a scan rate of 20 mV/s. Identical concentration of Au NPs was used for comparison.

Figure 2.3.13. Control experiments of Au NPs deposited on amorphous carbon, Ketjen Black. (a) UV/vis spectra, (b) TEM image, (c) Cyclic voltammetry stability test in 0.10 M KOH with 1.0 M CH_3OH in a saturated N_2 at a scan rate of 20 mV/s, and (d) Nyquist plot measured in 0.10 M KOH + 1.0 M CH_3OH solution measured at 0.35 V. The R_{CT} of 358.1 ohm is obtained.

Figure 2.3.14. (a) Cyclic voltammograms of $(Au/GO)_6$ thin film thermal treated at 150 ˚C in 0.10 M KOH with different concentrations of CH_3OH. Inset shows the plot of log (*i*) against log (CH_3OH) at different concentrations of CH_3OH. (b) The corresponding Tafel plot with a representative linear fit. All measurements were carried out in a saturated N_2 at a scan rate of 20 mV/s.

Figure 2.3.15. Plots of log(*I*) against log (C_{CH3OH}) at different potentials in Tafel range. The measurements were carried out in a saturated N_2 with a scan rate of 20 mV/s. The slope is 0.89 for both curves.

Chapter 3.

Figure 3.2.8. (a) UV-vis absorbance spectra of (red) CD-PEG-FA, (black) CD-PEG-FA/ZnPc and (blue) free ZnPc. (b) Fluorescence sprectra of (solid line) free ZnPc, (dotted line) CD-PEG-FA/ZnPc with an excitation wavelength of 650 nm.

Figure 3.2.9. (a, b) AFM and (c, d) dynamic light scattering (DLS) of (a, c) CD-PEG-FA and (b, d) CD-PEG-FA/ZnPc.

Figure 3.2.10. CCK-8 based cell viability assays with HeLa cells with different concentration of CD, CD-PEG and CD-PEG-FA.

Figure 3.2.11. CCK-8 based cell viability assays with HeLa cells with different concentration of CD-PEG-FA/ZnPc.

Figure 3.2.12. (a-d) Bright field and fluorescence images of HeLa cells treated with CD derivatives (50 μg/ml) for 12 h. (a) CD-PEG, (b) CD-PEG-FA, (c) CD-PEG-FA/ZnPc and (d) CD-PEG-FA/ZnPc pre-treated with folic acid. Fluorescence signals of (blue) CDs and (red) ZnPc were observed at 461 nm (λ_{ex} = 358 nm) and 665 nm (λ_{ex} = 647 nm), respectively. Scale bar is 20 μm.

Figure 3.2.13. Bright field and fluorescence images of HeLa cells treated with CD-PEG-FA/ZnPc (50 μg/ml) for 12 h. Fluorescence signals of (blue) CDs and (red) ZnPc were observed by using Deltavision high-resolution microscopy. Scale bar is 20 μm.

Figure 3.2.14. Fluorescence of CD-PEG/ZnPc was measured in folate receptor overexpressed cell (MDA-MB-231 cells) and folate receptor deficient cell (A549 cells) by In-cell analyzer 2000 after 12 h incubation. No significant fluorescence of CD and ZnPc were observed in A549 cells and CD-PEG/ZnPc treated MDA-MB-231 cells. Scale bar is 20 μm.

Figure 3.2.15. (a-d) (top panel) Bright field and fluorescence images of HeLa cells treated with CD derivatives (50 μg/ml) for 12 h followed by irradiation for 10 min with a 660 nm laser (30 mW/cm^2) and (bottom panels) live and dead cells colored green and red, respectively by live/dead assay. (a) CD-PEG, (b) CD-PEG-FA, (c) CD-PEG-FA/ZnPc and (d) CD-PEG-FA/ZnPc with pretreatment of excess free FA. Scale bar is 100 μm. (e, f) Quantitative evaluation of photodynamic effect. (e) Singlet oxygen detection test using a singlet oxygen sensor green (SOSG) reagent. Time-dependent fluorescent intensity ($\lambda_{ex}/\lambda_{em}$ = 504/530 nm) with irradiation by using a 660 nm laser (30 mW/cm^2). Concentration of ZnPc and SOSG used are 3.8 and 2.5 μM, respectively. Note that the addition of cell lysate (1 μL) in CD-PEG-FA/ZnPc did not change the effective concentrations of ZnPc and SOSG. (f) Cell viability assay depending on the

concentration of ZnPc loaded CD-PEG-FA and ZnPc with and without irradiation for 10 min. All experiments were carried out in triplicate and the error bars represent the standard deviation.

Figure 3.2.16. Fluorescence image of HeLa cells which were treated with CD-PEG-FA/ZnPc (50 μg/ml) for 12 h followed by irradiation with a 660-nm laser (30 mW/cm^2) for 10 min. Live and dead cells were colored green and red, respectively by live/dead assay. Scale bar is 100 μm.

Figure 3.2.17. (a) Fluorescence of ZnPc (excited at 660 nm) in tumor was imaged after 12 h injection of CD-PEG-FA/ZnPc, CD-PEG/ZnPc, and CD-PEG-FA (0.5 mg of ZnPc/kg mouse). (b) CD-PEG-FA/ZnPc suspensions were injected into tail veins of tumor-bearing mice and the fluorescent signals were obtained at various time points (1, 2, 6, 12, 24, and 48 h). (c) *Ex vivo* fluorescence images of major organs of mice. The fluorescent signals corresponding to ZnPc (excited at 660 nm) from major organs, tumor, and skin were obtained after 12 h of i.v. injection of CD-PEG-FA/ZnPc and CD-PEG/ZnPc into tumor-bearing mice. FA-conjugated CD delivered and released ZnPc to tumor effectively, in contrast with the CD lacking FA. (d, e) Relative tumor volumes measured over time after the tumor-bearing mice were treated with various CD derivatives. Tumor-bearing mice were separated into 6 groups: (i) PBS control; (ii) CD-PEG-FA without irradiation; (iii) CD-PEG-FA with irradiation; (iv) CD-PEG/ZnPc without irradiation; (v) CD-PEG/ZnPc with irradiation; (vi) CD-PEG-FA/ZnPc without irradiation; (vii) CD-PEG-FA/ZnPc with irradiation (n = 4 for each group). Irradiation was performed using a 660-nm laser at 0.3 W/cm^2. Tumor volumes were measured over 10 days. It is notable that no significant increase in tumor volume was observed for 8 days in mice treated with CD-PEG-FA/ZnPc with irradiation. P values were calculated by Student's t-test: * for $p < 0.05$, $n = 4$.

Figure 3.3.1. Schematic illustration of the synthesis of heterodimeric Ag-CD NPs derived from polysaccharides. (a) Schematic representation of the synthesis of CD NPs from chitosan and alginate precursors followed by growth of Ag NPs on the CDs. (b) Representative TEM image of the Ag-CD_{Chi} NPs. (c) UV/vis absorption and PL spectra of the CDs in solutions prepared from (left) chitosan (CD_{Chi}) and (right) alginate (CD_{Alg}) with varying excitation wavelengths from 320 to 410 nm with an interval of 10 nm. The inset shows the photographs of the respective CD and Ag-CD NPs solutions under ambient light and UV irradiation at 365 nm (conc. 0.10 mg/mL). The samples were prepared with 600 μL of HCl added during the synthesis of the CDs.

Figure 3.3.2. Photoluminescence spectra of (a) Ag-CD_{Chi} and (b) Ag-CD_{Alg} with varying excitation wavelengths from 320 to 410 nm with an interval of 10 nm.

Figure 3.3.3. Proposed formation mechanism of heterodimeric Ag-CD NPs.

Figure 3.3.4. FT-IR spectra of CDs and Ag-CD NPs (a) Pristine chitosan, CD_{Chi}, and Ag-CD_{Chi}, and (b) pristine alginate, CD_{Alg}, and Ag-CD_{Alg}.

Figure 3.3.5. XPS analysis of CDs and Ag-CD NPs. (a) Survey spectra of CD_{Chi} and Ag-CD_{Chi}, (b-d) deconvoluted high-resolution spectra of (b) the Ag 3d region of Ag-CD_{Chi}, (c) the Cl 2p region of CD_{Chi}, and (d) the Cl 2p region of Ag-CD_{Chi}. (e) Survey spectra of CD_{Alg} and Ag-CD_{Alg} and (f) the deconvoluted high-resolution Ag 3d region of Ag-CD_{Alg}. Each sample was prepared with 600 μl of 1 M HCl.

Figure 3.3.6. Deconvoluted high-resolution XPS spectra of the C 1s peak of (a) CD_{Chi} and (b) Ag-CD_{Chi}, and (c) the chemical compositions of CD_{Chi} and Ag-CD_{Chi}. The numbers in the top right-hand corner of the graphs indicate the volume (μl) of 1.0 M HCl additive used in the formation of CD_{Chi}.

Figure 3.3.7. Deconvoluted high-resolution XPS spectra of the C 1s peak of (a) CD_{Alg} and (b) Ag-CD_{Alg} and (c) the chemical compositions of CD_{Alg} and Ag-CD_{Alg}. The number in the graph represents the volume (μl) of 1.0 M HCl additive used in the formation of CD_{Alg}.

Figure 3.3.8. Proposed chemical mechanism of Ag reduction on the surface of a CD upon photoexcitation according to the combined results of FT-IR and high-resolution XPS. The photoexcited electrons from the CD reduce the Ag^+ ions to Ag NPs on the surface of the CD to afford heterodimeric Ag-CD NPs.

Figure 3.3.9. Representative high-resolution TEM images of Ag-CD_{Chi} NPs. (a) Aberration-corrected TEM image of Ag-CD_{Chi} NPs (scale bar: 5 nm) and the corresponding digital diffractograms of the Ag NPs and the CD, respectively. (b) Energy-filtered TEM (EFTEM) image of Ag-CD_{Chi} NPs (scale bar: 10 nm) with composed elemental images of Ag, C, and Cl. (c) STEM-HAADF image of Ag-CD_{Chi} NPs (scale bar: 10 nm) and the corresponding monochromated STEM-EEL spectra of points along the line on a heterodimeric Ag-CD_{Chi} NP.

Figure 3.3.10. TEM images of Ag-CD_{Chi} NPs where the CD_{Chi} particles were prepared with different additives: (a) HCl, (b) HBr, and (c) acetic acid. The role of Cl^- ions in the formation of Ag NPs was further characterized when the reaction was conducted in different acids, such as HBr and acetic acid (AcOH).

Figure 3.3.11. Optical images of samples prepared (top panel) without CD and (lower panel) with CD. AgCl, AgBr, and silver acetate were synthesized under the same conditions used for Ag-$CD_{Chi\text{-}Cl}$, Ag-$CD_{Chi\text{-}Br}$, and Ag-CD_{AA} in the absence of CD.

Photoluminescence spectra of BN-CD under varying excitation wavelengths from 320 to 420 nm with 10-nm increments. (e) The bulk production of BN-CD powder and PVA film under daylight and UV illumination at 365 nm.

Figure 4.2.2. (a) Normal TEM, (b) high-resolution TEM images and (c) the distribution of particle size of BN-CD.

Figure 4.2.3. XRD diffraction patterns of CDs. N-CDs and BN-CD have a broad peak at 0.47 nm and 0.42, respectively. Due to the incorporation of heteroatom within the carbon framework, the interlayer spacing is increased compared to that of bulk graphite (0.344 nm). In addition, BN-CD showed another peak at 0.74 nm, which is ascribed to the oxide-induced O-containing groups and inserted H_2O molecules.

Figure 4.2.4. (a) UV-vis absorbance and PL spectra of N-CD. Inset shows N-CD suspension (conc. 0.01 mg/mL) (left) under room light and (right) UV illumination at 365 nm. (b) PL spectra of N-CD under varying excitation wavelengths from 300 to 420 nm with 10-nm increments. Excitation and emission contour plots of (c) N-CD and (d) BN-CD.

Figure 4.2.5. (a) PL spectra of N-CD and BN-CD powder. (b) Photograph images of CDs powder under daylight and 8 W and 100 W UV illumination at a wavelength of 365 nm. (c) PL spectra of N-CD and BN-CD embedded within PVA film at a concentration of 0.1 wt % of CDs. (d) Photograph images of CDs film under 8 W UV illumination.

Figure 4.2.6. Quantum yield (QY) of N-CD, BN-CD0.5, BN-CD, and BN-CD2 in reference to quinine sulfate.

Figure 4.2.7. (a) UV-vis absorbance of BN-CD0.5 and BN-CD2. (b, c) PL spectra of (b) BN-CD0.5 and (c) BN-CD2. (d) Emission shifts of all CDs prepared with increased excitation wavelength.

Figure 4.2.8. (a) UV-vis absorbance and (b) PL spectra of non-doped plain CD. CD has 2.1% of quantum yield at 360 nm and red-shift (90 nm) in emission spectra. It results from heterogeneous oxygen functional groups on the surface of CD.

Figure 4.2.9. Chemical structures of N-CD and BN-CD. (a) FT-IR spectra and (b) XPS survey spectra of N-CD and BN-CD. (c) High-resolution XPS spectra of B1s, C1s and N1s of N-CD and BN-CD. The XPS survey spectrum indicates the presence of 3.51% B and 12.16% N in BN-CD.

Figure 4.2.10. The chemical compositions of N-CD and BN-CD determined by XPS.

Figure 4.2.11. Photophysical properties of N-CD and BN-CD. (a) Normalized fluorescence decay profiles of CDs monitored at 450 nm with excitation at 375 nm, and (b) the femtosecond-resolved fluorescence decay kinetics of CDs probed at 450 nm with excitation at 365 nm. Note that the timescales are significantly different in (a) and (b). (c) The energy level diagram and schematic structures of the corresponding CDs with their relevant photophysical transitions.

Figure 4.2.12. Normalized fluorescence decay profiles of CDs monitored at different emission wavelength of (a) 430 nm, (b) 450 nm and (c) 480 nm under excitation at 375 nm.

Figure 4.2.13. Femtosecond-resolved fluorescence decay profiles of CDs at different emission wavelength of (a) 430 nm, (b) 450 nm and (c) 480 nm under excitation at 365 nm.

Figure 4.2.14. Time-resolved emission spectra of N-CD excited at various wavelengths of (a) 375 nm, (b) 450 nm and (c) 510 nm.

Figure 4.15. DFT calculations of N-CD and BN-CD. (a, b) Electronic densities of states (DOSs) and modelled structures for (a) N-CD and (b) BN-CD (brown, C; white, H; red, O; blue, N; and green, B atoms). (c, d) The oscillation strengths and Gaussian functions (FWHM = 0.46 eV) for (c) N-CD and d) BN-CD. The charge distributions of HOMOs and LUMOs that contribute to the first one (N-CD) or two (BN-CD) main peaks are marked with asterisks in (c) and (d).

Figure 4.2.16. Chemical structures of BN-CD determined from DFT calculation. When B-OH group is located away from graphitic N on edge site, high total energy is obtained. Thus, B-OH next to graphitic N is the most stable structure with lower total energy.

Figure 4.2.17. (a) Two N-C=O groups representing N-CD and (b) six N-C=O groups representing BN-CD. Model calculation results showing that the dipole transition enhancement is mainly caused by enriched edge groups.

Figure 4.2.18. Single-molecule spectroscopy of N-CD and BN-CD. (a, b) Time-dependent photoluminescence traces of (a) single N-CD and (b) single BN-CD with a single-step photobleaching. The percentages were calculated from collection of N-CD (n = 311) and BN-CD (n = 225). Inset images are single N-CD and BN-CD under 375 nm illumination. (c-e) Box plot comparison of single N-CD and BN-CD bleached in one step. (c) single-step photobleaching time, (d) photons per frame and (e) total photon numbers before photobleaching. The average single-step photobleaching times (τ_{avg}) was 993 ± 397 s and 1138 ± 400 s for N-CD and BN-CD, respectively. The laser power was 50 W/cm^2 and the camera exposure time was 200 ms per frame. Spheres indicate minima and maxima. Squares indicate the average values and notches represent the confidence interval at the confidence level of 95%.

510 nm. (a, b) CNS-Water and (c,d) CNS-DMF.

Figure 4.3.12. (a) Optical images of CNS suspension in each solvent under excitation at 360 nm. (b) Calculated CIE coordinates from the PL spectra of solvents with different polarity under excitation at 360 nm. (c) Stoke shifts at 480 nm excitation as a function of solvent polarity factor, $E_T(30)$. (d) Calculated CIE coordinates from the PL spectra of solvents with different polarity under excitation at 480 nm. EG, EGME, and MeCN is ethylene glycol, 2-methoxylethanol, and acetonitrile, respectively. Inset is the optical images excited at 360 and 480 nm.

Figure 4.3.13. (a–e) UV/Vis and PL spectra of CNS in (a) ethylene glycol (EG), (b) methanol (MeOH), (c) 2-methoxyethanol (EGME), (d) *n*-butyl alcohol (*n*-BuOH), and (e) isopropyl alcohol.

Figure 4.3.14. (a–e) UV/Vis and PL spectra of CNS in (a) acetonitrile (MeCN), (b) dimethyl sulfoxide (DMSO), (c) *N*-methyl-2-pyrrolidone (NMP), (d) acetone, and (e) THF.

Figure 4.3.15. PL spectra and optical images of CNS in water, ethanol, IPA, DMSO, and DMF excited at 480 nm. As polarity decreased, 589 nm of emission peak in water was blue-shifted to 548 nm in DMF. According to the emission peak shifts, the PL color was also changed from red to green.

List of Tables

Chapter 1. Hybrid Nanomaterials based on Defective Nanocarbons

1.1. Introduction of defective nanocarbons

Over the past decades, defective nanocarbons such as graphene oxide (GO) and carbon nanoparticles (CDs) have been studied extensively for their interesting and in many cases unique properties and application potentials.[1] They possess sp^2 graphitic structure and large surface area and exhibit high intrinsic electronic, magnetic and optical properties.[2,3] Especially, defective induced from the abundant oxygen groups is affected or modulated to their outstanding properties.[4] Interestingly, hybrid nanomaterials based on defective nanocarbons shows the synergetic effect, when conjugated with small molecules, polymer, and metal nanoparticles. These hybrid nanomaterials have high efficiency in various applications such as bioimaging, therapy, photocatalyst, organic catalyst and electrocatalyst, and photovoltaic devices.

1.1.1 Graphene oxide

Graphene, which consists of sp^2 hybridized carbon atoms arranged in a honeycomb lattice, has the remarkable physical, chemical and electronic properties.[5] Graphene and its derivatives has led to a wide range of applications such as in light emitting diodes,[6] photodetectors,[7] batteries,[8] and supercapacitors.[9] In addition, graphene is adjusted to bio applications such as drug delivery, tissue engineering, stem cell research and biomedical imaging.[10] The preparation method of graphene has several synthetic approaches, such as chemical vapor deposition (CVD),[11] liquid-phase exfoliation,[12] and electrochemical exfoliation.[13] However, graphene has the limitation to low solubility in polar solvent and lack of functional groups, which is difficult to synthesize the hybrid nanomaterials in solvent.

To solve this issues, graphene oxide (GO), which is graphene derivate possessing oxygen functional groups, have been received attention due to their large surface area, strong hydrophilic and water soluble properties. GO is obtained by chemical exfoliation (Hummers method), which uses potassium permanganate in concentrated sulfuric acid to oxidize graphite.[14] Therefore, an individual GO sheet decorated with oxygen functional groups have in the form of hydroxyl and epoxy groups decorate the basal plane, whereas carboxyls, carbonyls, lactones and quinones are located primarily at the edges (Figure 1.1a and 1.1c).[15,16] The reduced graphene oxide (rGO) is achieved from the removal of oxygen containing functional groups in GO through thermal and chemical reduction (Figure 1.1c).[17]

Interestingly, due to oxygen groups, GO shows the excellent properties such as electronic, optical, thermal, mechanical, and electrochemical properties, as well as chemical reactivity.[18] The ratio of sp^2 and sp^3 carbon on GO can be controlled the conductivity (Figure 1.1d).[19] In addition, this different sp^2 fraction of GO the reduction of oxygen groups is influenced to the unique optical characteristics. After reduction of GO, photoluminescence (PL) is enhanced because of the increased small sp^2 domains (Figure 1.1e).[20]

Therefore, due to large surface area, oxygen functional groups, high conductivity, and optical properties, GO play an important role as supporting materials and catalyst for bio and energy applications.

1.1.2. Carbon nanoparticles

Carbon nanoparticles (CDs), a new class of below 10 nm size of nanocarbons, have been attracted great interest as alternative for toxic semiconducting quantum dots and organic dyes due to high optical properties, high aqueous solubility, photostability, biocompatibility, and non-toxicity.[21] However, unlike other nanocarbons, the most outstanding properties of CDs are high optical behavior, the abundant functional groups, and electron transfer ability.[22]

First, CDs has high quantum yield over 20%, unlike other nanocarbons such as fullerene and graphene oxide.[23] Due to sp^2 graphitic domains embedded on sp^3 carbon matrix of CDs, the efficient radiative recombination has been occurred before the excited-electron relaxation. There are a lot of effect to obtain high optical properties by heteroatom doping (N, B, and S),[24,25] surface passivation[26] and crosslinking[27] (Figure 1.2). Recently, not only high PL but also the tunable PL has been reported for a wide range of applications (Figure 1.3).[28-31]

Second, the abundant functional groups of CDs such as oxygen and amine are facilitated with the chemical modification small molecules to polymer by covalent bonding, which results in high dispersity in aqueous phase.[3] After passivation with these molecules, the optical properties of CDs is enhanced due to homogeneous surface states (Figure 1.4). Third, electron transfer ability is the one of unique properties of CDs (Figure 1.5a).[32] When irradiated under UV or visible light, the electron and hole is excited, and then transfers them to neighborhood ions or molecules. From this properties, the efficiency of photocatalyst or photovoltaic devices is influenced due to the increased charge separation and transfer in visible light.[33,34] In addition, this photo-excited electron can be reduced from metal ions to metal nanoparticles without reductant (Figure 1.5b).[35]

The synthetic method is divided into bottom-up and top-down method. Bottom-up method is the carbonization of small molecules biomass and polymer through microwave, hydrothermal method, acid treatment and electrochemical method (Figure 1.6).[36] In contrast, top-down method is based on the cutting of graphitic structure such as graphene, carbon nanotube, and carbon fiber, which have one or a few later of graphene and connected chemical groups on

the edges (Figure 1.7).[37]

Therefore, the remarkable properties of CDs has the promising applications such as bioimaging, drug delivery, sensor, photocatalyst, and photovoltaic devices.[38] However, although CDs is the promising nanocarbons with unique properties, it is still challenging to apply for new application due to the undefined structure from a lot of synthetic method and carbon sources. Therefore, the apparent synthesis from distinct carbon sources is necessary in a wide range of applications. Furthermore, the surface passivation or the photo-reduction of metal ion need to be more elaborate and modulated for the enhanced efficiency in various fields.

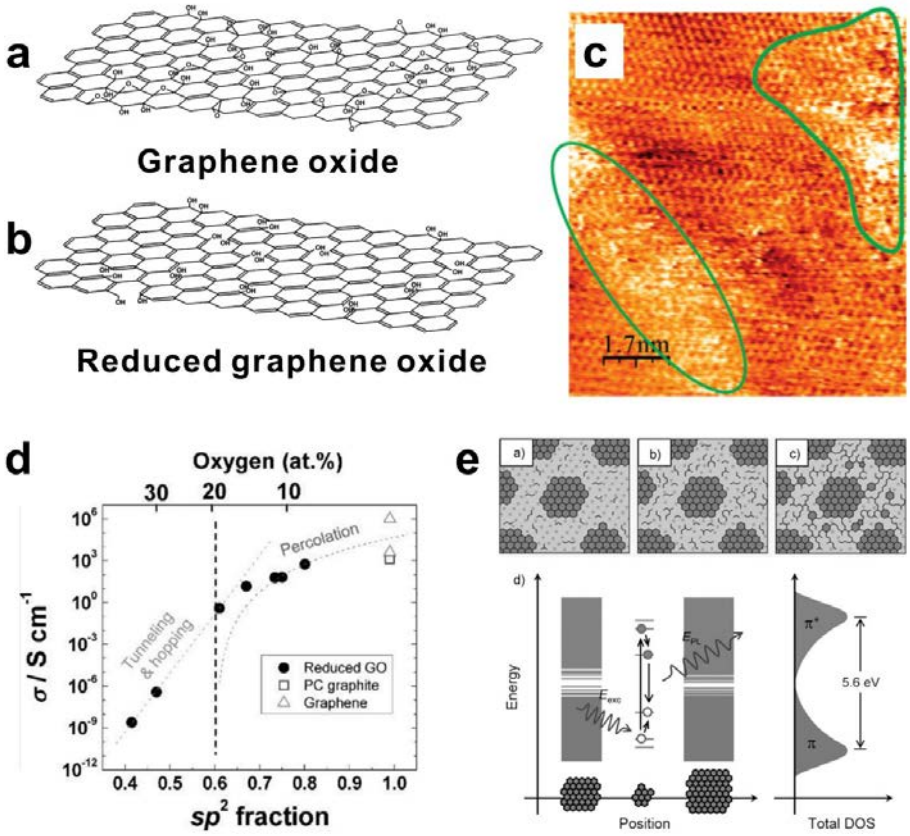

Figure 1.1. The structure model of (a) graphene oxide and (b) reduced graphene oxide. Reprinted with permission from ref 16. Copyright 1998 Elsevier. (c) STM images of graphene oxide contained oxygen groups. Reprinted with permission from ref 15. Copyright 2007 American Chemical Society. (d). Conductivity of thermally reduced GO as a function of the sp^2 carbon fraction. Reprinted with permission from ref 19. Copyright 2009 Wiley. (e) Structural models of GO at different stages of reduction and band structure of GO. Reprinted with permission from ref 20. Copyright 2010 Wiley.

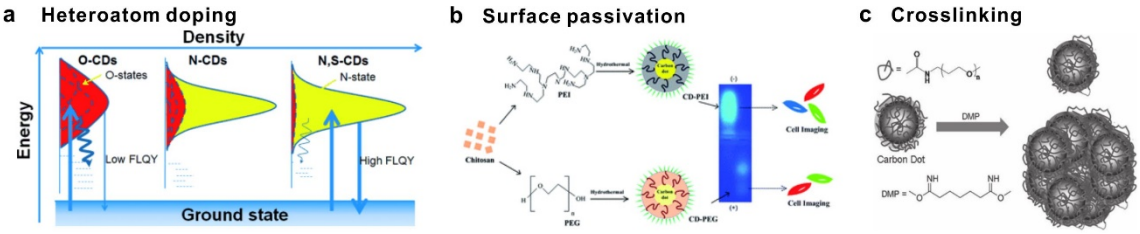

Figure 1.2. Synthesis of high optical properties of carbon nanoparticles. (a) Heteroatom doping. Reprinted with permission from ref 25. Copyright 2013 Wiley. (b) Surface passivation. Reprinted with permission from ref 26. Copyright 2014 Royal Society of Chemistry. (c) Crosslinking. Reprinted with permission from ref 27. Copyright 2013 Wiley.

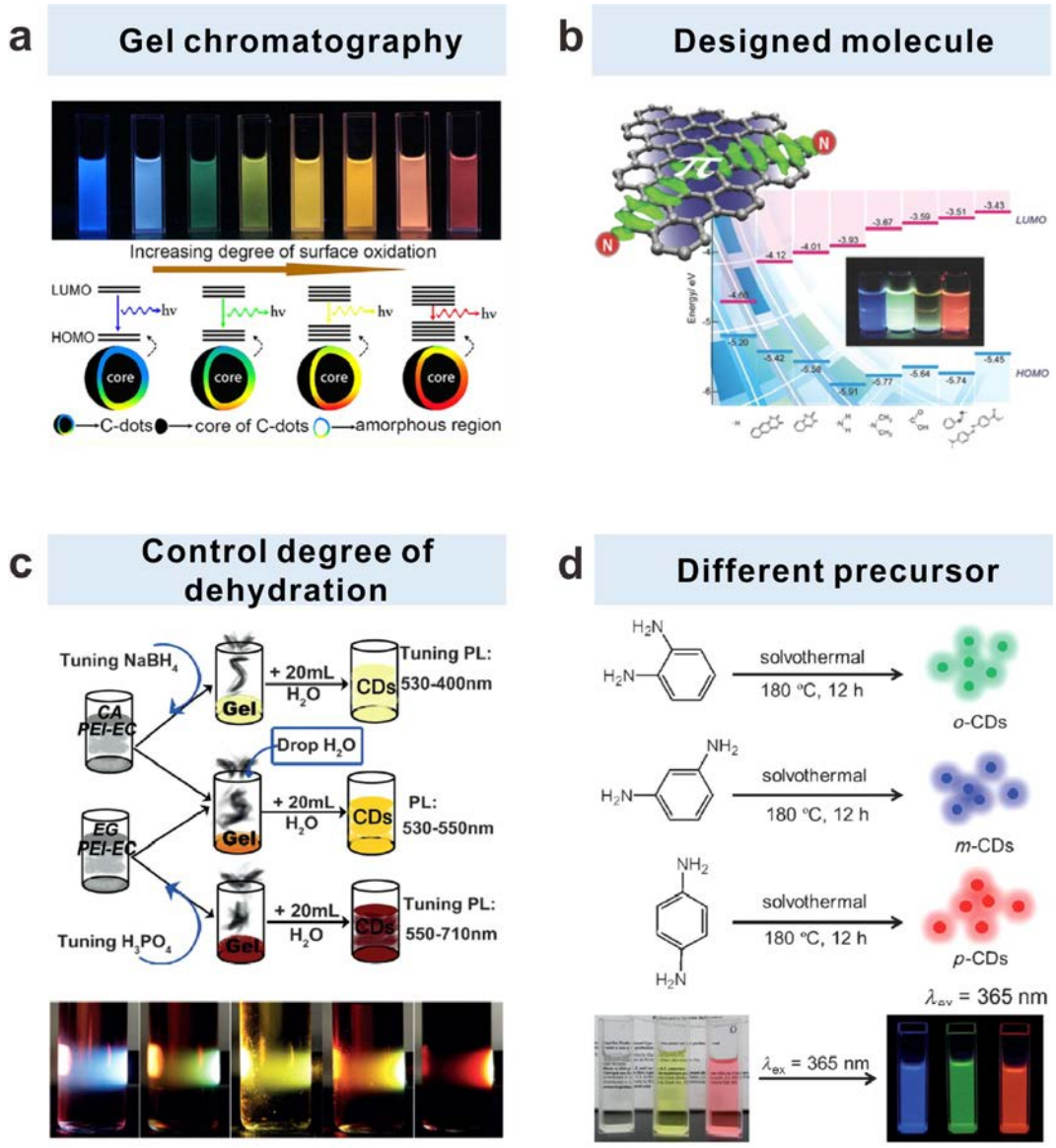

Figure 1.3. Synthesis of tunable optical properties of carbon nanoparticles (a) Separation. Reprinted with permission from ref 28. Copyright 2016 American Chemical Society. (b) Surface passivation. Reprinted with permission from ref 29. Copyright 2016 Wiley. (c) Different synthetic condition. Reprinted with permission from ref 30. Copyright 2015 Wiley. (d) Different precursor. Reprinted with permission from ref 31. Copyright 2015 Wiley.

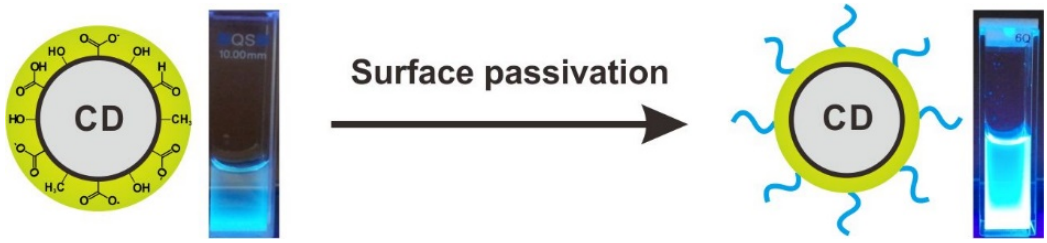

Figure 1.4. Surface passivation effect on the optical properties of carbon nanoparticles.

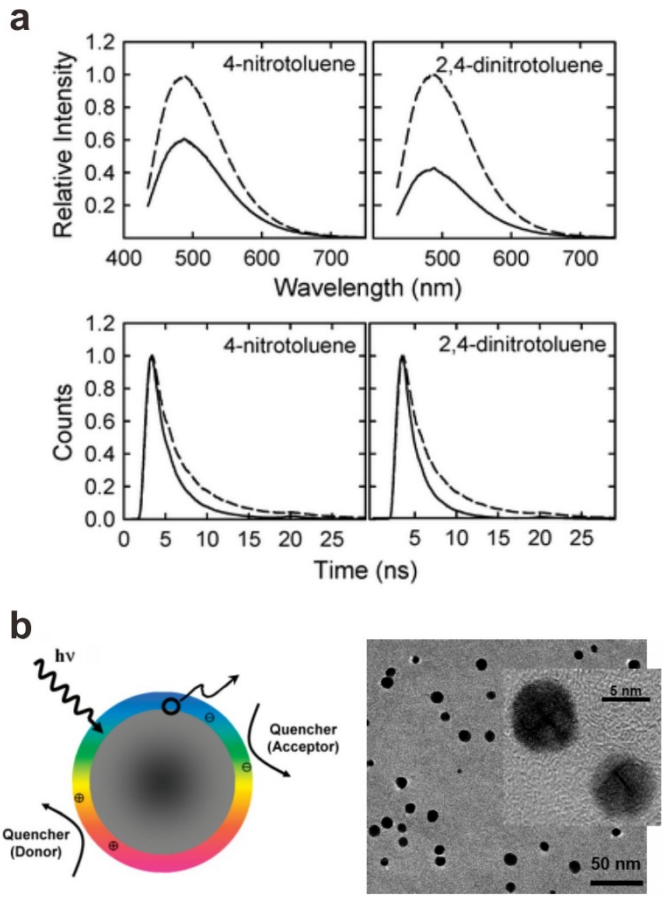

Figure 1.5. (a) Top: luminescence emission spectra (425 nm excitation) of the carbon nanoparticles in toluene without (dotted line) and with the indicated quenchers (both 0.016 M, solid line). Bottom: luminescence decays (407 nm excitation, monitored with 470 nm narrow bandpass filter) of the carbon nanoparticles without (dotted line) and with the quenchers (both 0.028 M, solid line). Reprinted with permission from ref 32. Copyright 2009 Royal Society of Chemistry. (b) Synthesis of metal nanoparticles through photo-reduction. Reprinted with permission from ref 35. Copyright 2011 American Chemical Society.

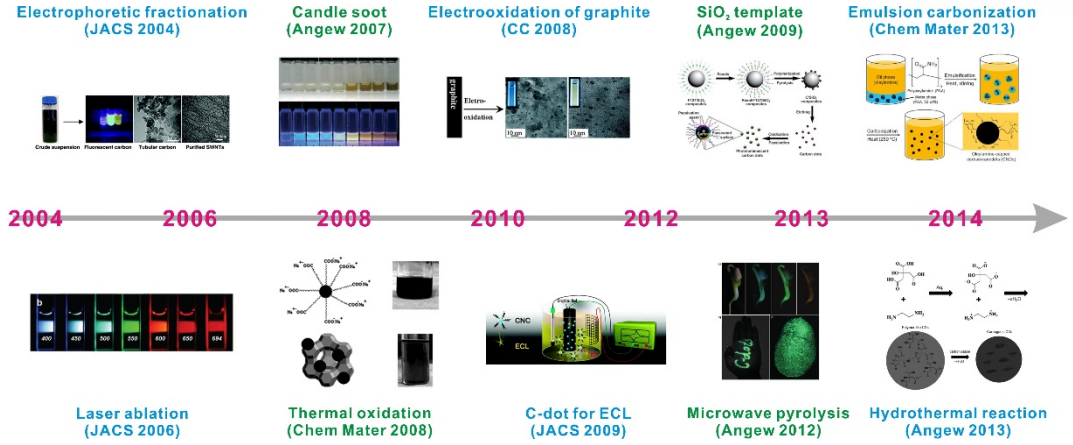

Figure 1.6. Synthetic method of carbon nanoparticles.

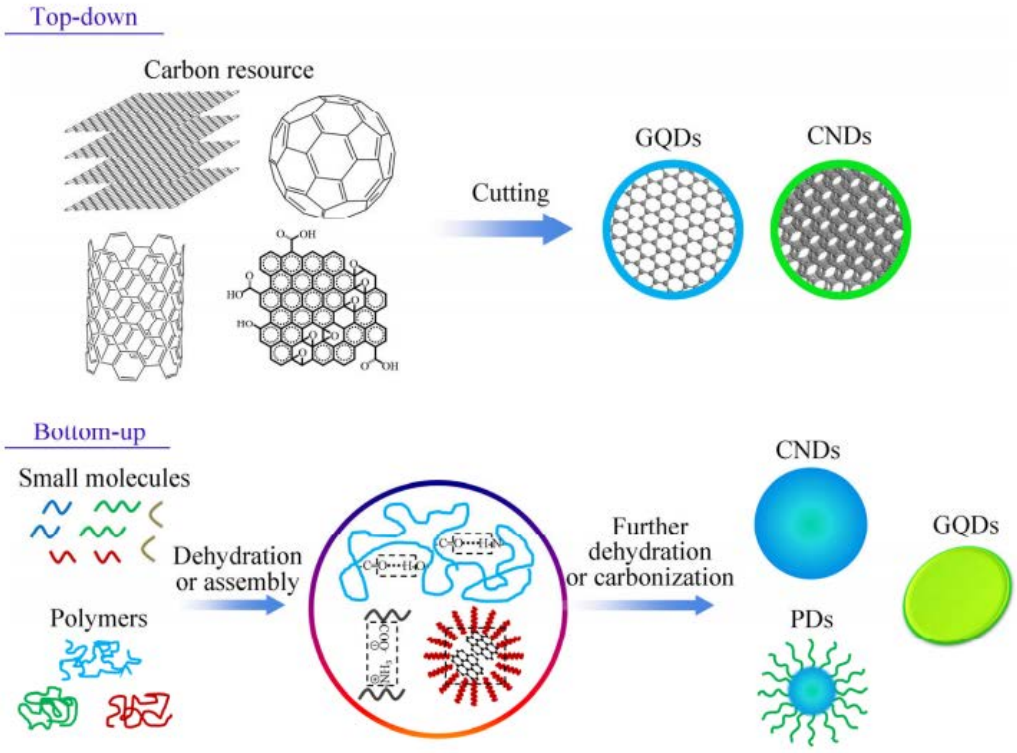

Figure 1.7. The main approaches to fabricating carbon nanoparticles: "Top-down" cutting from different carbon sources and "bottom-up" synthesis carbon molecules or polymers. Reprinted with permission from ref 37. Copyright 2015 Springer.

1.2. Development of hybrid materials based on nanocarbons

To date, a broad range of functional materials such as organic molecules, nanoparticles, polymers, and biomaterials have been reported for hybrid materials based on nanocarbons.[18] GO and CDs acts as supporting templates for metal nanoparticles or organic molecules due to their abundant oxygen group, large surface area. Also, electron-hole transfer pathway or reservoir due to electron transfer properties exhibit in hybrid nanomaterials. Thus, this hybrid nanomaterials show the excellent synergetic effects, which results in high efficiency and stability in various applications.

1.2.1. Hybrid nanomaterials based on graphene oxide

To synthesize hybrid nanomaterials with metal nanoparticles, there are two methods; one is *in situ*, another is *ex situ* method. *In situ* method is the growth of metal ions on GO through the reduction or hydrothermal reaction. Due to hydroxyl and carboxylic groups on GO, metal precursor is attached, nucleated, and grow to metal nanoparticles by reducing agent such as sodium borohydride and high temperature. Although this method need one-step process, the morphology and size control of metal nanoparticles is complicated. For example, Zhuo *et al*. is synthesized Au-GO hybrid nanomaterials by *in situ* reduction; however, Au nanoparticles have a wide size distribution (Figure 1.8a).[39]

Another method is *ex situ*, which is the attachment of as-synthesized metal nanoparticle and GO by covalent or noncovalent interactions such as van der Waals interactions, hydrogen bonding, π–π stacking, or electrostatic interactions.[40] Despite nanoparticles need to synthesize in advanced, well-distributed of uniform size and a lot of amounts of metal nanoparticles on GO is developed. However, the method reported previously have shown the surface modification of GO with polymer or small molecules to effectively anchor the nanoparticles (Figure 1.8b).[41]

Besides nanoparticles, organic molecules or polymers is conjugated on GO through π–π stacking, hydrophobic interaction, and covalent bonding. The functionalization of organic molecules enhances the stability of GO in solution (Figure 1.9a).[42] Furthermore, the optical, chemical, and physical properties of GO is modulated according to the kinds of functionalized molecules (Figure 1.9b).[43]

Other possible approache for hybrid nanomaterials is layer-by-layer (LbL) assembly, which make 3D hybrid nanostructure. The LbL method is achieved through the sequential adsorption of oppositely charged components by attractive forces such as electrostatic interactions, and hydrogen boding.[44] Thus, the thickness and composition of hybrid composite materials can be modulated, which has highly ordered and multilayered structure (Figure 1.10a). Furthermore, due to the increased electron mobility from the space between layers, LbL method results in high

catalytic efficiency (Figure 1.10b).[45]

1.2.2. Hybrid nanomaterials based on carbon nanoparticles

CDs also possess the abundant oxygen functional groups, as shown in graphene oxide. Thus, the similar approaches on CDs have been developed, recently. First, surface modification with small molecules and polymer can tune the optical properties of CDs. For example, spiropyrans passivated CDs shows switchable PL behaviors in UV and visible light (Figure 1.11a).[46] In addition, the passivation with polymer such as poly (ethylene glycol) and poly (ethyleneimine) induced to the enhanced PL intensity and biocompatibility.

Hybrid nanomaterials with CDs and metal oxide nanoparticles have been reported, including iron oxide,[47] zinc oxide,[48] silica,[49] and titania (TiO_2).[49] In specific, TiO_2/CDs is synthesized *in situ* or *ex situ* method (Figure 1.11b). Due to small size (< 10 nm), CDs is attached on the surface of TiO_2 particles (100 nm). Also, the reduction method of metal ion in existence of CDs produces metal/CDs nanocomposites. Furthermore, CDs is combined with 2D nanomaterials such as graphene oxide[50] (Figure 1.11d) and C_3N_4[51] (Figure 1.11c). Because of the functional groups of each nanomaterials, CDs on 2D nanosheets is synthesized after thermal treatment.

CDs/Metal nanoparticles have been synthesized through the chemical, thermal, and photoreduction. Table 1.1 show silver (Ag)/CDs hybrid nanomaterials. Metal ions are attached the oxygen groups on the surface of CDs, and grow by redundant, heat and light. However, the morphology and size of metal nanoparticles on CDs is complicated. Furthermore, the existence of CDs in hybrid nanomaterials is not distinguished in TEM images. Therefore, more study is needed for the homogeneous hybrid nanomaterials based on CDs.

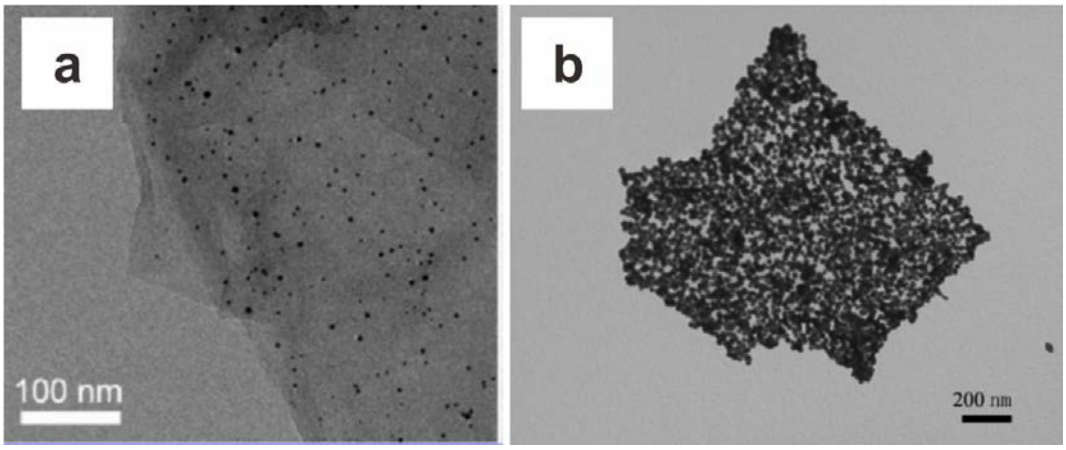

Figure 1.8. (a) *In situ* growth of Au nanoparticles on graphene oxide. Reprinted with permission from ref 39. Copyright 2013 American Chemical Society. (b) *Ex situ* of hybrid nanomaterials with Au and PDDA functionalized graphene oxide. Reprinted with permission from ref 41. Copyright 2010 American Chemical Society.

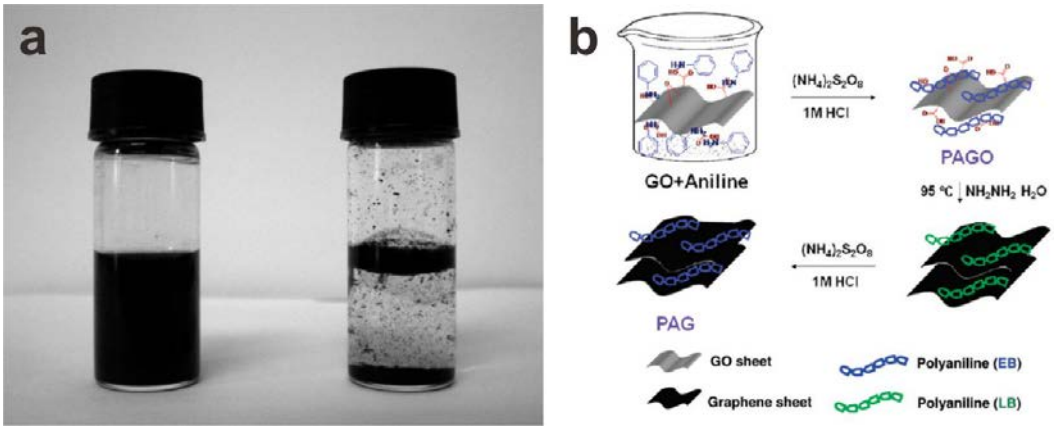

Figure 1.9. (a) Photo of aqueous dispersion (0.1 mg mL^{-1}) of reduced graphene oxide-methylene green (left) and reduced graphene oxide (right). Reprinted with permission from ref 42. Copyright 209 American Chemical Society. (b) Schematic illustration of the process for preparation of polyanilines/graphene oxide or polyanilines/reduced graphene oxide nanocomposites by *in situ* polymerization of aniline monomer in the presence of GO under acidic conditions. Reprinted with permission from ref 43. Copyright 2010 American Chemical Society.

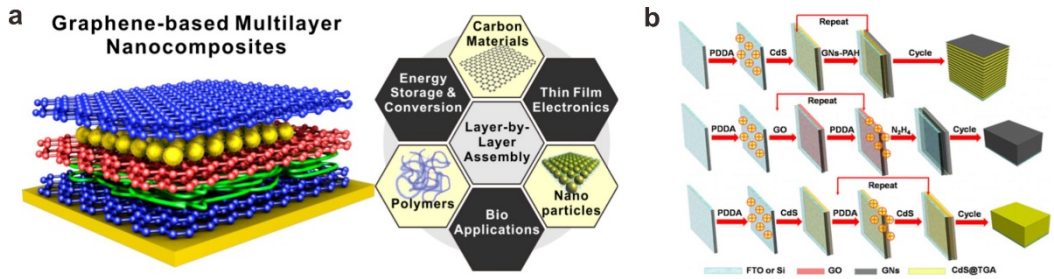

Figure 1.10. (a) Summary of the applications of graphene-based nanocomposites prepared by layer-by-layer (LbL) assembly. Reprinted with permission from ref 44. Copyright 2015 American Chemical Society. (b) Schematic Illustration for LbL Self-Assembly of graphene oxide−CdS QDs, Pure graphene oxide, and Pure CdS QDs Multilayered Films. Reprinted with permission from ref 45. Copyright 2014 American Chemical Society.

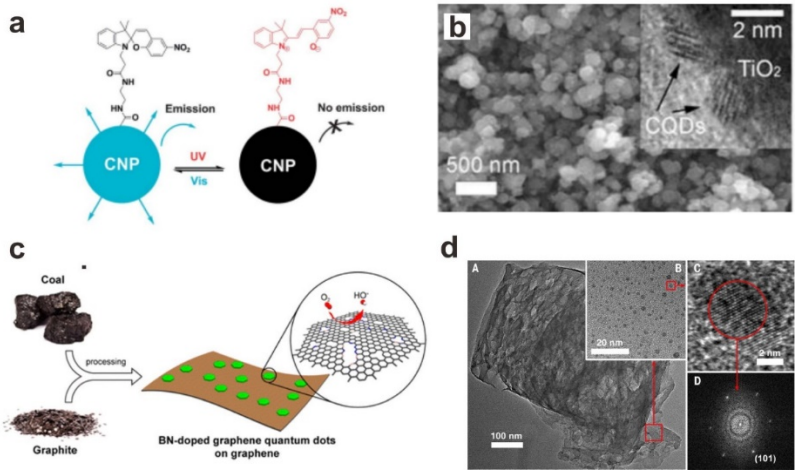

Figure 1.11. (a) Schematic illustration of light-induced fluorescence modulation of the spiropyran-functionalized carbon nanoparticles. Reprinted with permission from ref 46. Copyright 2013 Royal Society of Chemistry. (b) SEM and TEM images of TiO_2/carbon nanoparticles. Reprinted with permission from ref 49. Copyright 2010 Wiley. (c) Illustration of the preparation procedure for the boron and nitrogen doped carbon nanoparticles/graphene oxide. Reprinted with permission from ref 50. Copyright 2014 American Chemical Society. (d) TEM image of a grain of the carbon nanoparticles/C_3N_4 composite. Reprinted with permission from ref 51. Copyright 2015 Science.

Table 1.1. Ag/CDs hybrid nanomaterials

Ref.	Journal	Method	Morphology (Size in hybrid structure)	TEM image
[1]	**Nat. Photonics** 2013, 7, 732	Photo reduction (Our work)	Nanoparticle on the surface of CD (Ag: 3 nm, CD: 6 nm)	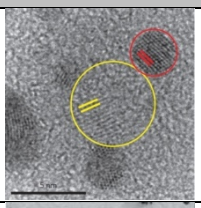
[2]	**Chem. Comm.** 2014, 50, 6592	Photo reduction	Aggregated nanoparticles (Ag: 30 nm, CD: undefined)	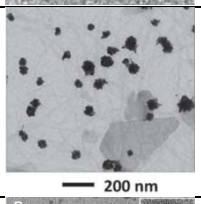
[3]	**Langmuir** 2013, 29, 16135	Thermal reduction	Single particle (Ag: 2 ~ 4 nm, CD: undefined)	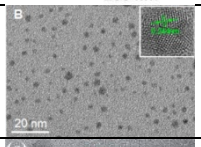
[4]	**Nanoscale** 2013, 5, 12558	Thermal reduction	Undefined dimeric structure (Ag: 0.5 nm, CD: 2.5 nm)	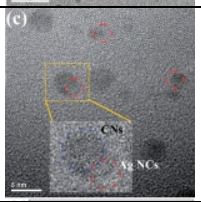
[5]	**Anal. Chem.** 2014, 86, 6689	Thermal reduction	Aggregated nanoparticle (Ag: 5 nm, CD: undefined)	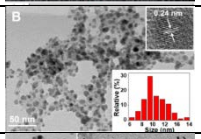
[6]	**J. Mater. Chem.** 2011, 21, 17638	Chemical reduction	Single particle (Ag: 5 nm, CD: undefined)	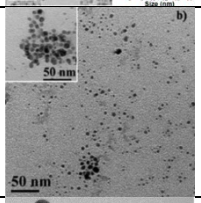
[7]	**Anal. Chem.** 2014, 86, 5002	Chemical reduction	Single particle (Ag: 18 nm, CD: undefined)	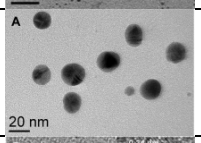
[8]	**ACS Catal.** 2014, 4, 328	Self-reduction	Single particle (Ag: 5 nm, CD: undefined)	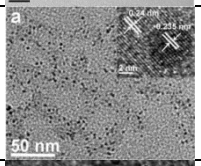
[9]	**Chem. Comm.** 2013, 49, 1079	Ag^{+} detection	Single particle (Ag: undefined, CD: undefined)	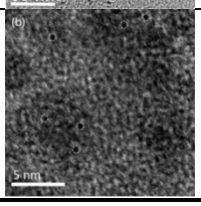

1.3. Application of hybrid materials based on nanocarbons

1.3.1. Biological application

Both GO and CDs are found to be feasible for drug delivery and therapeutic applications, because of biocompatibility and non-toxicity (Figure 1.12a).[5] The advantage of chemical modification of GO and CDs with organic molecules and polymer is the aqueous dispersity and colloidal stability. The characteristics of GO and CDs render it as a chemically versatile template with a high surface-to-volume ratio and oxygen groups, which can applied to a variety of biomedical applications such as imaging and cancer therapy.[52,53] Especially, CDs have reported simultaneous bioimaging and photodynamic therapy have been reported (Figure 1.12b).[54] Green emission of CDs is conjugated with photosensitizer, which results in high efficiency in therapy *in vivo* and *in vitro*. However, the targeted theranostics, a combination of diagnostics and therapy, is still challenging *in vivo* as well as *in vitro*.

1.3.2. Energy application

In fact, the research field in hybrid nanomaterials with GO and CDs is limited in bio application. However, recently, many efforts have been presented in energy application including photocatalyst, electrocatalyst, supercapacitor and photovoltaic devices (Figure 1.13a).[55]

First, in CDs, Haitao *et al*. demonstrate the high photo-catalytic yield (55.7 μmol g^{-1} h^{-1}) of CDs/Cu_2O for the reduction of CO_2 into methanol.[56] Furthermore, Au/CDs show 63.8% conversion efficiently and 99.9% selectivity for oxidation of cyclohexane to cyclohexanone under visible light.[57] C_3N_4/CDs is synthesized for the efficient water splitting, which show the highest catalytic efficiency and stability due to the high absorption and electron transfer behavior of CDs.[51] In addition, Ag-CDs hybrid nanomaterials synthesized by photo-reduction exhibits the excellent efficiency in light-emitting diode (current efficiency of 27.16 cd A^{-1} and a luminous efficiency of 18.54 lm W^{-1}) and solar cell (power conversion efficiency of 8.31% and an internal quantum efficiency of 99%) (Figure 1.13b).[58]

Second, in GO, PANI/GO hybrid composite exhibit the specific capacitance of 555 F g^{-1} at a discharge current density of 0.2 A g^{-1} and 92% of stability due to high conductivity of GO.[59] Furthermore, GO is limited to the aggregation of nanoparticles, which results in high efficiency in electrocatalyst. For example, Pt/GO show the enhanced catalytic efficiency rather that activated carbon (Figure 1.13c).[60] However, new metal and GO hybrid nanomaterials is imperative in electrocatalyst, because platinum has high cost and low durability.

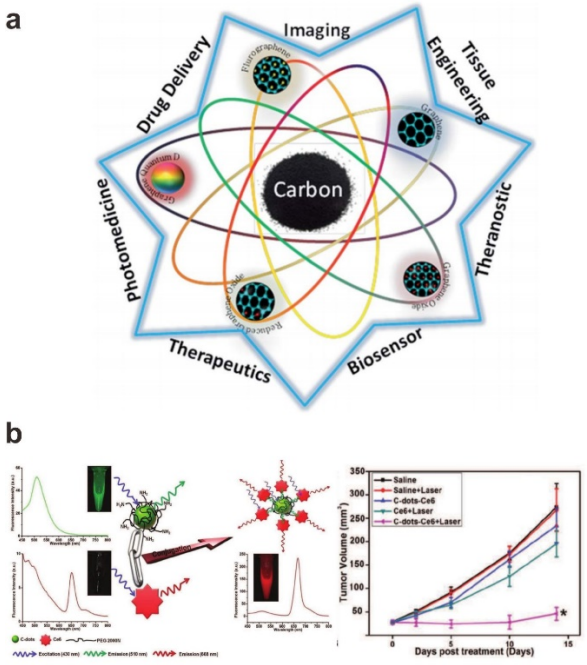

Figure 1.12. (a) The scheme represents the wide range bio applications of nanocarbons. Reprinted with permission from ref 5. Copyright 2015 Royal Society of Chemistry. (b) CDs/Ce6 composites and MGC803 tumor growth curves after various treatments. Reprinted with permission from ref 54. Copyright 2012 Wiley.

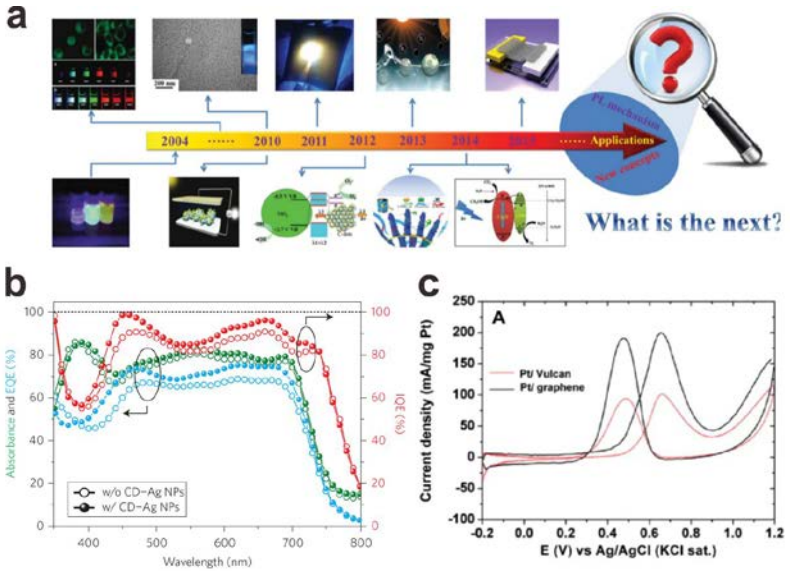

Figure 1.13. (a) Timeline showing recent progress and future outlook on the applications of carbon nanoparticles. Reprinted with permission from ref 55. Copyright 2015 Wiley. (b) Internal quantum efficiency of PTB7:PC71BM-based PSCs with Ag-carbon nanoparticles. Reprinted with permission from ref 58. Copyright 2013 Nature Publishing Group. (c) Cyclic voltammograms of Pt/graphene and Pt/Vulcan for methanol oxidation. Reprinted with permission from ref 60. Copyright 2009 Elsevier.

1.4. Overview of thesis

This thesis describes new hybrid nanomaterials based on defective nanocarbons for bio and energy applications. First, GO and CDs functionalized with small molecules, polymer, and metal nanoparticles is introduced in chapter 2 and 3. In addition, high PL intensity and solvent-dependent behavior of CDs is presented in chapter 4. The detailed information of PL properties of CDs is described in chapter 4.1.

Chapter 2 presents the synthesis of hybrid nanomaterials based on Au nanoparticles and GO nanosheet. In chapter 2.2, DMAP functionalized Au and GO nanocomposites is prepared, and they used as organic catalyst for the reduction of nitroarenes. In chapter 2.3, Au-GO film is developed through LbL method, which shows the high methanol oxidation catalytic efficiency.

Chapter 3 introduces hybrid nanomaterials based on CDs functionalized with polymer or metal nanoparticles. In chapter 3.2, CDs passivated with PEG and functionalized with folic acid as targeting molecules is developed for simultaneous bioimaging and photodynamic therapy. In chapter 3.3, heterodimeric structure of Ag-CD is synthesized through photo-reduction under UV light. The interface and SPR effect of Ag-CD can be easily modulated with the additives.

Chapter 4 is demonstrated the origin of PL properties of CDs. In chapter 4.2, the origin of high PL intensity of dual heteroatom doped CDs is elucidated through the structure analysis, photophysical properties, DFT calculation, and single molecule spectroscopy of heteroatom doped CDs. The graphitic structure, less oxygen group and none nitrogen related traps results in high PL properties in dual heteroatom doped CDs. Chapter 4.3 introduces the solvatochromic hybrid carbon nanosheets synthesized by hydrothermal reaction of small carbon molecules in the presence of GO. This nanosheets show solvent polarity-dependent emission, which is achieved on a wide range of wavelength from blue to orange. It results from the different energy level due to shape-tunable properties of nanosheets according to solvent polarity.

1.5. References

1. Stankovich, S.; Dikin, D. A.; Dommett, G. H. B.; Kohlhaas, K. M.; Zimney, E. J.; Stach, E. A.; Piner, R. D.; Nguyen, S. T.; Ruoff, R. S. Graphene-Based Composite Materials. *Nature* **2006,** *442*, 282-286.
2. Dreyer, D. R.; Park, S.; Bielawski, C. W.; Ruoff, R. S. The Chemistry of Graphene Oxide. *Chem. Soc. Rev.* **2010,** *39*, 228-240.
3. Wang, Y. F.; Hu, A. G. Carbon Quantum Dots: Synthesis, Properties and Applications. *J. Mater. Chem. C* **2014,** *2*, 6921-6939.
4. Zhu, Y. W.; Murali, S.; Cai, W. W.; Li, X. S.; Suk, J. W.; Potts, J. R.; Ruoff, R. S. Graphene and Graphene Oxide: Synthesis, Properties, and Applications. *Adv. Mater.* **2010,** *22*, 3906-3924.
5. Nurunnabi, M.; Parvez, K.; Nafiujjaman, M.; Revuri, V.; Khan, H. A.; Feng, X. L.; Lee, Y. K. Bioapplication of Graphene Oxide Derivatives: Drug/Gene Eelivery, Imaging, Polymeric Modification, Toxicology, Therapeutics and Challenges. *RSC. Adv.* **2015,** *5*, 42141-42161.
6. Wu, J. B.; Agrawal, M.; Becerril, H. A.; Bao, Z. N.; Liu, Z. F.; Chen, Y. S.; Peumans, P. Organic Light-Emitting Diodes on Solution-Processed Graphene Transparent Electrodes. *ACS Nano* **2010,** *4*, 43-48.
7. Liu, Z. Y.; Parvez, K.; Li, R. J.; Dong, R. H.; Feng, X. L.; Mullen, K. Transparent Conductive Electrodes from Graphene/PEDOT:PSS Hybrid Inks for Ultrathin Organic Photodetectors. *Adv. Mater.* **2015,** *27*, 669-675.
8. Wu, Z. S.; Ren, W. C.; Wen, L.; Gao, L. B.; Zhao, J. P.; Chen, Z. P.; Zhou, G. M.; Li, F.; Cheng, H. M. Graphene Anchored with Co_3O_4 Nanoparticles as Anode of Lithium Ion Batteries with Enhanced Reversible Capacity and Cyclic Performance. *ACS Nano* **2010,** *4*, 3187-3194.
9. Wu, Z. S.; Parvez, K.; Feng, X. L.; Mullen, K. Graphene-Based in-plane Micro-Supercapacitors with High Power and Energy Densities. *Nat. Commun.* **2013,** *4*, 2487.
10. Goenka, S.; Sant, V.; Sant, S. Graphene-Based Nanomaterials for Drug Delivery and Tissue Engineering. *J. Controlled Release* **2014,** *173*, 75-88.
11. Zhang, Y.; Zhang, L. Y.; Zhou, C. W. Review of Chemical Vapor Deposition of Graphene and Related Applications. *Acc. Chem. Res.* **2013,** *46*, 2329-2339.
12. Hernandez, Y.; Nicolosi, V.; Lotya, M.; Blighe, F. M.; Sun, Z. Y.; De, S.; McGovern, I. T.; Holland, B.; Byrne, M.; Gun'ko, Y. K.; Boland, J. J.; Niraj, P.; Duesberg, G.; Krishnamurthy, S.; Goodhue, R.; Hutchison, J.; Scardaci, V.; Ferrari, A. C.; Coleman, J. N. High-Yield Production of Graphene by Liquid-Phase Exfoliation of Graphite. *Nat. Nanotechnol.* **2008,** *3*, 563-568.

13. Parvez, K.; Wu, Z. S.; Li, R. J.; Liu, X. J.; Graf, R.; Feng, X. L.; Mullen, K. Exfoliation of Graphite into Graphene in Aqueous Solutions of Inorganic Salts. *J. Am. Chem. Soc.* **2014,** *136*, 6083-6091.
14. Hummers, W. S.; Offeman, R. E. Preparation of Graphitic Oxide. *J. Am. Chem. Soc.* **1958,** *80*, 1339-1339.
15. Gomez-Navarro, C.; Weitz, R. T.; Bittner, A. M.; Scolari, M.; Mews, A.; Burghard, M.; Kern, K. Electronic Transport Properties of Individual Chemically Reduced Graphene Oxide Sheets. *Nano Lett.* **2007,** *7*, 3499-3503.
16. He, H. Y.; Klinowski, J.; Forster, M.; Lerf, A. A New Structural Model for Graphite Oxide. *Chem. Phys. Lett.* **1998,** *287*, 53-56.
17. Pei, S. F.; Cheng, H. M. The Reduction of Graphene Oxide. *Carbon* **2012,** *50*, 3210-3228.
18. Chen, D.; Feng, H. B.; Li, J. H. Graphene Oxide: Preparation, Functionalization, and Electrochemical Applications. *Chem. Rev.* **2012,** *112*, 6027-6053.
19. Mattevi, C.; Eda, G.; Agnoli, S.; Miller, S.; Mkhoyan, K. A.; Celik, O.; Mastrogiovanni, D.; Granozzi, G.; Garfunkel, E.; Chhowalla, M. Evolution of Electrical, Chemical, and Structural Properties of Transparent and Conducting Chemically Derived Graphene Thin Films. *Adv. Funct. Mater.* **2009,** *19*, 2577-2583.
20. Eda, G.; Lin, Y. Y.; Mattevi, C.; Yamaguchi, H.; Chen, H. A.; Chen, I. S.; Chen, C. W.; Chhowalla, M. Blue Photoluminescence from Chemically Derived Graphene Oxide. *Adv. Mater.* **2010,** *22*, 505-509.
21. Sun, Y. P.; Zhou, B.; Lin, Y.; Wang, W.; Fernando, K. A. S.; Pathak, P.; Meziani, M. J.; Harruff, B. A.; Wang, X.; Wang, H. F.; Luo, P. J. G.; Yang, H.; Kose, M. E.; Chen, B. L.; Veca, L. M.; Xie, S. Y. Quantum-Sized Carbon Dots for Bright and Colorful Photoluminescence. *J. Am. Chem. Soc.* **2006,** *128*, 7756-7757.
22. Fernando, K. A. S.; Sahu, S.; Liu, Y. M.; Lewis, W. K.; Guliants, E. A.; Jafariyan, A.; Wang, P.; Bunker, C. E.; Sun, Y. P. Carbon Quantum Dots and Applications in Photocatalytic Energy Conversion. *ACS Appl. Mater. Inter.* **2015,** *7*, 8363-8376.
23. Cao, L.; Meziani, M. J.; Sahu, S.; Sun, Y. P. Photoluminescence Properties of Graphene versus Other Carbon Nanomaterials. *Acc. Chem. Res.* **2013,** *46*, 171-180.
24. Li, Y.; Zhao, Y.; Cheng, H. H.; Hu, Y.; Shi, G. Q.; Dai, L.; Qu, L. T. Nitrogen-Doped Graphene Quantum Dots with Oxygen-Rich Functional Groups. *J. Am. Chem. Soc.* **2012,** *134*, 15-18.
25. Dong, Y. Q.; Pang, H. C.; Yang, H. B.; Guo, C. X.; Shao, J. W.; Chi, Y. W.; Li, C. M.; Yu, T. Carbon-Based Dots Co-Doped with Nitrogen and Sulfur for High Quantum Yield and Excitation-Independent Emission. *Angew. Chem. Int. Ed.* **2013,** *52*, 7800-7804.
26. Sachdev, A.; Matai, I.; Gopinath, P. Implications of Surface Passivation on Physicochemical and Bioimaging Properties of Carbon Dots. *RSC Adv.* **2014,** *4*, 20915-

20921.

27. Anilkumar, P.; Cao, L.; Yu, J. J.; Tackett, K. N.; Wang, P.; Meziani, M. J.; Sun, Y. P. Crosslinked Carbon Dots as Ultra-Bright Fluorescence Probes. *Small* **2013,** *9*, 545-551.
28. Ding, H.; Yu, S. B.; Wei, J. S.; Xiong, H. M. Full-Color Light-Emitting Carbon Dots with a Surface-State-Controlled Luminescence Mechanism. *ACS Nano* **2016,** *10*, 484-491.
29. Tetsuka, H.; Nagoya, A.; Fukusumi, T.; Matsui, T. Molecularly Designed, Nitrogen-Functionalized Graphene Quantum Dots for Optoelectronic Devices. *Adv. Mater.* **2016**.
30. Hu, S.; Trinchi, A.; Atkin, P.; Cole, I. Tunable Photoluminescence across the Entire Visible Spectrum from Carbon Dots excited by White Light. *Angew. Chem. Int. Ed.* **2015,** *54*, 2970-2974.
31. Jiang, K.; Sun, S.; Zhang, L.; Lu, Y.; Wu, A.; Cai, C.; Lin, H. Red, Green, and Blue Luminescence by Carbon Dots: Full-Color Emission Tuning and Multicolor Cellular Imaging. *Angew. Chem. Int. Ed.* **2015,** *54*, 5360-5363.
32. Wang, X.; Cao, L.; Lu, F. S.; Meziani, M. J.; Li, H.; Qi, G.; Zhou, B.; Harruff, B. A.; Kermarrec, F.; Sun, Y. P. Photoinduced Electron Transfers with Carbon Dots. *Chem. Commun.* **2009,** 3774-3776.
33. Yeh, T. F.; Teng, C. Y.; Chen, S. J.; Teng, H. S. Nitrogen-Doped Graphene Oxide Quantum Dots as Photocatalysts for Overall Water-Splitting under Visible Light Illumination. *Adv. Mater.* **2014,** *26*, 3297-3303.
34. Huang, J. J.; Zhong, Z. F.; Rong, M. Z.; Zhou, X.; Chen, X. D.; Zhang, M. Q. An Easy Approach of Preparing Strongly Luminescent Carbon Dots and Their Polymer Based Composites for Enhancing Solar Cell Efficiency. *Carbon* **2014,** *70*, 190-198.
35. Cao, L.; Sahu, S.; Anilkumar, P.; Bunker, C. E.; Xu, J. A.; Fernando, K. A. S.; Wang, P.; Guliants, E. A.; Tackett, K. N.; Sun, Y. P. Carbon Nanoparticles as Visible-Light Photocatalysts for Efficient CO_2 Conversion and Beyond. *J. Am. Chem. Soc.* **2011,** *133*, 4754-4757.
36. Lim, S. Y.; Shen, W.; Gao, Z. Q. Carbon Quantum Dots and Their Applications. *Chem. Soc. Rev.* **2015,** *44*, 362-381.
37. Zhu, S. J.; Song, Y. B.; Zhao, X. H.; Shao, J. R.; Zhang, J. H.; Yang, B. The Photoluminescence Mechanism in Carbon Dots (Graphene quantum dots, Carbon nanodots, and Polymer dots): Current State and Future Perspective. *Nano Res.* **2015,** *8*, 355-381.
38. Baker, S. N.; Baker, G. A. Luminescent Carbon Nanodots: Emergent Nanolights. *Angew. Chem. Int. Ed.* **2010,** *49*, 6726-6744.
39. Zhuo, Q. Q.; Ma, Y. Y.; Gao, J.; Zhang, P. P.; Xia, Y. J.; Tian, Y. M.; Sun, X. X.; Zhong, J.; Sun, X. H. Facile Synthesis of Graphene/Metal Nanoparticle Composites via Self-

Catalysis Reduction at Room Temperature. *Inorg. Chem.* **2013,** *52*, 3141-3147.

40. Yin, P. T.; Shah, S.; Chhowalla, M.; Lee, K. B. Design, Synthesis, and Characterization of Graphene-Nanoparticle Hybrid Materials for Bioapplications. *Chem. Rev.* **2015,** *115*, 2483-2531.
41. Fang, Y. X.; Guo, S. J.; Zhu, C. Z.; Zhai, Y. M.; Wang, E. K. Self-Assembly of Cationic Polyelectrolyte-Functionalized Graphene Nanosheets and Gold Nanoparticles: A Two-Dimensional Heterostructure for Hydrogen Peroxide Sensing. *Langmuir* **2010,** *26*, 11277-11282.
42. Liu, H.; Gao, J.; Xue, M.; Zhu, N.; Zhang, M.; Cao, T. Processing of Graphene for Electrochemical Application: Noncovalently Functionalize Graphene Sheets with Water-Soluble Electroactive Methylene Green. *Langmuir* **2009,** *25*, 12006-12010.
43. Zhang, K.; Zhang, L. L.; Zhao, X.; Wu, J. Graphene/Polyaniline Nanofiber Composites as Supercapacitor Electrodes. *Chem. Mater.* **2010,** *22*, 1392-1401.
44. Lee, T.; Min, S. H.; Gu, M.; Jung, Y. K.; Lee, W.; Lee, J. U.; Seong, D. G.; Kim, B.-S. Layer-by-Layer Assembly for Graphene-based Multilayer Nanocomposites: Synthesis and Applications. *Chem. Mater.* **2015,** *27*, 3785-3796.
45. Xiao, F.-X.; Miao, J.; Liu, B. Layer-by-Layer Self-Assembly of CdS Quantum Dots/Graphene Nanosheets Hybrid Films for Photoelectrochemical and Photocatalytic Applications. *J. Am. Chem. Soc.* **2014,** *136*, 1559-1569.
46. Liao, B.; Long, P.; He, B. Q.; Yi, S. J.; Ou, B. L.; Shen, S. H.; Chen, J. Reversible Fluorescence Modulation of Spiropyran-Functionalized Carbon Nanoparticles. *J. Mater. Chem. C* **2013,** *1*, 3716-3721.
47. Zhang, H. C.; Ming, H.; Lian, S. Y.; Huang, H.; Li, H. T.; Zhang, L. L.; Liu, Y.; Kang, Z. H.; Lee, S. T. Fe_2O_3/Carbon Quantum Dots Complex Photocatalysts and Their Enhanced Photocatalytic Activity under Visible Light. *Dalton T* **2011,** *40*, 10822-10825.
48. Suzuki, K.; Malfatti, L.; Carboni, D.; Loche, D.; Casula, M.; Moretto, A.; Maggini, M.; Takahashi, M.; Innocenzi, P. Energy Transfer Induced by Carbon Quantum Dots in Porous Zinc Oxide Nanocomposite Films. *J. Phys. Chem. C* **2015,** *119*, 2837-2843.
49. Li, H. T.; He, X. D.; Kang, Z. H.; Huang, H.; Liu, Y.; Liu, J. L.; Lian, S. Y.; Tsang, C. H. A.; Yang, X. B.; Lee, S. T. Water-Soluble Fluorescent Carbon Quantum Dots and Photocatalyst Design. *Angew. Chem. Int. Ed.* **2010,** *49*, 4430-4434.
50. Fei, H. L.; Ye, R. Q.; Ye, G. L.; Gong, Y. J.; Peng, Z. W.; Fan, X. J.; Samuel, E. L. G.; Ajayan, P. M.; Tour, J. M. Boron- and Nitrogen-Doped Graphene Quantum Dots/Graphene Hybrid Nanoplatelets as Efficient Electrocatalysts for Oxygen Reduction. *ACS Nano* **2014,** *8*, 10837-10843.
51. Liu, J.; Liu, Y.; Liu, N.; Han, Y.; Zhang, X.; Huang, H.; Lifshitz, Y.; Lee, S.-T.; Zhong, J.; Kang, Z. Metal-Free Efficient Photocatalyst for Stable Visible Water Splitting via a

Two-Electron Pathway. *Science* **2015,** *347*, 970-974.

52. Li, J. L.; Tang, B.; Yuan, B.; Sun, L.; Wang, X. G. A Review of Optical Imaging and Therapy using Nanosized Graphene and Graphene Oxide. *Biomaterials* **2013,** *34*, 9519-9534.
53. Luo, P. J. G.; Yang, F.; Yang, S. T.; Sonkar, S. K.; Yang, L. J.; Broglie, J. J.; Liu, Y.; Sun, Y. P. Carbon-Based Quantum Dots for Fluorescence Imaging of Cells and Tissues. *RSC Adv.* **2014,** *4*, 10791-10807.
54. Huang, P.; Lin, J.; Wang, X.; Wang, Z.; Zhang, C.; He, M.; Wang, K.; Chen, F.; Li, Z.; Shen, G. Light-Triggered Theranostics Based on Photosensitizer-Conjugated Carbon Dots for Simultaneous Enhanced-Fluorescence Imaging and Photodynamic Therapy. *Adv. Mater.* **2012,** *24*, 5104-5110.
55. Li, X.; Rui, M.; Song, J.; Shen, Z.; Zeng, H. Carbon and Graphene Quantum Dots for Optoelectronic and Energy Devices: a Review. *Adv. Funct. Mater.* **2015,** *25*, 4929-4947.
56. Li, H.; Zhang, X.; MacFarlane, D. R. Carbon Quantum Dots/Cu_2O Heterostructures for Solar-Light-Driven Conversion of CO_2 to Methanol. *Adv. Energy Mater.* **2015,** *5*, 1401077.
57. Liu, R.; Huang, H.; Li, H.; Liu, Y.; Zhong, J.; Li, Y.; Zhang, S.; Kang, Z. Metal Nanoparticle/Carbon Quantum Dot Composite as a Photocatalyst for High-Efficiency Cyclohexane Oxidation. *ACS Catalysis* **2013,** *4*, 328-336.
58. Choi, H.; Ko, S. J.; Choi, Y.; Joo, P.; Kim, T.; Lee, B. R.; Jung, J. W.; Choi, H. J.; Cha, M.; Jeong, J. R.; Hwang, I. W.; Song, M. H.; Kim, B. S.; Kim, J. Y. Versatile Surface Plasmon Resonance of Carbon-Dot-Supported Silver Nanoparticles in Polymer Optoelectronic Devices. *Nat. Photonics* **2013,** *7*, 732-738.
59. Xu, J. J.; Wang, K.; Zu, S. Z.; Han, B. H.; Wei, Z. X. Hierarchical Nanocomposites of Polyaniline Nanowire Arrays on Graphene Oxide Sheets with Synergistic Effect for Energy Storage. *ACS Nano* **2010,** *4*, 5019-5026.
60. Li, Y. M.; Tang, L. H.; Li, J. H. Preparation and Electrochemical Performance for Methanol Oxidation of Pt/Graphene Nanocomposites. *Electrochem. Commun.* **2009,** *11*, 846-849.

Chapter 2. Hybrid Gold Nanoparticle-Graphene Oxide Nanosheets and Their Applications

2.1. Introduction

2.1.1. Hybrid Nanomaterials based on Graphene Oxide

In *Chapter 2*, large surface area and the abundant oxygen groups of graphene oxide (GO) is used as the supporting templates for gold nanoparticle (Au). GO can support to restrict the aggregation of nanoparticles in solution and solid state. Also, the high conductivity and electron mobility of GO is influenced to the efficiency in the various applications.

First, the mixture of Au and GO is synthesized with positive DMAP-Au and negative GO by covalent bonding.[1] Because of uniform size and high yield of Au nanoparticles as well as the catalytic effect of GO, it results in high catalytic efficiency for nitroarene reduction, compared with other hybrid nanomaterials.

Second, Au-GO film is developed through LbL method for methanol oxidation, which shows the significant effect in the stability and efficiency.[2] LbL method offers the opportunity to develop new type of 3D structure with controlled thickness. Due to the space between the layers and a high concentration of Au NPs on large surface area of GO, the catalytic efficiency in methanol oxidation is significantly enhanced.

2.1.2. Experimental

Preparation of GO

Graphene oxide is synthesized from graphite powder by a modified Hummers method.[3] In a pretreatment step that ensures complete oxidation, amounts of graphite powders (1 g), $K_2S_2O_8$ (0.5 g) and P_2O_5 (0.5 g) were added to 3 mL of concentrated H_2SO_4 with stirring. The mixture is kept at 80 °C for 4.5 hours, and then the mixture diluted with 1 L of DI water. The mixture is filtered and washed to remove all traces of acid. The solid dried overnight under ambient conditions.

For the oxidation step, the pretreated graphite is added to the 26 mL of H_2SO_4. 3 g of $KMnO_4$ was added slowly in an ice bath to ensure the temperature remained below 10 °C. Then, this mixture reacts at 35 ℃ for 2 hr and then added distilled water (46 mL) in ice bath. This mixture is stirred for 2 hours at 35 ℃, after which the heating is stopped and the mixture diluted

with 140 mL of water and 2.5 mL of 30% H_2O_2 is added to the mixture, resulting in a brilliant yellow color along with bubbling. The mixture is allowed to settle for at least a day after which the clear supernatant is decanted. The remaining mixture is filtered and washed with a 1 L of 10% HCl solution. The resulting solid is dried in air and diluted in distilled water that is put through dialysis for 2 weeks to remove any remaining metal. After which the products was centrifuged and washed several times with distilled water to neutralization and remove residual species. Finally, the dark brown GO powders were obtained through drying at 50 °C in vacuum oven for a day.

Preparation of DMAP–Au nanoparticles

The DMAP–Au nanoparticles were prepared according to a literature method.[4] In brief, 30 mM aqueous metal chloride solution ($HAuCl_4 \cdot 3H_2O$, 30 mL) was added to a 25 mM solution of tetraoctylammonium bromide in toluene (80 mL). A 0.40 M solution of freshly prepared $NaBH_4$ (25 mL) was added to the stirred mixture, which caused an immediate reduction to occur. After 30 min, the two phases were separated and the toluene phase was subsequently washed with 0.10 M H_2SO_4, 0.10 M NaOH, and H_2O (three times), and then dried over anhydrous Na_2SO_4. An aqueous 4-dimethylaminopyridine (DMAP) solution (0.10 M, 1.0 mL) was added to aliquots (1.0 mL) of the as-prepared nanoparticle mixtures. This concentration of DMAP was found to be sufficient to affect the complete and spontaneous phase transfer of the nanoparticles. Direct phase transfer across the organic/aqueous boundary was completed within 1 h without additional stirring.

2.1.3. References

1. Choi, Y.; Bae, H. S.; Seo, E.; Jang, S.; Park, K. H.; Kim, B. S. Hybrid Gold Nanoparticle-Reduced Graphene Oxide Nanosheets as Active Catalysts for Highly Efficient Reduction of Nitroarenes. *J. Mater. Chem.* **2011,** *21*, 15431-15436.
2. Choi, Y.; Gu, M.; Park, J.; Song, H. K.; Kim, B. S. Graphene Multilayer Supported Gold Nanoparticles for Efficient Electrocatalysts Toward Methanol Oxidation. *Adv. Energy Mater.* **2012,** *2*, 1510-1518.
3. Hummers, W. S.; Offeman, R. E. Preparation of Graphitic Oxide. *J. Am. Chem. Soc*. **1958,** *80*, 1339-1339.
4. Gittins, D. I.; Caruso, F. Spontaneous Phase Transfer of Nanoparticulate Metals from Organic to Aqueous Media. *Angew. Chem. Int. Ed.* **2001,** *40*, 3001-3004.

2.2. Hybrid Gold Nanoparticle-Graphene Oxide Nanosheets as Active Catalysts for Efficient Reduction of Nitroarene

2.2.1. Abstract

We demonstrate a simple, one-step synthesis of hybrid gold nanoparticle-graphene oxide nanosheets (Au-GO) through electrostatic self-assembly. This method affords a facile means of controlling over the effective concentration of the active Au nanoparticles onto the graphene sheets, but also offers the necessary stability of the resulting Au-GO nanostructure for catalytic transformation. Furthermore, this hybrid Au-GO is successfully employed in the catalytic reduction of a series of nitroarenes with a high catalytic activity. Through the careful investigations of the catalyst, we find the synergistic catalytic effect of Au nanoparticles and GO, further highlighting the significance of hybrid Au-GO nanostructure. Considering the wide potential applications of a two-dimensional graphene sheet as a host material for a variety of nanoparticles, the approach developed here may lead to new possibilities for the fabrication of hybrid nanoparticles - graphene nanosheet structures endowed with multiple functionalities.

2.2.2. Introduction

Graphene, a monolayer of aromatic carbon lattice has drawn a tremendous amount of attention in recent years in many fields of science and engineering.[2] The significant attraction can be attributed to its extraordinary electrical, optical, electrical, and mechanical properties of the graphene and related carbon nanostructures.[3-6] While earlier synthetic method of the graphene was challenging, there have been considerable advances in the synthetic and processing methods such as micromechanical exfoliation, oxidation/reduction protocols, epitaxial growth, and vapor deposition,[7-9] which allows the realization of the graphene-based materials into the realm of the current nanotechnology.[10-13] Among various types of graphene and related carbon nanostructures, a stable suspension of graphene oxide (GO) is the common choice over pristine graphene with its facile synthetic nature in a controlled, scalable, and reproducible manner.[14,15] The abundant oxygen-containing functional groups such as epoxide, alcohol, and carboxylic acids provides GO with excellent aqueous dispersity and also offers anchors for further chemical modifications.

Taking full advantages of the surface functional groups, together with its large specific

---

** Chapter 2.2. is reproduced in part with permission of "J. Mater. Chem.* ***2011****, 21, 15431". Copyright 2011 Royal Society of Chemistry.*

surface area, GO nanosheet is a promising support for the creation of hybrid nanomaterials, particularly for its catalytic applications.[16] To date, a number of examples have been reported to host a variety of metal, metal oxide, semiconducting, and magnetic nanoparticles on the surface of GO, including Pd,[17-19] Pt,[20-23] Au,[24-27] TiO_2,[28-31] Fe_3O_4.[32] Many of these examples find the applications primarily for electrocatalyst of the hybrid nanocomposites, however, few papers have been reported on the utilization of metal nanoparticles anchored on the graphenes and its catalytic activity in an organic transformation up to now.[17,33] For example, Mullhaupt and co-workers have reported the graphite oxide as supports for Pd nanoparticles, demonstrating the potential in Suzuki-Miyaura coupling reaction.[17]

In this study, we present a simple and facile approach of integrating gold nanoparticles (Au NPs) into the surface of graphene nanosheets based on the electrostatic self-assembly. This method not only provides a facile means of controlling the effective concentration of the active Au NPs, but also offers the necessary stability of the resulting nanocomposite. Furthermore, we exploit that the resulting hybrid gold nanoparticle-graphene oxide nanosheets (Au-GO) exhibit an excellent catalytic activity and selectivity toward the reduction of a series of model nitroarenes (Figure 2.2.1). For their mature synthetic protocols and catalytic properties, here we choose the Au NPs, but this method can be easily extended to other nanoparticles of sufficient surface charges. Considering the broad range of potential applications of two-dimensional graphene sheet as a host material in integrating a variety of nanoparticles, the approach developed here may lead to new possibilities for the fabrication of hybrid nanoparticle-graphene structures endowed with multiple functionalities.

2.2.3. Experimental

2.2.3.1. Preparation of hybrid Au–GO nanocomposites

The resulting GO suspension (15 mL, 0.50 mg mL^{-1}) was mixed with 5.0 mL of DMAP–Au nanoparticles (1 : 3 v/v ratio *vs.* GO, $r_{Au/GO}$ = 0.33), followed by stirring at room temperature for 3 h. Then, the resulting mixture was centrifuged and thoroughly washed with ethanol and deionized water (3 times) to remove free Au nanoparticles. Finally, the precipitate was redispersed in 5.0 mL of water. In addition, the amount of NPs was controlled by changing the volume ratio (v/v ratio of DMAP–Au : GO) from 3 : 1, 1 : 1, 1 : 3, 1 : 5, to 1 : 15.

2.2.3.2. Catalytic reduction of 4-nitrophenol by hybrid Au–GO nanocomposites

As a representative example, 0.25 mLof 1.49×10^{-4} M (0.50 mol% with respect to the gold concentration) Au–GO ($r_{Au/GO}$ = 0.33) was mixed with 1.0 mL of 2.22 M $NaBH_4$ (300 equiv.

to the substrate, >97%, TCI) solution, and the mixture was sonicated for 1 min at room temperature. Then, 10 mL of 7.50×10^{-4} M 4-nitrophenol (>99%, Aldrich) was added to the mixture and was allowed to stir until the deep yellow solution became colorless. The yellow color of the solution gradually vanished, indicating the reduction of 4-nitrophenol. The reaction progress was checked by assessing a small portion of the reaction mixture at a regular time interval (5 min). The concentration of 4-nitrophenol was determined spectrophotometrically at a wavelength of 400 nm using a SINCO S-3150 spectrophotometer.

2.2.3.3. Characterizations

The ζ-potential of colloidal suspensions at pH 6–8 was measured using a zeta potential analyzer (Malvern, Zetasizer nano-zs). The surface morphology of the samples was investigated using atomic force microscopy (AFM, Nanoscope V, Veeco) via a tapping mode and energy-filtering transmission electron microscope (TEM, Carl Zeiss-LIBRA 120). The composition of each component within the hybrid Au–GO was measured by using a thermogravimetric analyzer (TGA, TA Instrument). The fluorescence emission spectra of the hybrid solution were recorded by a fluorometer (Varian). An element analyzer (Thermo Scientific) determined the weight percentages of carbon, hydrogen, nitrogen, and oxygen of the hybrid Au–GO.

2.2.4. Results and discussion

2.2.4.1. Synthesis of hybrid Au-GO nanocomposites

GO suspensions were initially prepared according to the modified Hummers method from a commercial graphite powder.[34,35] Following the sonication for exfoliation of graphite oxide, the chemical functional groups introduced on the surface of graphene sheet such as carboxylic acids (COOH) render the prepared GO suspension negatively charged over a wide pH conditions ($GO\text{-}COO^-$). For example, the resulting $GO\text{-}COO^-$ nanosheets exhibit a fairly good colloidal stability with a zeta-potential of -44 ± 0.9 mV. The as-prepared colloidal suspension of GO mainly comprises of single-layered graphene nanosheet, possessing a thickness of about 0.7 nm with a lateral dimension of 0.70 – 1.5 μm, as determined by atomic force microscopy (AFM). In parallel, the positively charged Au NPs were prepared based on the spontaneous phase transfer of organic soluble Au NPs across aqueous phase by use of a readily available organic compound, 4-dimethylaminopyridine (DMAP), which ensures the monodispersity of the nanoparticles along with the necessary stability in aqueous solvents.[1] The resulting DMAP-coated Au NPs show an average diameter of 6 nm with a high surface potential of +35 mV. With the two oppositely charged nanostructures in hand, we have coupled them to form a stable hybrid nanocomposite

based on the electrostatic self-assembly between positively charged Au NPs and negatively charged GO-COO^- nanosheets. As soon as the Au NPs are added into the GO suspension, the precipitate is formed, which undergo successive cycles of centrifugation to remove unbound free Au NPs and redispersed in water. The obtained black homogeneous aqueous dispersion was stable without any noticeable aggregates for more than a month (Figure 2.2.1b).

2.2.4.2. Characterization of hybrid Au-GO nanocomposites

While varying the relative ratio of Au NPs to GO (hereafter, $r_{Au/GO}$) at a fixed amount of GO, we found that there is an optimum ratio between the Au NPs and GO that is required to provide the necessary aqueous stability to hybrid Au-GO (Figure 2.2.1a). The zeta-potential increases from -44 ± 0.9 mV (pure GO) to -26 ± 0.4 mV ($r_{Au/GO}$ = 0.33). Consequently, for catalytic applications, here we choose rAu/GO = 0.33, thus ensuring the stability of the composite during the reaction in aqueous media (Figure 2.2.1b). Furthermore, the zeta-potential even reversed to +2.7 ± 1.8 mV in the presence of excess Au NPs ($r_{Au/GO}$ = 3) which does not readily redisperse in water due to aggregation at this ratio (Figure 2.2.1c). UV/vis spectroscopy further supports that the surface plasmon resonance peak of starting Au NPs (λ_{max} = 514 nm) is not altered significantly after the formation of hybrid Au-GO (λ_{max} = 526 nm) (Figure 2.2.1d). It is also of note that the peak from DMAP is observed in the spectra of Au-GO hybrid.

The typical transmission electron microscopy (TEM) and AFM images exhibits the hybrid composite prepared from the hybrid Au-GO ($r_{Au/GO}$ = 0.33). The graphene sheets are covered with a high density of Au NPs as shown in all images. Interestingly, we found that the edges of graphene sheets as well as the basal planes are covered with Au NPs, although the densities are still higher at the edges due to the higher distribution of surface functional groups at the edges (Figure 2.2.2) ; however, given the strong interaction between Au NPs even with basal plane as observed in the TEM, we could not exclude the contribution arising from other intermolecular interactions such as the $\pi - \pi$ interactions between the residual π conjugated domains in GO and the aromatic surface stabilizer of Au NPs, namely, DMAP (Figure 2.2.3a). HR-TEM reveals the highly crystalline nature of Au NPs with a lattice spacing of 2.39 Å, as has been reported in literature (Figure 2.2.3b).[35] In addition, the AFM image supports the self-assembled structure of hybrid Au-GO. We found that the GO sheets bearing NPs are more corrugated as compared to the initial state of the GO before the assembly (Figure 2.2.3c). The AFM line scan also represents the individual Au NPs of approximately 6.0 nm in diameter are deposited onto the surface of functionalized GO with a height of 1.2 nm.

Independent of these observations, the Au NPs anchored on the surface of graphene nanosheets effectively quench the intrinsic fluorescence of the GO nanosheets, thus serving to further highlight the strong interactions between the two components (Figure 2.2.4).[36]

Thermogravimetric analysis (TGA) was employed to determine the relative composition of each component within hybrid Au-GO (Figure 2.2.5). As shown in the TGA curve, initial mass loss of water followed by the rapid decomposition of hybrid Au-GO is observed from the decomposition of labile oxygen-containing surface functional groups on GO. The relative composition can be determined from the final decomposed product, which suggests that approximately 62% Au NPs are contained in the hybrid Au-GO ($r_{Au/GO}$ = 0.33). Other hybrid Au-GO structures with varying composition ratio exhibit a similar trend of relative ratio of Au NPs with respect to the GO (Figure 2.2.5).

2.2.4.3. Application: Reduction of nitroarenes

After the careful investigation of the hybrid Au-GO nanocomposites prepared, it was employed in the catalytic reduction of a series of nitroarenes in the presence of $NaBH_4$ as a hydrogen source, because Au NPs are well known to be effective in the conversion of nitroarenes. Nitroarenes are typically found in industrial products and agricultural waste waters and known to be harmful and hazardous. As such, there are various physical, biological, and chemical methods such as adsorption, microbial degradation, and electrochemical treatment as well as catalytic reactions developed for the removal of nitroarenes. Among them, selective hydrogenation of nitroarenes to the corresponding aminoarenes is known as one of the fundamental reactions for the synthesis and manufacture of fine and industrial chemicals for the production of pharmaceutical and agrochemical products, dyes, rubbers, and polymers.

To evaluate the catalytic activity of hybrid Au-GO, we first tested the reduction of 4-nitrophenol with hybrid Au-GO ($r_{Au/GO}$ = 0.33). As shown in Figure 2.2.6a, the UV/vis spectra of the reaction mixture was monitored with the progress of the catalytic reduction of 4-nitrophenol. Specifically, the absorption of 4-nitrophenol at 400 nm decreases rapidly with a concomitant increase in the peak at 300 nm, which is attributed to the reduced product, 4-aminophenol. The isosbestic point between the two peaks is also observed, suggesting that the two principal species are responsible for the reaction conversion. From the UV/vis spectra, therefore, the pseudo-first-order reaction kinetics was applied to determine the reaction rate constant. From the linear relations of $\ln(C_t/C_0)$, shown in Figure 2.2.6b, we found that the rate constant, k, for this reaction is 0.124 min^{-1}, which is comparable to those reported previously.[37]

The control experiments further elucidated the reaction mechanism of hybrid Au-GO catalyst for the reduction of nitroarenes. To our surprise, the control experiment wherein GO is used exclusively in the above reaction yielded appreciable reduction of the reactant albeit at much lower efficiency under the reaction condition tested initially (5.0 mol% of catalyst, 50 equiv. of $NaBH_4$ to substrate). However, most notably when the amount of $NaBH_4$ is increased considerably (300 equiv. to substrate), the reaction proceeds in a highly effective manner

compared to 50 equiv. of $NaBH_4$, and it is also proved to occur well even in the absence of Au NPs. We then investigated to optimize the amount of catalyst as well as the amount of the $NaBH_4$ introduced during the reduction. After careful examinations, we found that not only the Au NPs, but also GO at its reduced state, which are commonly referred to as a reduced graphene oxide (rGO), is playing a key role in enhancing the catalytic efficiency of the reaction. Because $NaBH_4$ is commonly used to reduce GO to rGO,[38] the added reductant $NaBH_4$ in the course of nitroarenes can simultaneously reduce the GO, which in turn, the resulting rGO is responsible for the observed catalytic activity. In concert with our observation, Bao and co-workers have recently reported that rGO is capable of reducing nitroarenes with high efficiency at room temperature.[39] They attributed this catalytic activity of rGO to the unique electronic structure of the zigzag edges of graphene. This is an interesting observation using carbon material exclusively as a catalyst for organic transformation; nevertheless, it should be pointed out that our hybrid Au-GO still exhibits better catalytic activity relative to Au NP and GO nanosheets in all cases alone on account of the combined, synergistic catalytic effects of each component.

As shown in the Figure 2.2.7d, when the reaction rate constant, *k*, of each catalyst is compared, the Au-GO hybrid shows a strikingly higher catalytic efficiency (6.478 min^{-1}) than that from the respective catalyst, Au (0.069 min^{-1}) and GO (0.038 min^{-1}) (note the sum of rate constant from each Au and GO is significantly smaller than that of Au-GO hybrid). Other experiments under different reaction conditions all produced the identical results of increased catalytic activity in the hybrid Au-GO catalyst compared to individual component (Figure 2.2.7e). It is worth mentioning that the catalytic efficiency of GO is relatively higher at low catalyst content, whereas the catalytic efficiency of Au NPs becomes higher at high content of catalyst used. On the other hand, the catalytic efficiency of GO tends to increase upon addition of more $NaBH_4$ in all cases, which supports the key role of rGO in this reaction. We postulate that such increased catalytic activity of hybrid Au-GO is attributable to two factors: GO nanosheet that can promote the adsorption of reactants and facilitate the reaction kinetics with its free electrons on the surface and the additional stability of catalytic Au NPs supported by the graphene nanosheet that prevent the aggregation of NPs, which is common issues in using NP catalyst in organic transformation.

We have further investigated the catalytic activity of hybrid Au-GO for the reduction of other nitroarene analogues (Table 2.2.1). Here, we choose to run the reactions in the presence of 0.50 mol% of catalyst with 300 equiv. of $NaBH_4$ to clearly monitor the conversion efficiency of the reaction. As shown in Table 2.2.1, we found that our Au-GO hybrid exhibits high reactivity with excellent yields toward a series of model nitrophenols and anilines compounds regardless of the types and position of the substituents. For example, the Au-GO catalysts led to complete conversion of 4-aminophenol within 30 min (Table 2.2.1, entry 1). Interestingly, when the reduction of 4-, 3-, and 2-nitrophenols were catalyzed by Au-GO nanosheet, the 3- and 2-nitrophenols showed a better activity than that of 4-nitrophenol. Remarkably, the turnover

frequency (TOF) in entry 2 is 2400 s^{-1}, calculated by the moles of nitroarene consumed per moles of the hybrid Au-GO catalyst per 1 s under the present reaction condition. To the best of our knowledge, this is the highest activity of reduction of nitroarenes using Au NPs reported to date. Once again, this result highlights the utility of our hybrid Au-GO catalyst by the synergistic catalytic effect of Au NPs and GO nanosheet. As shown in the second series of experiments performed with various nitroanilines, the hybrid Au-GO still exhibits good catalytic activity. It is also interesting to note that the 3-nitroaniline displays the best conversion efficiency than other analogues, as similarly observed with the nitrophenols.

Finally, we have conducted identical reactions at various temperatures and observed the subtle increase in temperature has a significant impact on the reaction rate constants. The obtained rate constants were plotted to provide the activation energy of the reaction, which corresponds to be approximately 85.9 kJ/mol by deducing the Arrhenius plot (Figure 2.2.7f).

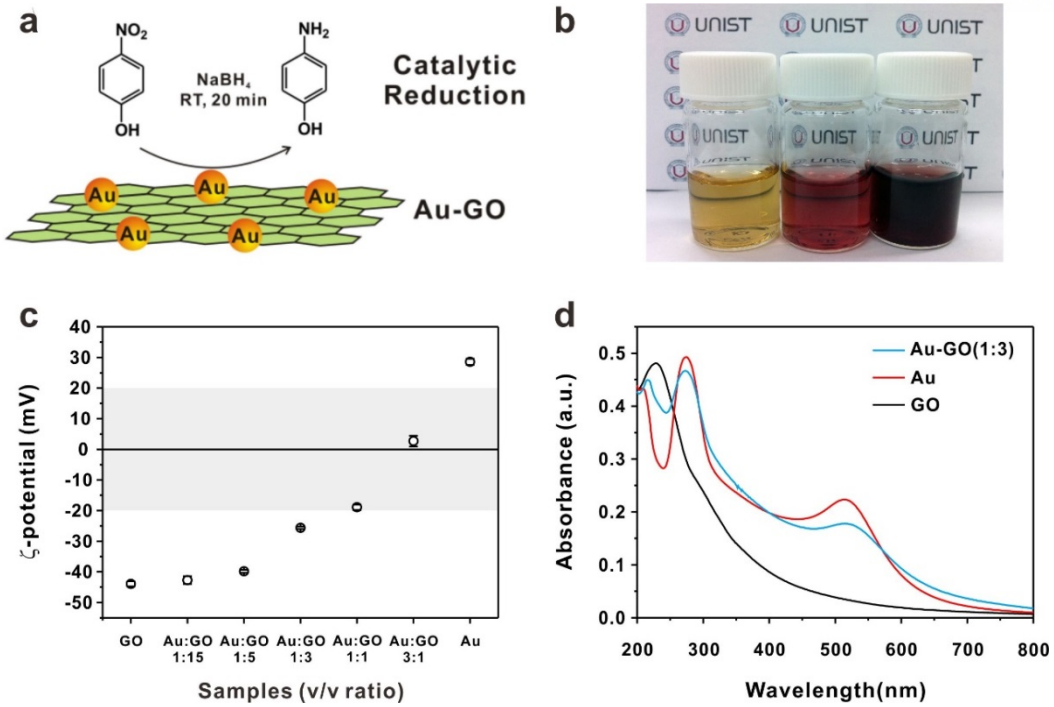

Figure 2.2.1. (a) Schematic illustration of electrostatic self-assembly of Au nanoparticles on GO nanosheets and their catalytic applications. (b) The corresponding images of suspensions of (left) GO, (middle) Au NPs, and (right) hybrid Au-GO ($r_{Au/GO}$ = 0.33). (c) Zeta-potential and (d) UV/vis spectra of hybrid Au-GO with different volume ratios of each component. All values are the average of three individual measurements with a standard deviation as an error bar.

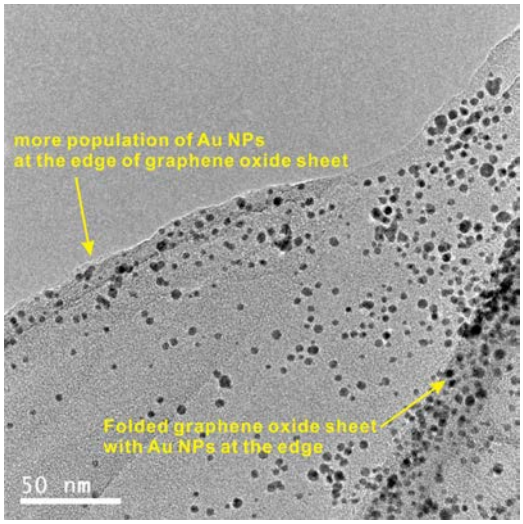

Figure 2.2.2. TEM image of hybrid Au-GO nanocomposites ($r_{Au/GO}$ = 0.33). More Au NPs are distributed to the edges of GO nanosheets possibly due to the higher distribution of surface functional groups at the edges.

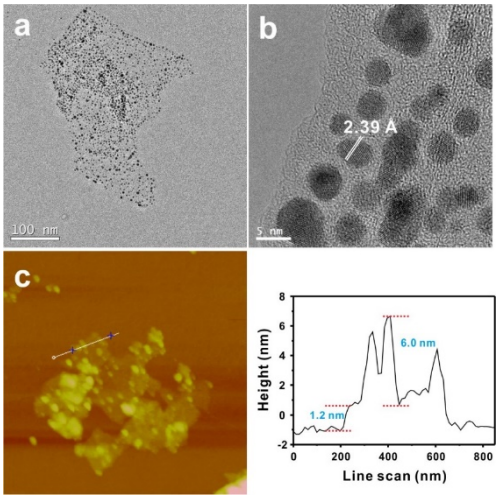

Figure 2.2.3. (a,b) TEM and (c) AFM images of hybrid Au-GO with a corresponding line scan profile. The scale is 5 μm × 5 μm × 10 nm.

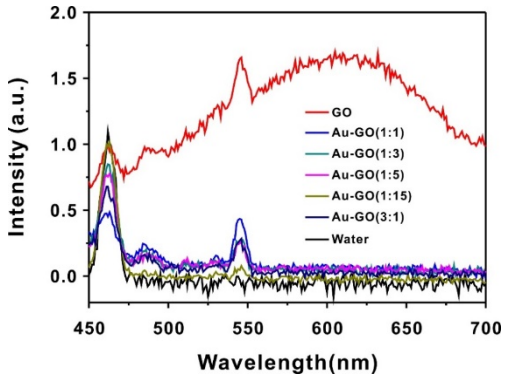

Figure 2.2.4. Fluorescence spectra of the hybrid Au-GO nanocomposites with a varying ratio of each component (λ_{ex} = 430 nm, λ_{em} = 450 - 700 nm). The intrinsic fluorescence of GO is quenched after the formation of hybrid Au-GO.

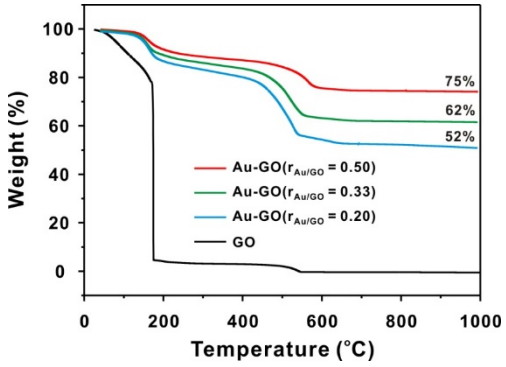

Figure 2.2.5. TGA thermograms of the hybrid Au-GO nanocomposites with a varying ratio of each component. The thermograms were obtained at a scan rate of 10 °C/min under air. The relative composition of Au NPs within the hybrid Au-GO is represented in each scan.

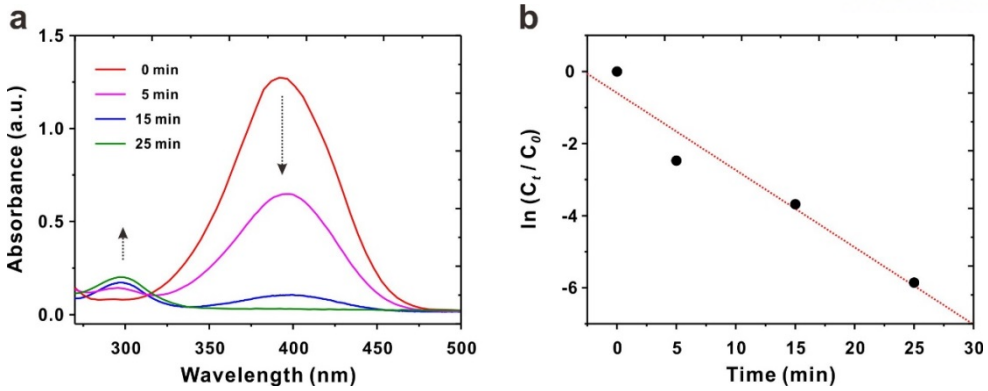

Figure 2.2.6. (a) Time-dependent UV/vis absorption spectra for the reduction of 4-nitrophenol over hybrid Au-GO catalyst in aqueous media at 298 K. (b) Plot of ln(C_t/C_0) versus time for the reduction of 4-nitrophenol. 5.0 mol% of catalyst and 50 equiv. of $NaBH_4$ are used for the reaction.

Table 2.2.1. Reduction of various nitroarenes using hybrid Au-GO catalyst[a]

Entry	Substrate	Product	Time/min	TOF (s^{-1})
1	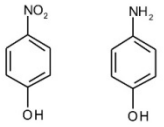		30	400
2	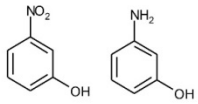		5	2400
3	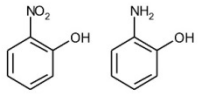		6	2000
4	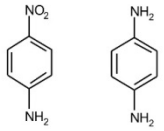		40	300
5	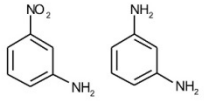		10	1200
6	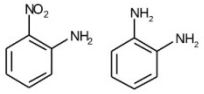		14	857

[a] Reaction condition: 10 ml of 7.50 × 10^{-4} M nitroarene, 0.25 mL of 1.49 × 10^{-4} M hybrid Au-GO (0.50 mol% with respect to the gold concentration), 1.0 ml of 2.22 M $NaBH_4$ (300 equiv. to the substrate).

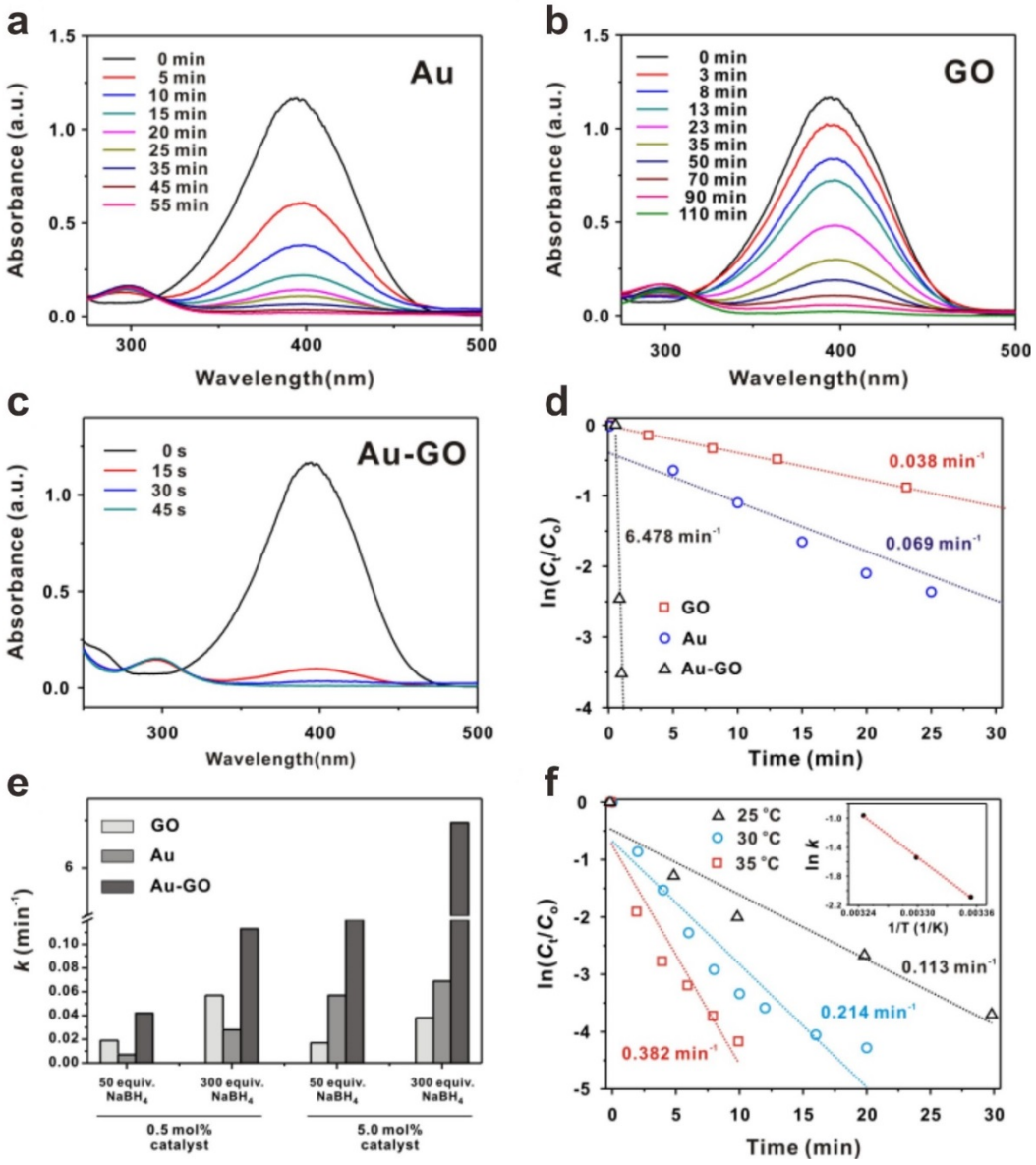

Figure 2.2.7. (a - c) Time-dependent UV/vis absorption spectra for the reduction of 4-nitrophenol over (a) Au, (b) GO, and (c) Au-GO catalyst in aqueous media at 298 K. (d) Plot of $\ln(C_t/C_0)$ versus time for the reduction of 4-nitrophenol with different catalysts. All catalysts are used at the same molar ratio of 5.0 mol% of catalyst and 300 equiv. of $NaBH_4$ for the reaction. (e) Comparison of reaction rate constants of all catalysts in this study. (f) Plot of $\ln(C_t/C_0)$ versus time and (inset) corresponding Arrhenius plot for the reduction of 4-nitrophenol over hybrid Au-GO catalysts under different temperatures at 0.50 mol% of catalyst and 300 equiv. of $NaBH_4$.

2.2.5. Conclusion

In conclusion, we have developed a simple, one-step synthesis of hybrid gold (Au) nanoparticles -graphene oxide (GO) nanosheets based on the electrostatic self-assembly of two oppositely charged suspensions of Au nanoparticles with GO nanosheets. This method affords a facile means of controlling over the effective concentration of the active Au nanoparticles onto the graphene sheets, but also offers the necessary stability of the resulting Au-GO nanostructure for catalytic transformation. The prepared hybrid Au-GO is successfully employed in the catalytic reduction of a series of nitroarenes with a high catalytic activity by the synergistic catalytic effect of Au nanoparticles and GO, further highlighting the importance of hybrid Au-GO nanostructure. Considering the wide potential applications of a two-dimensional graphene sheet as a host material for a variety of nanoparticles, the approach developed here may lead to new possibilities for integrating active nanoparticles with graphene nanosheets for advanced electronic, energy, and catalytic applications

2.2.6. References

1. Gittins, D. I.; Caruso, F. Spontaneous Phase Transfer of Nanoparticulate Metals from Organic to Aqueous Media. *Angew. Chem. Int. Ed.* **2001,** *40*, 3001-3004.
2. Novoselov, K. S.; Geim, A. K.; Morozov, S. V.; Jiang, D.; Zhang, Y.; Dubonos, S. V.; Grigorieva, I. V.; Firsov, A. A. Electric Field Effect in Atomically Thin Carbon Films. *Science* **2004,** *306*, 666-669.
3. Stankovich, S.; Dikin, D. A.; Dommett, G. H. B.; Kohlhaas, K. M.; Zimney, E. J.; Stach, E. A.; Piner, R. D.; Nguyen, S. T.; Ruoff, R. S. Graphene-Based Composite Materials. *Nature* **2006,** *442*, 282-286.
4. Balandin, A. A.; Ghosh, S.; Bao, W. Z.; Calizo, I.; Teweldebrhan, D.; Miao, F.; Lau, C. N. Superior Thermal Conductivity of Single-Layer Graphene. *Nano Lett.* **2008,** *8*, 902-907.
5. Lee, Z.; Jeon, K. J.; Dato, A.; Erni, R.; Richardson, T. J.; Frenklach, M.; Radmilovic, V. Direct Imaging of Soft-Hard Interfaces Enabled by Graphene. *Nano Lett.* **2009,** *9*, 3365-3369.
6. Loh, K. P.; Bao, Q. L.; Eda, G.; Chhowalla, M. Graphene Oxide as a Chemically Tunable Platform for Optical Applications. *Nat. Chem.* **2010,** *2*, 1015-1024.
7. Eda, G.; Fanchini, G.; Chhowalla, M. Large-Area Ultrathin Films of Reduced Graphene Oxide as aTtransparent and Flexible Electronic Material. *Nat. Nanotechnol.* **2008,** *3*, 270-274.
8. Kim, K. S.; Zhao, Y.; Jang, H.; Lee, S. Y.; Kim, J. M.; Kim, K. S.; Ahn, J. H.; Kim, P.; Choi, J. Y.; Hong, B. H. Large-Scale Pattern Growth of Graphene Films for Stretchable Transparent Electrodes. *Nature* **2009,** *457*, 706-710.
9. Novoselov, K. S.; Jiang, D.; Schedin, F.; Booth, T. J.; Khotkevich, V. V.; Morozov, S. V.; Geim, A. K. Two-Dimensional Atomic Crystals. *P. Nat. Acad. Sci. USA* **2005,** *102*, 10451-10453.
10. Dikin, D. A.; Stankovich, S.; Zimney, E. J.; Piner, R. D.; Dommett, G. H. B.; Evmenenko, G.; Nguyen, S. T.; Ruoff, R. S. Preparation and Characterization of Graphene Oxide Paper. *Nature* **2007,** *448*, 457-460.
11. Li, X. L.; Zhang, G. Y.; Bai, X. D.; Sun, X. M.; Wang, X. R.; Wang, E.; Dai, H. J. Highly Conducting Graphene Sheets and Langmuir-Blodgett Films. *Nat. Nanotechnol.* **2008,** *3*, 538-542.
12. Balapanuru, J.; Yang, J. X.; Xiao, S.; Bao, Q. L.; Jahan, M.; Polavarapu, L.; Wei, J.; Xu, Q. H.; Loh, K. P. A Graphene Oxide-Organic Dye Ionic Complex with DNA-Sensing and Optical-Limiting Properties. *Angew. Chem. Int. Ed.* **2010,** *49*, 6549-6553.
13. Li, Y.; Hu, Y.; Zhao, Y.; Shi, G. Q.; Deng, L. E.; Hou, Y. B.; Qu, L. T. An Electrochemical

Avenue to Green-Luminescent Graphene Quantum Dots as Potential Electron-Acceptors for Photovoltaics. *Adv. Mater.* **2011,** *23*, 776-780.

14. Li, D.; Muller, M. B.; Gilje, S.; Kaner, R. B.; Wallace, G. G. Processable Aqueous Dispersions of Graphene Nanosheets. *Nat. Nanotechnol.* **2008,** *3*, 101-105.
15. Park, S.; Ruoff, R. S. Chemical Methods for the Production of Graphenes. *Nat. Nanotechnol.* **2009,** *4*, 217-224.
16. Kamat, P. V. Graphene-Based Nanoassemblies for Energy Conversion. *J. Phys. Chem. Lett.* **2011,** *2*, 242-251.
17. Scheuermann, G. M.; Rumi, L.; Steurer, P.; Bannwarth, W.; Mulhaupt, R. Palladium Nanoparticles on Graphite Oxide and Its Functionalized Graphene Derivatives as Highly Active Catalysts for the Suzuki-Miyaura Coupling Reaction. *J. Am. Chem. Soc.* **2009,** *131*, 8262-8270.
18. Guo, S. J.; Dong, S. J.; Wang, E. K. Three-Dimensional Pt-on-Pd Bimetallic Nanodendrites Supported on Graphene Nanosheet: Facile Synthesis and Used as an Advanced Nanoelectrocatalyst for Methanol Oxidation. *ACS Nano* **2010,** *4*, 547-555.
19. Yang, J.; Tian, C. G.; Wang, L.; Fu, H. G. An Effective Strategy for Small-Sized and Highly-Dispersed Palladium Nanoparticles Supported on Graphene with Excellent Performance for Formic Acid Oxidation. *J. Mater. Chem.* **2011,** *21*, 3384-3390.
20. Yoo, E.; Okata, T.; Akita, T.; Kohyama, M.; Nakamura, J.; Honma, I. Enhanced Electrocatalytic Activity of Pt Subnanoclusters on Graphene Nanosheet Surface. *Nano Lett.* **2009,** *9*, 2255-2259.
21. Zhou, Y. G.; Chen, J. J.; Wang, F. B.; Sheng, Z. H.; Xia, X. H. A Facile Approach to the Synthesis of Highly Electroactive Pt Nanoparticles on Graphene as an Anode Catalyst for Direct Methanol Fuel Cells. *Chem. Commun.* **2010,** *46*, 5951-5953.
22. Guo, S. J.; Wen, D.; Zhai, Y. M.; Dong, S. J.; Wang, E. K. Platinum Nanoparticle Ensemble-on-Graphene Hybrid Nanosheet: One-Pot, Rapid Synthesis, and Used as New Electrode Material for Electrochemical Sensing. *ACS Nano* **2010,** *4*, 3959-3968.
23. Zhang, S.; Shao, Y. Y.; Liao, H. G.; Engelhard, M. H.; Yin, G. P.; Lin, Y. H. Polyelectrolyte-Induced Reduction of Exfoliated Graphite Oxide: A Facile Route to Synthesis of Soluble Graphene Nanosheets. *ACS Nano* **2011,** *5*, 1785-1791.
24. Muszynski, R.; Seger, B.; Kamat, P. V. Decorating Graphene Sheets with Gold Nanoparticles. *J. Phys. Chem. C* **2008,** *112*, 5263-5266.
25. Fang, Y. X.; Guo, S. J.; Zhu, C. Z.; Zhai, Y. M.; Wang, E. K. Self-Assembly of Cationic Polyelectrolyte-Functionalized Graphene Nanosheets and Gold Nanoparticles: A Two-Dimensional Heterostructure for Hydrogen Peroxide Sensing. *Langmuir* **2010,** *26*, 11277-11282.
26. Hong, W. J.; Bai, H.; Xu, Y. X.; Yao, Z. Y.; Gu, Z. Z.; Shi, G. Q. Preparation of Gold

Nanoparticle/Graphene Composites with Controlled Weight Contents and Their Application in Biosensors. *J. Phys. Chem. C* **2010,** *114*, 1822-1826.

27. Wang, Y.; Zhang, S.; Du, D.; Shao, Y. Y.; Li, Z. H.; Wang, J.; Engelhard, M. H.; Li, J. H.; Lin, Y. H. Self Assembly of Acetylcholinesterase on a Gold Nanoparticles-Graphene Nanosheet Hybrid for Organophosphate Pesticide Detection using Polyelectrolyte as a Linker. *J. Mater. Chem.* **2011,** *21*, 5319-5325.
28. Hu, Y. S.; Kienle, L.; Guo, Y. G.; Maier, J. High Lithium Electroactivity of Nanometer-Sized Rutile TiO_2. *Adv. Mater.* **2006,** *18*, 1421-1426.
29. Wang, D. H.; Choi, D. W.; Li, J.; Yang, Z. G.; Nie, Z. M.; Kou, R.; Hu, D. H.; Wang, C. M.; Saraf, L. V.; Zhang, J. G.; Aksay, I. A.; Liu, J. Self-Assembled TiO_2-Graphene Hybrid Nanostructures for Enhanced Li-Ion Insertion. *ACS Nano* **2009,** *3*, 907-914.
30. Zhang, X. Y.; Li, H. P.; Cui, X. L.; Lin, Y. H. Graphene/TiO_2 Nanocomposites: Synthesis, Characterization and Application in Hydrogen Evolution from Water Photocatalytic Splitting. *J. Mater. Chem.* **2010,** *20*, 2801-2806.
31. Manga, K. K.; Wang, S.; Jaiswal, M.; Bao, Q. L.; Loh, K. P. High-Gain Graphene-Titanium Oxide Photoconductor Made from Inkjet Printable Ionic Solution. *Adv. Mater.* **2010,** *22*, 5265-5270.
32. Li, B. J.; Cao, H. Q.; Shao, J.; Qu, M. Z.; Warner, J. H. Superparamagnetic Fe_3O_4 Nanocrystals@Graphene Composites for Energy Storage Devices. *J. Mater. Chem.* **2011,** *21*, 5069-5075.
33. Tang, Z. H.; Shen, S. L.; Zhuang, J.; Wang, X. Noble-Metal-Promoted Three-Dimensional Macroassembly of Single-Layered Graphene Oxide. *Angew. Chem. Int. Ed.* **2010,** *49*, 4603-4607.
34. Hummers, W. S.; Offeman, R. E. Preparation of Graphitic Oxide. *J. Am. Chem. Soc*. **1958,** *80*, 1339-1339.
35. Hong, T. K.; Lee, D. W.; Choi, H. J.; Shin, H. S.; Kim, B. S. Transparent, Flexible Conducting Hybrid Multi layer Thin Films of Multiwalled Carbon Nanotubes with Graphene Nanosheets. *ACS Nano* **2010,** *4*, 3861-3868.

2.3. Graphene Multilayer Supported Gold Nanoparticles for Efficient Electrocatalysts toward Methanol Oxidation

2.3.1. Abstract

We report a simple method of integrating electroactive gold nanoparticles (Au NPs) with graphene oxide (GO) nanosheet support by layer-by-layer (LbL) assembly for the creation of 3-dimensional electrocatalytic thin films that are active towards methanol oxidation. This approach involves the alternating assembly of two oppositely charged suspensions of Au NPs with GO nanosheets based on electrostatic interactions. The GO nanosheets not only serve as structural components of the multilayer thin film, but also potentially improve the utilization and dispersion of Au NPs by taking advantages of the high catalytic surface area and the electronic conduction of graphene nanosheets. Furthermore, we found that the electrocatalytic activity of the multilayer thin films of Au NPs with graphene nanosheet is highly tunable with respect to the number of bilayers and thermal treatment, benefiting from the advantageous features of LbL assembly. Because of the highly versatile and tunable properties of LbL assembled thin films coupled with electrocatalytic NPs, we anticipate that the general concept presented here will offer new types of electrocatalysts for direct methanol fuel cells.

2.3.2. Introduction

Harnessing energy from green resources and developing suitable storage systems are the top priorities in current researches on energy systems. Direct methanol fuel cells (DMFCs) have received a considerable attention as an attractive power source for various systems due to their high energy density, ease of handling and processing, low operation temperatures and environmental benignity.[1-3] Despite significant progress in the development of efficient DMFCs, it is desirable to develop highly efficient and cost-effective electrocatalysts for key reaction in DMFCs such as methanol oxidation.[4-6] Although platinum or its alloys are the most popular choices for electrocatalysts, they usually suffer from several disadvantages such as poisoning effect, corrosion to some electrolytes, and high cost, all of which hamper the commercialization of DMFCs.[7-10] Therefore, recent efforts have been geared toward the development of more efficient catalyst without compromising the performance of the devices. Recently, the unique

---

properties of gold nanoparticles (Au NPs) were found to exhibit superior electrocatalytic activity towards CO oxidation, methanol oxidation, water gas shift reaction, and electro-oxidation.[11-14] However, there are still obstacles in utilizing Au NPs because they often experience irreversible aggregation during electrocatalytic cycles, leading to a significant loss of nanoscale catalytic effect. Thus, they need a proper electrocatalytic support in order to preserve the intrinsic surface properties as it is known that the support materials have a strong influence on the electrocatalytic activity of the NPs.[15-17]

Among many potential candidates for electrocatalytic support, graphene, a monolayer of two-dimensional carbon lattice, is an appealing choice with its remarkable electrical, thermal, and mechanical properties.[18-20] In particular, solution processable graphene nanosheets typically prepared by chemical exfoliation present unique advantages in a controlled, scalable, and reproducible production of single sheet graphene dispersions.[21-23] Taking full advantage of the surface functional groups and high conductivity together with its high specific surface area, graphene nanosheet is an excellent substrate for hosting and growing nanomaterials for high-performance electrochemical and electrocatalytic applications.[24] A number of examples have been reported to host a variety of metal, metal oxide, semiconducting, and magnetic nanoparticles on the surface of graphene nanosheets for the creation of electroactive hybrid nanomaterials;[25-29] however, few papers have reported the utilization of Au NPs anchored on the graphene nanosheets and its electrocatalytic activity.[30]

In that regard, layer-by-layer (LbL) assembly offers a variety of opportunities for preparing multilayer thin films of desired functions with a nanometer scale control over the composition and thickness as a true nanoscale blending method.[31,32] The integration of graphenes and related nanostructures into multilayer films by LbL assembly has been recently demonstrated from a number of examples;[33-35] yet, many of these studies are limited in creating electrically conducting structures and utilizing them in transparent electrodes. Herein, we report the integration of electroactive Au NPs with a graphene oxide nanosheet support by LbL assembly for the creation of 3-dimensional electrocatalytic thin films that are active toward methanol oxidation (Figure 2.3.1).

In specific, positively charged 4-dimethylaminopyridine (DMAP) coated Au NPs and negatively charged graphene oxide (GO) nanosheets are assembled based on the electrostatic interactions on a silicon wafer or ITO-coated glass to afford the multilayer thin films of Au NPs supported by GO nanosheets. In this study, the GO nanosheet not only serves as a structural component of the multilayer thin film, but also potentially improves the utilization and dispersion of Au NP catalysts by taking advantages of high catalytic surface area, chemical stability, and the electronic conduction of graphene nanosheet. Furthermore, we found that the electrocatalytic activity of the multilayer thin films of Au NPs with graphene nanosheet is highly tunable with respect to the number of bilayers, assembly conditions, and post-treatment, benefiting from the

advantageous features of LbL assembly. Here we choose the Au NPs for their mature synthetic protocols and fine catalytic activity, yet this method can be readily extended to other NPs of sufficient surface charges that can be assembled by electrostatic LbL assembly. Considering the wide-ranging potential applications of two-dimensional graphene sheets as host material for a variety of NPs, the approach developed here may lead to new possibilities for the fabrication of hybrid NP-graphene structures endowed with multiple functionalities.

2.3.3. Experimental

2.3.3.1. Layer-by-layer assembly of $(Au/GO)_n$ multilayer film

Silicon and ITO-coated glass substrate was cleaned by piranha solution to remove any organic contamination and treated with (3-aminopropyl)triethoxysilane to introduce hydrophilic and positively charged surface. The substrate was dipped into negatively charged GO solution (0.5 mg/mL) at pH 4 for 10 min. It was then dipped into DI water for 1 min three times to remove loosely bound GO. Subsequently, the substrate was then dipped into positively charged DMAP-coated Au NPs solution for 10 min, and washed with DI water three times for 1 min, which afford one-bilayer film of $(Au/GO)_1$. The above procedures were repeated to achieve the desired number of bilayers. These as-assembled $(Au/GO)_n$ multilayer films were subjected thermal reduction at 100 ^oC or 150 ^oC for 12 h in an oven.

2.2.3.2. Electrocatalytic characterizations

Electrochemical experiments were performed on Biologic science instrument, VSP using a standard three electrode cell. A platinum wire was used as a counter electrode and Hg/HgO as a reference. The working electrode was $(Au/GO)_n$ multilayer thin film. Cyclic voltammetry (CV) and linear sweep voltammetry (LSV) were performed between 0.0 to 0.6 V in 0.1 M KOH solution with or without 1.0 M methanol solution at room temperature at a scan rate of 20 mV/s. Electrochemical impedance spectroscopy (EIS) measurements were carried out in the frequency range from 100 kHz to 100 mHz under AC stimulus of 10 mV in amplitude.

2.2.3.3. Characterizations

The ζ-potential of colloidal suspensions was measured using Malvern, Zetasizer nano-zs. The absorbance of the thin films was characterized by using UV/vis spectroscopy (VARIAN, Cary 5000). The surface morphology of the samples was investigated using atomic force microscopy (AFM, Nanoscope V, Veeco), scanning electron microscopy (SEM, FEI, NOVA NANOSEM230) and transmission electron microscope (TEM, Carl Zeiss-LIBRA 120).

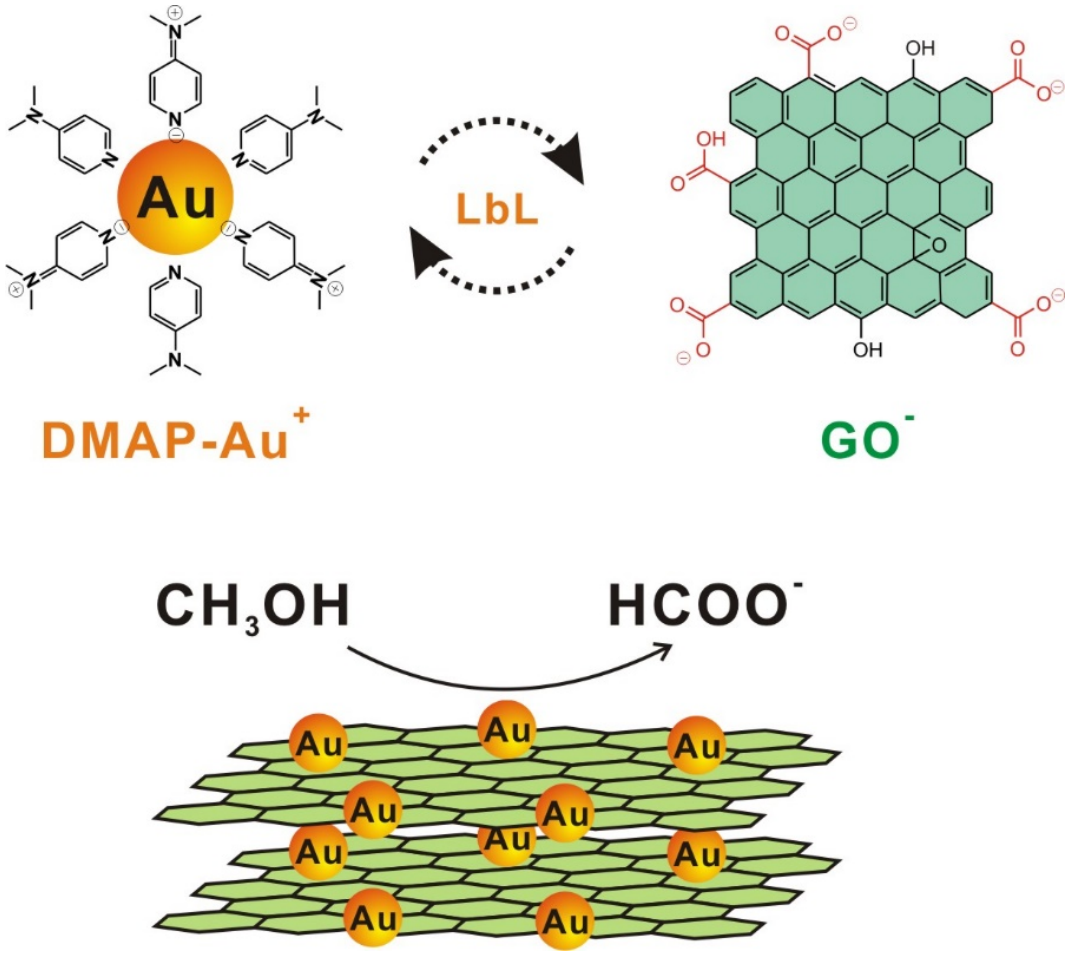

Figure 2.3.1. Schematic representation of layer-by-layer (LbL) assembled $(Au/GO)_n$ multilayer thin film for methanol oxidation.

2.3.4. Results and discussion

2.3.4.1. Synthesis of GO and Au nanoparticles

In order to introduce the GO into an LbL system based on the electrostatic interactions, a negatively charged GO suspension was initially prepared according to the modified Hummers method from a commercially available graphite powder.[36] Following sonication for exfoliation of the graphite oxide, the chemical functional groups introduced on the surface of the graphene sheet such as carboxylic acids rendered the prepared GO suspension negatively charged over a wide range of pH conditions and displayed the pH-responsive features. Consistent with other reports, the changes of ζ-potential with external pH conditions are typical characteristics for weak polyelectrolytes that allow the tuning of internal structures within the multilayer thin film.[37] Atomic force microscopy (AFM) further revealed that the prepared GO suspension mainly comprised a single-layer graphene nanosheet having a thickness of approximately 0.70 nm with lateral dimensions of 0.70–1.5 μm (Figure 2.3.2). Subsequently, positively charged Au NPs were prepared based on the spontaneous phase transfer of organic soluble Au NPs across the aqueous phase using 4-dimethylaminopyridine (DMAP), a readily available organic ligand that affords the necessary stability in aqueous solution.[38] The resulting DMAP-coated Au NPs had an average diameter of 6 nm with a high surface potential of +35 mV at pH 11.

2.3.4.2. Synthesis of GO multilayer supported Au nanoparticles

With these two stable suspensions of Au NPs and GO, we have fabricated multilayer films by repeatedly dip-coating onto a planar silicon substrate or ITO-coated glass slide to afford the multilayer in an architecture of $(Au/GO)_n$ (n = number of bilayers (BL), typically n = 2 - 10) (Figure 2.3.3). After the LbL assembly, the multilayer thin films of $(Au/GO)_n$ were subjected to a mild thermal reduction process to restore the electrical conductivity according to the previous protocols.[39,40] Moreover, we postulate here that the DMAP ligands that were present on the surface of Au NPs would prevent the effective electrocatalytic activity during the oxidation of methanol, as it is well known that the surface passivating ligands play an important role in controlling the activity of NPs at the interface between NPs and electrolytes during the electrocatalytic reactions.[41] Consequently, in this study we chose two different temperatures to the melting point of DMAP ligands (110 ˚C), 100 ˚C and 150 ˚C to see the effect of the surface ligand mobility within the multilayers during the electrocatalytic oxidation of methanol.

As shown in Figure 2.3.3, the successful growth of multilayers was monitored by the gradual increase of characteristic surface plasmon absorbance of Au NPs within the multilayer film. As similarly observed in other report, the surface plasmon broadens when assembled within

the multilayer film and exhibits the bathochromic red-shift compared to individual Au NPs (λ_{max} = 514 nm), which resulted from the coupled plasmon interactions of Au NPs in close proximity within the same layer and/or adjacent layers.[42] Interestingly, the absorbance of the multilayer film decreased upon thermal treatment and the overall broad spectra blue-shifted from ca. 620 nm to 540 nm, indicating the reorganization of the as-assembled Au NPs within the multilayer film. This effect is particularly pronounced in the 8-bilayer film after thermal treatment due to the increased amount of Au NPs as illustrated by the sudden drop of absorbance. In addition, the linear growth curve clearly demonstrates the uniform multilayer formation after each assembly.

According to the representative AFM images, the initial depositions of only a few layers displayed overlaid sheets of GO with a high density of Au NPs that were anchored well on the surface of the graphene nanosheets (Figure 2.3.4 and Figure 2.3.5). Interestingly, the edges of individual graphene sheets were clearly visible in the as-assembled 2-bilayer film, whereas the individual sheets appeared to stack together as the number of bilayers increased. The surface roughness generally increased with the progress of LbL assembly, regardless of the post-treatment. On the other hand, for example, surface root-mean-square roughness (R_{rms}) values of 2- and 6-bilayers were determined to be 6.97 and 6.83 nm, respectively, which decreased to 5.65 and 6.19 nm after thermal annealing at 150 $^{\circ}$C (averaged over 10 × 10 μm^2). The decreased surface roughness can be ascribed to the reorientation of Au NPs with the increased mobility of the ligand and the densification of the thin film during thermal treatment. This observation is consistent with reduced aggregation of Au NPs within the multilayers after thermal treatment as suggested in the UV/vis spectra. Additionally, the scanning electron microscopy (SEM) and transmission electron microscopy (TEM) images illustrate the successful deposition of Au NPs on top of the GO nanosheets leading to the increased density of Au NPs and GO nanosheet without significant changes in the size of Au NPs (Figure 2.3.6 and 2.3.7).

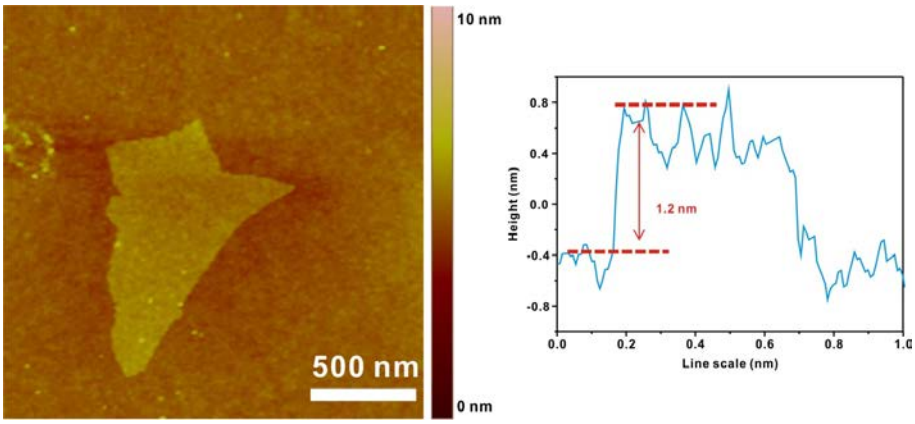

Figure 2.3.2. Representative AFM image of graphene oxide nanosheet with a corresponding line scan.

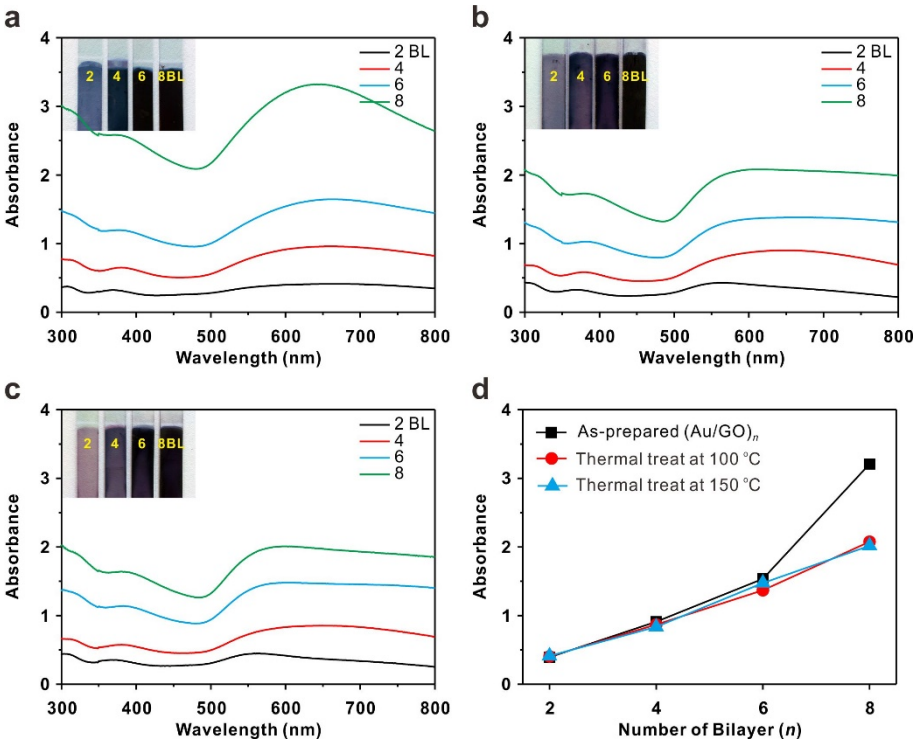

Figure 2.3.3. (a-c) UV/vis absorbance spectra of $(Au/GO)_n$ multilayer thin films. (a) as-prepared, (b) thermal treated at 100 °C and (c) thermal treated at 150 °C. (d) The corresponding absorbance maxima at 600 nm according to the number of bilayers. Inset image represents the samples measured.

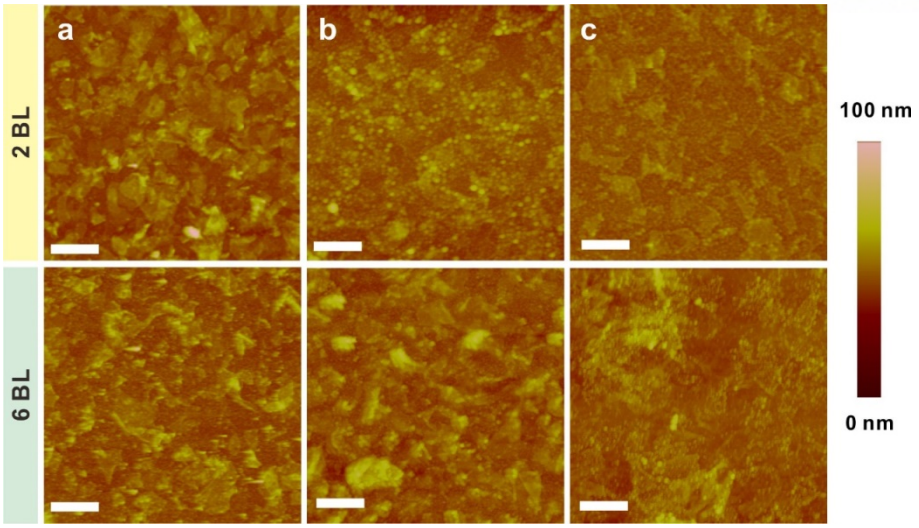

Figure 2.3.4. Representative AFM images of $(Au/GO)_n$ multilayer thin films of 2- and 6-bilayer. (a) as-assembled films, (b) thermal treated at 100 ˚C and (c) thermal treated at 150 ˚C. The scale bar of each image is 1 μm. Note the surface morphology changes in the $(Au/GO)_n$ multilayer films after thermal treatment.

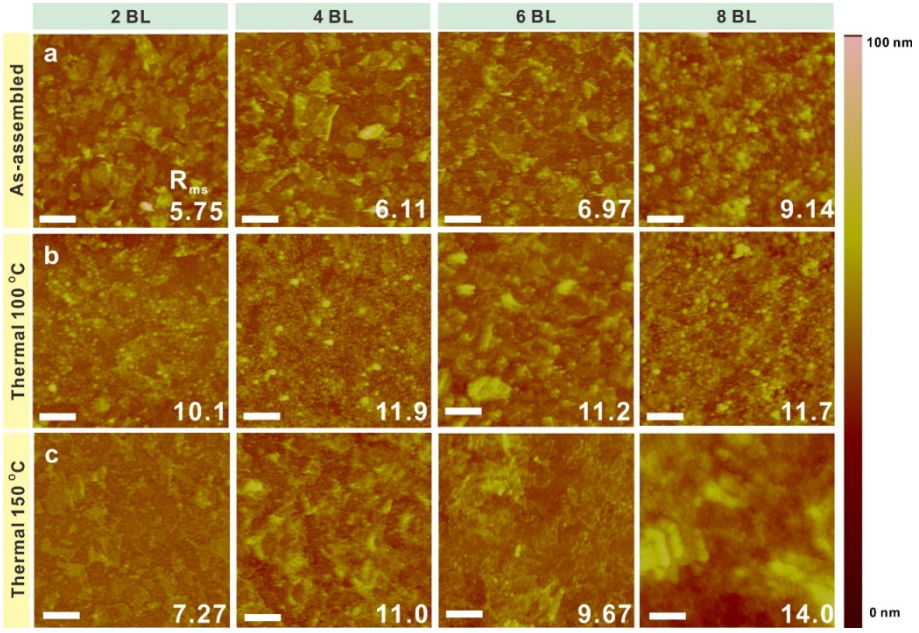

Figure 2.3.5. AFM images of $(Au/GO)_n$ multilayer thin films. (a) as-assembled films, (b) thermal treated at 100 ˚C and (c) thermal treated at 150 ˚C. The scale bar of each image is 5 μm. The number in the figure indicates the root-mean-square (RMS) surface roughness.

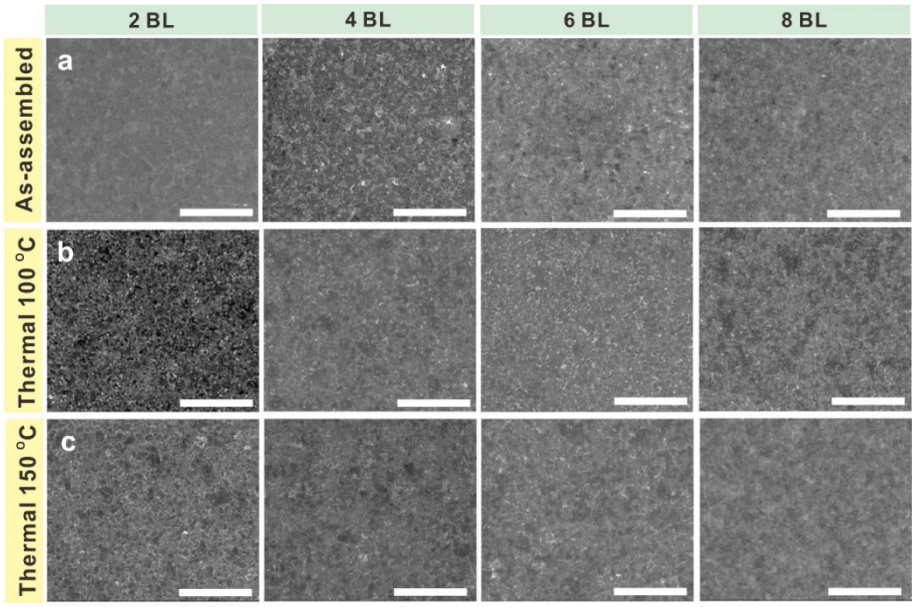

Figure 2.3.6. SEM images of $(Au/GO)_n$ multilayer thin films. (a) as-assembled films, (b) thermal treated at 100 ˚C and (c) thermal treated at 150 ˚C. The scale bar of each image is 5 μm.

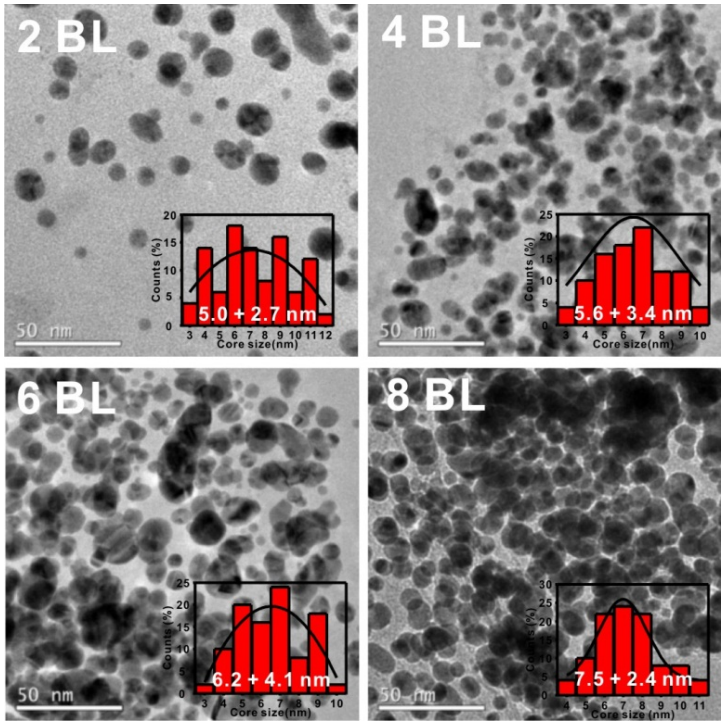

Figure 2.3.7. TEM images of as-assembled $(Au/GO)_n$ multilayer thin films with a histogram of size distribution of Au nanoparticles.

2.3.4. Application: Methanol oxidation

After careful examination of the assembled $(Au/GO)_n$ multilayers films, the electrochemical characteristics toward the oxidation of methanol were first investigated by running the cyclic voltammetry of the multilayer thin films in a 0.10 M KOH solution with and without methanol under N_2 atmosphere (Figure 2.3.8). In the absence of methanol, the forward sweep shows an onset potential of 0.35 V (vs Hg/HgO), which indicates the adsorption of OH^- and subsequent formation of surface oxide on Au NPs at a higher potential as described in the following reactions (1) and (2).

$$Au + OH^- \rightarrow Au\text{-}OH_{ads}^{(1-\lambda)-} + \lambda e^- \quad (1)$$

$$Au\text{-}OH_{ads}^{(1-\lambda)-} + OH^- \rightarrow AuO + H_2O + (2-\lambda)e^- \quad (2)$$

,where OH_{ads} represents the directly chemisorbed OH^- on Au, and the charge transfer coefficient λ varies between 0 and 1 depending on the extent of the faradaic reaction (0 for a non-faradaic reaction and 1 for a faradaic reaction).

In the backward sweep, a reduction peak at 0.12 V was observed, which corresponds to the reduction of the surface oxide layer and desorption of OH^- from the Au NPs.[43] It is of note that both oxidation and reduction peaks in all samples appear nearly at the same position irrespective of the number of bilayers; however, the samples treated at 150 ˚C generally exhibited superior electrocatalytic activity to those treated at 100 ˚C. Interestingly, we found that the current density of the $(Au/GO)_n$ multilayer films treated at 150 ˚C increased as the number of bilayers increased, up to 6-bilayer; however, the current density subsequently diminished as in Figure 2.3.8d. When 1.0 M of methanol was added to the system, the cyclic voltammograms changed significantly; for example, large anodic current peaks at 0.38 and 0.36 V and cathodic current peak at 0.11 and 0.17 V were observed for the 6-bilayer film treated at 100 ˚C and 150 ˚C, respectively. Cyclic voltammetry of $(Au/GO)_6$ thin films thermal treated at 150 ˚C samples showed that the anodic peak currents are linearly proportional to the square root of scan rates, providing the electrocatalytic oxidation of methanol is governed by diffusion-controlled process (Figure 2.3.9).

The enhanced current at all voltage ranges is attributed to the improved kinetics of methanol oxidation promoted by the following catalytic conversion reaction (3) on the surface of the Au NPs with surface adsorbed OH^- as well as the solution OH^- that yields more number of electrons upon oxidation of methanol. In general, λ is regarded as 0 as presented in Figure 2.3.1.

$$CH_3OH + Au\text{-}OH_{ads}^{(1-\lambda)-} + 4OH^- \rightarrow \quad HCOO^- + Au + 4H_2O + (4-\lambda)e^- \quad (3)$$

The control experiment of LbL-assembled all-GO multilayer films of $(GO/GO)_n$ did not

show any measurable peak under the identical potential window, confirming the key role of Au NPs responsible for the electrocatalytic oxidation of methanol in our system (Figure 2.3.10).[34,35,44,45] Moreover, the thermal treatment of $(Au/GO)_6$ film at a higher temperature 300 ˚C does not improve the electrocatalytic activity toward the methanol oxidation significantly, albeit the electronic conductivity increased considerably compared to that after thermal treatment at 150 ˚C, suggesting the ligand mobility atop Au NPs is critical in enhancing the overall electrocatalytic activity (Figure 2.3.10).

As demonstrated already in Figure 2.3.8d, we found that there is an optimum film thickness present when the forward anodic peak is plotted with respect to the number of bilayers (all insets in Figure 2.3.8). In all samples, the current density increased with the number of bilayers, obviously due to the increased concentration of active Au NPs within the multilayer films up to 6 bilayers. On the other hand, the forward anodic peak current began to decrease after the 6-bilayer film, possibly due to the limited diffusion of methanol into the hybrid electrode with increased thickness as well as to the reduced electron and mass transfer to outer NPs as similarly observed in other work (Figure 2.3.11).[46] This observation features the importance of LbL assembly which can afford the precise control over the architecture of the electrode in achieving the best performance with a given set of components via simple electrode fabrication technique.

The active amount of Au NPs can be obtained from the inductively-coupled plasma – mass spectrometry (ICP-MS), which allows us to attain mass-specific peak currents of 44 and 90 mA/mg for the 6-bilayer film treated at 100 ˚C and 150 ˚C, respectively, in 0.10 M KOH with 1.0 M CH_3OH. This value is superior to the recent report of 50 mA/mg from Pt NPs embedded within the polyelectrolyte multilayers, suggesting the highly efficient catalytic activity of a $(Au/GO)_n$ multilayer electrode without using high-cost Pt catalyst.[46] Also, Zhang and co-workers reported 48.6 mA/mg in 0.10 M KOH and 5.0 M CH_3OH with Au NPs supported on a commercial activated carbon (Vulcan XC-72R).[47] In case of our $(Au/GO)_6$ film after 150 ˚C treatment, we found significantly higher catalytic activity of 273 mA/mg under the identical reaction condition.

Although more stringent stability tests are necessary in order to meet the requirements for actual fuel cell performance, we observe that the multiple electrocatalytic cycles of $(Au/GO)_6$ films thermal treated at 150 ˚C show a stable electrochemical response over 100 cycles with a retention of 88% (Figure 2.3.12a and 2.3.12b). In a clear contrast, the free Au NPs without GO support have a significantly lower cyclic stability of 44% with a low current density (0.107 mA/cm^2 *vs* 0.696 mA/cm^2 of $(Au/GO)_6$ film), emphasizing the critical role of graphene nanosheet as a chemically stable support in preserving the catalytic active surface of Au NPs during electrochemical cycles (Figure 2.3.12c and 2.3.12d). Moreover, the Au NPs supported on conductive amorphous Ketjen Black does not show comparable stability (52.3%), suggesting a unique 3-dimensional LbL structure is critical in preventing the coalescence of high surface energy Au NPs each other (Figure 2.3.13).

Further investigation was made into the electrochemical characteristics of methanol oxidation in the 6-bilayer $(Au/GO)_6$ film after thermal treatment at 150 ˚C. Under the increasing concentration of methanol, the anodic peak current (i_a) increased linearly with methanol concentration as shown in Figure 2.3.14.

The cathodic peak current (i_c), on the other hand, decreased with increasing methanol concentration, which could be attributed to reduced Au oxide coverage upon sweeping to negative potential. Figure 2.3.14b displays the Tafel plot of the methanol oxidation as a function of methanol concentration at a scan rate of 20 mV/s. The Tafel plot has two distinct linear ranges that change its slope significantly at 0.15 V, corresponding to the potential of maximum cathodic peak current. The Tafel slope of 267 ± 2.4 mV/dec is obtained for the potential range of 0.15 – 0.25 V with a calculated transfer coefficient, αn, of 0.22. This suggests that the first charge transfer is the rate-determining step.[48-50] The overall reaction order of methanol oxidation with respect to the concentration of methanol can be estimated from the slope of linear fit of 0.89 at different potentials (Figure 2.3.15), which suggests that the methanol oxidation mechanism in the Tafel ranges remains constant irrespective of increasing concentration of methanol.[47]

Electrochemical impedance spectroscopy provides good information of the kinetics and interfacial resistance that are critical in the evaluation of the electrochemical reactions.[51,52] The charge transfer resistances (R_{ct}) of the methanol oxidation reaction at the surface of Au NPs within the $(Au/GO)_n$ multilayer film are measured with varying number of bilayers and thermal treatment. As demonstrated in Figure 2.3.16, the Nyquist plot determined the R_{ct} values of 6-bilayer films that are for lower than those of 8-bilayer film, such as 7362 ohm (6 bilayer) and 18807 ohm (8 bilayer) in 100 ˚C treated samples and 118.3 ohm (6 bilayer) and 1859 ohm (8 bilayer) in 150 ˚C samples, respectively. This result indicates the 6-bilayer films possess the better electrocatalytic performance than that of the 8-bilayer film which is in good agreement with the previous data.[53] The Nyquist plot also clearly supports the claim that heat treatment at 150 ˚C can reduce the interfacial resistance of Au NPs for an enhanced catalytic activity toward methanol oxidation. Once again, this supports our postulation of the enhanced mobility of surface ligand upon heat treatment above its melting point.

In addition, when we increased the assembly pH of GO from 4 to 11, the electrocatalytic activity could be further controlled due to the changes in the amount of Au NPs on the graphene sheets as well as the internal structure of electrode, which led to influence the overall catalytic activity (Figure 2.3.17). This result further highlights the potential of LbL assembly in fine tuning the catalytic activity of the current system toward the development of more efficient electrocatalyst and it will be the subject of our on-going endeavour.

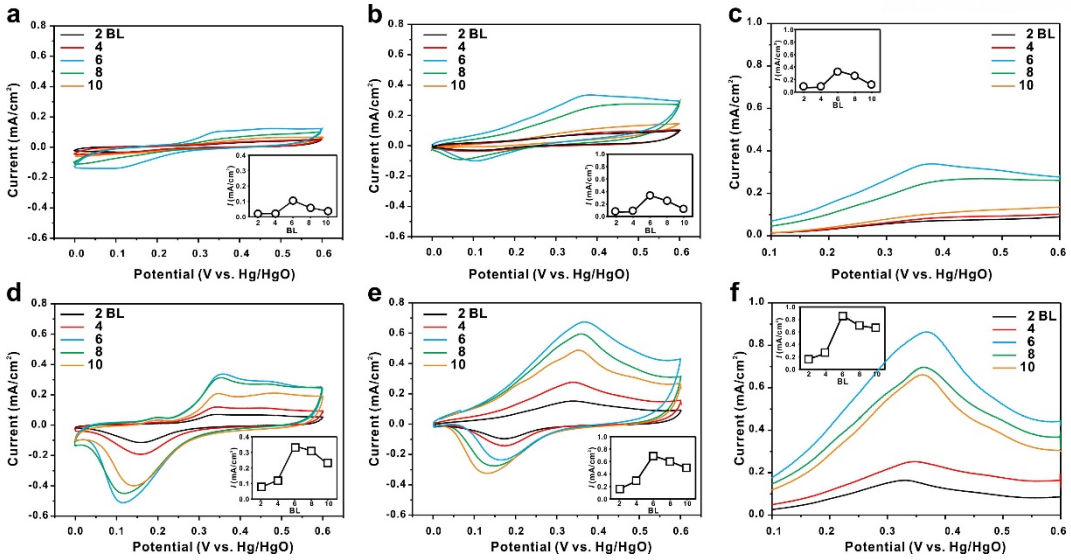

Figure 2.3.8. (a,b,d,e) Cyclic voltammograms (CV) of $(Au/GO)_n$ multilayer thin films thermal treated at (a) 100 ˚C and (d) 150 ˚C samples measured in 0.10 M KOH without CH_3OH. (b) 100 ˚C and (e) 150 ˚C samples measured in 0.10 M KOH with 1.0 M CH_3OH. (c, f) Linear sweep voltammetry (LSV) of $(Au/GO)_n$ thin films thermal treated at (c) 100 ˚C and (f) 150 ˚C measured in 0.10 M KOH with 1.0 M CH_3OH. The insets in all images show the current density plot as a function of number of bilayer (BL). All measurements were carried out in a saturated N_2 at a scan rate of 20 mV/s.

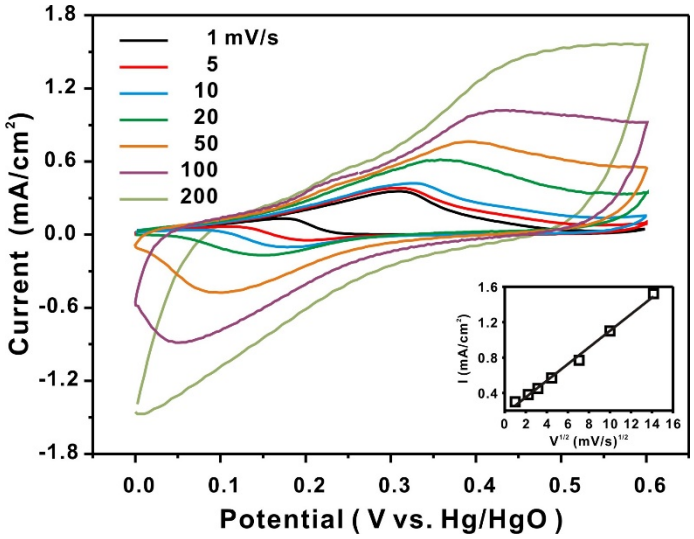

Figure 2.3.9. Cyclic voltammetry of $(Au/GO)_6$ thin films thermal treated at 150 ˚C samples measured in 0.10 M KOH with 1.0 M CH_3OH in a saturated N_2 with various scan rates. The inset represents the linear response of current density with respect to the square root of scan rates.

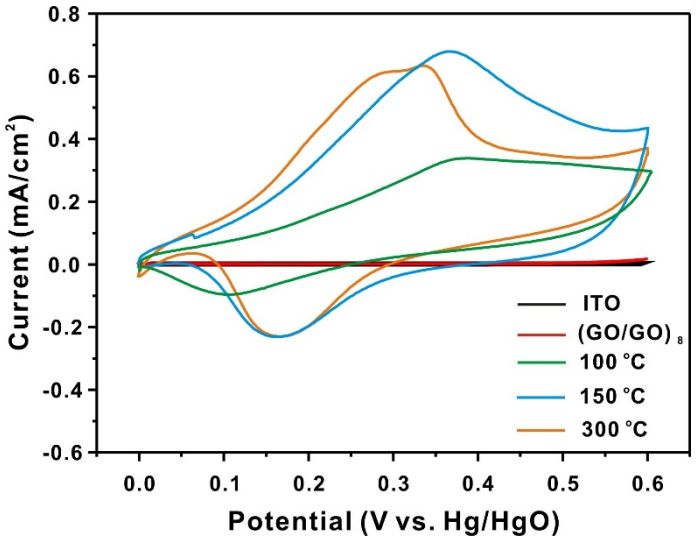

Figure 2.3.10. Cyclic voltammograms of $(GO/GO)_6$ and $(Au/GO)_6$ thin films thermal treated at 100 ˚C, 150 ˚C, and 300 ˚C measured in 0.10 M KOH with 1.0 M CH_3OH in a saturated N_2 at a scan rate of 20 mV/s. Note that the plain ITO-glass substrate and $(GO/GO)_6$ thin film do not contribute to the catalytic activity toward methanol oxidation.

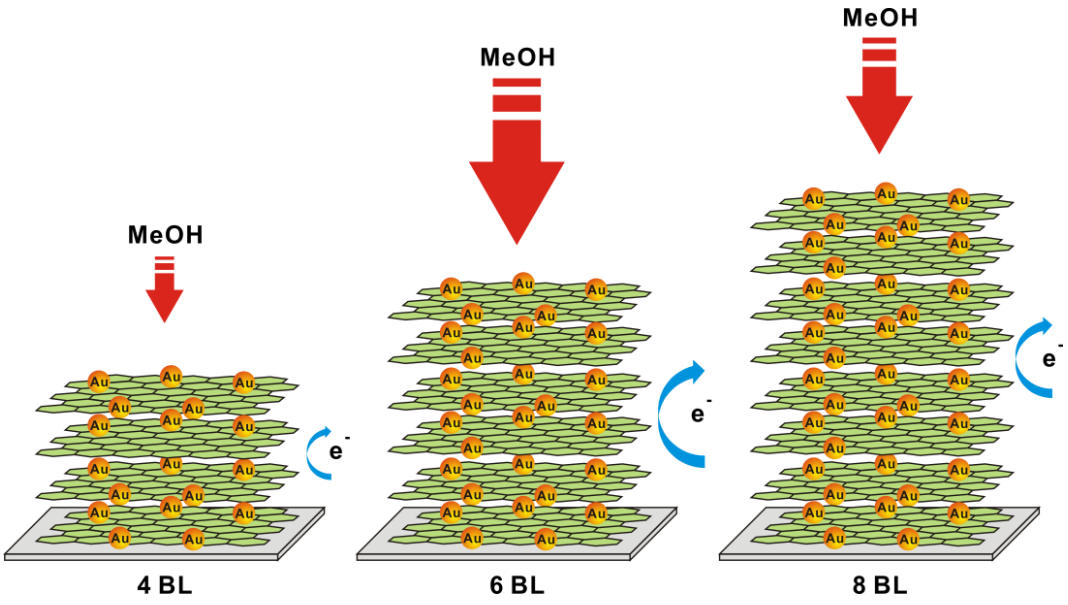

Figure 2.3.11. Schematic representation of the possible mechanism of electrocatalytic activity of $(Au/GO)_n$ toward methanol oxidation depending on the number of bilayers (BL). Two factors such as methanol diffusion into the electrode and electron and mass transfer from the electrode govern the fine balance of multilayered hybrid electrode in the observed electrocatalytic activity.

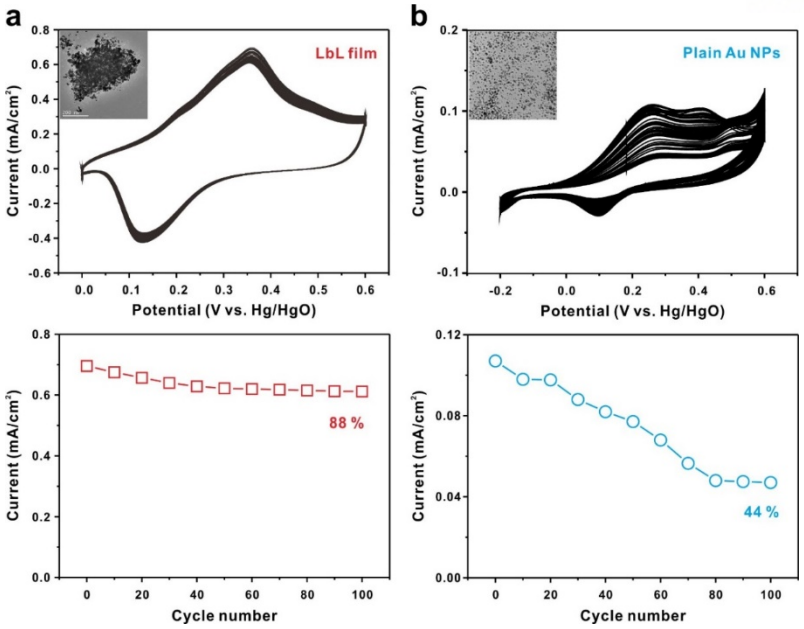

Figure 2.3.12. Cyclic voltammetry stability test of (a) $(Au/GO)_6$ thin film thermal treated at 150 ˚C samples, (b) DMAP-Au NPs on a glassy carbon electrode. Both samples were measured in 0.10 M KOH with 1.0 M CH_3OH in a saturated N_2 at a scan rate of 20 mV/s. Identical concentration of Au NPs was used for comparison.

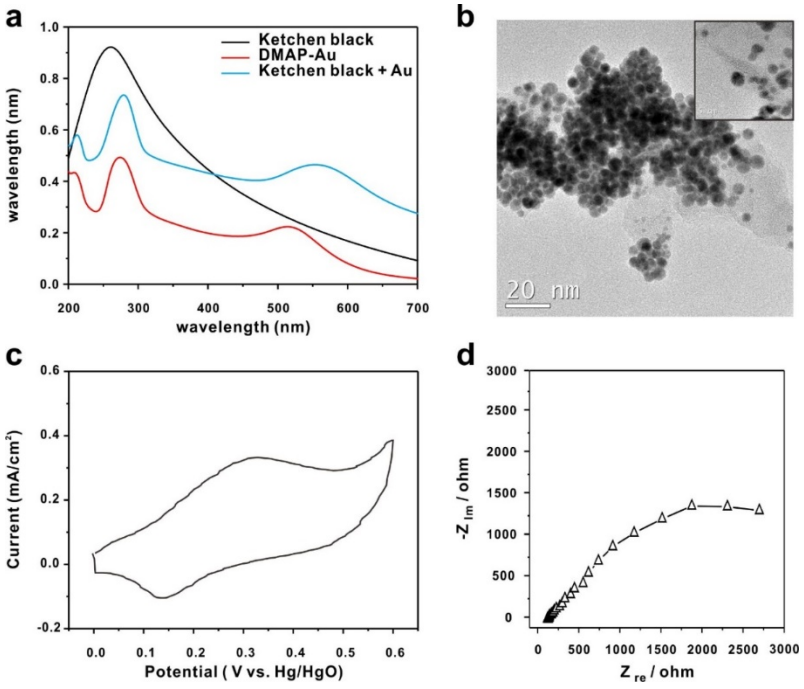

Figure 2.3.13. Control experiments of Au NPs deposited on amorphous carbon, Ketjen Black. (a) UV/vis spectra, (b) TEM image, (c) Cyclic voltammetry stability test in 0.10 M KOH with 1.0 M CH_3OH in a saturated N_2 at a scan rate of 20 mV/s, and (d) Nyquist plot measured in 0.10 M KOH + 1.0 M CH_3OH solution measured at 0.35 V. The R_{CT} of 358.1 ohm is obtained.

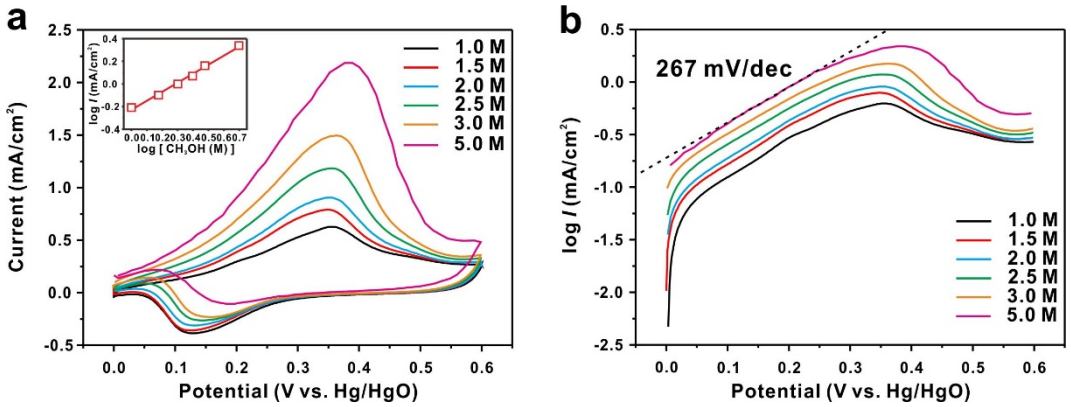

Figure 2.3.14. (a) Cyclic voltammograms of $(Au/GO)_6$ thin film thermal treated at 150 ˚C in 0.10 M KOH with different concentrations of CH_3OH. Inset shows the plot of log (*i*) against log (CH_3OH) at different concentrations of CH_3OH. (b) The corresponding Tafel plot with a representative linear fit. All measurements were carried out in a saturated N_2 at a scan rate of 20 mV/s.

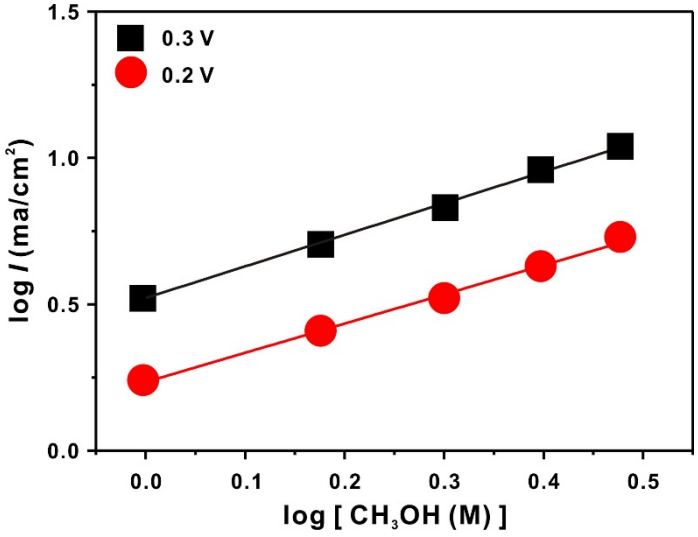

Figure 2.3.15. Plots of log(*I*) against log (C_{CH3OH}) at different potentials in Tafel range. The measurements were carried out in a saturated N_2 with a scan rate of 20 mV/s. The slope is 0.89 for both curves.

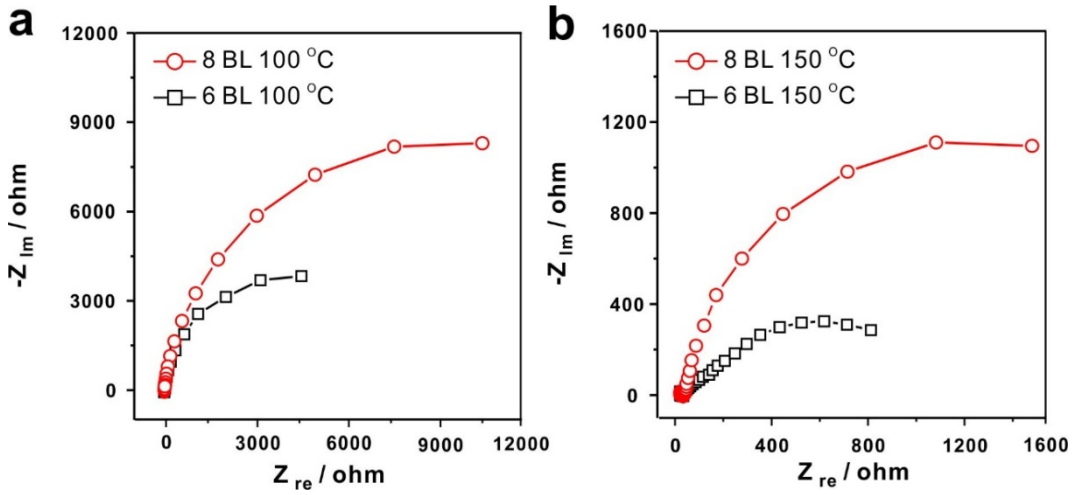

Figure 2.3.16. Nyquist plots of impedance on $(Au/GO)_n$ thin films in 0.10 M KOH and 1.0 M CH_3OH solution measured at 0.35 V. (a) 6- and 8-bilayer films after thermal treatment at 100 ˚C, and (b) at 150 ˚C.

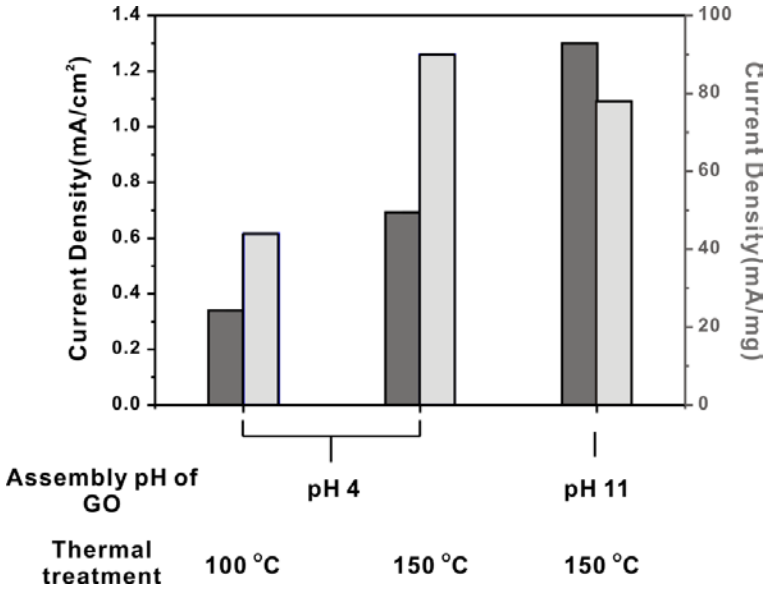

Figure 2.3.17. Comparison of current density and mass-averaged current density of various sample of $(Au/GO)_6$ thin films treated at different temperatures and assembled at different pH conditions of GO.

2.3.5. Conclusion

In conclusion, we have developed a simple approach of integrating electroactive gold nanoparticles (Au NPs) with graphene oxide (GO) nanosheet support by layer-by-layer (LbL) assembly for the creation of 3-dimensional electrocatalytic thin films that are active toward methanol oxidation. This approach involves the electrostatic interaction of two oppositely charged suspensions of the GO nanosheet with Au NPs. The LbL method can not only control the amount of Au NPs on a graphene sheet, but also enhance the stability of Au NPs when combined with graphene sheet. Furthermore, the Au-GO hybrid multilayer was successfully employed in the catalytic activity of methanol oxidation in alkaline conditions. Through careful investigations of the catalyst, we could control the catalytic efficiency with changes of the number of bilayers and thermal treatment temperature. Because of the highly versatile and tunable properties of LbL-assembled thin films of hybrid electrocatalyst, we anticipate that the general concept presented here offers a new design of electrocatalyst for direct methanol fuel cell (DMFC). Considering the wide-ranging potential applications of a two-dimensional graphene sheet as a host material for a variety of NPs, the approach developed here may lead to new possibilities for the fabrication of hybrid NP-graphene structures endowed with multiple functionalities.

2.3.6. References

1. Yamaguchi, T.; Zhou, H.; Nakazawa, S.; Hara, N. An Extremely Low Methanol Crossover and Highly Durable Aromatic Pore-Filling Electrolyte Membrane for Direct Methanol Fuel Cells. *Adv. Mater.* **2007,** *19*, 592-596.
2. Wen, Z. H.; Liu, J.; Li, J. H. Core/shell Pt/C Nanoparticles Embedded in Mesoporous Carbon as a Methanol-Tolerant Cathode Catalyst in Direct Methanol Fuel Cells. *Adv. Mater.* **2008,** *20*, 743-747.
3. Zhong, C. J.; Luo, J.; Fang, B.; Wanjala, B. N.; Njoki, P. N.; Loukrakpam, R.; Yin, J. Nanostructured Catalysts in Fuel Cells. *Nanotechnology* **2010,** *21*, 4027-4036.
4. Arico, A. S.; Bruce, P.; Scrosati, B.; Tarascon, J. M.; Van Schalkwijk, W. Nanostructured Materials for Advanced Energy Conversion and Storage Devices. *Nat. Mater.* **2005,** *4*, 366-377.
5. Hu, Y. S.; Guo, Y. G.; Sigle, W.; Hore, S.; Balaya, P.; Maier, J. Electrochemical Lithiation Synthesis of Nanoporous Materials with Superior Catalytic and Capacitive Activity. *Nat. Mater.* **2006,** *5*, 713-717.
6. Gao, M. R.; Gao, Q.; Jiang, J.; Cui, C. H.; Yao, W. T.; Yu, S. H. A Methanol-Tolerant Pt/$CoSe_2$ Nanobelt Cathode Catalyst for Direct Methanol Fuel Cells. *Angew. Chem. Int. Ed.* **2011,** *50*, 4905-4908.
7. Kua, J.; Goddard, W. A. Oxidation of Methanol on 2nd and 3rd Row Group VIII Transition Metals (Pt, Ir, Os, Pd, Rh, and Ru): Application to Direct Methanol Fuel Cells. *J. Am. Chem. Soc.* **1999,** *121*, 10928-10941.
8. Burke, L. D.; Collins, J. A.; Horgan, M. A.; Hurley, L. M.; O'Mullane, A. P. The Importance of the Active States of Surface Atoms with regard to the Electrocatalytic Behaviour of Metal Electrodes in Aqueous Media. *Electrochim. Acta* **2000,** *45*, 4127-4134.
9. Song, Y.; Garcia, R. M.; Dorin, R. M.; Wang, H. R.; Qiu, Y.; Coker, E. N.; Steen, W. A.; Miller, J. E.; Shelnutt, J. A. Synthesis of Platinum Nanowire Networks using a Soft Template. *Nano Lett.* **2007,** *7*, 3650-3655.
10. Sun, Y.; Zhuang, L.; Lu, J.; Hong, X.; Liu, P. Collapse in Crystalline Structure and Decline in Catalytic Activity of Pt Nanoparticles on Reducing Particle Size to 1 nm. *J. Am. Chem. Soc.* **2007,** *129*, 15465-15467.
11. Maye, M. M.; Lou, Y. B.; Zhong, C. J. Core-Shell Gold Nanoparticle Assembly as Novel Electrocatalyst of CO Oxidation. *Langmuir* **2000,** *16*, 7520-7523.
12. Lou, Y. B.; Maye, M. M.; Han, L.; Luo, J.; Zhong, C. J. Gold-Platinum Alloy Nanoparticle Assembly as Catalyst for Methanol Electrooxidation. *Chem. Commun.* **2001,** 473-474.

13. Haruta, A. When Gold is not Noble: Catalysis by Nanoparticles. *Chem. Rec.* **2003,** *3*, 75-87.

14. Rodriguez, J. A.; Liu, P.; Hrbek, J.; Evans, J.; Perez, M. Water-Gas Shift Reaction on Cu and Au Nanoparticles Supported on CeO_2 and ZnO: Intrinsic Activity and Importance of Support Interactions. *Angew. Chem. Int. Ed.* **2007,** *46*, 1329-1332.

15. Yoo, E.; Okata, T.; Akita, T.; Kohyama, M.; Nakamura, J.; Honma, I. Enhanced Electrocatalytic Activity of Pt Subnanoclusters on Graphene Nanosheet Surface. *Nano Lett.* **2009,** *9*, 2255-2259.

16. Gao, Y. J.; Ma, D.; Hu, G.; Zhai, P.; Bao, X. H.; Zhu, B.; Zhang, B. S.; Su, D. S. Layered-Carbon-Stabilized Iron Oxide Nanostructures as Oxidation Catalysts. *Angew. Chem. Int. Ed.* **2011,** *50*, 10236-10240.

17. Liang, Y. Y.; Li, Y. G.; Wang, H. L.; Zhou, J. G.; Wang, J.; Regier, T.; Dai, H. J. Co_3O_4 Nanocrystals on Graphene as a Synergistic Catalyst for Oxygen Reduction Reaction. *Nat. Mater.* **2011,** *10*, 780-786.

18. Stankovich, S.; Dikin, D. A.; Dommett, G. H. B.; Kohlhaas, K. M.; Zimney, E. J.; Stach, E. A.; Piner, R. D.; Nguyen, S. T.; Ruoff, R. S. Graphene-Based Composite Materials. *Nature* **2006,** *442*, 282-286.

19. Balandin, A. A.; Ghosh, S.; Bao, W. Z.; Calizo, I.; Teweldebrhan, D.; Miao, F.; Lau, C. N. Superior Thermal Conductivity of Single-Layer Graphene. *Nano Lett.* **2008,** *8*, 902-907.

20. Lee, Z.; Jeon, K. J.; Dato, A.; Erni, R.; Richardson, T. J.; Frenklach, M.; Radmilovic, V. Direct Imaging of Soft-Hard Interfaces Enabled by Graphene. *Nano Lett.* **2009,** *9*, 3365-3369.

21. Novoselov, K. S.; Jiang, D.; Schedin, F.; Booth, T. J.; Khotkevich, V. V.; Morozov, S. V.; Geim, A. K. Two-Dimensional Atomic Crystals. *P. Nat. Acad. Sci. USA* **2005,** *102*, 10451-10453.

22. Eda, G.; Fanchini, G.; Chhowalla, M. Large-Area Ultrathin Films of Reduced Graphene Oxide as a Transparent and Flexible Electronic Material. *Nat. Nanotechnol.* **2008,** *3*, 270-274.

23. Kim, K. S.; Zhao, Y.; Jang, H.; Lee, S. Y.; Kim, J. M.; Kim, K. S.; Ahn, J. H.; Kim, P.; Choi, J. Y.; Hong, B. H. Large-scale pattern growth of graphene films for stretchable transparent electrodes. *Nature* **2009,** *457*, 706-710.

24. Zhou, Y. G.; Chen, J. J.; Wang, F. B.; Sheng, Z. H.; Xia, X. H. A Facile Approach to the Synthesis of Highly Electroactive Pt Nanoparticles on Graphene as an Anode Catalyst for Direct Methanol Fuel Cells. *Chem. Commun.* **2010,** *46*, 5951-5953.

25. Wu, Z. S.; Wang, D. W.; Ren, W.; Zhao, J.; Zhou, G.; Li, F.; Cheng, H. M. Anchoring Hydrous RuO_2 on Graphene Sheets for High-Performance Electrochemical Capacitors.

Adv. Funct. Mater. **2010,** *20*, 3595-3602.

26. Guo, S. J.; Dong, S. J.; Wang, E. K. Three-Dimensional Pt-on-Pd Bimetallic Nanodendrites Supported on Graphene Nanosheet: Facile Synthesis and Used as an Advanced Nanoelectrocatalyst for Methanol Oxidation. *ACS Nano* **2010,** *4*, 547-555.
27. Bai, H.; Li, C.; Shi, G. Q. Functional Composite Materials Based on Chemically Converted Graphene. *Adv. Mater.* **2011,** *23*, 1089-1115.
28. Kou, R.; Shao, Y. Y.; Mei, D. H.; Nie, Z. M.; Wang, D. H.; Wang, C. M.; Viswanathan, V. V.; Park, S.; Aksay, I. A.; Lin, Y. H.; Wang, Y.; Liu, J. Stabilization of Electrocatalytic Metal Nanoparticles at Metal-Metal Oxide-Graphene Triple Junction Points. *J. Am. Chem. Soc.* **2011,** *133*, 2541-2547.
29. Qu, Q. T.; Yang, S. B.; Feng, X. L. 2D Sandwich-like Sheets of Iron Oxide Grown on Graphene as High Energy Anode Material for Supercapacitors. *Adv. Mater.* **2011,** *23*, 5574-5580.
30. Zhu, C. Z.; Guo, S. J.; Zhai, Y. M.; Dong, S. J. Layer-by-Layer Self-Assembly for Constructing a Graphene/Platinum Nanoparticle Three-Dimensional Hybrid Nanostructure Using Ionic Liquid as a Linker. *Langmuir* **2010,** *26*, 7614-7618.
31. Decher, G. Fuzzy Nanoassemblies: Toward Layered Polymeric Multicomposites. *Science* **1997,** *277*, 1232-1237.
32. Hammond, P. T. Form and Function in Multilayer Assembly: New Applications at the Nanoscale. *Adv. Mater.* **2004,** *16*, 1271-1293.
33. Hong, T. K.; Lee, D. W.; Choi, H. J.; Shin, H. S.; Kim, B. S. Transparent, Flexible Conducting Hybrid Multi layer Thin Films of Multiwalled Carbon Nanotubes with Graphene Nanosheets. *ACS Nano* **2010,** *4*, 3861-3868.
34. Hong, J.; Han, J. Y.; Yoon, H.; Joo, P.; Lee, T.; Seo, E.; Char, K.; Kim, B. S. Carbon-Based Layer-by-Layer Nanostructures: From Films to Hollow Capsules. *Nanoscale* **2011,** *3*, 4515-4531.
35. Lee, D. W.; Hong, T. K.; Kang, D.; Lee, J.; Heo, M.; Kim, J. Y.; Kim, B. S.; Shin, H. S. Highly Controllable Transparent and Conducting Thin Films using Layer-by-Layer Assembly of Oppositely Charged Reduced Graphene Oxides. *J. Mater. Chem.* **2011,** *21*, 3438-3442.
36. Hummers, W. S.; Offeman, R. E. Preparation of Graphitic Oxide. *J. Am. Chem. Soc.* **1958,** *80*, 1339-1339.
37. Li, D.; Muller, M. B.; Gilje, S.; Kaner, R. B.; Wallace, G. G. Processable Aqueous Dispersions of Graphene Nanosheets. *Nat. Nanotechnol.* **2008,** *3*, 101-105.
38. Gittins, D. I.; Caruso, F. Spontaneous Phase Transfer of Nanoparticulate Metals from Organic to Aqueous Media. *Angew. Chem. Int. Ed.* **2001,** *40*, 3001-3004.
39. Chen, W. F.; Yan, L. F. Preparation of Graphene by a Low-Temperature Thermal

Reduction at Atmosphere Pressure. *Nanoscale* **2010,** *2*, 559-563.

40. Kwon, J.; Lee, S. H.; Park, K. H.; Seo, D. H.; Lee, J.; Kong, B. S.; Kang, K.; Jeon, S. Simple Preparation of High-Quality Graphene Flakes without Oxidation Using Potassium Salts. *Small* **2011,** *7*, 864-868.
41. Burcham, L. J.; Badlani, M.; Wachs, I. E. The Origin of the Ligand Effect in Metal Oxide Catalysts: Novel Fixed-Bed in situ Infrared and Kinetic Studies during Methanol Oxidation. *J. Catal.* **2001,** *203*, 104-121.
42. Yuan, W. Y.; Li, C. M. Direct Modulation of Localized Surface Plasmon Coupling of Au Nanoparticles on Solid Substrates via Weak Polyelectrolyte-Mediated Layer-by-Layer Self Assembly. *Langmuir* **2009,** *25*, 7578-7585.
43. Assiongbon, K. A.; Roy, D. Electro-Oxidation of Methanol on Gold in Alkaline Media: Adsorption Characteristics of Reaction Intermediates Studied using Time Resolved Electro-Chemical Impedance and Surface Plasmon Resonance Techniques. *Surf. Sci.* **2005,** *594*, 99-119.
44. Hong, J.; Char, K.; Kim, B. S. Hollow Capsules of Reduced Graphene Oxide Nanosheets Assembled on a Sacrificial Colloidal Particle. *J. Phys. Chem. Lett.* **2010,** *1*, 3442-3445.
45. Hwang, H.; Joo, P.; Kang, M. S.; Ahn, G.; Han, J. T.; Kim, B. S.; Cho, J. H. Highly Tunable Charge Transport in Layer-by-Layer Assembled Graphene Transistors. *ACS Nano* **2012,** *6*, 2432-2440.
46. Zhang, X.; Zan, X. J.; Su, Z. H. Polyelectrolyte Multilayer Supported Pt Nanoparticles as Catalysts for Methanol Oxidation. *J. Mater. Chem.* **2011,** *21*, 17783-17789.
47. Yan, S. H.; Zhang, S. C.; Lin, Y.; Liu, G. R. Electrocatalytic Performance of Gold Nanoparticles Supported on Activated Carbon for Methanol Oxidation in Alkaline Solution. *J. Phys. Chem. C* **2011,** *115*, 6986-6993.
48. Luo, J.; Njoki, P. N.; Lin, Y.; Mott, D.; Wang, L. Y.; Zhong, C. J. Characterization of Carbon-Supported AuPt Nanoparticles for Electrocatalytic Methanol Oxidation Reaction. *Langmuir* **2006,** *22*, 2892-2898.
49. Kowal, A.; Li, M.; Shao, M.; Sasaki, K.; Vukmirovic, M. B.; Zhang, J.; Marinkovic, N. S.; Liu, P.; Frenkel, A. I.; Adzic, R. R. Ternary Pt/Rh/SnO_2 Electrocatalysts for Oxidizing Ethanol to CO_2. *Nat. Mater.* **2009,** *8*, 325-330.
50. Mustain, W. E.; Prakash, J. Kinetics and Mechanism for the Oxygen Reduction Reaction on Polycrystalline Cobalt-Palladium Electrocatalysts in Acid Media. *J. Power Sources* **2007,** *170*, 28-37.
51. Lee, E. P.; Peng, Z. M.; Chen, W.; Chen, S. W.; Yang, H.; Xia, Y. N. Electrocatalytic Properties of Pt Nanowires Supported on Pt and W Gauzes. *ACS Nano* **2008,** *2*, 2167-2173.
52. Chang, B. Y.; Park, S. M. Electrochemical Impedance Spectroscopy. *Annu. Rev. Anal.*

Chem. **2010,** *3,* 207-229.

53. Kim, J.; Lee, S. W.; Hammond, P. T.; Shao-Horn, Y. Electrostatic Layer-by-Layer Assembled Au Nano particle/MWNT Thin Films: Microstructure, Optical Property, and Electrocatalytic Activity for Methanol Oxidation. *Chem. Mater.* **2009,** *21,* 2993-3001.

Chapter 3. Hybrid Nanocomposites based on Carbon Nanoparticles

3.1. Introduction

3.1.1. Hybrid nanomaterials based on carbon nanoparticles

The unique properties of carbon nanoparticles (CDs) such as high optical properties, aqueous solubility, and electron transfer ability are facilitating to apply for bioimaging, photovoltaic devices and photocatalyst. However, low PL intensity of non-doped CDs is limited in bio applications. Also, the morphologies of metal-CDs nanocomposites are difficult to control by photo-reduction. Therefore, in *chapter 3*, the effective hybrid nanomaterials based on CDs is developed, which possess not only high PL intensity and targeting ability in cancer cell in CDs but also the controlled and homogeneous morphologies in metal-CDs.

First, polymer-passivated CDs are developed for high biocompatibility, non-toxicity, and high PL intensity in CDs. Also, the additional functionalization of targeting molecules on CDs is enhanced the efficiency in bioimaging and photodynamic therapy.

Second, hybrid Ag-CD nanomaterials are developed through photo-reduction in UV light. Due to the abundant oxygen groups and electron transfer behavior of CDs, heterodimeric Ag-CD structure is synthesized. Furthermore, the interface between Ag and CDs can be easily controlled with the additives.

3.2. Highly Biocompatible Carbon Nanoparticles for Simultaneous Bioimaging and Targeted Photodynamic Therapy in Vitro and in Vivo

3.2.1. Abstract

Photosensitizer (PS) has hydrophobic properties and consequently suffers from aqueous solubility. To overcome these limitations, there have been considerable efforts to develop carriers for delivery of PS. Herein, we describe a novel design of highly biocompatible, fluorescent, folic acid (FA) functionalized carbon nanoparticles (CDs) as a carrier for zinc phthalocyanine (ZnPc) PS to achieve simultaneous biological imaging and targeted photodynamic therapy. FA is modified on the PEG-passivated CD (CD-PEG) for the targeted delivery to FA-positive cancer cells and ZnPc is loaded onto FA modified CD-PEG (CD-PEG-FA) by π- π stacking interactions. These CD-PEG-FA/ZnPc exhibits an excellent targeted delivery of photosensitizer, leading to simultaneous imaging and significant targeted therapy after irradiation *in vitro* and *in vivo*. We anticipate that the present CD-based targeted delivery of the PS would offer convenient and effective platform for the enhanced photodynamic therapy to treat cancers in the near future.

3.2.2. Introduction

Biological labels that allow cellular imaging are receiving increasing attention in fluorescence microscopy, laser technology, and nanotechnology.[1] These labels are useful for tracking intracellular transport and biochemical phenomena in disease diagnosis and therapy.[2,3] Although fluorescent organic dyes and genetically engineered proteins are still widely employed as promising luminescent biological labels, semiconducting nanoparticles (quantum dots) have garnered considerable attention because of their superior physical and chemical properties such as high photoluminescence and stability together with tunable photophysical properties.[4-6] Despite these notable advantages, the implementation of quantum dots to broader clinical setting is still limited due to their intrinsic toxicity and potential environmental concerns associated with the heavy metals present in the quantum dots.[7,8]

Longstanding interest in the search of benign alternatives has triggered the recent development of carbon nanoparticles (also known as C-dots, CDs) as a new class of biolabels by

---

* *Chapter 3.2. is reproduced in part with permission of "Adv. Funct. Mater.* ***2014****, 24, 5781". Copyright 2014 WILEY-VCH Verlag GmbH & Co. KGaA, Weinheim.*

virtue of their biocompatibility, low toxicity, simple preparation and high stability while retaining the advantageous photophysical features of quantum dots.[9-11] CDs are generally composed of a mixed phase of sp^2- and sp^3-hybridized carbon nanostructures in the form of conjugated carbon clusters functionalized with oxygen-bearing functional groups.[12] On top of the high fluorescence properties of CDs, their unique chemical structures allow the integration of active therapeutic molecules into the sp^2 carbon frame, and their surface functional groups enable further conjugation with other molecules such as biological affinity ligands. These unique characteristics make CDs ideal for simultaneous diagnosis and therapeutics (theranostics), which lead to advances in personalized medicine.[13-15]

Photodynamic therapy has been widely practiced as a promising non-invasive therapeutic modality for the treatment of cancer.[16] In the process of photodynamic therapy, photosensitizers (PS) are irradiated by a specific wavelength of light, which triggers the generation of reactive oxygen species from intracellular oxygen that consequently induce cell death and necrosis of proximal tissues.[17,18] However, the limited solubility and poor selectivity of PS often pose challenges which inevitably require a carrier system to increase their aqueous solubility and enhance cellular internalization.[19,20] A number of approaches have been proposed to incorporate PS into carriers such as liposomes, polymeric nanoparticles, gold nanoparticles, carbon nanotubes and graphenes.[21-27] Also, in order to increase the local concentration of PSs in cancer cells and avoid side effects, a common strategy is a direct conjugation of carriers with targeting ligands, such as monoclonal antibodies, proteins, peptides, steroids and folic acid.[28-30] Although many of these carriers provide an effective means to increase the solubility and selectivity in aqueous media, it is still a challenging endeavor to combine *in vivo* therapeutic, imaging, and targeting capabilities into a single carrier.

In this work, we report a novel design of highly biocompatible, fluorescent, folic acid (FA) functionalized CD as a carrier for zinc phthalocyanine (ZnPc) PS to achieve simultaneous biological imaging and targeted photodynamic therapy (Figure 3.2.1). The biocompatible and tumor-targeted FA conjugated CD is designed to selectively accumulate in tumors and to activate ZnPc upon irradiation, which enhances the selectivity and the therapeutic efficacy of photodynamic therapy both *in vitro* and *in vivo*. Specifically, the CDs are synthesized via the thermal decomposition of α-cyclodextrin as a sugar-derived molecular precursor. The surface of CDs is subsequently passivated with poly(ethylene glycol) diamine (PEG) to enhance its fluorescence as well as to increase the biocompatibility.[31] Surface-passivating ligands are known to play a pivotal role in increasing the fluorescence efficiency by decreasing the effective hole-trapping after generation of the exciton pair on the surface of CDs.[32] The PEG-passivated CD (CD-PEG) is further modified with FA to afford CD-PEG-FA for the targeted delivery to FA-positive cancer cells. FA is an ideal ligand for the folate receptors that are overexpressed in various

types of human cancer cells owing to its high affinity for cancerous cells and stability.[33] In addition, as a second generation PS, ZnPc possesses a good cytotoxic efficiency.[34]

3.2.3. Experimental

3.2.3.1. Preparation of CDs

α-Cyclodextrin, poly(ethylene glycol) diamine (Mw = 1,500 g/mol), folic acid, and zinc phthalocyanine (ZnPc) were purchased from Sigma-Aldrich. H_2SO_4, HNO_3, and K_2CO_3 were purchased from Daejung Chemical (Korea). CDs were synthesized by dehydrating carbohydrates using concentrated sulfuric acid. In this case, 2.00 g of α-cyclodextrin was slowly added to 8 ml of H_2SO_4, to which 5 ml of water was added to dissolve α-cyclodextrin. The black solution was stirred vigorously for 1 h and then diluted with 40 ml of water. The solution was then centrifuged at 4000 rpm for 10 min, and the supernatant was discarded. The precipitate was washed twice with distilled water, re-suspended in 5 ml of water and 6 ml of HNO_3 (22.5 mM), and sonicated for 1 h. The resulting solution was refluxed under nitrogen for 12 h at 120 °C and then neutralized with K_2CO_3. After excess K_2CO_3 was removed, the CDs were subjected to extensive dialysis (SpectraPore MWCO 1,000) for 1 day to remove excess salts.

3.2.3.2. Surface passivation of CDs with PEG and FA

To passivate the CDs, the solutions were diluted one to ten parts with distilled water and refluxed for 72 h at 120 °C with poly(ethylene glycol) diamine (PEG, 150 mM). After the reflux, each of the samples was subjected to extensive dialysis against water for 2 days. To prepare the FA-conjugated CD-PEG, FA (10 mM) and 1-ethyl-3-(3-dimethylaminopropyl) carbodiimide (EDC, 10 mM) were mixed in 1.0 mL of distilled water saturated with $NaHCO_3$, followed by incubation with CD-PEG (1.0 mg/ml) at room temperature for 18 h. The amount of conjugated FA in CD-PEG-FA, as estimated by measuring the UV/Vis absorbance, was 5.8 mg/ml-CD-PEG-FA. Then, the mixture was subjected to extensive dialysis against distilled water for purification for 2 days. For ZnPc loading to CD-PEG-FA, an ethanolic solution of ZnPc (2.0 mg) was subjected to solvent evaporation prior to mixing with CD-PEG-FA (1.0 mg/ml). Then, the mixture was sonicated for 1 h on an ice bath and filtered through polyvinylidene difluoride (PVDF) syringe filters (0.2 μm).

3.2.3.3. Synthesis of ZnPc loaded on CD-PEG-FA

The loading capacity of ZnPc to CD-PEG-FA, calculated from the standard curve of the

UV-vis absorbance of ZnPc, was about 60 μg of ZnPc per milligram of CD-PEG-FA. To estimate the ZnPc loading to CD-PEG-FA, the fluorescence emission spectra of ZnPc (0.4 μM) were obtained at an excitation wavelength of 650 nm with or without CD-PEG-FA (1.0 mg/ml) by using a fluorometer (BioTek, U.S.A.)

3.2.3.4. Characterizations

UV/vis spectrophotometer (UV-2550, Shimadzu) was used to record the absorbance for concentration control and comparison. Absorbance curves were compared to ascertain the similarity in concentration, after which the samples were adjusted for comparison. Fluorescence data were obtained by using a fluorometer (Agilent). Three-dimensional fluorescence spectrum of the CDs was obtained with an FP-8300 spectrofluorometer (JASCO). Transmission electron microscopy (TEM, JEM-2100, JEOL) and atomic force microscopy (AFM, Dimension 3100, Veeco) analyses were performed to investigate the size and morphology of the CDs. To confirm the functional groups after passivation, XPS (K-alpha, Thermo Fisher) and FT-IR (Agilent) analyses were performed.

3.2.3.5. Photoluminescence lifetime measurement

The exciton lifetime was determined by the time-correlated single photon counting (TCSPC) technique. A computer-controlled diode laser with 375 nm wavelength, 54 ps pulse width, and 40 MHz repetition rate was used as an excitation source. The PL emission was spectrally resolved by using some collection optics and a monochromator (PicoQuant). The TCSPC module (PicoHarp 300E, PicoQuant) with a MCP-PMT (R3809U-5x series, Hamamatsu) was used for ultrafast detection. The total instrument response function (IRF) for PL decay was less than 30 ps, and the temporal time resolution was less than 10 ps. Deconvolution of the actual fluorescence decay and IRF was performed by using a fitting software (FlouFit, PicoQuant) to deduce the time constant associated with each exponential decay.

3.2.3.6. Bioimaging and photodynamic therapy i*n vitro*

Cell counting kit-8 (CCK-8) was purchased from Dojindo Laboratories (Japan). Live/dead® viability/cytotoxicity kit and singlet oxygen sensor green (SOSG) reagent were purchased from Molecular Probes (USA). 10X PBS phosphate buffered saline (PBS), Dulbecco's Modified Eagle's Medium (DMEM), and fetal bovine serum (FBS) were purchased from WELGENE (Korea).

Cell culture

HeLa cell lines and MDA-MD-231 cell lines were grown in DMEM containing 4.5 g/L D-glucose containing 10% FBS, 1% penicillin, and streptomycin, under an atmosphere of 5% CO_2 and at 37 °C. A549 cell lines were grown in RPMI 1640 with same components and conditions.

Cellular toxicity test

To investigate the cytotoxicity of the CDs, we carried out the CCK-8 cell viability assay. HeLa cells (1×10^4 cells/well) were seeded in a 96-well plate for 24 h, and CDs were treated with the HeLa cells at varying concentrations (0–450 μg/mL) in serum-containing media. After 12 h incubation, the cells were carefully washed with 1X PBS; then, CCK-8 assay solution with serum-free media was added, incubation was carried out for 1 h, and the absorbance at 450 and 670 nm was measured by using a microplate reader (Molecular Devices, Inc., USA). To investigate the quantitative cell viability related to the photodynamic effect of CD-PEG-FA/ZnPc, HeLa cells (1×10^4 cells/well) were plated in a 96-well plate, incubated for 24 h, and incubated with various concentrations of CD-PEG-FA/ZnPc. After 12 h incubation, each well was irradiated with a 660-nm LED laser (Mikwang Electronics, 30 mW/cm^2) for 10 min, and then, the medium was replaced with a serum-containing medium. After further incubation for 12 h, the CCK-8 cell viability assay was performed as described above. All experiments were carried out in triplicate.

Cellular imaging

HeLa cells (1.2×10^5 cells/well) were seeded in a 4-well glass plate. After 24 h incubation, CDs derivatives were added to each well in a serum-free medium for 12 h. To confirm the effect of folate receptor-mediated cell uptake, free FA was excessively treated for 2 h prior to treating FA-conjugated CD derivatives. After 12 h incubation, the cells were carefully rinsed with 1X PBS, and the medium was replaced with a serum-containing medium. MDA-MB-231 cells and A549 cells were also prepared with same procedure excluding free FA treat. Cell images were obtained using a Ti inverted fluorescence microscope with a 10X (1.4 numerical aperture) objective (Olympus, Japan), a Deltavision high-resolution microscope, and In-cell analyzer 2000 (GE Healthcare, Korea). To investigate the photodynamic effect, CD-PEG-FA/ZnPc (50 μg/ml) with a serum-free medium was treated with HeLa cells (1.2×10^5 cells/well), which had been preincubated in a 12-well plate for 24 h. After the medium exchange to a serum-containing medium, the cells were irradiated with a 660-nm fiber-coupled laser (LaserLab, Korea, 30 mW/cm^2) for 10 min. After further 4 h incubation, each well was treated with Live/Dead assay reagent, based on the manufacturer's protocol. Then, fluorescence images of the cells were obtained by using a Ti inverted fluorescence microscope with a 10X objective.

Singlet oxygen detection

The SOSG reagent is highly selective to singlet oxygen (SO), and it emits strong green fluorescence in the presence of SO at 530 nm (λ_{ex}= 504 nm). SOSG (2.5 μM) dissolved in 2% methanol was added to ZnPc (3.8 μM) and CD-PEG-FA/ZnPc (1.0 mg/ml), and then, the generation of SO was induced by irradiation using a 660-nm LED (30 mW/cm^2). After time-dependent irradiation, green fluorescence emission from the samples was observed at 530 nm by using a fluorometer (BioTek, USA).

3.2.3.7. Bioimaging and photodynamic therapy *in vivo*

In vivo targeting and bio-distribution study

Male BALB/c-nude mice (6 weeks old) were purchased from Japan SLC, Inc. (Shizuoka, Japan). All animal experiments were carried out in compliance with the Institutional Animal Care and Use Committees (IACUC) of Seoul National University. Tumor-bearing mice were prepared by subcutaneously injecting a suspension of the Hela cells (6×10^6 cells) in sterilized 1X PBS (*n* = 4). When the tumor size reached ~70 mm^3, CD-PEG-FA/ZnPc, CD-PEG/ZnPc, and CD-PEG-FA in 1X PBS solution (0.5 mg ZnPc/kg) were injected into tail veins of the tumor-bearing mice. As a control, one goup of mice was treated with the same volume of 1X PBS. Fluorescent signals of the mice were obtained by using an optical molecular imaging system, Optix MX3 (GE Healthcare, Korea) at various time points. To examine the biodistribution of the injected ZnPc, major organs (heart, lung, liver, etc.) were collected into a petri-dish after 12 h injection and imaged.

In vivo photodynamic therapy

Tumor-bearing mice were first prepared in four groups (n = 4). When the tumor size reached ~70 mm^3, the mice were treated with CD-PEG-FA/ZnPc, CD-PEG/ZnPc, and CD-PEG-FA in 1X PBS (0.5 mg ZnPc/kg) by intravenous injection. As a control, a group of mice was treated with the same volume of saline. The mice were segregated into 6 groups: (1) saline; (2) CD-PEG-FA without irradiation; (3) CD-PEG-FA with irradiation; (4) CD-PEG/ZnPc without irradiation; (5) CD-PEG/ZnPc with irradiation; (6) CD-PEG-FA/ZnPc without irradiation; (7) CD-PEG-FA/ZnPc with irradiation. For the irradiated groups, 660-nm laser (0.3 W/cm^2, 20 min) was used after 12 h of injection. The photodynamic therapeutic effects were investigated by monitoring the change in tumor volumes and body weight in each group every day up to 10 days. The tumor volumes were calculated by using the equation of length × (width)^2 × 1/2, where the length and width are the longest and shortest diameters (mm) of the tumor, respectively. The relative tumor volumes were calculated relative to the initial volumes.

Statistical analysis

All data show the mean corrected values ± SD of at least three independent experiments. Significant differences were determined based on the Student's t-test where differences were considered significant ($p < 0.05$). Statistical analyses were performed with the GraphPad Software.

3.2.4. Results and discussion

3.2.4.1. Synthesis of high PL of PEG passivated and FA functionalized CD (CD-PEG-FA)

The suspension of as-prepared CD was highly stable in aqueous solution with a zeta-potential of –39.8 ± 0.45 mV. The negative surface charge clearly indicated the presence of surface functional groups such as carboxylic acid and alcohol groups, imparting sufficient colloidal stability to the CDs. As shown in Figure 3.2.2a, the broad UV/vis absorption of as-prepared CD and surface passivated CD-PEG and CD-PEG-FA at approximately 230 nm represent a typical absorption of an aromatic system, reminiscence of sp^2-carbon network.[35] In addition, the successful functionalization of FA onto the CD surface was clearly evident from the peak at 283 nm.[36] The zeta-potentials of CD-PEG and CD-PEG-FA were determined to be –12.4 ± 0.75 and –8.24 ± 1.96 mV (pH 7.3), respectively, suggesting the loss of the carboxylic acid groups upon surface passivation. Moreover, CD-PEG and CD-PEG-FA displayed bright blue emission under UV irradiation (inset in Figure 3.2.2a). For a reference, the quantum yield (QY) of as-prepared CDs using quinine sulfate was measured to be 2.1%. After surface passivation, however, the QYs increased significantly to 7.8% for CD-PEG and 10.9% for CD-PEG-FA (Figure 3.2.3). Furthermore, the exciton lifetime was determined by the time-correlated single photon counting (TCSPC) technique, yielding 1.55, 4.13, and 5.52 ns for CD, CD-PEG, and CD-PEG-FA, respectively. This trend matches well with the QY of respective CD derivatives (Figure 3.2.4). The fluorescence emission maxima were located at 450 nm for both CD-PEG and CD-PEG-FA (λ_{ex} = 360 nm), and the broad emission peak maxima were strongly dependent on the excitation wavelength, similar to typical CDs reported (Figure 3.2.2b and 3.2.5).[37,38]

3.2.4.2. Characterizations of PEG passivated and FA functionalized CD

FT-IR spectroscopy revealed changes in chemical functional groups on CDs upon surface passivation. The as-prepared CDs showed peaks at 1068 (C-O stretching), 1608 (C=C stretching), 2848 and 2925 cm^{-1} (C-H stretching), and a broad peak at 3457 cm^{-1} that corresponded to carboxylic acid and hydroxyl groups, respectively (Figure 3.2.2c). Upon surface passivation, the presence of new bands at 1594 (N-H in-plane), 3283 (N-H stretching), and 1340 cm^{-1} (C-N stretching) confirmed the successful formation of amide groups by chemical

conjugation of the surface carboxylic acid groups of CDs with the amine-terminated PEG. Furthermore, the PEG surface passivation significantly increased the peak of C-O groups at 1102 cm^{-1}. After passivation with FA, CD-PEG-FA exhibited characteristic peaks at 1481, 1605, and 1697 cm^{-1} which correspond to FA.[39] In accordance with the above results, high-resolution X-ray photoelectron spectroscopy (XPS) measurements further provided the composition of the respective CDs and the successful surface passivation (Figure 3.2.6 and Table 3.2.1).

The size and morphology of CDs were observed by transmission electron microscopy (TEM) and atomic force microscopy (AFM). The TEM images showed a spherical morphology of CDs with an average diameter of 4.5 ± 0.2 nm for CD-PEG-FA (Figure 3.2.2d). The interlayer spacing of 0.34 nm, observed using high-resolution TEM, corresponds to that of graphitic carbon, representing the graphitic nature of CDs. The AFM line scans indicated that the diameter of CD, CD-PEG and CD-PEG-FA were approximately 3.5, 4.4, and 4.9 nm, respectively, consistent with the stepwise surface functionalization with PEG and FA of CDs (Figure 3.2.2e and 3.2.7).

3.2.4.3. Synthesis of ZnPc loaded on CD-PEG-FA

After characterization of the chemically functionalized CDs, ZnPc was loaded onto CD-PEG-FA by π- π stacking interactions. The CD-PEG-FA carrying ZnPc (CD-PEG-FA/ZnPc) exhibited red-shifted absorption peaks at 607 and 689 nm originated from ZnPc and strongly quenched fluorescence of ZnPc, suggesting the successful loading of ZnPc (Figure 3.2.8).[25,40-43] The characteristic fluorescence spectrum and QY of CD-PEG-FA also did not alter upon loading with ZnPc (6 wt% of ZnPc/CD-PEG-FA). AFM and dynamic light scattering (DLS) analysis showed no aggregation of CD-PEG-FA/ZnPc, suggesting the uniform loading of ZnPc onto the surface of CD-PEG-FA carrier by π- π stacking interactions (Figure 3.2.9).

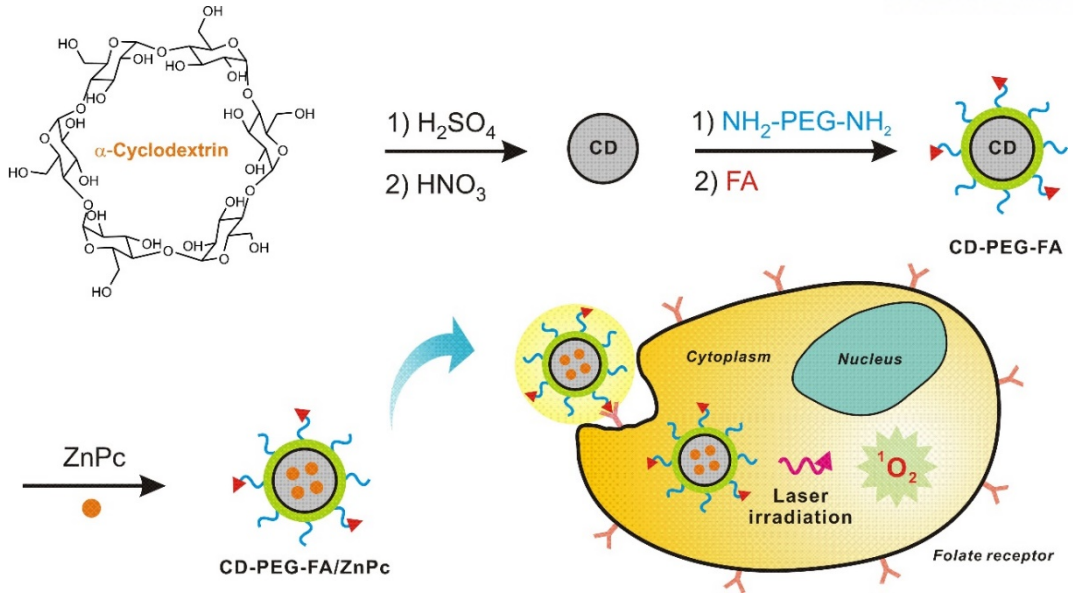

Figure 3.2.1. Schematic illustration of the preparation of carbon nanoparticles (CDs) from α-cyclodextrin and targeted photodynamic therapy with folic acid functionalized carbon nanodots loaded with zinc phthalocyanine (CD-PEG-FA/ZnPc).

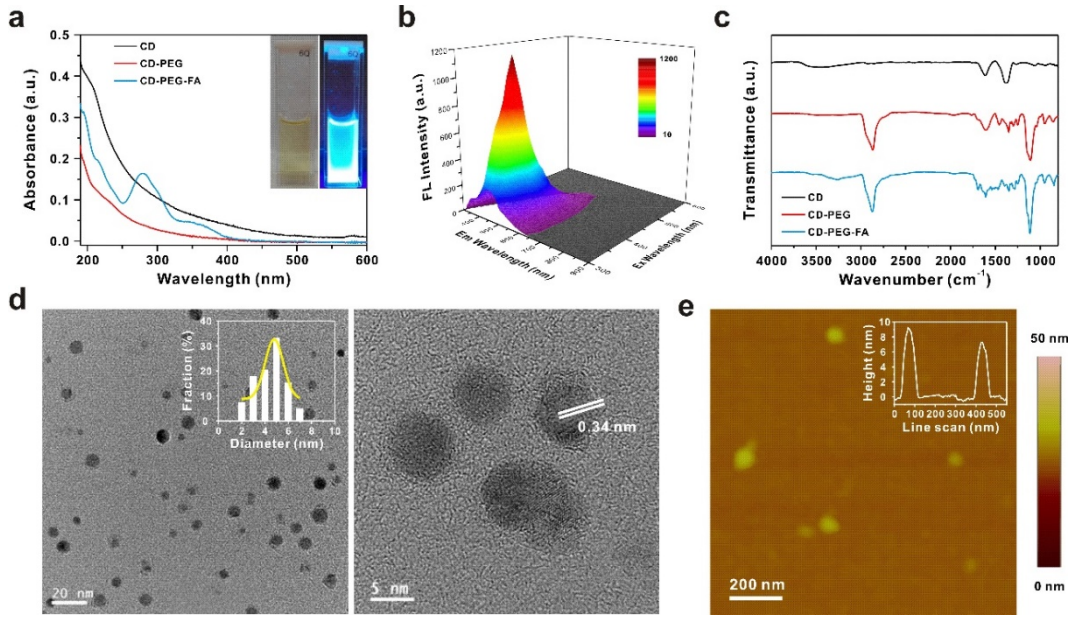

Figure 3.2.2. (a) UV-vis absorbance spectra of CD, CD-PEG, and CD-PEG-FA. Inset shows the CD-PEG-FA suspension (left) under room light and (right) UV illumination at 365 nm. (b) Three-dimensional fluorescence spectra of CD-PEG-FA under varying excitation wavelengths from 300 to 600 nm with 10-nm increments. (c) FT-IR spectra of CD, CD-PEG, and CD-PEG-FA. (d) TEM images of CD-PEG-FA with a corresponding size distribution histogram. (e) Representative height-mode AFM topography image of CD-PEG-FA with a line scan profile in the inset.

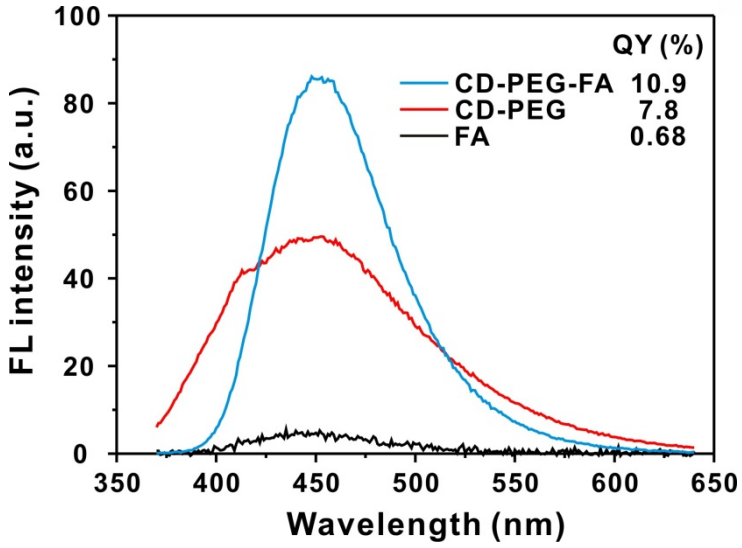

Figure 3.2.3. Fluorescence spectra of free FA, CD-PEG, and CD-PEG-FA. The QY increase after the FA conjugation is resulted from the successful surface passivation of CD with a small molecule like FA.

a

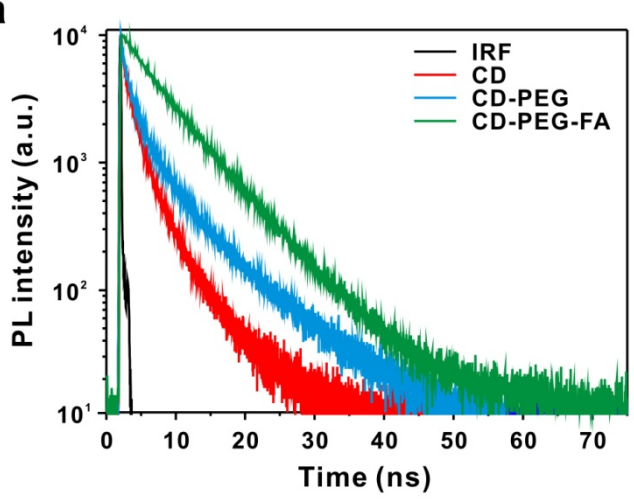

b

	CD	CD-PEG	CD-PEG-FA
t1 (ns)	6.23 (0.07)	9.7 (0.37)	7.21 (0.58)
t2 (ns)	1.96 (0.48)	2.85 (0.08)	3.84 (0.33)
t3 (ns)	0.44 (0.45)	0.60 (0.55)	0.14 (0.09)
X^2	1.04	1.2	1
$t_{average}$(ns)	1.55	4.13	5.52

Figure 3.2.4. (a) Time-resolved PL signal measure by time-correlated single photon counting (TCSPC) and (b) exiton lifetime of CD, CD-PEG and CD-PEG-FA.

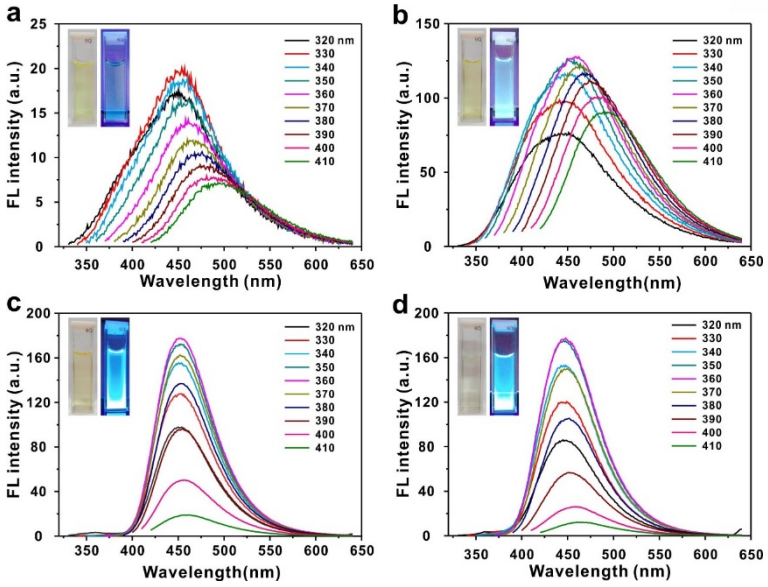

Figure 3.2.5. Fluorescence spectra of (a) CD, (b) CD-PEG, (c) CD-PEG-FA, and (d) CD-PEG-FA/ZnPc. Inset images represent the optical images of the respective CDs under (left) ambient light and (right) UV light at 365 nm.

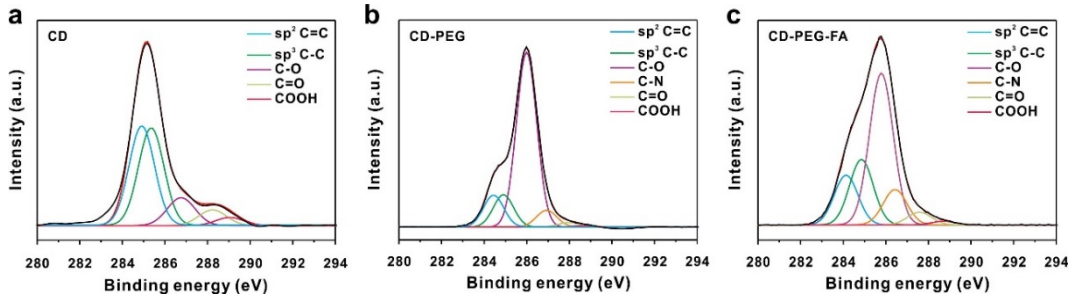

Figure 3.2.6. Deconvoluted high-resolution XPS C 1s peak of (a) CD, (b) CD-PEG, and (c) CD-PEG-FA.

Table 3.2.1. Elemental composition of CDs determined by XPS

	Carbon	Oxygen	Nitrogen
CD	17.39	50.48	0.79
CD-PEG	66.26	30.01	2.09
CD-PEG-FA	70.90	24.78	3.31

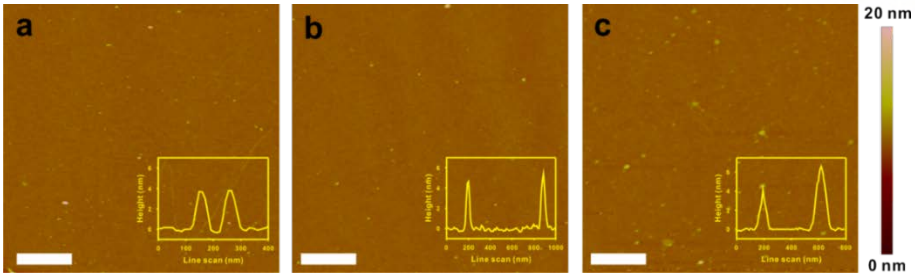

Figure 3.2.7. Height-mode AFM images of (a) CD, (b) CD-PEG and (c) CD-PEG-FA with corresponding line scan profiles. The scale bar is 1 μm.

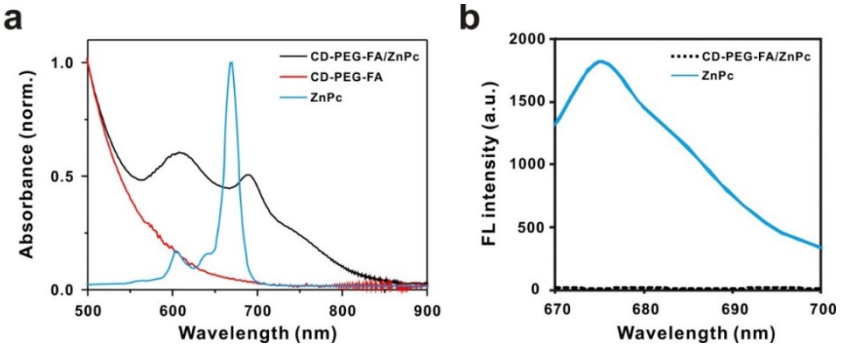

Figure 3.2.8. (a) UV-vis absorbance spectra of (red) CD-PEG-FA, (black) CD-PEG-FA/ZnPc and (blue) free ZnPc. (b) Fluorescence spectra of (solid line) free ZnPc, (dotted line) CD-PEG-FA/ZnPc with an excitation wavelength of 650 nm.

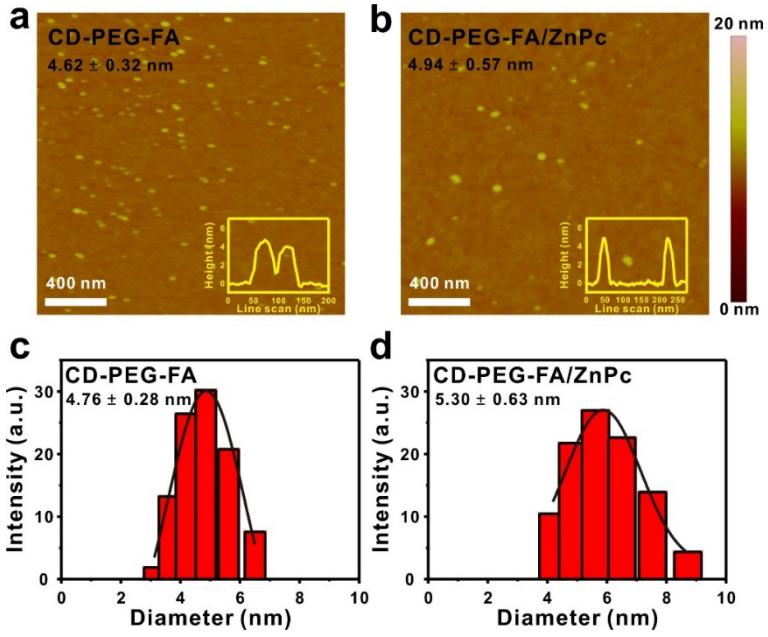

Figure 3.2.9. (a, b) AFM and (c, d) dynamic light scattering (DLS) of (a, c) CD-PEG-FA and (b, d) CD-PEG-FA/ZnPc.

3.2.4.4. Application: Targeted bioimaging

To investigate the efficacy of targeted delivery and photodynamic therapy of CD-PEG-FA/ZnPc, we employed a human cervical cancer HeLa cells which are known to overexpress the folate receptor-α.[44] Initially, a conventional CCK-8 based cell viability assay suggested the superior biocompatibility of CD and its derivatives toward the HeLa cells under the present working concentration ranges of the respective CD derivatives (5 – 100 μg/mL) (Figure 3.2.910 and 3.2.11).[45] As shown in Figure 3.2.12 and 3.2.13, the targeting of CD-PEG, CD-PEG-FA and CD-PEG-FA/ZnPc were evaluated after incubation with the HeLa cells for 12 h by monitoring the blue and red fluorescence of CD ($\lambda_{ex}/\lambda_{em}$ = 358/461 nm) and ZnPc ($\lambda_{ex}/\lambda_{em}$ = 647/665 nm), respectively, to probe the internalization of CD and ZnPc under a fluorescence microscope. As expected, the cells incubated with CD-PEG-FA displayed intense CD fluorescence in the cytoplasm, whereas CD-PEG exhibited no sign of internalization into the HeLa cells, albeit treated with an identical concentration of CD-PEG-FA. In accord with CD-PEG-FA, CD-PEG-FA/ZnPc was also internalized in the HeLa cells with prominent fluorescence signals of both blue (CD) and red (ZnPc) channel, indicating the successful intracellular delivery of ZnPc by the CD carrier. To clarify the targeting role of FA, a competition assay was performed with free FA. The folate receptors on the HeLa cells were first saturated with free FA followed by the introduction of CD-PEG-FA/ZnPc, which clearly demonstrated no cellular internalization (Figure 3.2.12d). The targeting affinity and efficacy based on the FA and folate receptor was further evaluated using folate receptor overexpressed (FR+) and folate receptor deficient (FR-) cell lines. After incubated with CD-PEG/ZnPc and CD-PEG-FA/ZnPc, FR+ MDA-MB-231 cells were monitored by fluorescence microscope, and FR- A549 cells were used as a negative control. Figure 3.2.14 showed that the fluorescent CD and ZnPc were localized with intracellular cytoplasm, indicating that CD-PEG-FA/ZnPc was effectively internalized into the cells through the close rapport between FA and FR. However, no significant fluorescence was observed in FR- A549 cells and even CD-PEG/ZnPc treated MDA-MB-231 cells.

Taken together, these results corroborate that the folate receptors overexpressed on the surface of the HeLa cells facilitate the recognition of the CD-PEG-FA and induce the preferential uptake of CD-PEG-FA by receptor-mediated endocytosis.[44,46,47] Since the passive targeting of PS is inadequate for *in vivo* photodynamic treatment through systemic administration, the modification of active targeting ligands to the surface of CD is critical to increase the local concentration of PS in tumors, thus helps to avoid the side effects and maximizes the therapeutic efficacy.

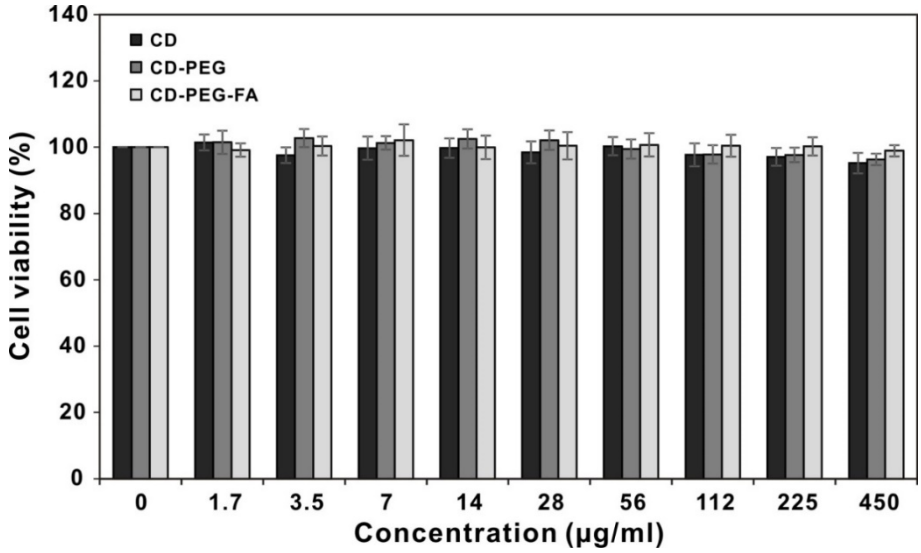

Figure 3.2.10. CCK-8 based cell viability assays with HeLa cells with different concentration of CD, CD-PEG and CD-PEG-FA.

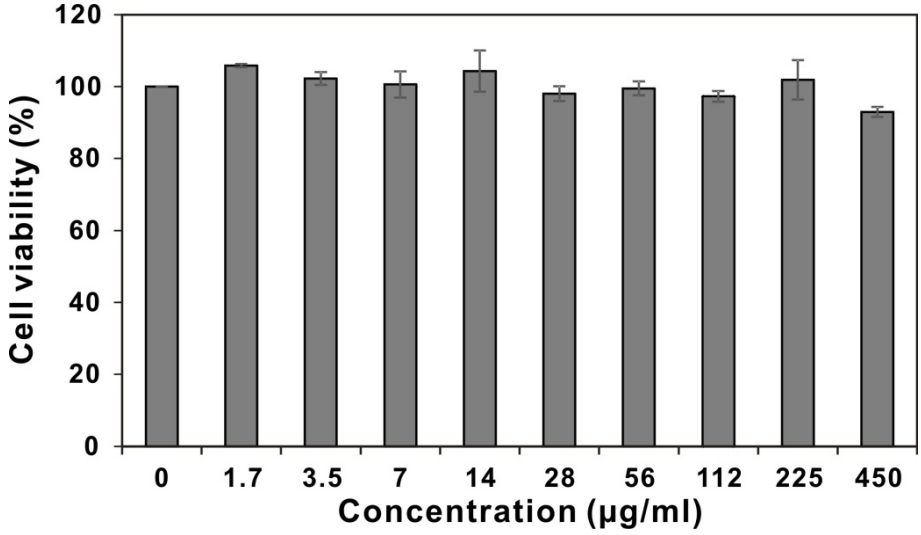

Figure 3.2.11. CCK-8 based cell viability assays with HeLa cells with different concentration of CD-PEG-FA/ZnPc.

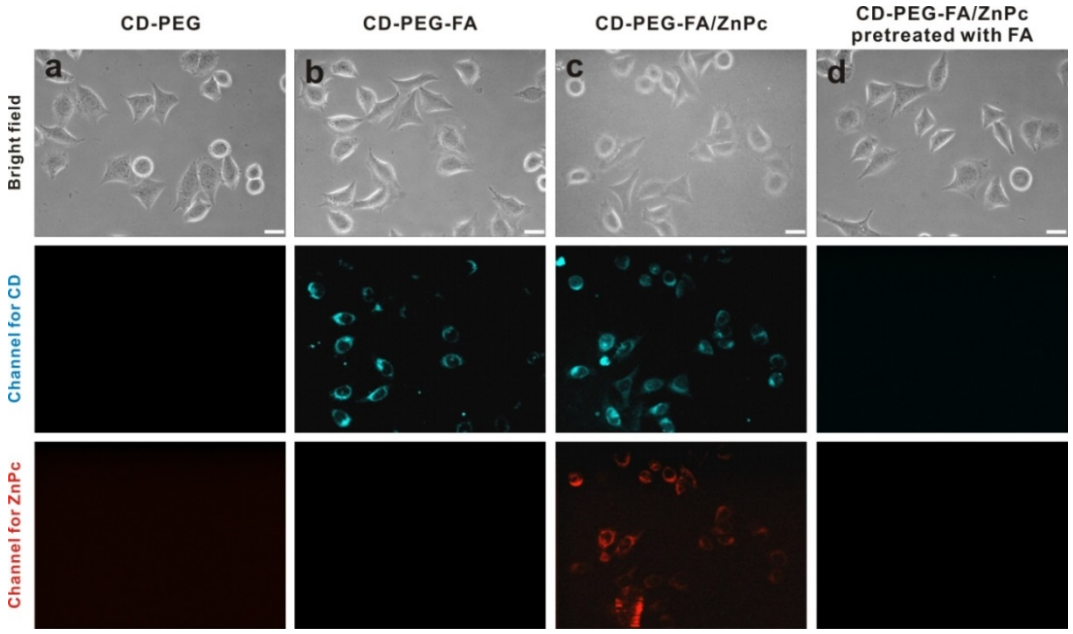

Figure 3.2.12. (a-d) Bright field and fluorescence images of HeLa cells treated with CD derivatives (50 μg/ml) for 12 h. (a) CD-PEG, (b) CD-PEG-FA, (c) CD-PEG-FA/ZnPc and (d) CD-PEG-FA/ZnPc pre-treated with folic acid. Fluorescence signals of (blue) CDs and (red) ZnPc were observed at 461 nm (λ_{ex} = 358 nm) and 665 nm (λ_{ex} = 647 nm), respectively. Scale bar is 20 μm.

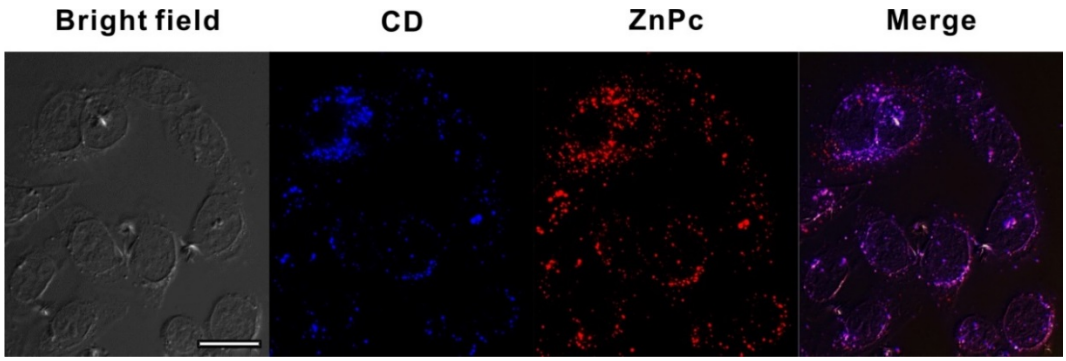

Figure 3.2.13. Bright field and fluorescence images of HeLa cells treated with CD-PEG-FA/ZnPc (50 μg/ml) for 12 h. Fluorescence signals of (blue) CDs and (red) ZnPc were observed by using Deltavision high-resolution microscopy. Scale bar is 20 μm.

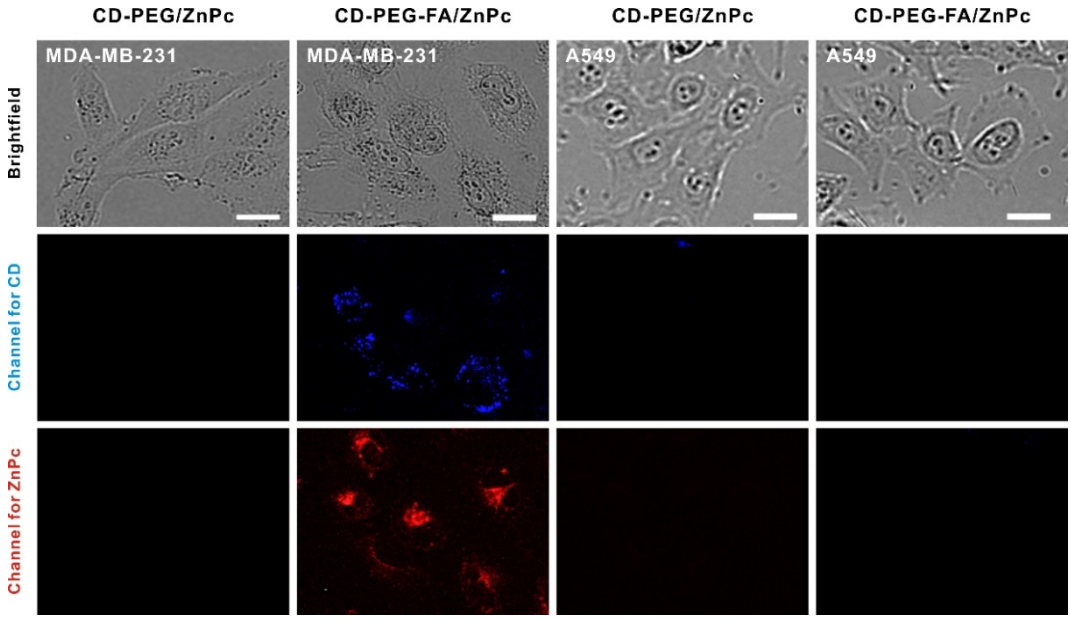

Figure 3.2.14. Fluorescence of CD-PEG/ZnPc was measured in folate receptor overexpressed cell (MDA-MB-231 cells) and folate receptor deficient cell (A549 cells) by In-cell analyzer 2000 after 12 h incubation. No significant fluorescence of CD and ZnPc were observed in A549 cells and CD-PEG/ZnPc treated MDA-MB-231 cells. Scale bar is 20 μm.

3.2.4.5. Application: Targeted photodynamic therapy *in vitro*

Next, we performed a photodynamic therapy on the HeLa cells with the CD derivatives (Figure 3.2.15). The cells were exposed to the CD derivatives for 12 h followed by laser irradiation (660 nm, 30 mW/cm^2) for 10 min. Significant cell death was observed in CD-PEG-FA/ZnPc, whereas other samples treated with CD-PEG, CD-PEG-FA and FA-pretreated CD-PEG-FA/ZnPc did not exhibit measurable photodynamic activity (Figure 3.2.15 and 3.2.16). In addition, the generation of the active singlet oxygen species via photo-induced energy transfer from ZnPc was quantified by using the singlet oxygen sensor green (SOSG) reagent;[48,49] the green fluorescence (λ_{em} = 525 nm) is known to increase when SOSG reacts with singlet oxygen generated from PS, which can be used for quantification for singlet oxygen generation.[50,51] Figure 3.2.15e shows the fluorescence intensity as a function of irradiation time that gradually increases upon irradiation with an LED light (30 mW/cm^2). While the control ZnPc without SOSG did not exhibit any fluorescence changes, ZnPc and CD-PEG-FA/ZnPc mixed with SOSG showed an increase in the fluorescence intensity upon irradiation. It is of note that SOSG alone showed increasing fluorescence intensity upon irradiation since SOSG itself can act as a PS and thus, generate singlet oxygen species.[52] Due to intramolecular energy transfer between ZnPc and CD, the CD-PEG-FA/ZnPc did not effectively generate singlet oxygen relative to free ZnPc with SOSG. However, singlet oxygen generation was considerably accelerated upon the addition of cell lysate (Figure 3.2.15e, t = 25 min), indicating the release of ZnPc from CD via the competitive displacement of ZnPc by interaction with biomolecules in cell lysate, thus enhancing the therapeutic efficiency of photodynamic therapy.

Quantitative CCK-8 cell viability assays, used to investigate the effects of concentration and laser irradiation, were carried out using the HeLa cells incubated for 12 h. For example, the cell viabilities of free ZnPc, CD-PEG-FA/ZnPc without irradiation, and CD-PEG-FA/ZnPc with irradiation were determined to be 60.9, 94.2, and 8.2%, respectively, at a concentration of 100 μg/mL. The result clearly confirms that the generation of singlet oxygen, and thus, the effective photodynamic action necessitates both suitable concentrations of PS and appropriate light irradiation. Moreover, the significant difference in the viability between the irradiated CD-PEG-FA/ZnPc and free ZnPc is consistent with the preferential internalization of CD-PEG-FA/ZnPc into the HeLa cells, which results in considerably improved therapeutic efficacy of photodynamic action.

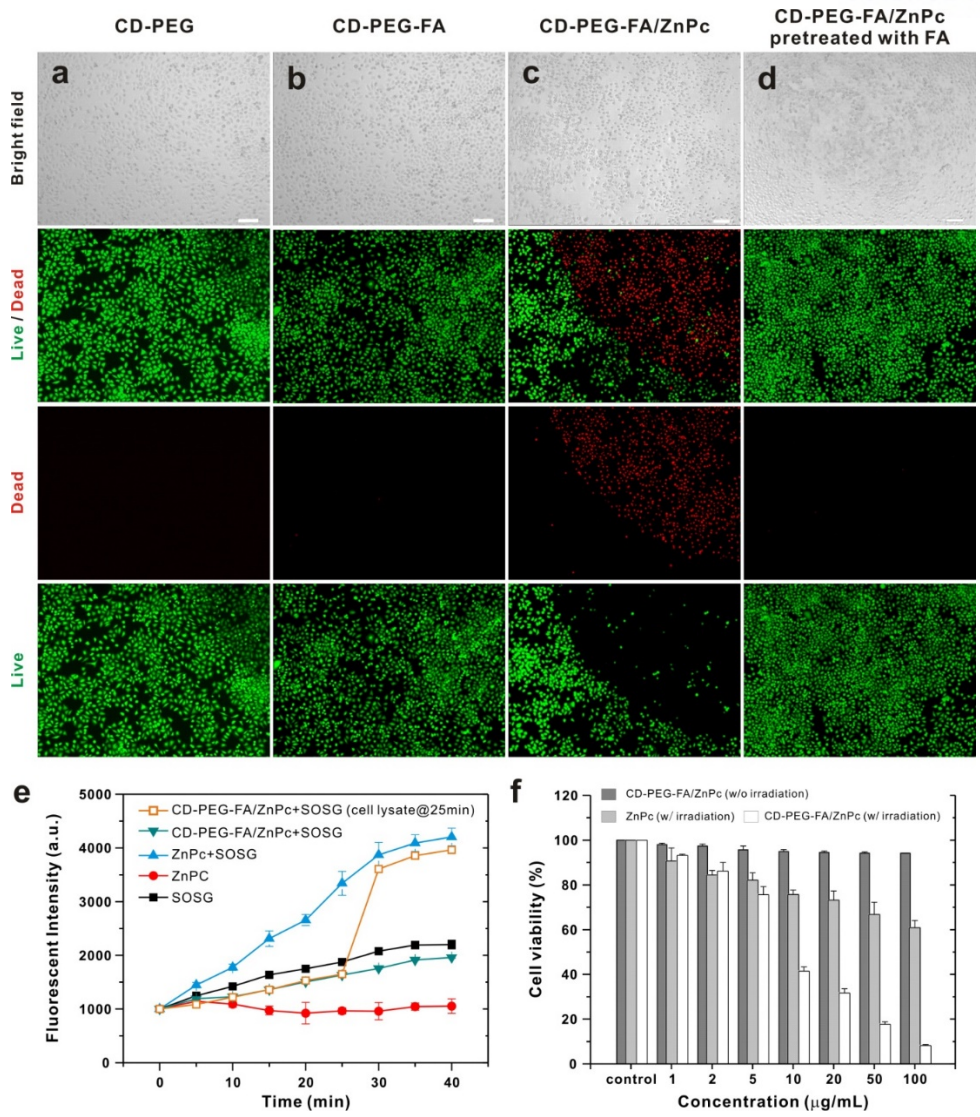

Figure 3.2.15. (a-d) (top panel) Bright field and fluorescence images of HeLa cells treated with CD derivatives (50 μg/ml) for 12 h followed by irradiation for 10 min with a 660 nm laser (30 mW/cm^2) and (bottom panels) live and dead cells colored green and red, respectively by live/dead assay. (a) CD-PEG, (b) CD-PEG-FA, (c) CD-PEG-FA/ZnPc and (d) CD-PEG-FA/ZnPc with pre-treatment of excess free FA. Scale bar is 100 μm. (e, f) Quantitative evaluation of photodynamic effect. (e) Singlet oxygen detection test using a singlet oxygen sensor green (SOSG) reagent. Time-dependent fluorescent intensity ($\lambda_{ex}/\lambda_{em}$ = 504/530 nm) with irradiation by using a 660 nm laser (30 mW/cm^2). Concentration of ZnPc and SOSG used are 3.8 and 2.5 μM, respectively. Note that the addition of cell lysate (1 μL) in CD-PEG-FA/ZnPc did not change the effective concentrations of ZnPc and SOSG. (f) Cell viability assay depending on the concentration of ZnPc loaded CD-PEG-FA and ZnPc with and without irradiation for 10 min. All experiments were carried out in triplicate and the error bars represent the standard deviation.

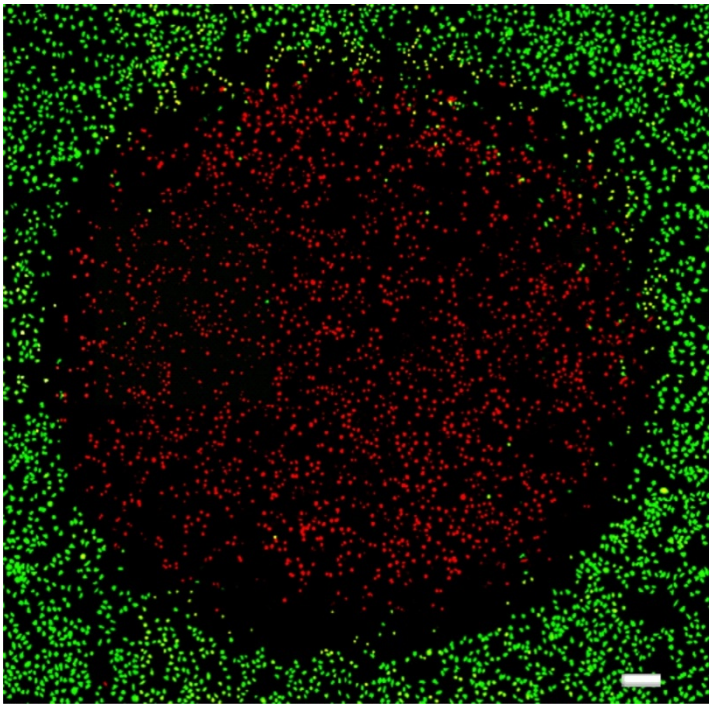

Figure 3.2.16. Fluorescence image of HeLa cells which were treated with CD-PEG-FA/ZnPc (50 μg/ml) for 12 h followed by irradiation with a 660-nm laser (30 mW/cm^2) for 10 min. Live and dead cells were colored green and red, respectively by live/dead assay. Scale bar is 100 μm.

3.2.4.6. Application: Targeted photodynamic therapy *in vivo*

Encouraged by the high PDT efficacy *in vitro*, we next investigated the PDT efficacy of the CD-mediated PS delivery system in animal model. Tumor-bearing mice were first prepared by subcutaneously injecting a suspension of the HeLa cells (6×10^6 cells) in sterilized 1X PBS solution into BALB/c nude mice (6 weeks old). To monitor biodistribution of the CD derivatives *in vivo*, the fluorescence images from whole body were obtained at designated time points after the various CD derivatives were injected into tail veins. As shown in Figure 3.2.17a and 3.2.17b, the mice treated with CD-PEG-FA/ZnPc showed strong fluorescence signal corresponding to ZnPc in tumors with gradual increase of fluorescence intensity over time in contrast to the mice treated with CD-PEG/ZnPc or CD-PEG-FA. Biodistribution of the CD derivatives were further examined by imaging major organs that were excised after sacrificing the mice administered with the CD derivatives. Fluorescence images of the major organs in Figure 3.2.17c showed that the fluorescence corresponding ZnPc were intense in liver and spleen rather than tumor in case of the mouse injected with CD-PEG/ZnPc, suggesting that most of the CDs omitting targeting ligand FA leaked out by circulation and prominently accumulated in reticuloendothelial system of liver and spleen.[53,54] These results showed that conjugation of FA to CD played an important role in greatly improving active tumor-targeting capability of ZnPc delivery vehicle to folate receptor-overexpressing tumors.

Finally, to investigate therapeutic efficacy *in vivo*, the changes of tumor volumes were monitored for 10 days after CD-PEG-FA, CD-PEG/ZnPc, and CD-PEG-FA/ZnPc (0.5 mg of ZnPc/kg of mouse) were intravenously injected to mice of which tumor volumes were ~70 mm^3. Same volume of saline was treated as a control and the relative tumor volumes were determined by comparing its volumes at different time points to their initial volumes (Figure 3.2.17d and 3.2.17e). After irradiation with 660-nm laser (0.3 W/cm^2, 20 min), the mice treated with CD-PEG-FA/ZnPc showed remarkable suppression of tumor growth compared to control mice for 8 days. However, the mice treated with the CDs lacking targeting moiety FA, with or without laser irradiation, showed no notable difference in tumor size compared to controls. The result was in agreement with *in vitro* data, indicating that combination of targeted delivery of ZnPc and light irradiation can effectively induce cancer cell death *in vivo*. Collectively, the *in vivo* study suggested that the present tumor-targeted CD based PDT therapeutic agent delivery system can effectively induce the accumulation of the PS loaded CDs in tumors and thus, achieved the enhanced therapeutic efficacy with relatively small quantity of ZnPc.

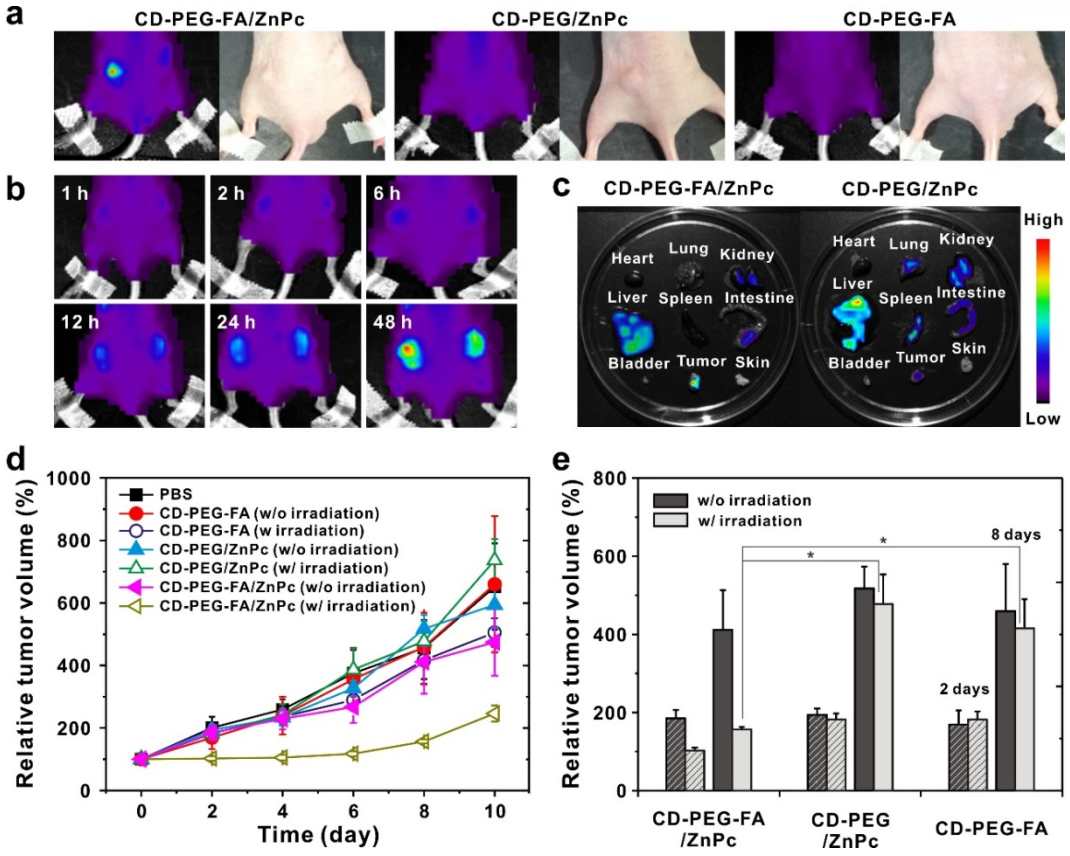

Figure 3.2.17. (a) Fluorescence of ZnPc (excited at 660 nm) in tumor was imaged after 12 h injection of CD-PEG-FA/ZnPc, CD-PEG/ZnPc, and CD-PEG-FA (0.5 mg of ZnPc/kg mouse). (b) CD-PEG-FA/ZnPc suspensions were injected into tail veins of tumor-bearing mice and the fluorescent signals were obtained at various time points (1, 2, 6, 12, 24, and 48 h). (c) *Ex vivo* fluorescence images of major organs of mice. The fluorescent signals corresponding to ZnPc (excited at 660 nm) from major organs, tumor, and skin were obtained after 12 h of i.v. injection of CD-PEG-FA/ZnPc and CD-PEG/ZnPc into tumor-bearing mice. FA-conjugated CD delivered and released ZnPc to tumor effectively, in contrast with the CD lacking FA. (d, e) Relative tumor volumes measured over time after the tumor-bearing mice were treated with various CD derivatives. Tumor-bearing mice were separated into 6 groups: (i) PBS control; (ii) CD-PEG-FA without irradiation; (iii) CD-PEG-FA with irradiation; (iv) CD-PEG/ZnPc without irradiation; (v) CD-PEG/ZnPc with irradiation; (vi) CD-PEG-FA/ZnPc without irradiation; (vii) CD-PEG-FA/ZnPc with irradiation (n = 4 for each group). Irradiation was performed using a 660-nm laser at 0.3 W/cm^2. Tumor volumes were measured over 10 days. It is notable that no significant increase in tumor volume was observed for 8 days in mice treated with CD-PEG-FA/ZnPc with irradiation. P values were calculated by Student's t-test: * for $p < 0.05$, $n = 4$.

3.2.5. Conclusion

In summary, we developed a novel theranostic platform based on FA-conjugated CD loaded with ZnPc in the present study. We have successfully demonstrated the targeted delivery of a PS via FA-mediated endocytosis of biocompatible CD-PEG-FA/ZnPc and therapeutic photodynamic efficacy by singlet oxygen generation from the internalized ZnPc upon light irradiation *in vitro* and *in vivo*. We anticipate that the present CD-based targeted delivery of the PS would offer a convenient and effective platform for enhanced photodynamic therapy to treat cancers in the near future because of its excellent biocompatibility, bioimaging and targeting capability, and therapeutic efficacy.

3.2.6. References

1. Weissleder, R. Scaling Down Imaging: Molecular Mapping of Cancer in Mice. *Nat. Rev. Cancer* **2002,** *2*, 11-18.
2. Willmann, J. K.; van Bruggen, N.; Dinkelborg, L. M.; Gambhir, S. S. Molecular Imaging in Drug Development. *Nat. Rev. Drug Discovery* **2008,** *7*, 591-607.
3. Barreto, J. A.; O'Malley, W.; Kubeil, M.; Graham, B.; Stephan, H.; Spiccia, L. Nanomaterials: Applications in Cancer Imaging and Therapy. *Adv. Mater.* **2011,** *23*, H18-H40.
4. Alivisatos, A. P. Semiconductor Clusters, Nanocrystals, and Quantum Dots. *Science* **1996,** *271*, 933-937.
5. Michalet, X.; Pinaud, F. F.; Bentolila, L. A.; Tsay, J. M.; Doose, S.; Li, J. J.; Sundaresan, G.; Wu, A. M.; Gambhir, S. S.; Weiss, S. Quantum Dots for Live Cells, *In Vivo* Imaging, and Diagnostics. *Science* **2005,** *307*, 538-544.
6. Medintz, I. L.; Uyeda, H. T.; Goldman, E. R.; Mattoussi, H. Quantum Dot Bioconjugates for Imaging, Labelling and Sensing. *Nat. Mater.* **2005,** *4*, 435-446.
7. Derfus, A. M.; Chan, W. C. W.; Bhatia, S. N. Probing the Cytotoxicity of Semiconductor Quantum Dots. *Nano Lett.* **2004,** *4*, 11-18.
8. Hardman, R. A Toxicologic Review of Quantum Dots: Toxicity Depends on Physicochemical and Environmental Factors. *Environ. Health Perspect.* **2006,** *114*, 165-172.
9. Yang, S. T.; Cao, L.; Luo, P. G. J.; Lu, F. S.; Wang, X.; Wang, H. F.; Meziani, M. J.; Liu, Y. F.; Qi, G.; Sun, Y. P. Carbon Dots for Optical Imaging *In Vivo*. *J. Am. Chem. Soc.* **2009,** *131*, 11308-11309.
10. Baker, S. N.; Baker, G. A. Luminescent Carbon Nanodots: Emergent Nanolights. *Angew. Chem. Int. Ed.* **2010,** *49*, 6726-6744.
11. Li, H. T.; Kang, Z. H.; Liu, Y.; Lee, S. T. Carbon Nanodots: Synthesis, Properties and Applications. *J. Mater. Chem.* **2012,** *22*, 24230-24253.
12. Ray, S. C.; Saha, A.; Jana, N. R.; Sarkar, R. Fluorescent Carbon Nanoparticles: Synthesis, Characterization, and Bioimaging Application. *J. Phys. Chem. C* **2009,** *113*, 18546-18551.
13. Huang, P.; Lin, J.; Wang, X. S.; Wang, Z.; Zhang, C. L.; He, M.; Wang, K.; Chen, F.; Li, Z. M.; Shen, G. X.; Cui, D. X.; Chen, X. Y. Light-Triggered Theranostics Based on Photosensitizer-Conjugated Carbon Dots for Simultaneous Enhanced-Fluorescence Imaging and Photodynamic Therapy. *Adv. Mater.* **2012,** *24*, 5104-5110.
14. Tang, J.; Kong, B.; Wu, H.; Xu, M.; Wang, Y. C.; Wang, Y. L.; Zhao, D. Y.; Zheng, G. F. Carbon Nanodots Featuring Efficient FRET for Real-Time Monitoring of Drug Delivery and Two-Photon Imaging. *Adv. Mater.* **2013,** *25*, 6569-6574.

15. Wang, Q. L.; Huang, X. X.; Long, Y. J.; Wang, X. L.; Zhang, H. J.; Zhu, R.; Liang, L. P.; Teng, P.; Zheng, H. Z. Hollow Luminescent Carbon Dots for Drug Delivery. *Carbon* **2013,** *59*, 192-199.
16. Dolmans, D. E. J. G. J.; Fukumura, D.; Jain, R. K. Photodynamic Therapy for Cancer. *Nat. Rev. Cancer* **2003,** *3*, 380-387.
17. Henderson, B. W.; Dougherty, T. J. How Does Photodynamic Therapy Work. *Photochem. Photobiol.* **1992,** *55*, 145-157.
18. Lovell, J. F.; Liu, T. W. B.; Chen, J.; Zheng, G. Activatable Photosensitizers for Imaging and Therapy. *Chem. Rev.* **2010,** *110*, 2839-2857.
19. Konan, Y. N.; Gurny, R.; Allemann, E. State of the Art in the Delivery of Photosensitizers for Photodynamic Therapy. *J. Photochem. Photobiol. B* **2002,** *66*, 89-106.
20. Bechet, D.; Couleaud, P.; Frochot, C.; Viriot, M. L.; Guillemin, F.; Barberi-Heyob, M. Nanoparticles as Vehicles for Delivery of Photodynamic Therapy Agents. *Trends Biotechnol.* **2008,** *26*, 612-621.
21. Derycke, A. S. L.; de Witte, P. A. M. Liposomes for Photodynamic Therapy. *Adv. Drug Delivery Rev.* **2004,** *56*, 17-30.
22. Son, K. J.; Yoon, H. J.; Kim, J. H.; Jang, W. D.; Lee, Y.; Koh, W. G. Photosensitizing Hollow Nanocapsules for Combination Cancer Therapy. *Angew. Chem. Int. Ed.* **2011,** *50*, 11968-11971.
23. Kuo, W. S.; Chang, C. N.; Chang, Y. T.; Yang, M. H.; Chien, Y. H.; Chen, S. J.; Yeh, C. S. Gold Nanorods in Photodynamic Therapy, as Hyperthermia Agents, and in Near-Infrared Optical Imaging. *Angew. Chem. Int. Ed.* **2010,** *49*, 2711-2715.
24. Obaid, G.; Chambrier, I.; Cook, M. J.; Russell, D. A. Targeting the Oncofetal Thomsen-Friedenreich Disaccharide Using Jacalin-PEG Phthalocyanine Gold Nanoparticles for Photodynamic Cancer Therapy. *Angew. Chem. Int. Ed.* **2012,** *51*, 6158-6162.
25. Tian, B.; Wang, C.; Zhang, S.; Feng, L. Z.; Liu, Z. Photothermally Enhanced Photodynamic Therapy Delivered by Nano-Graphene Oxide. *ACS Nano* **2011,** *5*, 7000-7009.
26. Li, F.; Park, S.; Ling, D.; Park, W.; Han, J. Y.; Na, K.; Char, K. Hyaluronic Acid-Conjugated Graphene Oxide/Photosensitizer Nanohybrids for Cancer Targeted Photodynamic Therapy. *J. Mater. Chem. B* **2013,** *1*, 1678-1686.
27. Zhu, Z.; Tang, Z. W.; Phillips, J. A.; Yang, R. H.; Wang, H.; Tan, W. H. Regulation of Singlet Oxygen Generation using Single-Walled Carbon Nanotubes. *J. Am. Chem. Soc.* **2008,** *130*, 10856-10857.
28. Sharman, W. M.; van Lier, J. E.; Allen, C. M. Targeted photodynamic therapy via receptor mediated delivery systems. *Adv. Drug Delivery Rev.* **2004,** *56*, 53-76.
29. Verma, S.; Watt, G. M.; Mal, Z.; Hasan, T. Strategies for Enhanced Photodynamic

Therapy Effects. *Photochem. Photobiol.* **2007,** *83*, 996-1005.

30. Schmitt, F.; Juillerat-Jeanneret, L. Drug Targeting Strategies for Photodynamic Therapy. *Anti-Cancer Agents Med. Chem.* **2012,** *12*, 500-525.
31. Choi, H.; Ko, S. J.; Choi, Y.; Joo, P.; Kim, T.; Lee, B. R.; Jung, J. W.; Choi, H. J.; Cha, M.; Jeong, J. R.; Hwang, I. W.; Song, M. H.; Kim, B. S.; Kim, J. Y. Versatile Surface Plasmon Resonance of Carbon-Dot-Supported Silver Nanoparticles in Polymer Optoelectronic Devices. *Nat. Photonics* **2013,** *7*, 732-738.
32. Sun, Y. P.; Zhou, B.; Lin, Y.; Wang, W.; Fernando, K. A. S.; Pathak, P.; Meziani, M. J.; Harruff, B. A.; Wang, X.; Wang, H. F.; Luo, P. J. G.; Yang, H.; Kose, M. E.; Chen, B. L.; Veca, L. M.; Xie, S. Y. Quantum-Sized Carbon Dots for Bright and Colorful Photoluminescence. *J. Am. Chem. Soc.* **2006,** *128*, 7756-7757.
33. Leamon, C. P.; Low, P. S. Folate-Mediated Targeting: From Diagnostics to Drug and Gene Delivery. *Drug Disc. Today* **2001,** *6*, 44-51.
34. Owens, J. W.; Smith, R.; Robinson, R.; Robins, M. Photophysical Properties of Porphyrins, Phthalocyanines, and Benzochlorins. *Inorg. Chim. Acta* **1998,** *279*, 226-231.
35. Tang, L. B.; Ji, R. B.; Cao, X. K.; Lin, J. Y.; Jiang, H. X.; Li, X. M.; Teng, K. S.; Luk, C. M.; Zeng, S. J.; Hao, J. H.; Lau, S. P. Deep Ultraviolet Photoluminescence of Water-Soluble Self-Passivated Graphene Quantum Dots. *ACS Nano* **2012,** *6*, 5102-5110.
36. Song, Y. C.; Shi, W.; Chen, W.; Li, X. H.; Ma, H. M. Fluorescent Carbon Nanodots Conjugated with Folic Acid for Distinguishing Folate-Receptor-Positive Cancer Cells from Normal Cells. *J. Mater. Chem.* **2012,** *22*, 12568-12573.
37. Qu, S. N.; Wang, X. Y.; Lu, Q. P.; Liu, X. Y.; Wang, L. J. A Biocompatible Fluorescent Ink Based on Water-Soluble Luminescent Carbon Nanodots. *Angew. Chem. Int. Ed.* **2012,** *51*, 12215-12218.
38. Zhu, S. J.; Meng, Q. N.; Wang, L.; Zhang, J. H.; Song, Y. B.; Jin, H.; Zhang, K.; Sun, H. C.; Wang, H. Y.; Yang, B. Highly Photoluminescent Carbon Dots for Multicolor Patterning, Sensors, and Bioimaging. *Angew. Chem. Int. Ed.* **2013,** *52*, 3953-3957.
39. Huang, H.; Yuan, Q.; Shah, J. S.; Misra, R. D. K. A New Family of Folate-Decorated and Carbon Nanotube-Mediated Drug Delivery System: Synthesis and Drug Delivery Response. *Adv. Drug Delivery Rev.* **2011,** *63*, 1332-1339.
40. Zhang, M.; Murakami, T.; Ajima, K.; Tsuchida, K.; Sandanayaka, A. S. D.; Ito, O.; Iijima, S.; Yudasaka, M. Fabrication of ZnPc/Protein Nanohorns for Double Photodynamic and Hyperthermic Cancer Phototherapy. *Proc. Natl. Acad. Sci. U. S. A.* **2008,** *105*, 14773-14778.
41. Sun, X. M.; Liu, Z.; Welsher, K.; Robinson, J. T.; Goodwin, A.; Zaric, S.; Dai, H. J. Nano-Graphene Oxide for Cellular Imaging and Drug Delivery. *Nano Res.* **2008,** *1*, 203-212.
42. Liu, Z.; Robinson, J. T.; Sun, X. M.; Dai, H. J. PEGylated Nanographene Oxide for

Delivery of Water-Insoluble Cancer Drugs. *J. Am. Chem. Soc.* **2008,** *130*, 10876-10877.

43. Karousis, N.; Ortiz, J.; Ohkubo, K.; Hasobe, T.; Fukuzumi, S.; Sastre-Santos, A.; Tagmatarchis, N. Zinc Phthalocyanine-Graphene Hybrid Material for Energy Conversion: Synthesis, Characterization, Photophysics, and Photoelectrochemical Cell Preparation. *J. Phys. Chem. C* **2012,** *116*, 20564-20573.
44. Wang, L. S.; Wu, L. C.; Lu, S. Y.; Chang, L. L.; Teng, I. T.; Yang, C. M.; Ho, J. A. A. Biofunctionalized Phospholipid-Capped Mesoporous Silica Nanoshuttles for Targeted Drug Delivery: Improved Water Suspensibility and Decreased Nonspecific Protein Binding. *ACS Nano* **2010,** *4*, 4371-4379.
45. Tao, H. Q.; Yang, K.; Ma, Z.; Wan, J. M.; Zhang, Y. J.; Kang, Z. H.; Liu, Z. In Vivo NIR Fluorescence Imaging, Biodistribution, and Toxicology of Photoluminescent Carbon Dots Produced from Carbon Nanotubes and Graphite. *Small* **2012,** *8*, 281-290.
46. Leamon, C. P.; Reddy, J. A. Folate-Targeted Chemotherapy. *Adv. Drug Delivery Rev.* **2004,** *56*, 1127-1141.
47. Dohmen, C.; Frohlich, T.; Lachelt, U.; Rohl, I.; Vornlocher, H. P.; Hadwiger, P.; Wagner, E. Defined Folate-PEG-siRNA Conjugates for Receptor-Specific Gene Silencing. *Mol. Ther. Nucleic Acids* **2012,** *1*, e7.
48. Bonnett, R. Photosensitizers of the Porphyrin and Phthalocyanine Series for Photodynamic Therapy. *Chem. Soc. Rev.* **1995,** *24*, 19-33.
49. MacDonald, I. J.; Dougherty, T. J. Basic Principles of Photodynamic Therapy. *J. Porphyrins Phthalocyanines* **2001,** *5*, 105-129.
50. Flors, C.; Fryer, M. J.; Waring, J.; Reeder, B.; Bechtold, U.; Mullineaux, P. M.; Nonell, S.; Wilson, M. T.; Baker, N. R. Imaging the Production of Singlet Oxygen *In Vivo* Using a New Fluorescent Sensor, Singlet Oxygen Sensor Green. *J. Exp. Bot.* **2006,** *57*, 1725-1734.
51. Gollmer, A.; Arnbjerg, J.; Blaikie, F. H.; Pedersen, B. W.; Breitenbach, T.; Daasbjerg, K.; Glasius, M.; Ogilby, P. R. Singlet Oxygen Sensor Green: Photochemical Behavior in Solution and in a Mammalian Cell. *Photochem. Photobiol.* **2011,** *87*, 671-679.
52. Ragas, X.; Jimenez-Banzo, A.; Sanchez-Garcia, D.; Batllori, X.; Nonell, S. Singlet Oxygen Photosensitisation by The Fluorescent Probe Singlet Oxygen Sensor Green. *Chem. Commun.* **2009,** 2920-2922.
53. Lammers, T.; Peschke, P.; Kuehnlein, R.; Subr, V.; Ulbrich, K.; Huber, P.; Hennink, W.; Storm, G. Effect of Intratumoral Injection on the Biodistribution and the Therapeutic Potential of HPMA Copolymer-Based Drug Delivery Systems. *Neoplasia* **2006,** *8*, 788-795.
54. Moon, H. K.; Lee, S. H.; Choi, H. C. *In Vivo* Near-Infrared Mediated Tumor Destruction by Photothermal Effect of Carbon Nanotubes. *ACS Nano* **2009,** *3*, 3707-3713.

3.3. Interface Controlled Synthesis of Heterodimeric Silver–Carbon Nanoparticles Derived from Polysaccharides

3.3.1. Abstract

Hybrid nanoparticles composed of multiple components can offer unique opportunities for understanding the nanoscale mechanism and advanced material applications. Here, we report the synthesis of heterodimeric silver-carbon dot nanoparticles (Ag-CD NPs) where Ag NP is grown on the surface of CDs derived from polysaccharide such as chitosan and alginate through the photoelectron transfer reaction between CD and Ag^+ ions. The nanoscale interface between the Ag NPs and the CDs is highly tunable depending on the precursor of CDs and the amount of additives, resulting in fine modification of photoluminescence of the CDs as well as the related surface plasmon resonance of the Ag NPs. This result demonstrates the critical role of interface between the hybrid nanoparticles in governing the electrical and optical properties of respective nanoparticles.

3.3.2. Introduction

With advances in the synthesis of nanoparticles, hybrid nanoparticles that consist of different components are emerging as an important class of materials.[1,2] These nanoparticles are attracting significant interest because their uniquely integrated multifunctional properties are difficult or even impossible to achieve in single-component nanoparticles. These unique features facilitate the application of hybrid nanoparticles in diverse fields, including catalysis,[3,4] sensors,[5] electronics,[6] diagnosis,[7] and therapy.[8] However, the development of facile strategies for the synthesis of multicomponent hybrid nanoparticles has been challenging. To date, there are a number of reports describing the preparation of complex, multimaterial nanoparticles, including core–shell nanoparticles,[9,10] fused-particle heterostructures,[11-14] segmented nanowires,[15,16] particles coated with other particles,[17,18] yolk–shell nanoparticles,[19-21] and more sophisticated anisotropic structures.[22,23] This recent progress allows for the fabrication of various nanoparticles with unique heterostructures; however, the majority of the hybrid nanoparticles are limited to the combination of noble-metal nanoparticles with magnetic or semiconducting nanoparticles.[24-27]

As a benign alternative to semiconducting quantum dots, carbogenic nanoparticles (also known as carbon dots, CDs) have recently received considerable attention by virtue of their interesting physical, optical, and chemical properties, such as their photoluminescence, photostability, and electron transfer behavior.[28-30] By taking advantages of their interesting photoinduced electron transfer phenomena, herein, we developed a facile synthesis of heterodimeric Ag-CD NPs, where Ag NPs are grown at the interface of CDs that originate from polysaccharides of chitosan and alginate (Figure 3.3.1). The interfacial interaction between the Ag NPs and CDs was tuned by changing the CD precursor and the additive during the formation of Ag NPs. The interfaces of the hybrid Ag-CD NPs were characterized with high-resolution transmission electron microscopy (HR-TEM) and electron energy loss spectroscopy (EELS) at atomic scale; the results revealed that the metallic Ag NPs were synthesized at the junction of the CDs. The precise tuning of the metal–carbon interface also allows for modification of the photoluminescence (PL) properties of CDs as well as the related surface plasmon resonance (SPR) of the Ag NPs. Although there are some previous reports on the growth of Ag NPs on the CDs including our own approach,[31-33] to the best of our knowledge, this work represents the first report of heterodimeric structures from Ag-CD NPs with a controlled nanoscale interface.

3.3.3. Experimental

3.3.3.1. Synthesis of CDs

Chitosan (M_w = 210,000), alginic acid sodium salt, ethylenediamine (99%) (EDA), and hydrobromic acid (48%) were purchased from Sigma-Aldrich. Hydrochloric acid (35%) was purchased from Daejung Chemical. CDs were initially synthesized by dehydrating carbohydrates using a commercial household microwave (700 W). To make chitosan-based carbon nanoparticles (CD_{Chi}), 9 mg of chitosan (0.052 mmol) was diluted with 10 ml water, and then different volumes (200 μL to 1000 μL) of 1.0 M HCl were added to dissolve the chitosan in the water. The solution was subsequently mixed with 694 μl of EDA (10.4 mmol) under vigorous stirring for 2 min. The solution was placed into a microwave oven and heated for 2 min. When the solution cooled to room temperature, a red-brown solid was obtained, which was dissolved in 2 ml of water and filtered with a syringe filter (0.45 μm) to remove salt and unreacted chitosan. CD_{Alg} (alginate-based carbon nanoparticles) was obtained by an identical protocol with alginate substituted for the chitosan. CD_{Chi} was also prepared with the additives of 1 M HBr or CH_3CO_2H instead of 1 M HCl using the same procedure.

3.3.3.2. Synthesis of heterodimeric Ag-CD hybrid nanomaterials

Solutions of 3.0 mg/ml of CD_{Chi} and 1.0 mg/ml of $AgNO_3$ were exposed to UV light with a wavelength of 365 nm for 3 min using a UV lamp (B-100AP high-intensity UV lamp, 100 W). Ag-CD_{Alg} was obtained by an identical protocol using CD_{Alg}. After the solution was irradiated with UV light for 3 min, its color changed from light-yellow to orange (Ag-CD_{Chi}) or red (Ag-CD_{Alg}).

3.3.3.3. Time-correlated single-photon counting (TCSPC) characterization

The exciton lifetime was determined by TCSPC technique. A computer-controlled diode laser with a 375-nm wavelength, a 54-ps pulse width, and a 40-MHz repetition rate was used as an excitation source. The PL emission was spectrally resolved using collection optics and a monochromator (PicoQuant). The TCSPC module (PicoHarp 300E, PicoQuant) with a MCP-PMT (R3809U-5x series, Hamamatsu) was used for ultrafast detection. The total instrument response function (IRF) for PL decay was less than 30 ps, and the temporal time resolution was less than 10 ps. The deconvolution of actual fluorescence decay and IRF was performed using fitting software (FlouFit, PicoQuant) to deduce the time constant associated with each exponential decay.

3.3.3.4. Characterizations

The functional groups of the CDs and the Ag-CD NPs were analyzed by XPS (K-alpha, Thermo Fisher) and FT-IR **(**Varian, Cray 660)**.** UV/vis absorption spectra and photoluminescence (PL) emission were measured on a Varian Cary 5000 spectrophotometer. The zeta potential of colloidal suspensions was measured using a zeta-potential analyzer (Malvern, Zetasizer Nano-ZS). The morphology and size of Ag-CD NPs were measured using transmission electron microscopy (TEM, JEOL JEM-2100, accelerating voltage of 200 kV). The higher-resolution imaging, EFTEM elemental analysis and high energy resolution EEL spectroscopy with monochromator and Quantum GIF 965 of Ag-CD NPs were performed in aberration-corrected TEM (FEI Titan3^{TM} G2 60-300 at 80 kV). A low kV operation of TEM and STEM (scanning TEM) significantly reduced the electron beam damage onto the specimens. X-ray diffraction (XRD) measurements were performed on a high-resolution X-ray diffractometer (Bruker Co.).

3.3.3.5. Finite-difference time-domain (FDTD) calculations

The E-field enhancement and extinction cross-section for Ag-CD NPs were calculated by FDTD method (FDTD Solutions 8.6, Lumerical). The numerical simulations were performed

in three-dimensional box which has a cell size of 0.1 nm with perfectly matched layers for all boundaries. For the Ag-CD NP model, their diameter and interparticle spacing were adjusted according to the TEM observation. The dielectric functions of Ag and CD in the UV/vis region were described by multi-coefficient fitted model of the experimental data by Palik. The Ag-CDs were illuminated by a total-field scattered-field plane wave source to obtain the extinction cross section as a function of wavelength by calculating the absorption and scattering cross sections

3.3.4. Results and discussion

3.3.4.1. Synthesis of Ag-CD_{Chi} and Ag-CD_{Alg}

Among many synthetic methods available, we employed microwave pyrolysis of chitosan or alginate in the presence of a surface passivating agent (ethylenediamine, $NH_2CH_2CH_2NH_2$) and a solubilizing additive (HCl) to prepare the respective CDs. Each carbon source belongs to a common polysaccharide extracted from biomass, such as crab or brown algae. The prepared CDs are thus denoted as CD_{Chi} and CD_{Alg} depending on the respective carbon precursor. Both CDs exhibit broad absorbance and characteristic PL with emission maxima that are highly dependent on the excitation wavelength similar to other reported CDs.[34,35] The CD_{Chi} generally shows relatively low PL, with a quantum yield (QY) of ~5%, compared to that of CD_{Alg} (QY ~ 10%) using quinine sulfate as a reference. The CDs were subsequently photoexcited by irradiation with UV light in the presence of $AgNO_3$, which led to the formation of Ag NPs on the surface of the CDs upon reduction of Ag^+ ions.[36] The successful formation of Ag NPs was monitored by changes in solution color as well as by the diminished PL under UV light (Figure 3.3.1c and 3.3.2). Most surprisingly, we found that only a single Ag NP was grown on each CD, as evidenced by the representative TEM image, which resulted exclusively in heterodimeric structures without the formation of other hybrid structures of different morphology (Figure 3.3.1). Notably, no Ag NP formation was observed in the absence of the CDs under identical reaction conditions in repeated control experiments.

3.3.4.2. Growth mechanism of Ag nanoparticles on CD_{Chi} and CD_{Alg}

The mechanism of controlled nucleation and directional growth of Ag NP can be attributed to the electron transfer between the photoexcited CDs and the Ag^+ ions, as similarly suggested in other dumbbell-shaped heterodimers such as Pt–Fe_3O_4 and Au–Fe_3O_4.[37,38] Specifically, Ag^+ ions (and also Cl^- ions) are attracted to the surface of CDs via electrostatic interactions with carboxylic acid, amine, and/or other functional groups. After the free electrons from the photoexcited CDs reach the Ag^+ ions at the surface, the interfacial junction allows more

electrons to pass through to the conductive Ag nucleation site and to recruit more Ag^+ ions, eventually leading to heterodimeric Ag-CD NPs (Figure 3.3.3). Although the literature contains a few previous reports describing the formation of CDs coated with metals such as Ag, Au, and Pt, all of them exhibit core–shell morphology with a CD core and a thin metallic shell.[39,40]

3.3.4.3. Structure of of Ag-CD_{Chi} and Ag- CD_{Alg}

To further support the formation mechanism, we performed FT-IR and high-resolution X-ray photoelectron spectroscopy (XPS). FT-IR spectroscopy revealed chemical information related to the functional groups that change during the course of the reaction (Figure 3.3.4). In particular, the fraction of carboxylic acid groups and other oxygen-bearing functional groups were diminished upon the formation of the Ag NPs on the surface of the CDs, irrespective of the type of CD. In accordance with the FT-IR data, XPS results provided further evidence of Ag NP formation and the associated changes in the surface functional groups on the CDs (Figure 3.3.5, 3.3.6, and 3.3.7). The survey scan identified the Ag NPs from the Ag 3d peaks at 368.19 and 374.38 eV and the characteristic features of sp^2- and sp^3-carbons that were functionalized with carbonyl and amine moieties on the particle surfaces. Furthermore, the deconvoluted high-resolution C 1s spectra revealed that both sp^2-carbon and hydroxyl groups of the CDs diminished considerably upon the synthesis of the Ag NPs, whereas the carbonyl groups increased concomitantly, suggesting their important role in reducing Ag^+ ions to metallic Ag NPs. Considering these evidences together, we propose that the hydroquinone-like (a combination of sp^2-carbons and hydroxyl groups) surface functional groups of CDs are oxidized to benzoquinone-like structures upon UV irradiation to promote the reduction of Ag^+ ions on the surface of photoexcited CDs (Figure 3.3.8). It is worthy to note that the high-resolution Cl 2p spectra indicated the presence of C–Cl at 197.9 ($2p_{3/2}$) and 199.6 eV ($2p_{1/2}$), respectively, which suggests the Cl atom is incorporated within the carbon framework during the formation of the CD.[41] The presence of C–Cl was further confirmed by FT-IR and elemental mapping data (Figure 3.3.4).

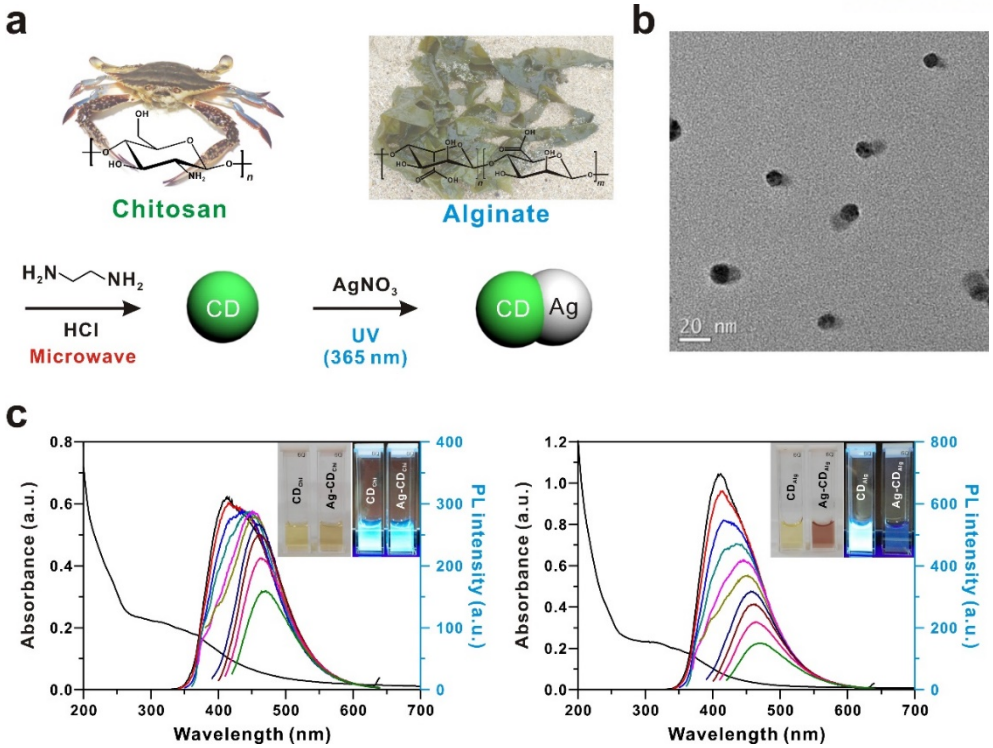

Figure 3.3.1. Schematic illustration of the synthesis of heterodimeric Ag-CD NPs derived from polysaccharides. (a) Schematic representation of the synthesis of CD NPs from chitosan and alginate precursors followed by growth of Ag NPs on the CDs. (b) Representative TEM image of the Ag-CD_{Chi} NPs. (c) UV/vis absorption and PL spectra of the CDs in solutions prepared from (left) chitosan (CD_{Chi}) and (right) alginate (CD_{Alg}) with varying excitation wavelengths from 320 to 410 nm with an interval of 10 nm. The inset shows the photographs of the respective CD and Ag-CD NPs solutions under ambient light and UV irradiation at 365 nm (conc. 0.10 mg/mL). The samples were prepared with 600 μL of HCl added during the synthesis of the CDs.

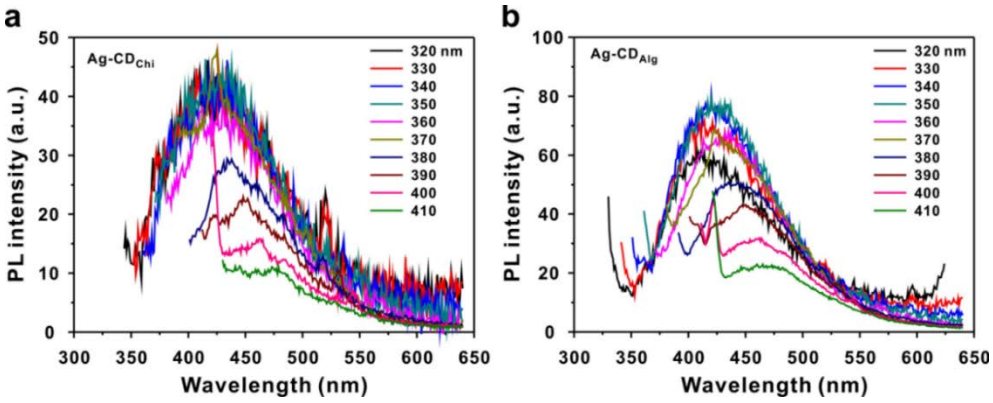

Figure 3.3.2. Photoluminescence spectra of (a) Ag-CD_{Chi} and (b) Ag-CD_{Alg} with varying excitation wavelengths from 320 to 410 nm with an interval of 10 nm.

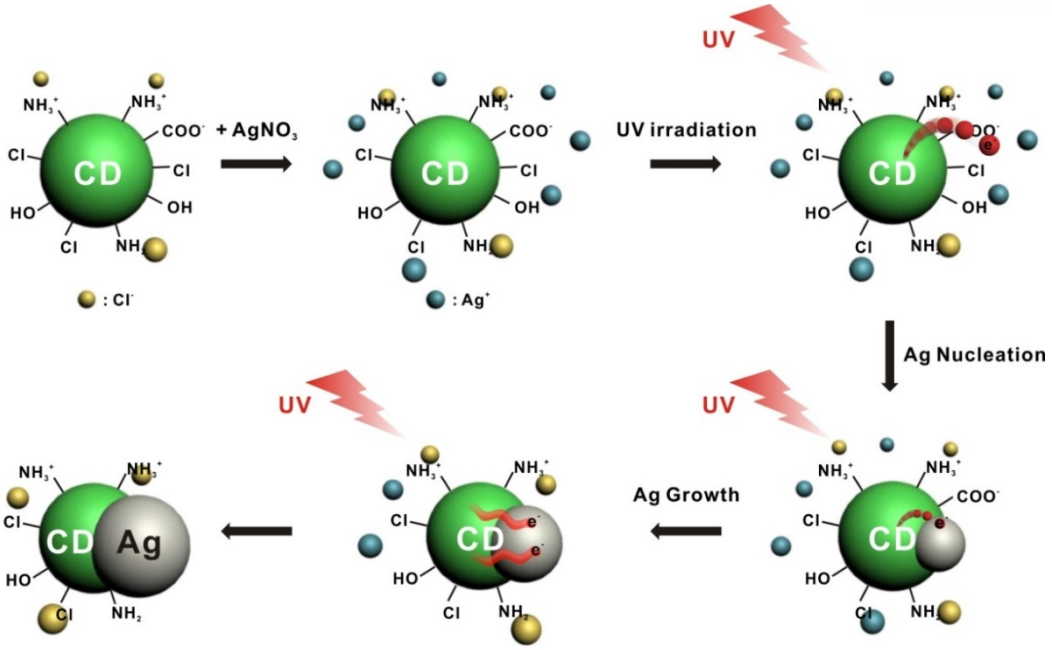

Figure 3.3.3. Proposed formation mechanism of heterodimeric Ag-CD NPs.

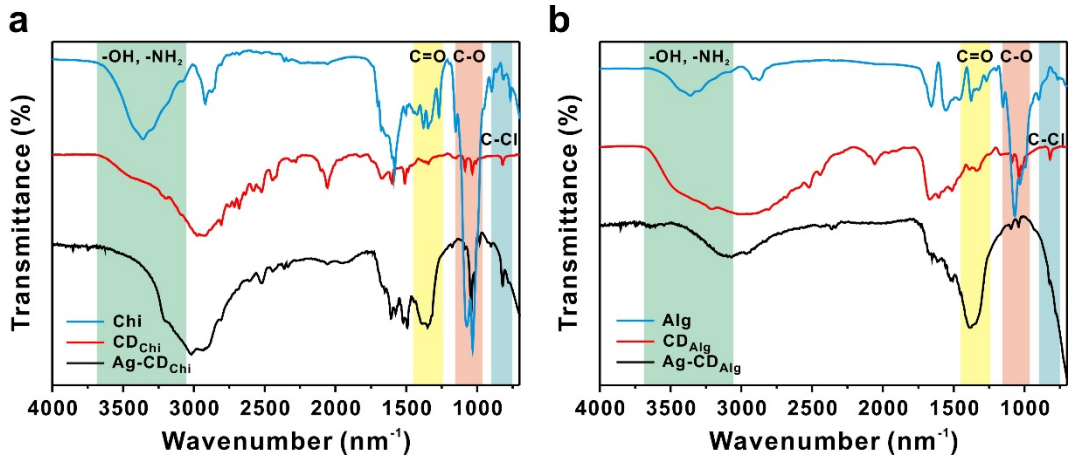

Figure 3.3.4. FT-IR spectra of CDs and Ag-CD NPs (a) Pristine chitosan, CD_{Chi}, and $Ag\text{-}CD_{Chi}$, and (b) pristine alginate, CD_{Alg}, and $Ag\text{-}CD_{Alg}$.

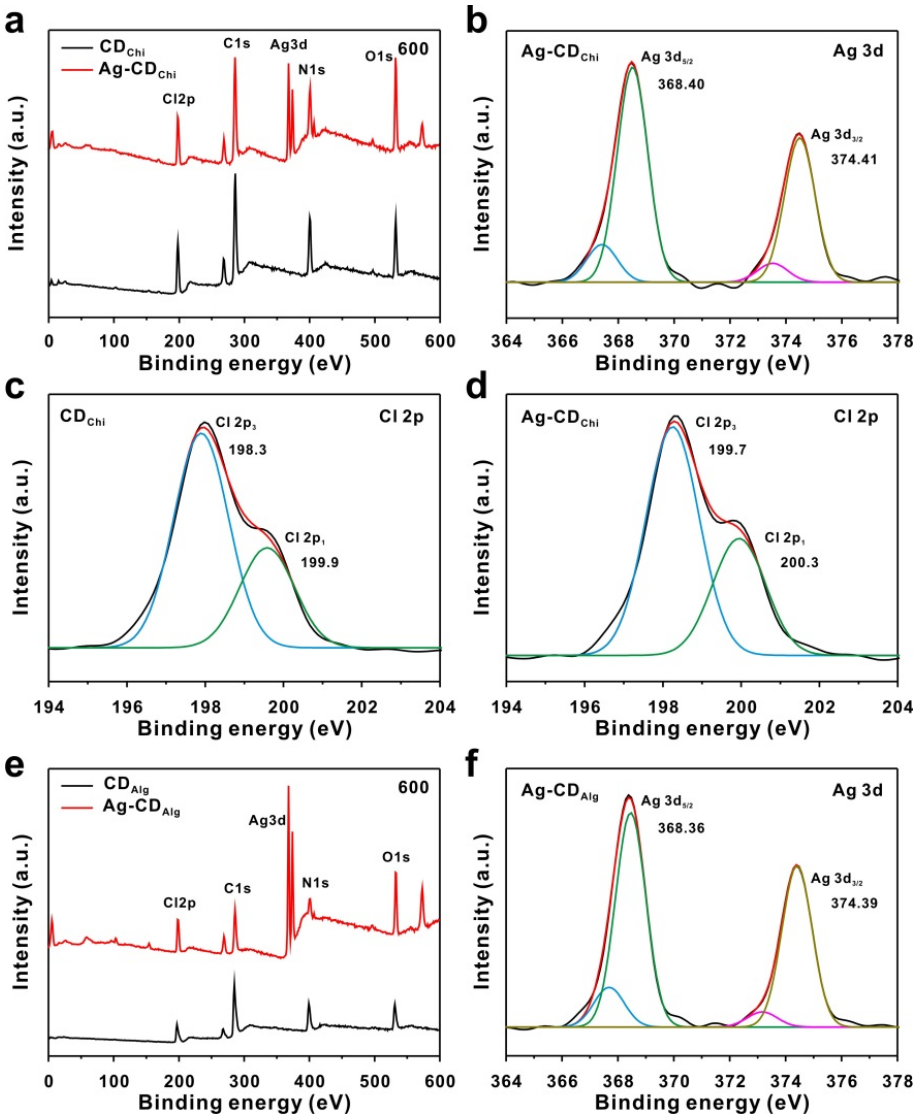

Figure 3.3.5. XPS analysis of CDs and Ag-CD NPs. (a) Survey spectra of CD_{Chi} and Ag-CD_{Chi}, (b-d) deconvoluted high-resolution spectra of (b) the Ag 3d region of Ag-CD_{Chi}, (c) the Cl 2p region of CD_{Chi}, and (d) the Cl 2p region of Ag-CD_{Chi}. (e) Survey spectra of CD_{Alg} and Ag-CD_{Alg} and (f) the deconvoluted high-resolution Ag 3d region of Ag-CD_{Alg}. Each sample was prepared with 600 μl of 1 M HCl.

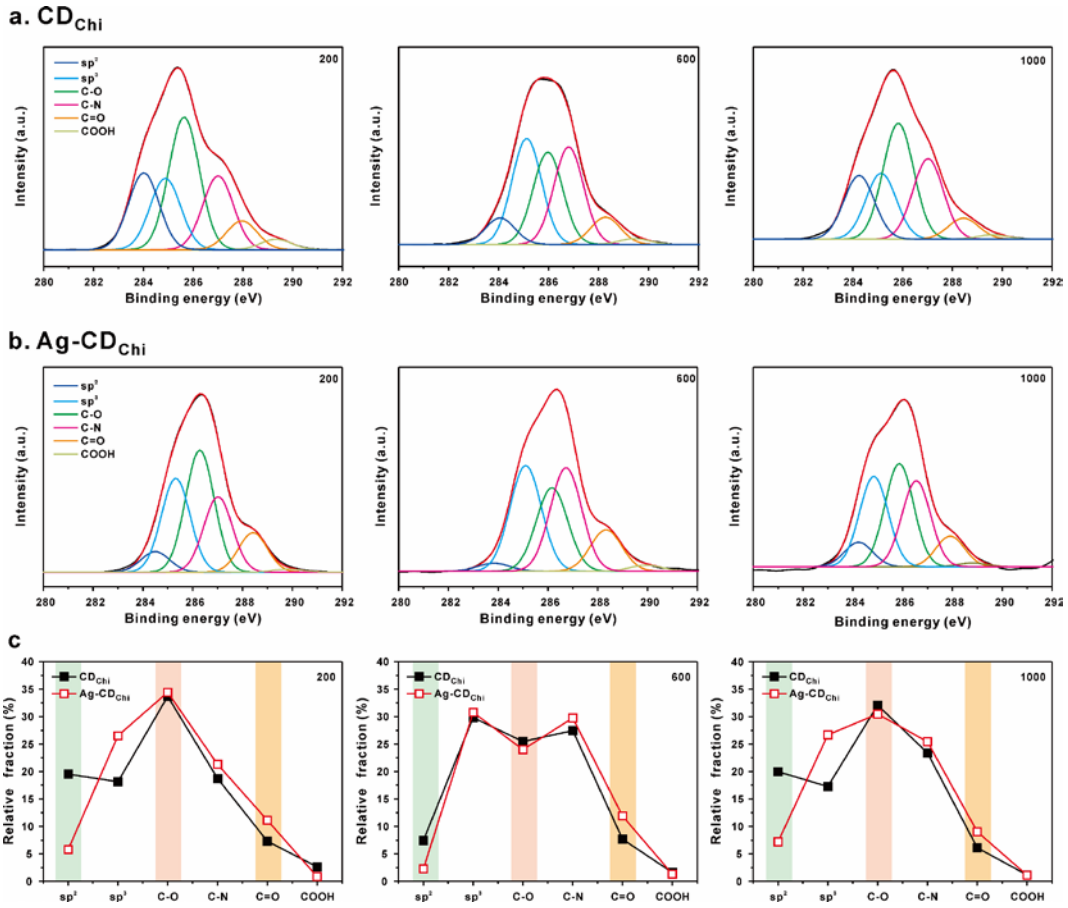

Figure 3.3.6. Deconvoluted high-resolution XPS spectra of the C 1s peak of (a) CD_{Chi} and (b) Ag-CD_{Chi}, and (c) the chemical compositions of CD_{Chi} and Ag-CD_{Chi}. The numbers in the top right-hand corner of the graphs indicate the volume (μl) of 1.0 M HCl additive used in the formation of CD_{Chi}.

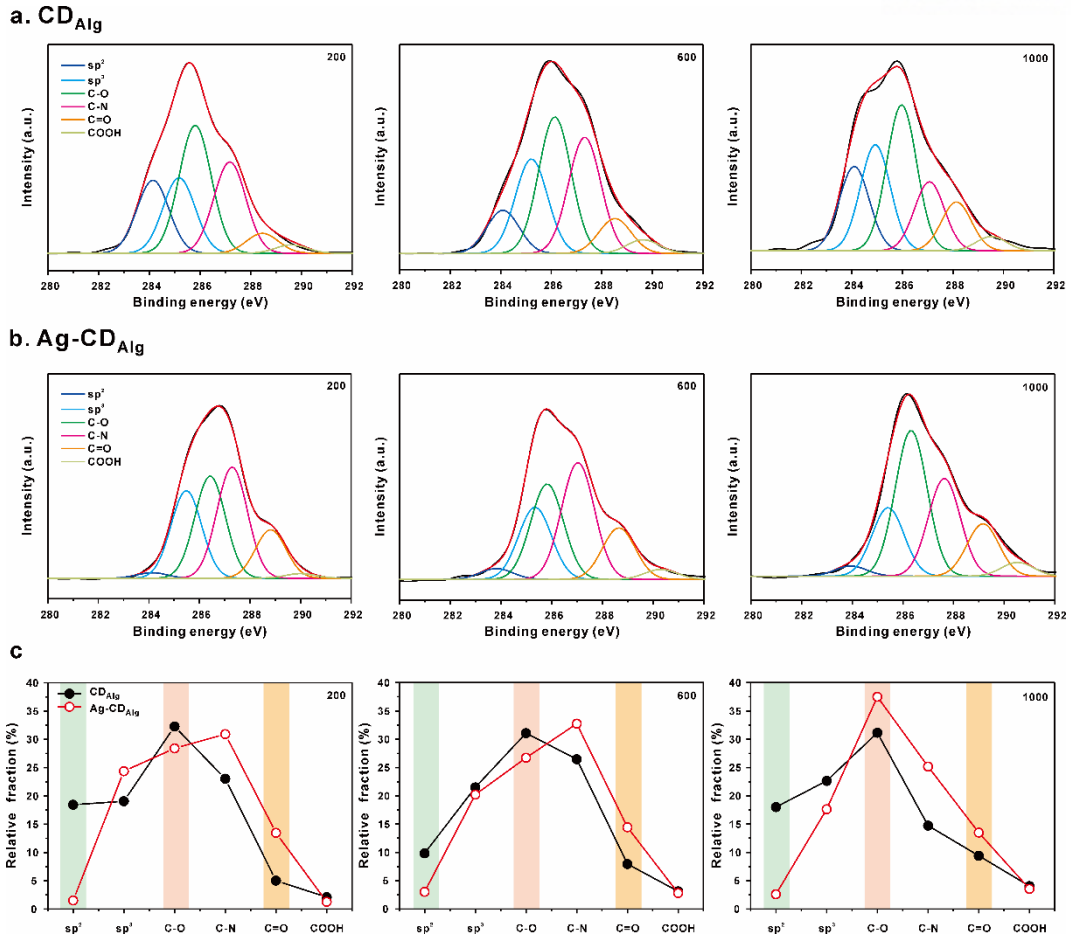

Figure 3.3.7. Deconvoluted high-resolution XPS spectra of the C 1s peak of (a) CD_{Alg} and (b) Ag-CD_{Alg} and (c) the chemical compositions of CD_{Alg} and Ag-CD_{Alg}. The number in the graph represents the volume (μl) of 1.0 M HCl additive used in the formation of CD_{Alg}.

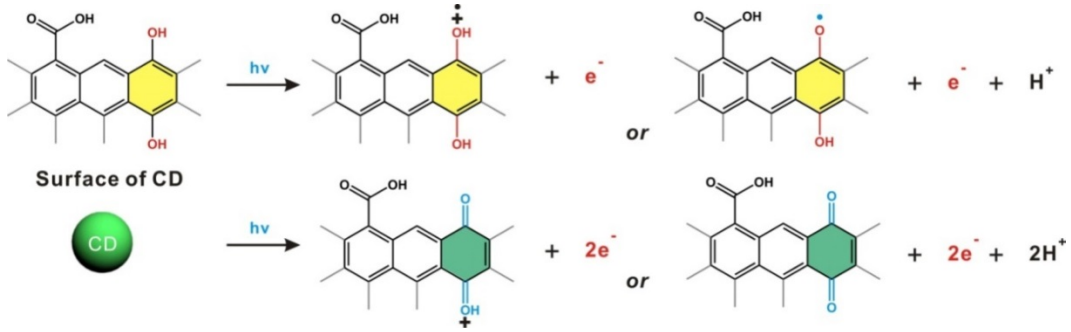

Figure 3.3.8. Proposed chemical mechanism of Ag reduction on the surface of a CD upon photoexcitation according to the combined results of FT-IR and high-resolution XPS. The photoexcited electrons from the CD reduce the Ag^+ ions to Ag NPs on the surface of the CD to afford heterodimeric Ag-CD NPs.

3.3.4.4. Morphologies of of Ag-CD_{Chi} and Ag- CD_{Alg}

The unique structure and interface of heterodimers established between metallic Ag NPs and non-metallic soft carbon-based CDs were further characterized by high-resolution aberration-corrected TEM operated at a low kV (Figure 3.3.9). To enhance the contrast of high resolution imaging of carbon-based CDs, we used a graphene support transferred onto Quantifoil holey carbon grid (Quantifoil Micromachined, R2/1, SPI supplies). As shown in Figure 3.3.9a, the heterodimeric structure of Ag-CD_{Chi} NPs is clearly demonstrated to have crystal lattice fringes of metallic Ag. However, a weak crystalline plane with a spacing of 0.277 nm was observed in the digital diffractogram of CD, indicating the presence of insoluble AgCl salt on the surface of the CDs, as evidenced by the weak (200) peak. The presence of AgCl corroborates the proposed mechanism by confirming the presence of Cl^- ions on the surface of the CDs through the electrostatic interaction with amine groups on the surface functional groups of the CDs and the associated Ag^+ ions. A control experiment of using acetic acid as an additive instead of HCl also produced the heterodimeric Ag-CD_{Chi} NPs, suggesting the role of H^+ in forming the nanostructures (Figure 3.3.10 and 3.3.11). Furthermore, the crystalline phase of the Ag-CD NPs was verified by the XRD spectrum (Figure 3.3.12). The associated elemental information of heterodimers was elucidated by energy-filtered TEM (EFTEM) and monochromated electron energy loss spectroscopy (mono EELS) (Figure 3.3.9b and 3.3.9c). The EFTEM image shows the distribution of each element—Ag, C, and Cl—on the heterodimer. As shown in Figure 3.3.9b, the Ag is localized on the Ag NP, whereas the C and Cl are mostly distributed on the CD. The monochromated STEM-EEL spectra of points along the line on heterodimeric Ag-CD_{Chi} NPs also reveal elemental concentration information related to the respective NPs on the basis of the C K-edge (285 eV), the Cl L2,3-edge (200 eV), and the Ag M4,5-edge (367 eV). Taken together, the high-resolution TEM, along with a number of other analytical analyses, support the successful formation of heterodimeric Ag-CD NPs.

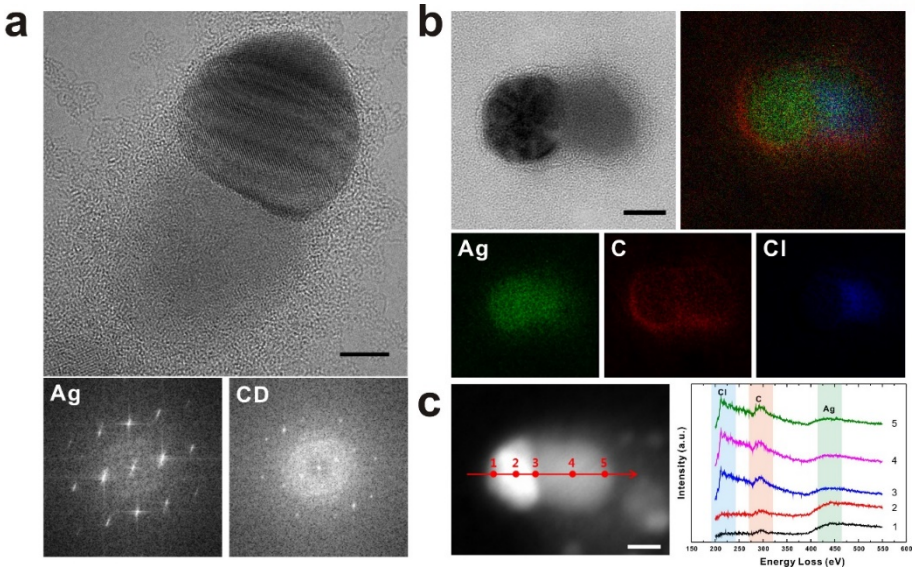

Figure 3.3.9. Representative high-resolution TEM images of Ag-CD_{Chi} NPs. (a) Aberration-corrected TEM image of Ag-CD_{Chi} NPs (scale bar: 5 nm) and the corresponding digital diffractograms of the Ag NPs and the CD, respectively. (b) Energy-filtered TEM (EFTEM) image of Ag-CD_{Chi} NPs (scale bar: 10 nm) with composed elemental images of Ag, C, and Cl. (c) STEM-HAADF image of Ag-CD_{Chi} NPs (scale bar: 10 nm) and the corresponding monochromated STEM-EEL spectra of points along the line on a heterodimeric Ag-CD_{Chi} NP.

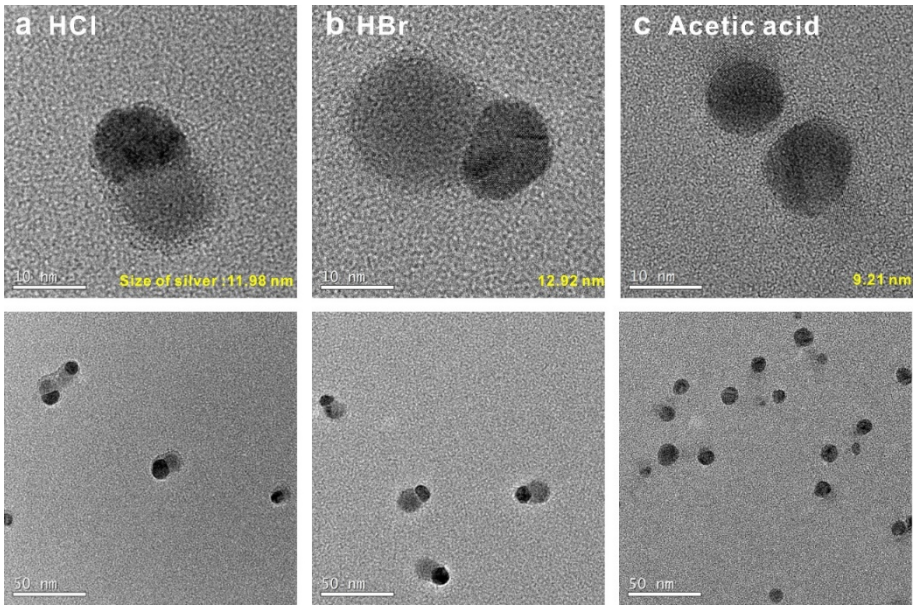

Figure 3.3.10. TEM images of Ag-CD_{Chi} NPs where the CD_{Chi} particles were prepared with different additives: (a) HCl, (b) HBr, and (c) acetic acid. The role of Cl^- ions in the formation of Ag NPs was further characterized when the reaction was conducted in different acids, such as HBr and acetic acid (AcOH).

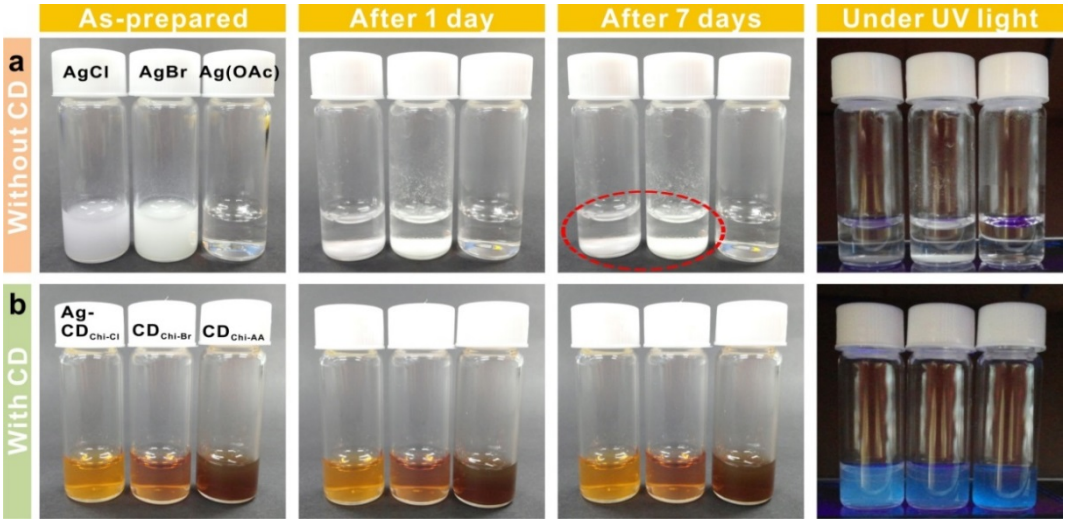

Figure 3.3.11. Optical images of samples prepared (top panel) without CD and (lower panel) with CD. AgCl, AgBr, and silver acetate were synthesized under the same conditions used for Ag-CD_{Chi-Cl}, Ag-CD_{Chi-Br}, and Ag-CD_{AA} in the absence of CD.

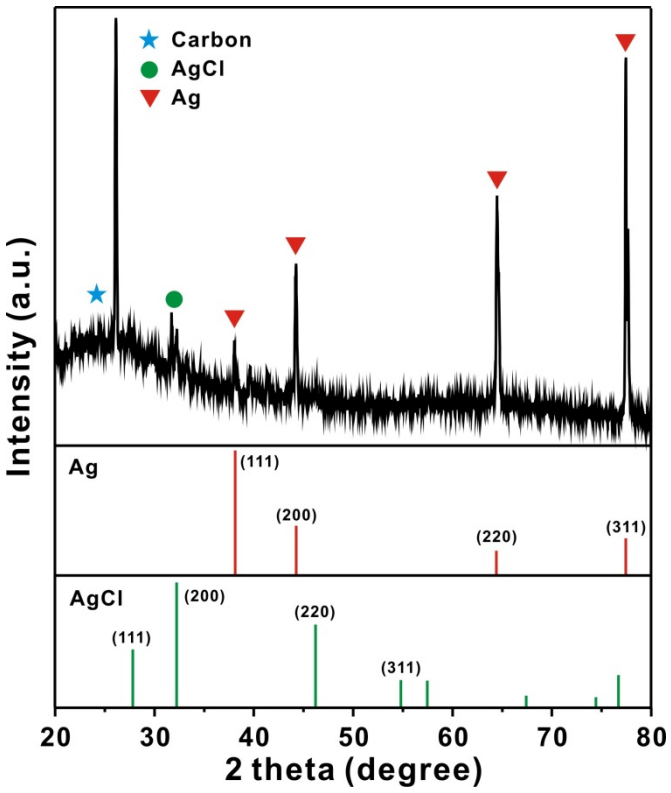

Figure 3.3.12. Representative XRD pattern of Ag-CD_{chi} NPs.

3.3.4.5. Controlling size and interface of of Ag-CD_{Chi} and Ag- CD_{Alg}

We found that the concentration of HCl added during the formation of the CDs is a critical parameter in controlling the size and the interface of Ag-CDs. The addition of HCl not only assists in enhancing the solubility of chitosan and alginate in aqueous solution for the synthesis of CDs, but the Cl^- ions in the resulting solution also affect the growth kinetics of Ag NPs during heterodimer formation. A series of TEM images shown in Figure 3.3.13a and 3.3.13b indicate that an increase in the concentration of HCl increases the size of the CDs. For example, the size of CD_{Chi} increased from 7.90 ± 0.73 to 13.1 ± 0.56 nm when the amount of 1 M HCl was changed from 200 to 1000 μL; similarly, the size of CD_{Alg} increased from 7.14 ± 0.87 to 13.1 ± 1.29 nm under identical conditions (Figure 3.3.13c). In addition, the size of the Ag NPs increased with increased concentration of HCl in both CDs. Interestingly, we found that the aspect ratio of CD_{Alg} in Ag-CD_{Alg} gradually increased with increasing HCl concentration, whereas that of CD_{Chi} in Ag-CD_{Chi} NPs remained almost constant (Figure 3.3.13d).

Most notably, the concentration of HCl can enable the fine-tuning of the interface between two components of the heterodimers (Figure 3.3.13e). Through the collection of a series of TEM images, we could clearly monitor the gradual changes of the overlapped area between the Ag and CD NPs (Figure 3.3.14). For instance, the eclipsing of the Ag and CD_{Chi} NPs at the interface was significantly reduced with increasing concentration of the HCl additive. In stark contrast, the trend was reversed in the case of Ag-CD_{Alg} NPs, such that the eclipsing between Ag and CD_{Alg} NPs increased with increasing concentration of HCl. We propose that the protonation of the chitosan precursor bearing amine groups affords greater solubilization of the chitosan precursor upon addition of HCl to the mixture. However, the opposite behavior was observed when the carboxylic acid groups on the alginate were treated with HCl. This opposite solubility trend of the two polysaccharides might lead to differences in the synthesis of CDs during the microwave carbonization. The fine structural tuning of the Ag NP and CD interface enables surface modification of the CDs and also changes the related optical properties of the Ag and CD NPs, such as the PL of CDs and the SPR of Ag NPs.

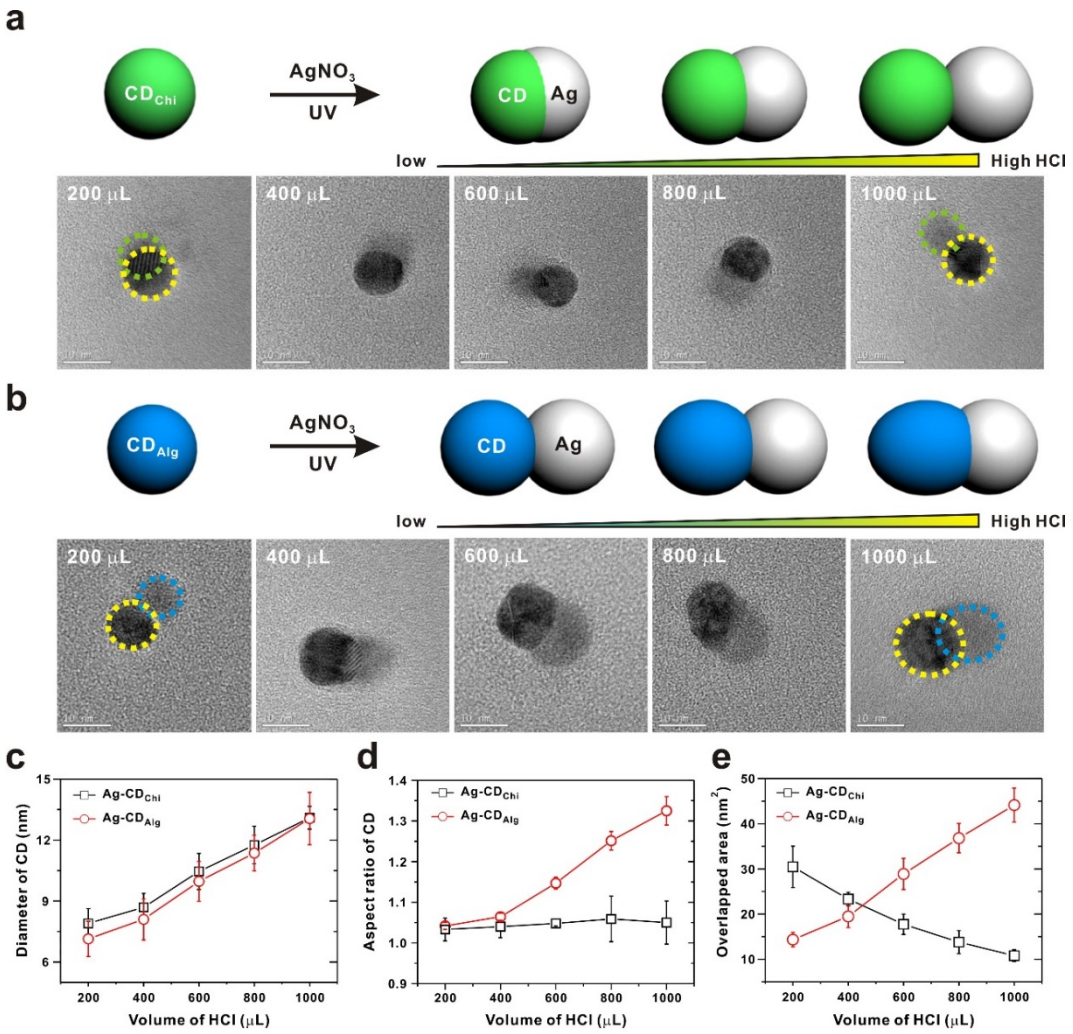

Figure 3.3.13. The effect of the HCl additive on tuning the nanoscale interface of the Ag-CD NPs. (a, b) Representative TEM images of (a) Ag-CD_{Chi} NPs and (b) Ag-CD_{Alg} NPs prepared with various amounts of 1 M HCl additive, as indicated in the image. Dotted lines were added to aid the identification of each NP. (c-e) Analysis of characteristics of the Ag-CD NPs. (c) The diameter of CDs in Ag-CD NPs, (d) the aspect ratio of CDs in Ag-CD NPs, and (e) the overlapped interfacial area of Ag and CD in Ag-CD_{Chi} and Ag-CD_{Alg} NPs. All analyses are reported as an average value of more than 50 individual measurements of TEM images and error bars indicate the standard deviations.

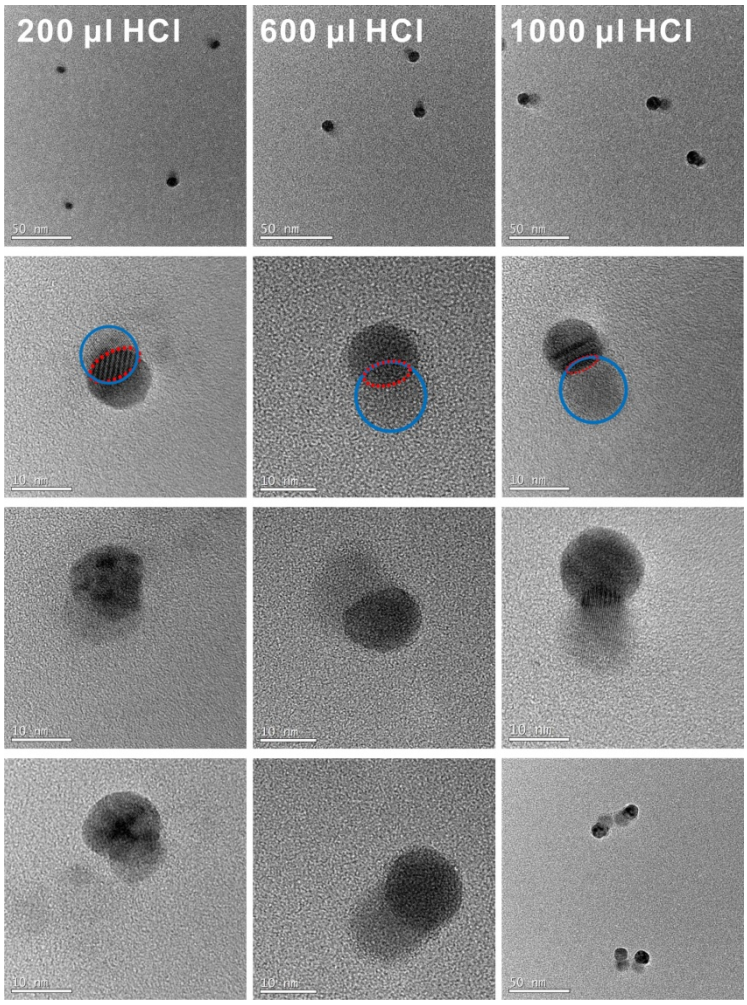

Figure 3.3.14. TEM images of Ag-CD_{Chi} prepared with various amounts of 1 M HCl additive, as indicated in the image. The overlapped area was calculated by assuming an oval shape interfacial area between Ag and CD NPs within the heterodimers (see below schematic representation of the interface). According to the calculation, the overlapped interface area (%) was reduced from 55.66 to 9.13% with increase of HCl from 200 to 1000 µl.

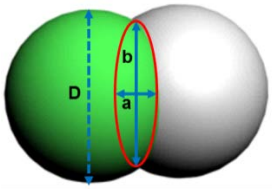

Overlapped area (nm^2) = $\pi \times \frac{a}{2} \times \frac{b}{2}$

(a = length of minor axis, b = length of major axis)

Overlappled area (%) = Overlapped area / CD area

3.3.4.6. Controlling photoluminescence of Ag-CD_{Chi} and Ag- CD_{Alg}

We performed various characterizations of all the Ag-CDs prepared using various amounts of HCl, including steady-state photoluminescence spectroscopy, time-correlated single photon counting (TCSPC), and QY measurements, to elucidate the effect of structural tuning of the Ag and CD NPs on their photophysical properties (Figure 3.3.15). The PL decay profiles of Ag-CD_{Chi} and Ag-CD_{Alg} NPs show a shorter decay lifetime compared to their counterpart CDs without Ag NPs, which can be deduced to fit bi-exponential decay parameters (Figure 3.3.17a anc 3.3.15b. From the fitting of the decay curves of representative 600 μL HCl samples, the average PL decay time of τ_{avg} (the exciton lifetime) was calculated to be 4.14 ns for Ag-CD_{Chi} and 2.58 ns for Ag-CD_{Alg}, which are shorter than those of the respective CDs free of Ag NPs: 4.39 ns for CD_{Chi} and 4.62 ns for CD_{Alg} (Table 3.3.1). In general, the PL of CDs is attributed to radiative combinations of electrons and holes confined at the defective surfaces of CDs.[28, 42] The exciton created on the surface of the CDs can be effectively quenched by the presence of neighboring metallic Ag NPs. Consequently, the lifetime of the exciton is decreased accordingly and is also highly dependent on the interparticle spacing between the CD and Ag NPs. As indicated by the opposite trend of interfacial overlapping between Ag-CD_{Chi} and Ag-CD_{Alg} NPs, the τ_{avg} of the Ag-CD_{Chi} NPs generally increases with decreasing overlap between the Ag and CD_{Chi}, whereas that tendency is reversed in the case of Ag-CD_{Alg}. Figures 3.3.15c and 3.3.15d shows the QYs of the CD and Ag-CD NP suspensions, which are in excellent agreement with the PL lifetime decay values. Sun and coworkers have reported that the deposition of metallic Au NPs around CDs effectively quenches or almost diminishes the PL in the CDs to a concentration far below the threshold of observation for plasmon absorption.[40] However, these heterodimeric Ag-CD NPs are unique in that the presence of the Ag NPs does not completely quench the PL of native CDs because of the controlled interface of the heterodimeric nanostructure. Independent of the PL measurements, we measured the zeta-potential of the NPs and found that the CDs and Ag-CD NPs all exhibited good colloidal stability that lasted for several months without any noticeable aggregation (Figures 3.3.15e and 3.3.15f). Due to amine groups of chitosan and carboxylic groups of alginate precursors, zeta-potential of CD_{Chi} has relatively higher values (more positively charged) than CD_{Alg}. Because the formation of heterodimeric Ag NPs on the surface of CDs requires the consumption of surface carboxylic acid and hydroxyl groups, the more overlapped area between Ag and CDs can lead to considerable changes in the zeta-potential of Ag-CD NPs. For example, we found that more oxygenated CD_{Alg} (34.2%, according to XPS data) compared to CD_{Chi} (25.3%) provided more active sites, thus leading to the rapid formation of Ag NPs in CD_{Alg}, which significantly increased the zeta-potential of Ag-CD_{Alg} NPs. These results clearly confirm that the nanoscale interface between Ag and CDs can be controlled precisely through the choice of the CD precursor and the additive.

3.3.4.7. SPR effect of Ag-CD_{Chi} and Ag- CD_{Alg}

Because SPR of metallic NPs is well known to be highly sensitive to the dielectric environment, the formation of Ag NPs on dielectric CDs with tunable interparticle spacing can significantly influence the local field generated by the Ag NPs. Thus, we simulated the electric field distribution using the three-dimensional finite-difference time-domain (FDTD) method to explore the electric field enhancement created at the junction of the heterodimeric Ag-CD NPs (Figure 3.3.16).[43] Figure 3.3.16a presents the simulated electric field intensity distribution and predicts the extinction spectra of representative Ag-CD_{Chi} NPs with varying degrees of interparticle spacing (200, 600, and 1000 μL of 1 M HCl). The overlapped area between Ag and CD_{Chi} decreases with increasing concentration of HCl in the case of Ag-CD_{Chi}; hence, we performed the simulation according to the data set collected from TEM images. We observed that less eclipsing of the Ag with the CD surface makes the electronic coupling of the Ag and CD NPs stronger, which leads to a significant electric field enhancement at the junction between the Ag and CD NPs (Figure 3.3.16b). In addition, the simulated extinction spectra are red-shifted with less overlap between the Ag and CD NPs, which is consistent with the UV/vis spectroscopy observations (Figure 3.3.16c). This simulation demonstrates that fine-tuning the interface between a dielectric material, a CD, and a metallic Ag NP can provide a unique means to control the SPR of Ag NPs.

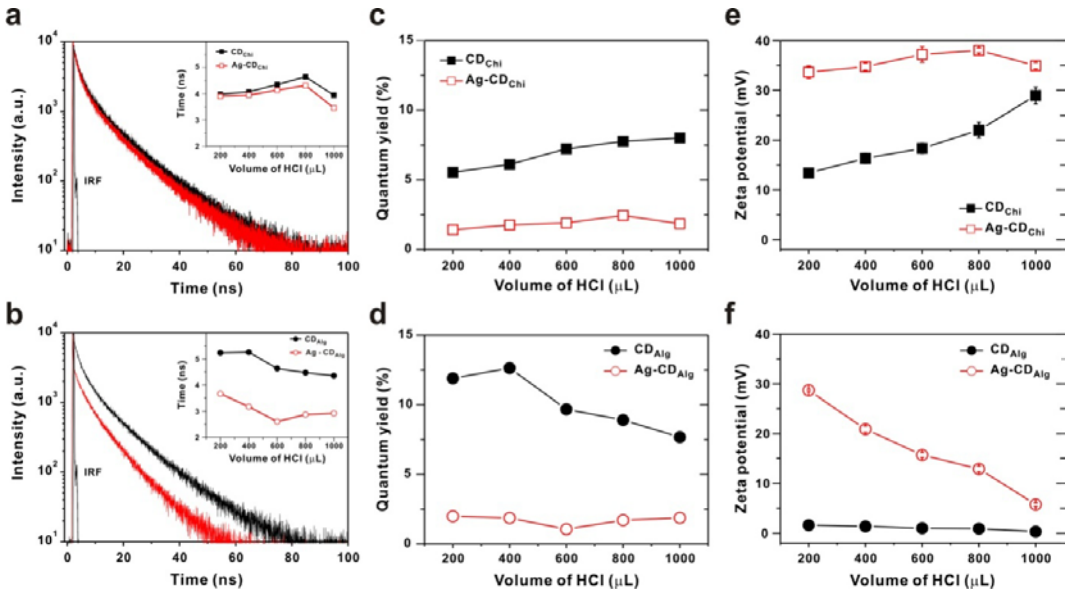

Figure 3.3.15. Photophysical properties and stability of Ag-CD NPs. (a, b) Photoluminescence decay profiles of (a) Ag-CD_{Chi} NPs and (b) Ag-CD_{Alg} NPs prepared with 600 μL of HCl. The inset shows the plot of the average decay time (τ_{avg}) of CDs (black) and Ag-CDs (red) as a function of the volume of HCl. (c, d) Quantum yields of CD and Ag-CD NP solutions, respectively, measured with quinine sulfate as a reference material. (e, f) Zeta-potentials of CD and Ag-CD NP suspensions, respectively.

Table 3.3.1. PL-decay time measured for all CDs and Ag-CDs. The decays were fitted with the deconvolution equation $I(t) = A_1e^{-t/\tau1} + A_2e^{-t/\tau2}$, where I(t), A, t, and τ_{avg} are the time-dependent PL intensity, the amplitude (noted as the normalized percent in the parentheses: $\tau_1 = (A_1\tau_1/(A_1\tau_1+A_2\tau_2))\times100$), the fitted PL decay time, and the averaged PL decay time ($\tau_{avg} = (A_1\tau_1+A_2\tau_2)/(A_1+A_2)$, respectively. The chi-squared (χ^2) values of the fittings were maintained below 2.

a

CD_{Chi}	200	400	600	800	1000
τ_1(ns)	10.43 (0.25)	10.59 (0.26)	11.23 (0.27)	11.34 (0.28)	11.28 (0.23)
τ_2(ns)	1.82 (0.75)	1.81 (0.74)	1.86 (0.73)	2.07 (0.72)	1.77 (0.77)
χ^2	2.14	2.02	1.89	1.09	1.70
τ_{avg} (ns)	3.97	4.09	4.39	4.67	3.96

b

$Ag\text{-}CD_{Chi}$	200	400	600	800	1000
τ_1(ns)	10.50 (0.25)	10.50 (0.26)	10.71 (0.26)	11.08 (0.25)	10.04 (0.21)
τ_2(ns)	1.70 (0.75)	1.83 (0.74)	1.83 (0.74)	2.00 (0.75)	1.73 (0.79)
χ^2	2.12	2.01	1.80	1.89	1.77
τ_{avg} (ns)	3.90	4.08	4.14	4.27	3.48

c

CD_{Alg}	200	400	600	800	1000
τ_1(ns)	10.64 (0.35)	10.90 (0.34)	11.39 (0.28)	11.06 (0.27)	11.24 (0.23)
τ_2(ns)	2.35 (0.65)	2.17 (0.66)	1.99 (0.72)	2.00 (0.73)	2.33 (0.77)
χ^2	1.59	1.96	1.63	1.45	2.09
τ_{avg} (ns)	5.25	5.14	4.62	4.45	4.38

d

$Ag\text{-}CD_{Alg}$	200	400	600	800	1000
τ_1(ns)	10.13 (0.29)	9.42 (0.25)	9.37 (0.14)	9.27 (0.22)	10.49 (0.15)
τ_2(ns)	1.04 (0.71)	1.07 (0.75)	1.48 (0.86)	1.05 (0.78)	1.62 (0.85)
χ^2	1.56	1.98	1.28	1.64	1.43
τ_{avg} (ns)	3.68	3.16	2.58	2.86	2.95

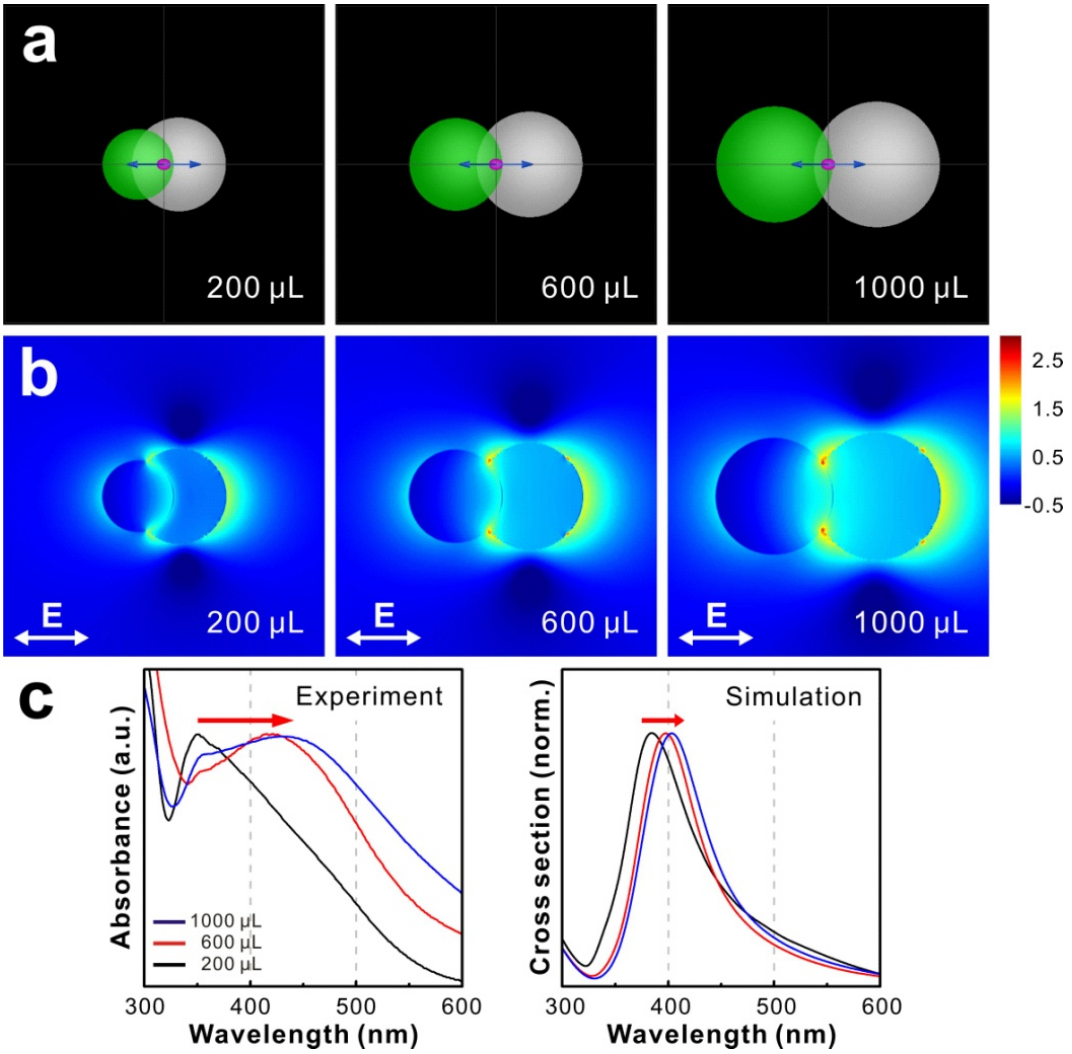

Figure 3.3.16. Simulation of the electric field distribution and extinction cross-section for Ag-CD_{Chi}. (a) 3D structures of Ag-CD_{Chi} NPs based on TEM images are modeled for FDTD simulation. The blue arrow and purple point indicate the direction of polarization and propagation of the source, respectively. (b) Simulated electric field intensity of Ag-CD_{Chi} NPs at 453 nm in log scale log($|E|^2$) collected with various amounts of HCl. The magnitude of the enhanced intensity is represented by the color scale. All calculations were performed for samples in water medium. (c) Comparison of the UV/vis spectra and the simulation data collected for Ag-CD_{Chi} NPs. The surface plasmon resonance (SPR) bands are red-shifted from 350 to 432 nm in experiments and from 385 to 404 nm in FDTD calculations with increasing amounts of HCl.

3.3.5. Conclusion

In summary, we synthesized heterodimeric Ag-CD NPs using the photoelectron transfer reaction of polysaccharide-derived CDs to Ag^+ ions. The interface between the Ag NPs and the CDs was precisely tunable through the choice of CD precursor and the amount of additive used during the formation of the CDs. The hybrid Ag-CD NPs were characterized with various techniques, including UV/vis, PL, FT-IR, XPS, HR-TEM, EELS, TCSPC, and zeta-potential measurements as well as FDTD simulations, which all indicated the formation Ag NPs at the junction of the CDs. Moreover, the precise tuning of the metal and carbon interface also enabled modification of the PL of the CDs as well as the related SPR of the Ag NPs. We anticipate that the electron transfer and surface plasmonic effect of these heterodimers will find their applications in the energy conversion systems or catalysts such as solar cells, electrocatalysts, and photocatalysts.

3.3.6. References

1. Costi, R.; Saunders, A. E.; Banin, U. Colloidal Hybrid Nanostructures: A New Type of Functional Materials. *Angew. Chem. Int. Ed.* **2010,** *49*, 4878-4897.
2. Cortie, M. B.; McDonagh, A. M. Synthesis and Optical Properties of Hybrid and Alloy Plasmonic Nanoparticles. *Chem. Rev.* **2011,** *111*, 3713-3735.
3. Sasaki, K.; Naohara, H.; Choi, Y. M.; Cai, Y.; Chen, W. F.; Liu, P.; Adzic, R. R. Highly Stable Pt Monolayer on PdAu Nanoparticle Electrocatalysts for the Oxygen Reduction Reaction. *Nat. Commun.* **2012,** *3*, 1115.
4. Wang, D. L.; Xin, H. L. L.; Hovden, R.; Wang, H. S.; Yu, Y. C.; Muller, D. A.; DiSalvo, F. J.; Abruna, H. D. Structurally Ordered Intermetallic Platinum-Cobalt Core-Shell Nanoparticles with Enhanced Activity and Stability as Oxygen Reduction Electrocatalysts. *Nat. Mater.* **2013,** *12*, 81-87.
5. Ibanez, F. J.; Zamborini, F. P. Reactivity of Hydrogen with Solid-State Films of Alkylamine-and Tetraoctylammonium Bromide-Stabilized Pd, PdAg, and PdAu Nanoparticles for Sensing and Catalysis Applications. *J. Am. Chem. Soc.* **2008,** *130*, 622-633.
6. Heo, M.; Cho, H.; Jung, J. W.; Jeong, J. R.; Park, S.; Kim, J. Y. High-Performance Organic Optoelectronic Fevices Enhanced by Surface Plasmon Resonance. *Adv. Mater*. **2011,** *23*, 5689-5693.
7. Gao, J. H.; Liang, G. L.; Cheung, J. S.; Pan, Y.; Kuang, Y.; Zhao, F.; Zhang, B.; Zhang, X. X.; Wu, E. X.; Xu, B. Multifunctional Yolk-Shell Nanoparticles: A Potential MRI Contrast and Anticancer Agent. *J. Am. Chem. Soc.* **2008,** *130*, 11828-11833.
8. Cho, N. H.; Cheong, T. C.; Min, J. H.; Wu, J. H.; Lee, S. J.; Kim, D.; Yang, J. S.; Kim, S.; Kim, Y. K.; Seong, S. Y. A Multifunctional Core-Shell Nanoparticle for Dendritic Cell-Based Cancer Immunotherapy. *Nat. Nanotechnol.* **2011,** *6*, 675-682.
9. Dabbousi, B. O.; RodriguezViejo, J.; Mikulec, F. V.; Heine, J. R.; Mattoussi, H.; Ober, R.; Jensen, K. F.; Bawendi, M. G. (CdSe)ZnS Core-Shell Quantum Dots: Synthesis and Characterization of a Size Series of Highly Luminescent Nanocrystallites. *J. Phys. Chem. B* **1997,** *101*, 9463-9475.
10. Shevchenko, E. V.; Bodnarchuk, M. I.; Kovalenko, M. V.; Talapin, D. V.; Smith, R. K.; Aloni, S.; Heiss, W.; Alivisatos, A. P. Gold/Iron Oxide Core/Hollow-Shell Nanoparticles. *Adv. Mater.* **2008,** *20*, 4323-4329.
11. Gu, H. W.; Zheng, R. K.; Zhang, X. X.; Xu, B. Facile One-Pot Synthesis of Bifunctional Heterodimers of Nanoparticles: A Conjugate of Quantum Dot and Magnetic Nanoparticles. *J. Am. Chem. Soc.* **2004,** *126*, 5664-5665.

12. Chen, J. Y.; Wiley, B.; McLellan, J.; Xiong, Y. J.; Li, Z. Y.; Xia, Y. N. Optical Properties of Pd-Ag and Pt-Ag Nanoboxes Synthesized via Galvanic Replacement Reactions. *Nano Lett.* **2005,** *5*, 2058-2062.
13. Saunders, A. E.; Popov, I.; Banin, U. Synthesis and Characterization of Organic-Soluble Ag/AgBr Dimer Nanocrystals. *Z. Anorg. Allg. Chem.* **2007,** *633*, 2414-2419.
14. Lee, H. J.; Habas, S. E.; Somorjai, G. A.; Yang, P. D. Localized Pd Overgrowth on Cubic Pt Nanocrystals for Enhanced Electrocatalytic Oxidation of Formic Acid. *J. Am. Chem. Soc*. **2008,** *130*, 5406-5407.
15. Gudiksen, M. S.; Lieber, C. M. Diameter-Selective Synthesis of Semiconductor Nanowires. *J. Am. Chem. Soc*. **2000,** *122*, 8801-8802.
16. Qin, L. D.; Park, S.; Huang, L.; Mirkin, C. A. On-Wire Lithography. *Science* **2005,** *309*, 113-115.
17. Zhu, C.; Zeng, J.; Tao, J.; Johnson, M. C.; Schmidt-Krey, I.; Blubaugh, L.; Zhu, Y. M.; Gu, Z. Z.; Xia, Y. N. Kinetically Controlled Overgrowth of Ag or Au on Pd Nanocrystal Seeds: From Hybrid Dimers to Nonconcentric and Concentric Bimetallic Nanocrystals. *J. Am. Chem. Soc.* **2012,** *134*, 15822-15831.
18. Yang, J.; Ying, J. Y. A General Phase-Transfer Protocol for Metal Ions and Its Application in Nanocrystal Synthesis. *Nat. Mater*. **2009,** *8*, 683-689.
19. Gao, J. H.; Liang, G. L.; Zhang, B.; Kuang, Y.; Zhang, X. X.; Xu, B. FePt@CoS_2 Yolk-Shell Nanocrystals as a Potent Agent to Kill HeLa Cells. *J. Am. Chem. Soc.* **2007,** *129*, 1428-1433.
20. Wu, X. J.; Xu, D. S. Formation of Yolk/SiO_2 Shell Structures Using Surfactant Mixtures as Template. *J. Am. Chem. Soc.* **2009,** *131*, 2774-2775.
21. Seh, Z. W.; Li, W. Y.; Cha, J. J.; Zheng, G. Y.; Yang, Y.; McDowell, M. T.; Hsu, P. C.; Cui, Y. Sulphur-TiO_2 Yolk-Shell Nanoarchitecture with Internal Void Space for Long-Cycle Lithium-Sulphur Batteries. *Nat. Commun.* **2013,** *4*, 1331.
22. Mokari, T.; Sztrum, C. G.; Salant, A.; Rabani, E.; Banin, U. Formation of Asymmetric One-Sided Metal-Tipped Semiconductor Nanocrystal Dots and Rods. *Nat. Mater*. **2005,** *4*, 855-863.
23. Buck, M. R.; Bondi, J. F.; Schaak, R. E. A Total-Synthesis Framework for the Construction of High-Order Colloidal Hybrid Nanoparticles. *Nat. Chem.* **2012,** *4*, 37-44.
24. Gu, H. W.; Yang, Z. M.; Gao, J. H.; Chang, C. K.; Xu, B. Heterodimers of Nanoparticles: Formation at a Liquid-Liquid Interface and Particle-Specific Surface Modification by Functional Molecules. *J. Am. Chem. Soc.* **2005,** *127*, 34-35.
25. Wang, C.; Daimon, H.; Sun, S. H. Dumbbell-Like Pt-Fe_3O_4 Nanoparticles and Their Enhanced Catalysis for Oxygen Reduction Reaction. *Nano Lett.* **2009,** *9*, 1493-1496.

26. Gao, J. H.; Gu, H. W.; Xu, B. Multifunctional Magnetic Nanoparticles: Design, Synthesis, and Biomedical Applications. *Acc. Chem. Res.* **2009,** *42*, 1097-1107.
27. Wang, C.; Xu, C. J.; Zeng, H.; Sun, S. H. Recent Progress in Syntheses and Applications of Dumbbell-Like Nanoparticles. *Adv. Mater.* **2009,** *21*, 3045-3052.
28. Sun, Y. P.; Zhou, B.; Lin, Y.; Wang, W.; Fernando, K. A. S.; Pathak, P.; Meziani, M. J.; Harruff, B. A.; Wang, X.; Wang, H. F., et al. Quantum-Sized Carbon Dots for Bright and Colorful Photoluminescence. *J. Am. Chem. Soc.* **2006,** *128*, 7756-7757.
29. Baker, S. N.; Baker, G. A. Luminescent Carbon Nanodots: Emergent Nanolights. *Angew. Chem. Int. Ed.* **2010,** *49*, 6726-6744.
30. Li, H. T.; Kang, Z. H.; Liu, Y.; Lee, S. T. Carbon Nanodots: Synthesis, Properties and Applications. *J. Mater. Chem.* **2012,** *22*, 24230-24253.
31. Shen, L. M.; Chen, M. L.; Hu, L. L.; Chen, X. W.; Wang, J. H. Growth and Stabilization of Silver Nanoparticles on Carbon Dots and Sensing Application. *Langmuir* **2013,** *29*, 16135-16140.
32. Liu, M. M.; Chen, W. Green Synthesis of Silver Nanoclusters Supported on Carbon Nanodots: Enhanced Photoluminescence and High Catalytic Activity for Oxygen Reduction Reaction. *Nanoscale* **2013,** *5*, 12558-12564.
33. Choi, H.; Ko, S. J.; Choi, Y.; Joo, P.; Kim, T.; Lee, B. R.; Jung, J. W.; Choi, H. J.; Cha, M.; Jeong, J. R., et al. Versatile Surface Plasmon Resonance of Carbon-Dot-Supported Silver Nanoparticles in Polymer Optoelectronic Devices. *Nat. Photonics* **2013,** *7*, 732-738.
34. Qu, S. N.; Wang, X. Y.; Lu, Q. P.; Liu, X. Y.; Wang, L. J. A Biocompatible Fluorescent Ink Based on Water-Soluble Luminescent Carbon Nanodots. *Angew. Chem. Int. Ed.* **2012,** *51*, 12215-12218.
35. Zhu, S. J.; Meng, Q. N.; Wang, L.; Zhang, J. H.; Song, Y. B.; Jin, H.; Zhang, K.; Sun, H. C.; Wang, H. Y.; Yang, B. Highly Photoluminescent Carbon Dots for Multicolor Patterning, Sensors, and Bioimaging. *Angew. Chem. Int. Ed.* **2013,** *52*, 3953-3957.
36. Wang, X.; Cao, L.; Lu, F. S.; Meziani, M. J.; Li, H.; Qi, G.; Zhou, B.; Harruff, B. A.; Kermarrec, F.; Sun, Y. P. Photoinduced Electron Transfers with Carbon Dots. *Chem. Commun.* **2009,** *45*, 3774-3776.
37. Wang, C.; Wei, Y. J.; Jiang, H. Y.; Sun, S. H. Tug-of-War in Nanoparticles: Competitive Growth of Au on Au-Fe_3O_4 Nanoparticles. *Nano Lett.* **2009,** *9*, 4544-4547.
38. Wang, C.; Yin, H. F.; Dai, S.; Sun, S. H. A General Approach to Noble Metal-Metal Oxide Dumbbell Nanoparticles and Their Catalytic Application for CO Oxidation. *Chem. Mater.* **2010,** *22*, 3277-3282.
39. Cao, L.; Sahu, S.; Anilkumar, P.; Bunker, C. E.; Xu, J. A.; Fernando, K. A. S.; Wang, P.; Guliants, E. A.; Tackett, K. N.; Sun, Y. P. Carbon Nanoparticles as Visible-Light

Photocatalysts for Efficient CO_2 Conversion and Beyond. *J. Am. Chem. Soc.* **2011,** *133*, 4754-4757.

40. Xu, J.; Sahu, S.; Cao, L.; Bunker, C. E.; Peng, G.; Liu, Y. M.; Fernando, K. A. S.; Wang, P.; Guliants, E. A.; Meziani, M. J., et al. Efficient Fluorescence Quenching in Carbon Dots by Surface-Doped Metals-Disruption of Excited State Redox Processes and Mechanistic Implications. *Langmuir* **2012,** *28*, 16141-16147.
41. Papirer, E.; Lacroix, R.; Donnet, J. B.; Nanse, G.; Fioux, P. XPS Study of the Halogenation of Carbon Black-Part 2. Chlorination. *Carbon* **1995,** *33*, 63-72.
42. Cao, L.; Wang, X.; Meziani, M. J.; Lu, F. S.; Wang, H. F.; Luo, P. J. G.; Lin, Y.; Harruff, B. A.; Veca, L. M.; Murray, D., et al. Carbon Dots for Multiphoton Bioimaging. *J. Am. Chem. Soc.* **2007,** *129*, 11318-11319.
43. Wen, F. F.; Ye, J.; Liu, N.; Van Dorpe, P.; Nordlander, P.; Halas, N. J. Plasmon Transmutation: Inducing New Modes in Nanoclusters by Adding Dielectric Nanoparticles. *Nano Lett.* **2012,** *12*, 5020-5026.

Chapter 4.1. Origin of Photoluminescence of Nanocarbons

4.1. Introduction

4.1.1. Origin of high photoluminescence of carbon nanoparticles

Carbon nanoparticles (CDs) have the outstanding photoluminescence (PL) properties, compared with other nanocarbons such as graphene oxide or fullerene. There are many efforts to synthesize high yield of PL of CDs through the modification of intrinsic and extrinsic states.[1] In addition, PL mechanism of CDs have been proposed to the quantum confinement effect, different degrees of sp^2 conjugation, surface states, and surface defects.[2] However, the origin of PL of CDs is still controversial and debatable, because the different structure of CDs synthesized from various synthetic methods and carbon sources interrupt to interpret PL mechanism of CDs.[3] Furthermore, the role model to explain high PL behavior of CDs have not been developed, to date.

Thus, in chapter 4.2, highly photoluminescent CDs are synthesized by dual heteroatom doping. Based on this new material, the origin of high PL of CDs is elucidated by the structural analysis, time-resolved emission spectroscopy, and density functional theory calculations, which results in graphitic structure and less surface traps of CDs.

4.1.2. Solvatochromic carbon nanosheets

Besides the synthesis of high PL intensity of carbon nanomaterials, the tunable emission of carbon nanomaterials have been developed for a wide range of applications. Different carbonization condition, controlled moral ratio of carbon sources, and surface modification with small or large molecules cause the tunable PL behavior of carbon nanomaterials from blue to red in UV or visible light.[4-7] Especially, surface state of carbon nanomaterials is mainly affected on the emission wavelength. Apart from these various synthetic method, external stimuli is also influenced the PL behavior of carbon nanomaterials. Depending on solvent polarity, the emission wavelength is shifted. Some examples in graphene oxide and CDs have been reported this properties; however, the emission range is very narrow from blue to green.[8,9] Furthermore, the emission shift do not occurred significantly in visible light.

In chapter 4.3, hybrid carbon nanosheets possessing solvent-dependent emission in visible light is described. These nanosheets have different PL color with various range of solvent, resulting in different energy level induced from the shape-tunable properties depending on polarity.

4.1.3. References

1. Ding, C. Q.; Zhu, A. W.; Tian, Y. Functional Surface Engineering of C-Dots for Fluorescent Biosensing and in Vivo Bioimaging. *Acc. Chem. Res.* **2014,** *47*, 20-30.
2. Zhu, S. J.; Song, Y. B.; Zhao, X. H.; Shao, J. R.; Zhang, J. H.; Yang, B. The Photoluminescence Mechanism in Carbon Dots (Graphene Quantum Dots, Carbon Nanodots, and Polymer Dots): Current State and Future Perspective. *Nano Res.* **2015,** *8*, 355-381.
3. Wang, Y. F.; Hu, A. G. Carbon Quantum Dots: Synthesis, Properties and Applications. *J. Mater. Chem. C* **2014,** *2*, 6921-6939.
4. Ding, H.; Yu, S. B.; Wei, J. S.; Xiong, H. M. Full-Color Light-Emitting Carbon Dots with a Surface-State-Controlled Luminescence Mechanism. *ACS Nano* **2016,** *10*, 484-491.
5. Jiang, K.; Sun, S.; Zhang, L.; Lu, Y.; Wu, A.; Cai, C.; Lin, H. Red, Green, and Blue Luminescence by Carbon Dots: Full-Color Emission Tuning and Multicolor Cellular Imaging. *Angew. Chem. Int. Ed.* **2015,** *54*, 5360-5363.
6. Hu, S.; Trinchi, A.; Atkin, P.; Cole, I. Tunable Photoluminescence across the Entire Visible Spectrum from Carbon Dots Excited by White Light. *Angew. Chem. Int. Ed.* **2015,** *54*, 2970-2974.
7. Tetsuka, H.; Nagoya, A.; Fukusumi, T.; Matsui, T. Molecularly Designed, Nitrogen-Functionalized Graphene Quantum Dots for Optoelectronic Devices. *Adv. Mater.* **2016**.
8. Zhu, S. J.; Zhang, J. H.; Qiao, C. Y.; Tang, S. J.; Li, Y. F.; Yuan, W. J.; Li, B.; Tian, L.; Liu, F.; Hu, R.; Gao, H. N.; Wei, H. T.; Zhang, H.; Sun, H. C.; Yang, B. Strongly Green-Photoluminescent Graphene Quantum Dots for Bioimaging Applications. *Chem. Commun.* **2011,** *47*, 6858-6860.
9. Cushing, S. K.; Li, M.; Huang, F. Q.; Wu, N. Q. Origin of Strong Excitation Wavelength Dependent Fluorescence of Graphene Oxide. *ACS Nano* **2014,** *8*, 1002-1013.

4.2. Integrative Approach toward Uncovering the Origin of Photoluminescence in Dual Heteroatom-Doped Carbon Nanoparticles

4.2.1. Abstract

The pursuit of exceptionally high photoluminescence (PL) and stability is critical in the development of novel fluorophores for use in challenging bioimaging and optoelectronic devices. Carbon nanoparticles (CDs) doped with heteroatoms provide a particularly attractive means of effectively tailoring their intrinsic properties and exploiting new phenomena. Here, we report a one-step, scalable synthesis of boron-and-nitrogen-doped CD (BN-CD) with outstanding optical properties unlike those of nitrogen-doped CD (N-CD) in solid state as well as solution. The detailed mechanistic framework was explored using a series of spectroscopic analyses and ultrafast spectroscopy coupled with density functional theory calculations, which all conclusively confirmed that the presence of more graphitic structures in the core and well-distributed surface states are responsible for the enhanced PL in BN-CD. Furthermore, single-molecule spectroscopy analysis demonstrated that a single BN-CD show higher PL intensities and enhanced photobleaching time. We anticipate that this study will aid in uncovering the full potential of CDs in various fields.

4.2.2. Introduction

Carbon-based nanomaterials, including graphene, car-bon nanotube, fullerene, and carbon nanodots have attracted significant attention because of their unique physical and chemical properties and their potential applications in a wide array of fields.[1] In particular, carbon nanoparticles (CDs) have emerged as a new class of optical materials by virtue of their interesting physical, optical, and chemical properties.[2,3] Their facile synthetic nature together with high photoluminescence (PL), photostability and biocompatibility have triggered the recent development of CDs as a benign alternative to conventional semiconducting quantum dots.[4,5] Significant research efforts have focused on producing CDs with controlled dimensions and surface properties, using a variety of synthetic methods.[6-8] Despite this recent progress, the wide range of synthetic protocols often complicates the interpretation of the photophysical aspects of CDs because the synthetic precursor, synthetic method and post-treatment can strongly influence these properties. In particular, the mechanism of PL from CDs has not yet been elucidated

conclusively; for example, the quantum confinement effect, surface defects, functional groups and degree of passivation on the surface have been proposed as the origin of PL in CDs.[9-12] This limitation in understanding of the origin of the PL poses a challenge for future development in the field.

Tailoring carbon nanomaterials with heteroatoms can effectively tune their electronic and chemical properties.[13] Among many heteroatoms, nitrogen, which has an atomic size comparable to that of neighboring carbon, has been the most widely employed heteroatom for the chemical doping of carbon nanomaterials including modulated bandgap in graphene,[14] high electrochemical activity in carbon nanotubes,[15] and tunable electron density and enhanced photophysical properties in graphene quantum dots.[16] In addition, recent approaches have extended to the co-doping of heteroatoms to take advantage of the synergetic coupling effect between heteroatoms, which facilitates the modulation of doping efficiency and charge distribution and enhanced optical properties.[17-19]

Judging by the current status of and potential for CDs, it is evident that the next step in the development of CDs will be tailoring the photophysical properties and elucidating the origin of PL in a controlled framework through a systematic study. To address these issues in the context of heteroatoms within the structure of the carbon, herein, we developed the heteroatom boron-and-nitrogen co-doped CD (BN-CD) through a single-step microwave synthesis from small molecule precursors. For comparison, we prepared non-doped plain CD, N-doped CD (N-CD) and boron-doped CD (B-CD) as a control. Because of their graphitic structure, relatively uniform surface states and less-abundant surface traps, BN-CD display a significant quantum yield (QY), outperforming plain CD, N-CD, B-CD and many other CDs reported to date (Table 4.2.1 and 4.2.2). It is true that there are many precedents on the incorporation of heteroatom in the CDs; however, in this study a detailed mechanistic framework was carefully developed by using a series of spectroscopic analyses, including X-ray photoelectron spectroscopy and ultrafast spectroscopy, coupled with theoretical calculations based on density functional theory (DFT), revealing that the origin of the high photophysical properties is the relatively abundant graphitic structures in the core and well-distributed surface states in BN-CD. Furthermore, single-molecule spectroscopy analysis confirmed the enhanced PL intensities and stabilities in a single BN-CD. We anticipate that this study will guide the future endeavor to uncover the full potential of CDs in various fields.

Table 4.2.1. Reference papers with citric acid based nitrogen- and sulfur-doped CDs

	Nitrogen source	Method	QY (%)	Reference
1	Ethylenediamine	Hydrothermal	94	*Sci. Rep*. **2014**, *4*, 5294
2	Ethylenediamine	Hydrothermal	80.6	*Angew. Chem. Int. Ed*. **2013**, *52*, 3953
3	Ethylenediamine	Hydrothermal	65.5	*Sens. Actuators, B* **2014**, *192*, 488
4	Ethylenediamine	Microwave	30.2	*Chem. Commun*. **2013**, *49*, 1103
5	Diethylenetriamine	Hydrothermal	88.6	*ACS Appl. Mater. Interfaces* **2013**, *5*, 13242
6	Urea	Microwave	14	*Angew. Chem. Int. Ed*. **2012**, *51*, 12215
7	Ethanolamine	Hydrothermal	50	*J. Am. Chem. Soc*. **2012**, *134*, 747
8	Ammonia	Microwave	39	*Part. Part. Syst. Charact*. **2014**, *31*, 1175
9	PEI	Microwave	30	*Chem. Commun*. **2013**, *49*, 1103
	Nitrogen and Sulfur source	**Method**	**QY (%)**	**Reference**
10	Thiourea	Hydrothermal	71	*Nanoscale* **2013**, *5*, 12272
11	Cysteine	Hydrothermal	73	*Angew. Chem. Int. Ed*. **2013**, *52*, 7800

Table 4.2.2. Reference papers with boron or boron- and nitrogen-doped CDs

	Carbon source	Boron Source	Method	QY (%)	Reference
1	Hydroquinone	BBr_3	Hydrothermal, 200 °C, 2 h	14	*Analyst* **2014**,*139*, 2322
2	N-(4-hydroxy phenyl)glycine	Boric acid	Hydrothermal, 300 °C, 2.5 h	11.4	*Anal. Chem*. **2013**, *85*, 10232
3	-	Phenylboronic acid	160 °C, 8 h	8.4	*Anal. Chem*. **2014**, *86*, 5323
4	Graphene	Boron oxide vapor	1100 °C, 4 h	-	*Anal. Chem*. **2014**, *86*, 4423
5	Citric acid, Diethylenetriamine	Boric acid	Hydrothermal, 170 °C, 1 h	39	*J. Phys. Chem. C* **2014**, *118*, 20034
6	Citric acid, Urea	Boric acid	Microwave, 4 min	10-15	*Carbon* **2015**, *83*, 173
7	Graphene	B_2H_6 vapor	arc discharge of graphite → HNO_3+H_2SO_4 sonication	2.5	*Chem. Phys. Lett.* **2014**, *595–596,* 203

4.2.3. Experimental

4.2.3.1. Preparation of CDs

Citric acid, ethylenediamine (99%, EDA), boric acid was purchased from Sigma-Aldrich. Carbon nanoparticles (CDs) were initially synthesized by dehydrating carbohydrates using a commercial household microwave (700 W). To prepare BN-CD, 960 mg of citric acid (5.0 mmol, Aldrich) and 310 mg of boric acid (5.0 mmol) were dissolved in 10 mL of water. To this transparent solution, 347 μL of EDA (5.0 mmol) was added under vigorous stirring for 2 min. The solution was placed into a microwave oven and heated for 2 min, and a yellow solid was obtained after cooling to room temperature. The solid was diluted in 5.0 mL of water. The yellow suspension was dialyzed (SpectraPore MWCO 500 – 1,000) for 2 days to remove salts and unreacted chemicals. To synthesize N-CD, microwave pyrolysis was performed in the absence of boric acid. BN-CD0.5 and BN-CD2 were prepared with 2.5 mmol (0.5 equiv. of citric acid and ethylene diamine) and 10 mmol (2 equiv. of citric acid and ethylene diamine) of boric acid, with the same concentrations of other precursors as described above. Non-doped plain CD was synthesized with 5 mmol of citric acid through hydrothermal method at 180 ºC for 6 hr. B-CD was synthesized with 5 mmol of boric acid and citric acid.

4.2.3.2. Characterizations

A UV/vis spectrophotometer (UV-2550, Shimadzu) was used to measure the absorbance of the CDs. The PL emission was determined with a Varian Cary 5000 spectrophotometer. The structure of the CDs was analyzed by XPS (K-alpha, Thermo Fisher) and FT-IR (Varian, Cray 660). The zeta potential was obtained using a zeta-potential analyzer (Malvern, Zetasizer Nano-ZS). The morphology and size of the CDs were measured using TEM (JEOL JEM-2100, accelerating voltage of 200 kV). XRD measurements were performed on a high-power X-ray diffractometer (Rigaku Co., D/MAZX 2500V/PC) from 10° to 50°.

4.2.3.3. Photoluminescence quantum yield (PLQY) measurement

The PLQY of solution and powder samples was measured using an integrating sphere method, as reported in the literature. The PLQY was determined by using the FLS980 spectrometer (Edinburgh Instruments Ltd.) with 360 nm excitation wavelength. The emission was measured using standard PMT and NIR-PMT detector.

4.2.3.4. Time-resolved fluorescence characterization

Picosecond–resolved fluorescence decay profiles were measured using a time-correlated single-photon counting spectrometer (Fluotime 300, Pico Quant). Femtosecond-resolved transients were obtained using the fluorescence upconversion technique. We used the output of an amplified ytterbium-based laser system (Pharos, Light Conversion), which produced ~170-fs pulses centered at 1030 nm with a 50-kHz repetition rate and an output power of 300 mW. The output beam was split into two parts to generate the pump and gate pulse trains. For the pump beam generation, the fundamental beam was used to pump an optical parametric amplifier (Orpheus, Light Conversion). The idler beam was sum-frequency mixed with the residual fundamental in a β-barium borate (BBO) crystal (type II). The pump pulse of 365 nm was attenuated to ~20 nJ at the sample in a femtosecond fluorescence upconversion spectrometer (Chimera, Light conversion) equipped with a photomultiplier (PMC – 100, Becker & Hickl's) and a monochromator (MSA – 130, solar Laser System). The pump beam polarization was set at the magic angle (54.7°) with respect to the upconversion crystal axis to eliminate the influence of anisotropy on the signal. The fluorescence transients were fitted to theoretical functions using Igor.

4.2.3.5. Computational method

The sp^2 carbon in CDs was modelled by an armchair-edge cluster with hydrogen-passivated unsaturated carbon sigma bonds. We introduced the proper number of edge functional groups, such as carbonyl, carboxylic acid groups, pyrrolic-N, graphitic-N and B-OH, to represent the N-CD and BN-CD. Various atomic configurations were optimized and their electronic structures were calculated by using the DFT method in VASP with the PBE exchange correlation functional. For some configurations that had an energy gap consistent with the experimental value, we performed time-dependent DFT calculations to determine the oscillator strength by using the Gaussian09 package with the B3LYP functional and 6-31G* basis set. The oscillator strength was broadened by a Gaussian function with a width of 0.46 eV.

4.2.3.6. Single molecule microscopy

Single CD particles were encapsulated with vesicles containing biotinylated lipids in order to immobilize the particles on a highly passivated substrate without chemical modification of particle surfaces as previously demonstrated for biomolecules.[2] Briefly, lipid films were prepared by mixing 1,2-dipalmitoyl-sn-glycero-3-phosphoethanolamine-N-(Cap Biotinyl) with dimyristoyl phosphatidylcholine (DMPC) (Avanti Polar Lipids, Inc.) dissolved in chloroform (1:100 molar ratio) and gently drying with nitrogen gas. The lipids were hydrated with buffer solution (100 μL) of 100 mM NaCl, and 25 mM Tris (pH 8.0). After hydration, 800 nM of

respective CDs (100 μL) was added to the solution, to make 400 nM concentration, corresponding to one molecule in a spherical volume of 200 nm diameter, and then the mixed lipid solution was repeatedly frozen in liquid nitrogen and thawed seven times. The solution was extruded through a membrane filter with 200 nm pores (Whatman, 800281) to create uniformly sized unilamellar vesicles.

Individual CDs particles were imaged in objective-type total internal reflection fluorescence microscopy (TIRF). Lipid vesicles containing N-CD or BN-CD particles were immobilized directly on polyethylene glycol coated quartz slide using biotin-neutravidin interaction. Imaging buffer was phosphate buffered saline (PBS) with no additives. TIRF microscope on Leica DMI6000B inverted optical microscope was equipped with 375 nm laser diode (L375P70MLD; Thorlabs), focused on the back focal plane of a high-numerical-aperture oil-immersion objective (HCX PL APO 160x/1.43 Oil CORR GSD; Leica). The PL emission was collected by the same objective and imaged onto a back-illuminated electron-multiplying charge-coupled device (EMCCD) camera (iXon DU-897; Andor) running at an exposure time of 200 ms.

4.2.4. Results and discussion

4.2.4.1. Synthesis of high photoluminescence of BN-CD

As a main control set, N-CD was prepared through microwave pyrolysis using citric acid in the presence of ethylenediamine as a nitrogen source and a surface-passivating agent. In the case of BN-CD, boric acid was additionally introduced as a source of boron (Figure 4.2.1a). The high-resolution transmission electron microscopy (HR-TEM) image of the BN-CD revealed a quasi-spherical structure with an average diameter of 2.8 ± 0.3 nm and interlayer spacings of 0.21 and 0.26 nm, which matched the (100) and (020) facets of graphite (Figure 4.2.1b and 4.2.2). X-ray diffraction (XRD) patterns of BN-CD displayed a broad peak assigned to an interlayer spacing of 0.42 nm, which was higher than the value found between the planes of bulk graphite (0.344 nm), suggesting the presence of heteroatoms within the carbon framework (Figure 4.2.3).

BN-CD showed two characteristic absorption peaks at 241 nm (sp^2-carbon network) and 351 nm (n-π^* transition of carbonyl groups). Although N-CD showed similar absorption peaks, a shoulder peak at 420 nm was also observed, indicating the presence of lower energy states resulting from surface defect-related emissive traps (Figure 4.2.4).[2] The BN-CD solution exhibited bright blue emission under UV irradiation with a maximum emission centered at 450 nm upon excitation at 350 nm (Figure 4.2.1c). Interestingly, the emission spectra of BN-CD showed excitation-independent behavior, whereas those of N-CD showed excitation dependence. The multicolor PL of CDs originates from a combination of quantum confinement effects and the distribution of different emissive surface traps, thus suggesting that BN-CD have a relatively

homogeneous distribution of surface states (Figure 4.2.1d and Figure 4.2.4 in the Supporting Information).[3] The synthetic simplicity of the bulk production of desired CDs constitutes another advantage of CDs over other quantum dots, yielding multigram-scale powders in only 2 min (an average isolated yield exceeding 75%, Figure 4.2.1e). Unlike other CDs reported, the powder and the PVA film of BN-CD displayed a highly blue PL under UV state devices (Figure 4.2.1e and 4.2.5). For example, QY of BN-CD powder exhibited 67.6%, whereas N-CD showed merely 1% (Table 4.2.3).

We further optimized the PL properties of BN-CD by controlling the molar ratio of boric acid to citric acid during the microwave pyrolysis (Figure 4.2.6). In general, the addition of boric acid during the synthesis improved the PL. The highest QY of BN-CD (80.8%) was achieved with an equimolar concentration of each precursor and is almost twice as bright as that of N-CD (40.2%), using an integrating sphere method based on quinine sulfate as a reference. The optical properties of CDs were considerably changed after the incorporation of boron atoms within their network (Figure 4.2.7). Furthermore, non-doped plain CDs (CD) and boron-doped CD (B-CD) had only 2.1% and 1.2% of QY due to heterogeneous surface states from oxygen functional groups (Figure 4.2.8).

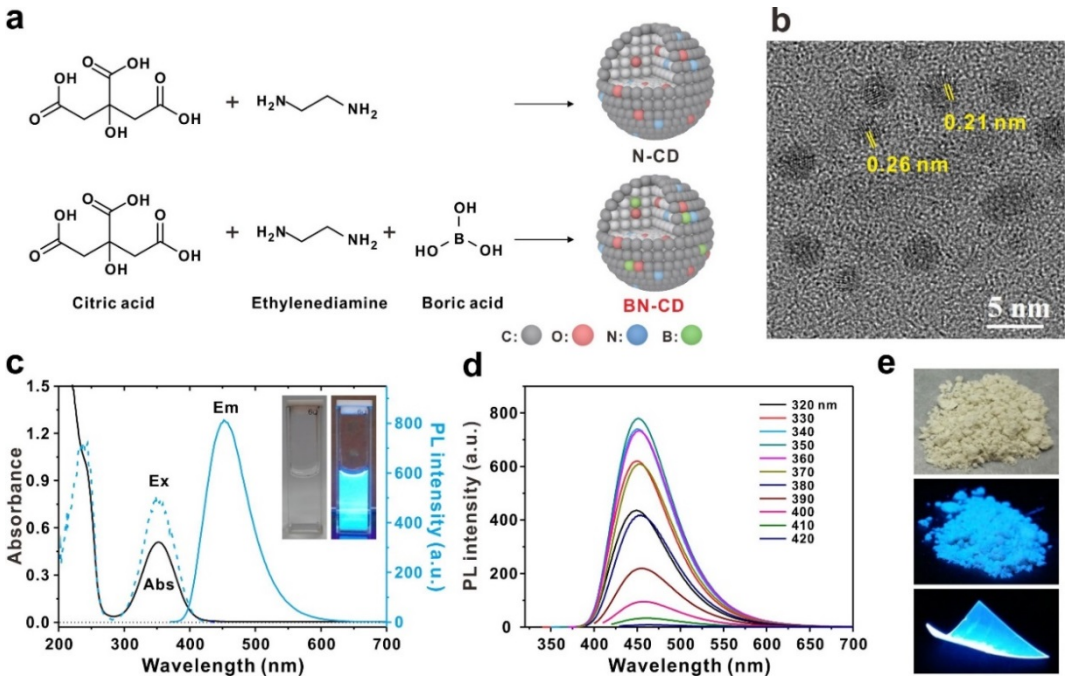

Figure 4.2.1. Synthesis and optical properties of BN-CD. (a) Synthetic scheme for N-CD and BN-CD. (b) High-resolution TEM image of BN-CD with the interlayer spacing measured. (c) UV-vis absorbance and photoluminescence spectra of BN-CD. Inset shows a BN-CD suspension (conc. 0.01 mg/mL) (left) under room light and (right) UV illumination at 365 nm. (d) Photoluminescence spectra of BN-CD under varying excitation wavelengths from 320 to 420 nm with 10-nm increments. (e) The bulk production of BN-CD powder and PVA film under daylight and UV illumination at 365 nm.

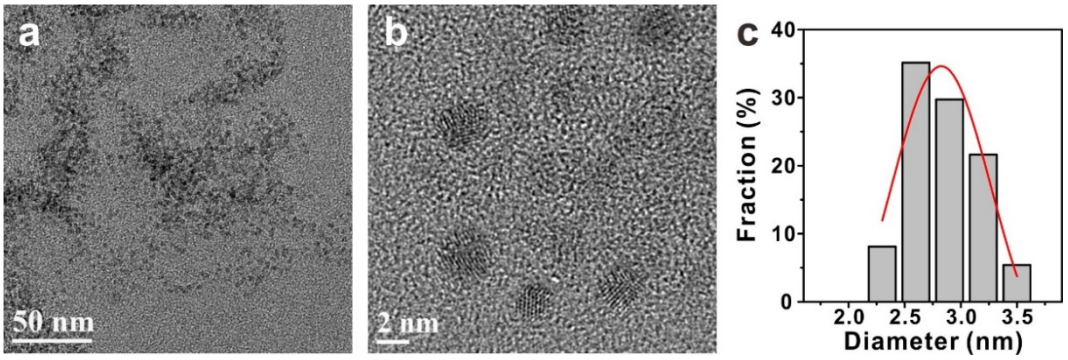

Figure 4.2.2. (a) Normal TEM, (b) high-resolution TEM images and (c) the distribution of particle size of BN-CD

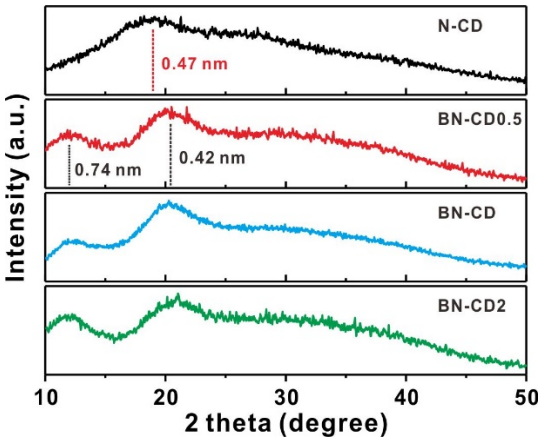

Figure 4.2.3. XRD diffraction patterns of CDs. N-CDs and BN-CD have a broad peak at 0.47 nm and 0.42, respectively. Due to the incorporation of heteroatom within the carbon framework, the interlayer spacing is increased compared to that of bulk graphite (0.344 nm). In addition, BN-CD showed another peak at 0.74 nm, which is ascribed to the oxide-induced O-containing groups and inserted H_2O molecules.

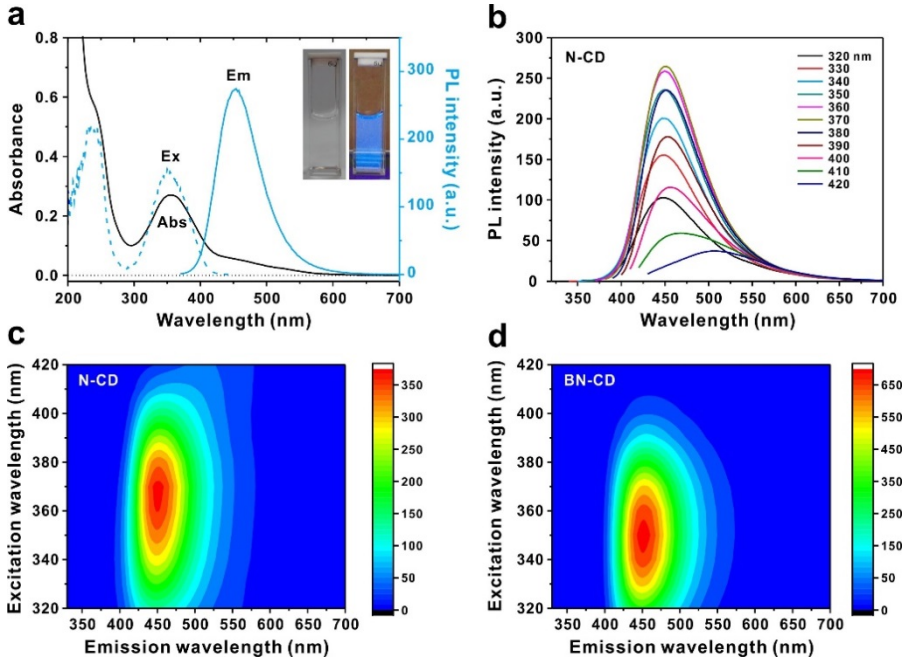

Figure 4.2.4. (a) UV-vis absorbance and PL spectra of N-CD. Inset shows N-CD suspension (conc. 0.01 mg/mL) (left) under room light and (right) UV illumination at 365 nm. (b) PL spectra of N-CD under varying excitation wavelengths from 300 to 420 nm with 10-nm increments. Excitation and emission contour plots of (c) N-CD and (d) BN-CD.

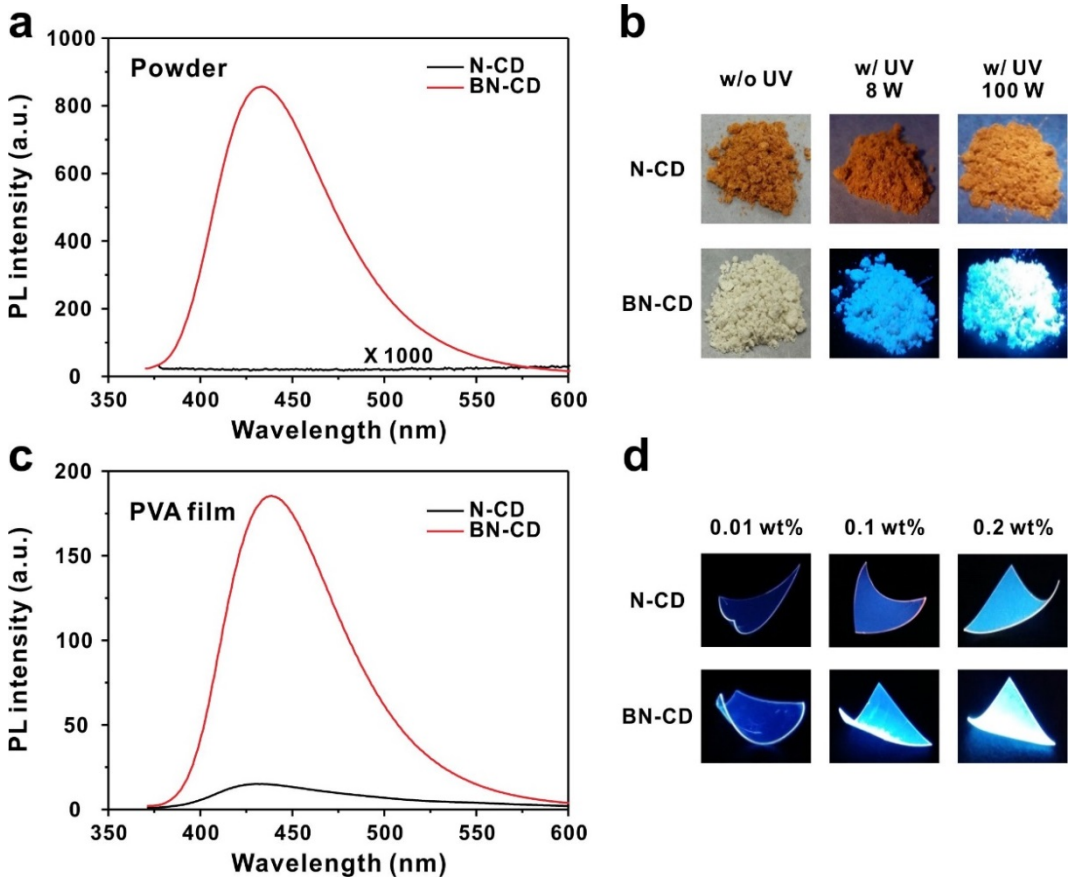

Figure 4.2.5. (a) PL spectra of N-CD and BN-CD powder. (b) Photograph images of CDs powder under daylight and 8 W and 100 W UV illumination at a wavelength of 365 nm. (c) PL spectra of N-CD and BN-CD embedded within PVA film at a concentration of 0.1 wt % of CDs. (d) Photograph images of CDs film under 8 W UV illumination. CDs films were prepared with different concentration of CDs in 10 wt % of PVA. While N-CD powder showed negligible PL, BN-CD displayed highly blue PL intensities. Furthermore, when the concentration of CDs is increased within PVA film, BN-CD show 12 times higher PL intensities than that of N-CD. Based on these results, BN-CD maintain their high PL properties in a solid state like powder and film.

Table 4.2.3. Quantum yield of N-CD and BN-CD measured by integrating shere method

Sample	Solution concentration			powder
	0.050 mg/ml	0.10 mg/ml	1.0 mg/ml	
N-CD	43.1%	47.5%	30.6%	~1%
BN-CD	80.9%	89.0%	73.7%	67.6%

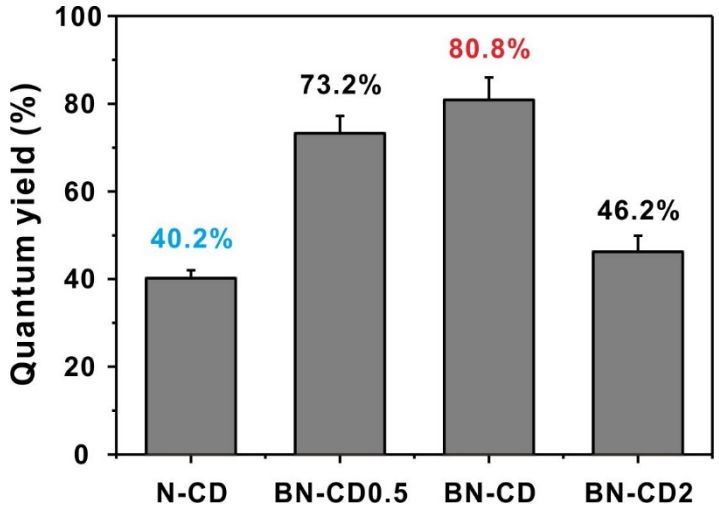

Figure 4.2.6. Quantum yield (QY) of N-CD, BN-CD0.5, BN-CD, and BN-CD2 in reference to quinine sulfate.

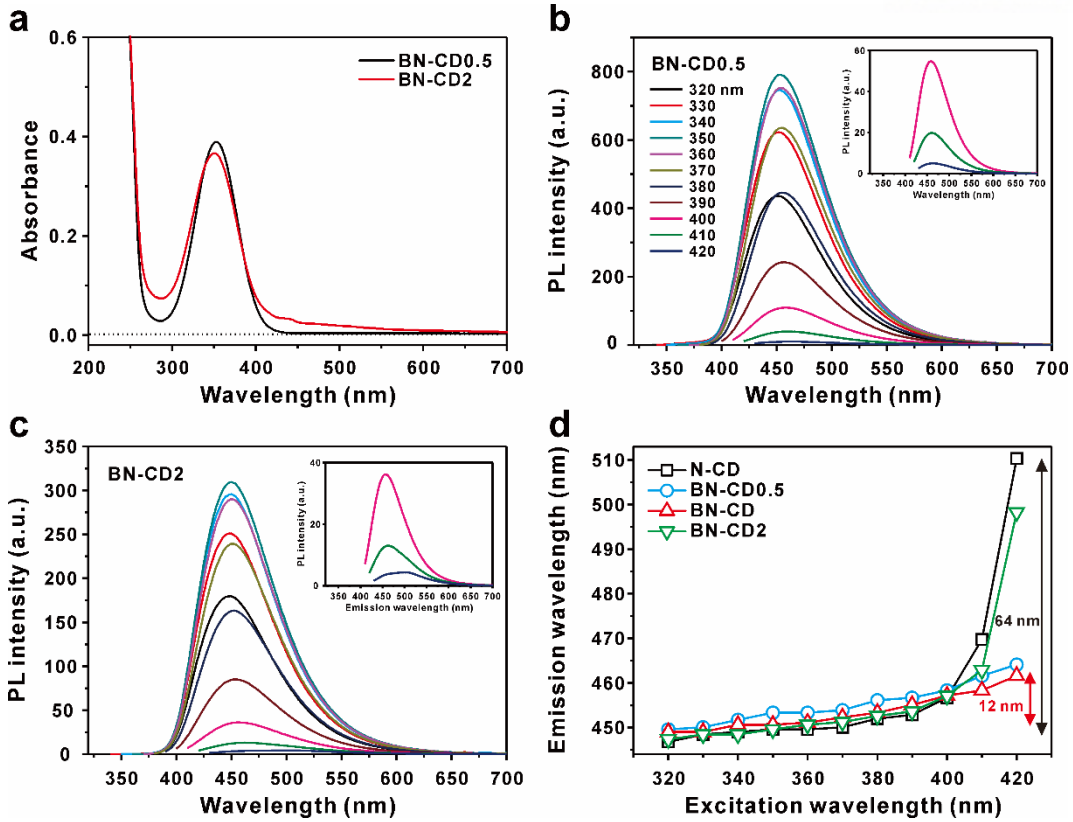

Figure 4.2.7. (a) UV-vis absorbance of BN-CD0.5 and BN-CD2. (b, c) PL spectra of (b) BN-CD0.5 and (c) BN-CD2. (d) Emission shifts of all CDs prepared with increased excitation wavelength.

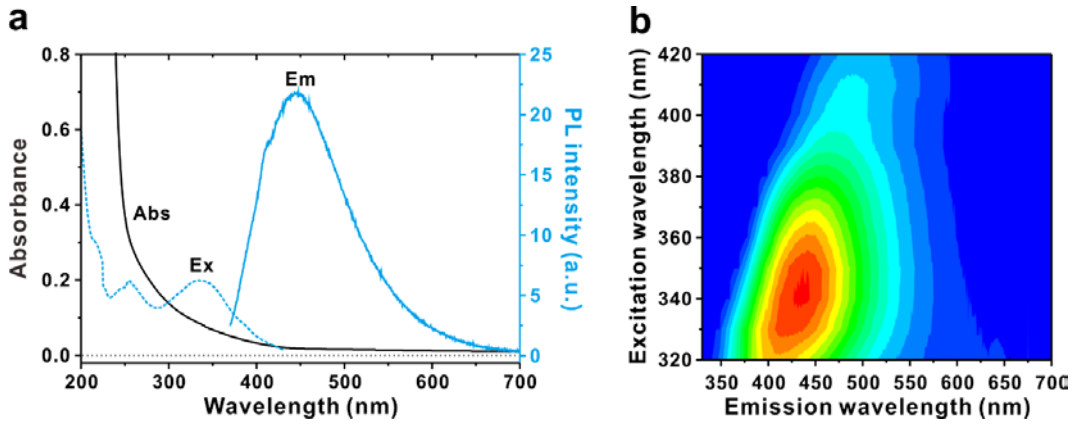

Figure 4.2.8. (a) UV-vis absorbance and (b) PL spectra of non-doped plain CD. CD has 2.1% of quantum yield at 360 nm and red-shift (90 nm) in emission spectra. It results from heterogeneous oxygen functional groups on the surface of CD.

4.2.4.2. Structure of high photoluminescence of BN-CD

To investigate the chemical composition and structure of N-CD and BN-CD, FT-IR, elemental analysis (EA) and X-ray photoelectron spectroscopy (XPS) measurements were performed. Both CDs displayed characteristic IR peaks at 1086 (C-O stretching), 1539 (C=C stretching), and 2838 and 2929 cm^{-1} (C-H stretching), and a broad peak at approximately 3455 cm^{-1} (O-H and N-H stretching) (Figure 4.2.9a). In addition, the successful doping of boron in the carbon framework was confirmed by the appearance of new peaks corresponding to B-O, B-C and B-N stretching in BN-CD.

According to EA and XPS, the major components of N-CD and BN-CD are C, N and O. Interestingly, the ratios of C/N and C/O were decreased in BN-CD compared with N-CD because of an increased N doping ratio, which was aided by B doping in the carbon network (Figure 4.2.9b, Table 4.2.4 and 4.2.5). Specifically, more nitrogen atoms, which are more-electronegative, were introduced to accommodate the charge density of the carbon matrix upon the introduction of less-electronegative boron atoms.[4] In accord with the FT-IR result, the deconvoluted high-resolution XPS spectrum of B1s in BN-CD also proved that B doping mostly occurs in the form of partially oxidized boron (BCO_2, BC_2O, 192.3 eV, 91.2%) with a minor contribution from B-N-C (191.5 eV, 9.8%) (Figure 4.2.9c).[5,6]

In the high-resolution C1s spectrum, BN-CD and N-CD showed different fractions of carbon-related bonding with N and O species. For example, BN-CD contained increased fractions of C=C and C=O bonds (284.74 and 287.92 eV), whereas the fractions of C-N and COOH groups (285.77 and 288.79 eV) were reduced relative to sites resulting from the presence of fewer carboxylic acid groups and more carbonyl groups (Figure 4.2.11); this finding is in good agreement with the result of the theoretical study. Interestingly, the N1s spectra also revealed different nitrogen configurations in BN-CD and N-CD (Figure 4.2.9c). Specifically, N-CD mainly consists of pyrrolic-N, whereas graphitic-N is the dominant nitrogen configuration in BN-CD (Figure 4.2.10). The different nitrogen constituents in N-CD and BN-CD indicate that graphitic-N plays an important role in enhancing the PL in CDs. Because of the electron transfer from graphitic-N to the π^* state of the sp^2-carbon cluster, a large amount of energy is released when electrons fall from the π^* back to the π state, leading to a significantly high PL intensity.[7,8] On the basis of these results, we suggest that the graphitic structure and oxygen-related functional groups of CDs are closely connected to their PL properties. In particular, B-doping contributes to changing the C and N configurations, in turn elevating the fraction of graphitic-C and N, generating well-distributed surface defect states, and improving the QY of BN-CD.

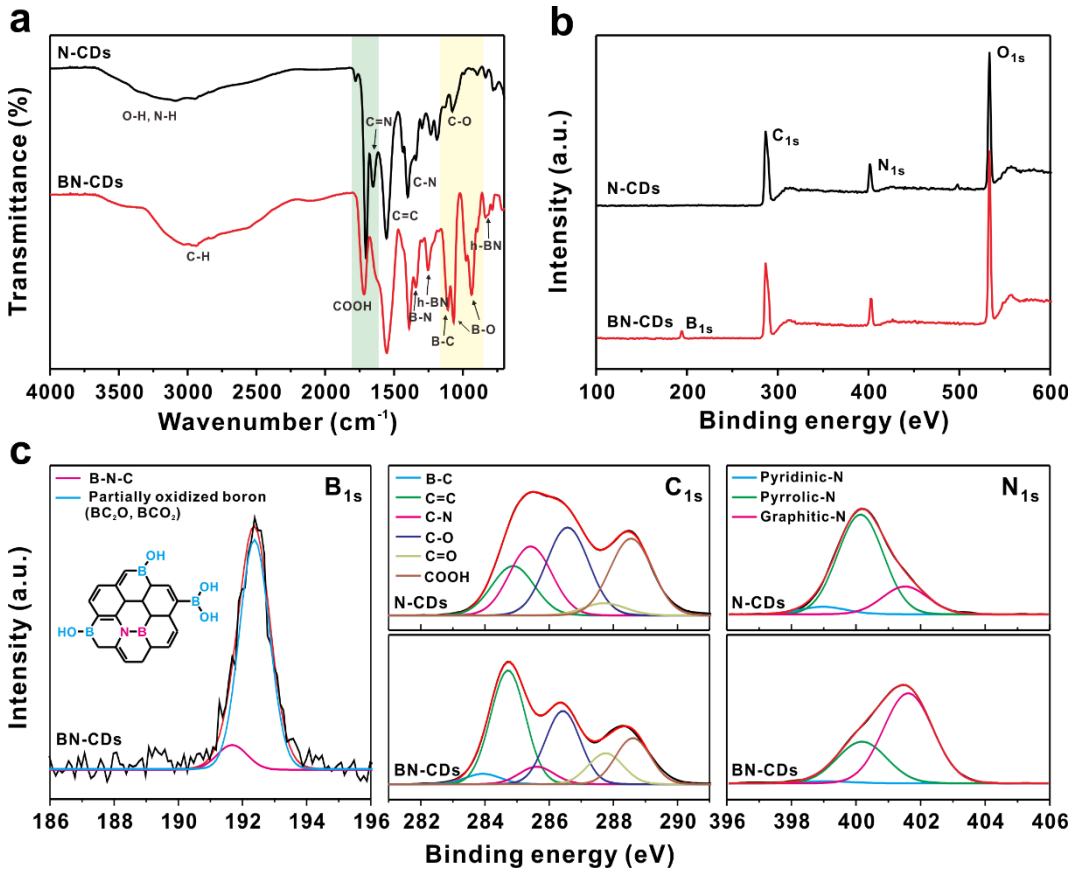

Figure 4.2.9. Chemical structures of N-CD and BN-CD. (a) FT-IR spectra and (b) XPS survey spectra of N-CD and BN-CD. (c) High-resolution XPS spectra of B1s, C1s and N1s of N-CD and BN-CD. The XPS survey spectrum indicates the presence of 3.51% B and 12.16% N in BN-CD.

Table 4.2.4. Elemental analysis of CDs

	N-CD	BN-CD0.5	BN-CD	BN-CD2
C	43.57	38.67	37.22	36.86
O	38.24	43.67	45.08	45.64
N	12.78	11.58	11.42	11.10
H	5.39	6.07	6.27	6.40
C/O	1.14	0.89	0.83	0.81
C/N	3.41	3.34	3.26	3.32

Table 4.2.5. Elemental composition of CDs determined by XPS

	N-CD	BN-CD
C	64.47	48.85
O	21.89	35.49
N	13.64	12.16
B	-	3.51
C/O	2.94	1.37
C/N	4.72	4.02

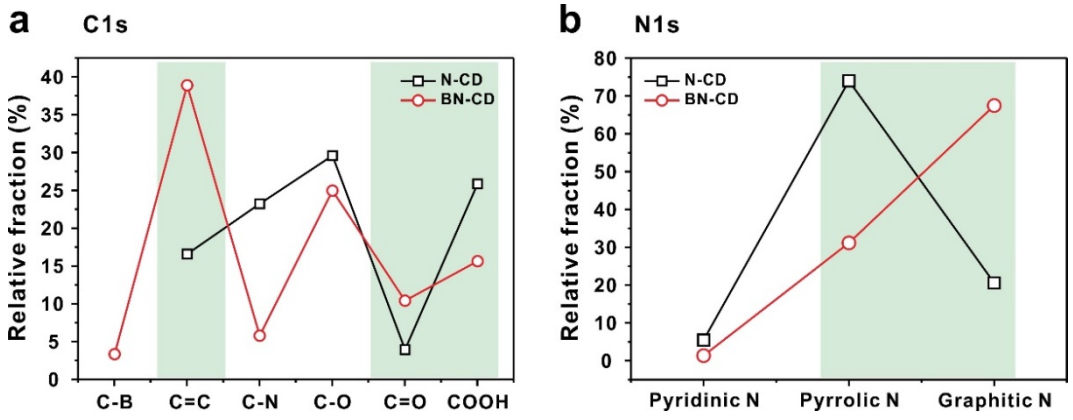

Figure 4.2.10. The chemical compositions of N-CD and BN-CD determined by XPS.

4.2.4.3. Photophysics properties of high photoluminescence of BN-CD

Based on the structural analysis, we propose that the high QY of BN-CD originates from their graphitic structure and less N-related defects (trap states). This assignment is independently supported by the fluorescence lifetime measurements of CDs. We investigated the ultrafast relaxation dynamics of CDs by measuring the emission lifetimes of BN-CD and N-CD. The representative results are listed in Table 4.2.6, obtained using both time-correlated single-photon counting (Figure 4.2.11a and 4.2.12) and fluorescence upconversion spectroscopy to uncover the PL dynamics on different timescales (Figure 4.2.12b and 4.2.13). The overall results can be summarized as follows. First, a multitude of lifetime components were observed spanning a few hundred femtoseconds to a few tens of nanoseconds. Such components have several characteristic timescales: ~200 fs (τ_1), 2-5 ps (τ_2), 330-440 ps (τ_3), 5 ns (τ_4) and 15 ns (τ_5). This result suggests that either several competing de activation pathways or a broad distribution of recombination rates exist in CDs.[9] Notably, the 5-ns lifetime component (τ_4) was unique to the N-CD sample. Second, the average lifetime (τ_{avg}), obtained by integrating the multi- exponential fit over time, was considerably shorter for N-CD than for BN-CD, which is in accordance with the lower QY of N-CD. For example, when compared at an emission wavelength of 450 nm, the ratio of the average lifetimes of N-CD and BN-CD was 0.54 ± 0.03, which is similar to the QY ratio of 0.67.

The temporal evolution of the PL of BN-CD was additionally investigated by time-resolved spectral measurements with picosecond accuracy (Table 4.2.7). Both N-CD and BN-CD have a longest lifetime component of 15 ns, which is attributed to the fluorescence lifetime of the core π-conjugated domains in CDs. The reduction of τ_{avg} in N-CD relative to BN-CD originated from the unique 5-ns component in N-CD at the expense of the longer 15-ns component. The lifetime of 5 ns is attributed to originate from trap states in N-CD having more nitrogen-related defect sites, as evidenced by the additional absorption band around 450 nm. This assignment was further supported by examining the change in the 5-ns component when the excitation wavelength was turned away from 375 nm, at which the CD core was dominantly excited (Figure 4.2.14). The fraction of the 5-ns component, for instance, increased from 0.22 to 0.31 as the excitation wavelength shifted from 375 to 450 nm; it further rose to 0.55 excited at 510 nm. In addition, the lifetime of the core region of the CD decreased from 15 ns to 9.8 ns and 8.4 ns when the excitation wavelength increased from 375 to 450 and 510 nm, respectively, resulting in a red shift of the fluorescence band. It follows that there is a size distribution of π-conjugated domains having different lifetimes and electronic transition energies in the core of the CDs.[10]

Based on the femtosecond upconversion fluorescence spectroscopy, the origins of the ~200-fs (τ_1) and the 2~5-ps (τ_2) components in Table 4.2.6 are assigned to electron-phonon interactions and relaxation from the bottom of the conduction band to the oxygen-related surface states, respectively.[11] The several-hundred picosecond component (τ_3) is originated from shallow surface trap states, which is also abundant in N-CD containing unique deep trap states.

Taking these results together with all of the spectroscopic data, we correlate the shorter lifetime in N-CD with the population of trap states and/or exciton formation, and the longer lifetime with the intrinsic and trap-mediated PL process that mainly occurred in BN-CD (Figure 4.2.11c). Specifically, because of the deep trap states and size distribution of sp^2 domains, N-CD exhibit relatively low PL efficiency and excitation-dependent behavior.

4.2.4.4. DFT calculation of high photoluminescence of BN-CD

In addition to the experimental investigations that account for the origin of the observed PL mechanism associated with the CD structure, we applied theoretical approaches based on DFT, using the Vienna Ab initio simulation package (VASP) with the Perdew-Burke-Ernzerhof (PBE) exchange correlation functional. The optical transition properties were calculated using the time-dependent DFT method for the oscillator strength with B3LYP/6-31G* (Figure 4.2.15).

Our model structures, with various atomic configurations for N-CD and BN-CD, were constructed by combining the experimental results from FT-IR, EA and XPS. The models involved a number of distinct functional groups and structures, such as carbonyl, carboxylic, B-OH, pyrrolic-N and graphitic-N groups. As shown in Figure 4.2.15a, the most stable configuration of N-CD involved pyrrolic-N adjacent to a carboxylic acid group (COOH), with a minor contribution from graphitic-N located next to a carbonyl group (C=O) along the edge. This abundant pyrrolic-N configuration, however, did not influence the DOS of N-CD, indicating that only graphitic-N is related to the optical properties of CDs. Conversely, in BN-CD, the most favorable atomic arrangement and configuration of boron occurred as B-OH with graphitic-N at edge sites, rather than within the carbon framework as B-N-C (Figure 4.2.15b). In addition, B-OH located next to graphitic-N serves similarly as carbonyl group, affecting the PL properties of BN-CD. Moreover, the relative connectivity of the B-OH group with respect to C and N was important to the total energy; for example, when B-OH was near the edge site of N in the arrangement of C-N-B-OH, the total energy was lower than that of N-C-B-OH by 2.24 eV (Figure 4.2.16). From these results, we conclude that the abundant carbonyl group/graphitic-N configuration within BN-CD is responsible for their superior photophysical properties.

When the oscillator strength was correlated with the PL enhancement of BN-CD, our model depicted main peaks at approximately 570 nm and 500 nm for N-CD and BN-CD, respectively (Figure 4.2.15c and 4.2.15d). The magnitude of the oscillator strength in BN-CD was

approximately two times larger than that of N-CD because two types of transitions occurred in BN-CD, as shown in the HOMO and LUMO models. The transition (denoted as an asterisk) in N-CD involved electron-hole recombination from the LUMO to the HOMO, whereas two distinct transitions—LUMO to HOMO-1 and LUMO+1 to HOMO-1—occurred in BN-CD. These results confirmed that the increased number of optical transitions can be mainly attributed to the edge chemistry of BN-CD, which involves graphitic-N and carbonyl groups. In contrast, the relatively few edge groups in N-CD do not significantly enhance their optical properties (Figure 4.2.17).

4.2.4.5. Single molecule spectroscopy of high photoluminescence of BN-CD

Ensemble spectroscopy studies often oversight single-particle behavior; therefore, we further characterized the photophysical properties of CDs at single-particle level using total internal reflection fluorescence microscopy (Figure 4.2.18 and Figure 4.2.19). Individual particles of both N-CD and BN-CD demonstrated the stable PL intensity with a considerable fraction (more than 85%) of single-step photobleaching and a small fraction of multistep photobleaching behavior, when examined 311 particles of N-CD and 225 particles of BN-CD (Table 4.2.8). It is of note that both CDs exhibited no photoblinking phenomenon in which fluorescence intensities hop between multiple levels. Stable PL of N-CD and BN-CD is in contrast with high PL fluctuations in previous studies of non-doped CDs,[2] but in accord with the reduced blinking by nitrogen doping.[12]

Moreover, time-dependent traces of single-step photobleaching in both CDs displayed significantly longer bleaching time (~ 1,000 s) that is far beyond that of organic fluorophores and one or two orders of magnitude longer than those of non-doped CDs (Figure 4.2.18a and 4.2.18b).[2] Collectively, the average photobleaching times (τ_{avg}) including all single and multistep were 818 ± 292 s and 1053 ± 266 s for N-CD and BN-CD, respectively, under total internal reflection irradiation of 50 W/cm^2 laser beam (Table 4.2.9). In addition, the BN-CD showed a brighter image compared to N-CD owing to the increased lifetime and quantum yield under identical laser illumination (inset images in Figure 4.2.18a and 4.2.18b).

To further confirm the origin of a higher PL in single BN-CD, we analyzed the total number of photons emitted before photobleaching for single-step bleaching traces, which constitutes the majority of single-particle traces over 85% (Figure 4.2.18c). Individual characteristics of BN-CD showed modest improvement compared to those of N-CD. Especially, the average photon flux per camera frame (200 ms) was also increased from 200 ± 13 for N-CD to 275 ± 24 for BN-CD (Figure 4.2.18d). Collectively, BN-CD emitted more than a million photons, which is 60% larger than that of N-CD, resulting in the synergistic contribution to the higher PL observed (Figure 4.2.18e).

Table 4.2.6. Excited state lifetime (τ) of N-CDs and BN-CDs in aqueous solution[a]

	λ_{em}[b] (nm)	Time (ps)					τ_{avg} (ps)[d]
		τ_1 (α_1)[c]	τ_2 (α_2)	τ_3 (α_3)	τ_4 (α_4)	τ_5 (α_5)	
N-CD	430	0.2 ± 0.03 (80 ± 14%)	5 ± 0.7 (10 ± 1%)	330 (3 ± 0.4%)	5000 (2 ± 0.2%)	15000 (5 ± 0.6%)	861 ± 91
	450	-	2.6 ± 0.27 (47 ± 3%)	330 (14 ± 0.4%)	5000 (7 ± 0.2%)	15000 (32 ± 0.9%)	5197 ± 135
	480	-	2.3 ± 0.65 (23 ± 4%)	330 (22 ± 0.8%)	5000 (10 ± 0.3%)	15000 (45 ± 2%)	7524 ± 300
BN-CD	430	0.2 ± 0.08 (72 ± 30%)	2.5 ± 0.68 (10 ± 4%)	440 (3 ± 0.7%)	-	15000 (15 ± 4%)	2263 ± 600
	450	-	1.5 ± 0.3 (25 ± 4%)	440 (11 ± 0.5%)	-	15000 (64 ± 3%)	9649 ± 450
	480	-	2.0 ± 2.1 (7 ± 5%)	440 (14 ± 0.8%)	-	15000 (79± 5%)	11912 ± 750

[a] The fluorescence decay curves fitted to the multi-exponential function:

$I(t) = \sum_i^n A_i \, e^{-t/\tau_i}$.

[b] Monitored emission wavelength.

[c] Fractional amplitude.

[d] The average lifetime (τ_{avg}) obtained using the following equation: $\tau_{avg} = \sum_i^n \alpha_i \tau_i$.

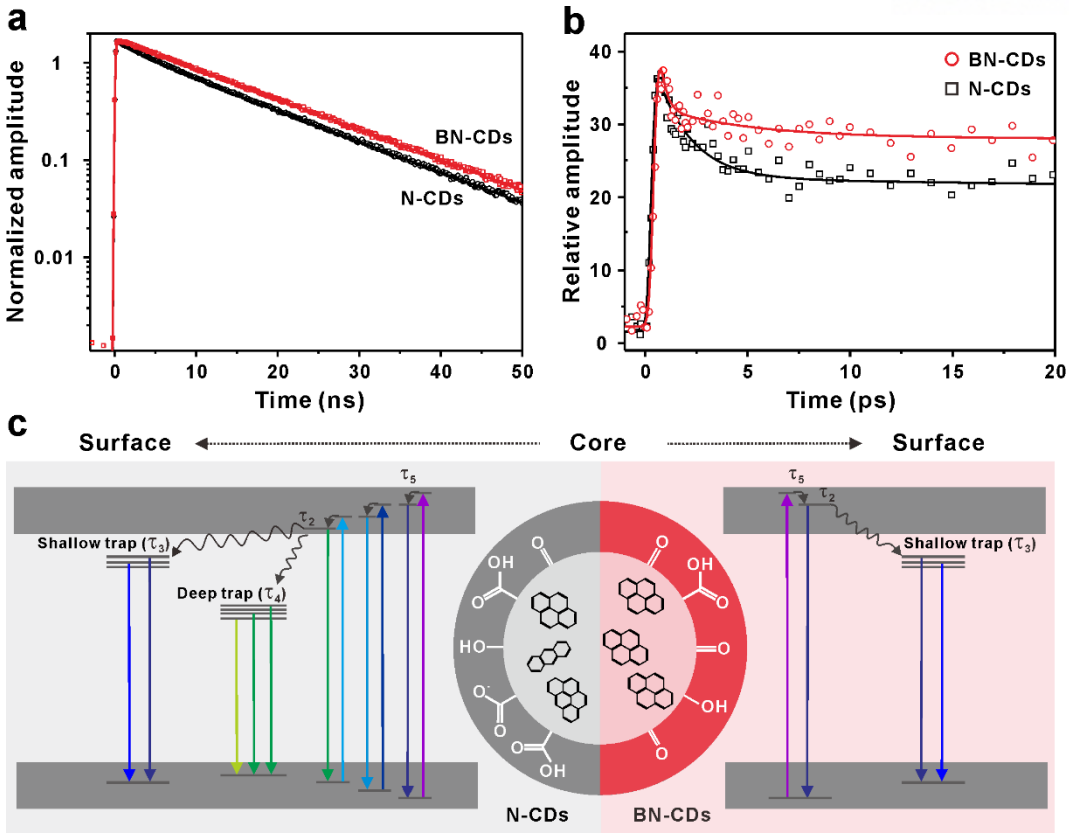

Figure 4.2.11. Photophysical properties of N-CD and BN-CD. (a) Normalized fluorescence decay profiles of CDs monitored at 450 nm with excitation at 375 nm, and (b) the femtosecond-resolved fluorescence decay kinetics of CDs probed at 450 nm with excitation at 365 nm. Note that the timescales are significantly different in (a) and (b). (c) The energy level diagram and schematic structures of the corresponding CDs with their relevant photophysical transitions.

Table 4.2.7. Photoluminescence decay time measured for N-CD and BN-CD obtained from time correlated single photon counting with excitation at 375 nm

Sample	τ_{em} (nm)	Time (ns)			τ_{avg} (ns)
		τ_1 (α_1)	τ_2 (α_2)	τ_3 (α_3)	
N-CD	430	0.330 (32%)	4.987 (17%)	14.812 (73%)	11.804
	450	0.330 (27%)	4.987 (14%)	14.812 (80%)	12.532
	480	0.330 (28%)	4.987 (13%)	14.812 (81%)	12.675
BN-CD	430	0.441 (16%)	-	15.102 (84%)	12.700
	450	0.441 (14%)	-	15.102 (86%)	12.986
	480	0.441 (15%)	-	15.102 (85%)	12.836

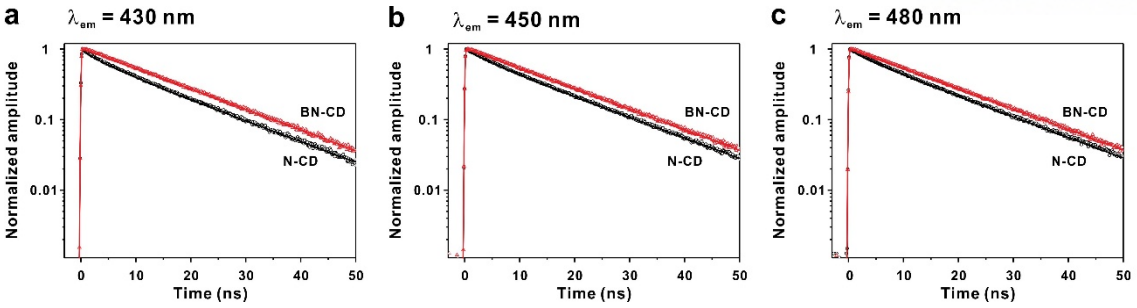

Figure 4.2.12. Normalized fluorescence decay profiles of CDs monitored at different emission wavelength of (a) 430 nm, (b) 450 nm and (c) 480 nm under excitation at 375 nm.

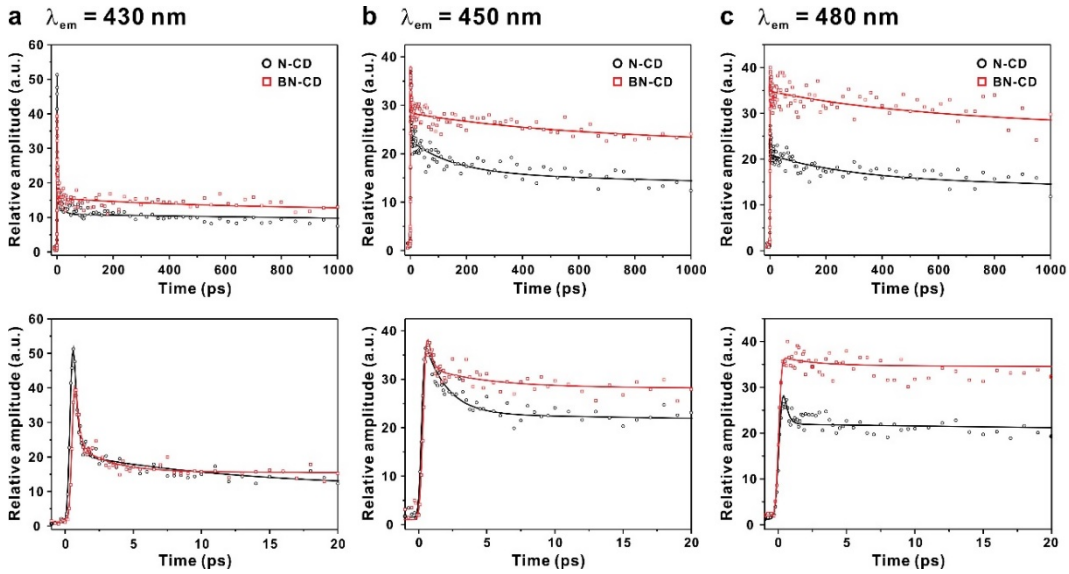

Figure 4.2.13. Femtosecond-resolved fluorescence decay profiles of CDs at different emission wavelength of (a) 430 nm, (b) 450 nm and (c) 480 nm under excitation at 365 nm.

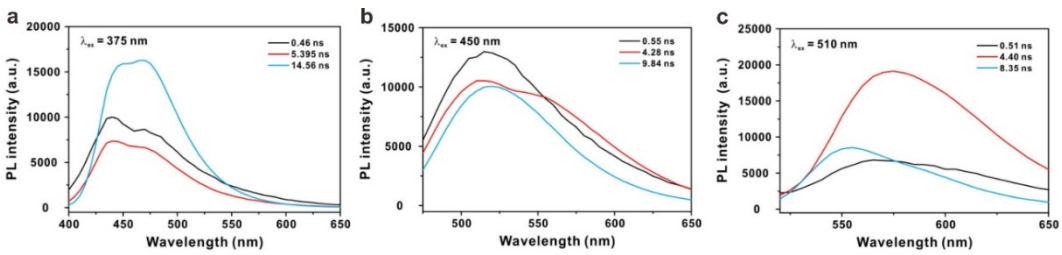

Figure 4.2.14. Time-resolved emission spectra of N-CD excited at various wavelengths of (a) 375 nm, (b) 450 nm and (c) 510 nm.

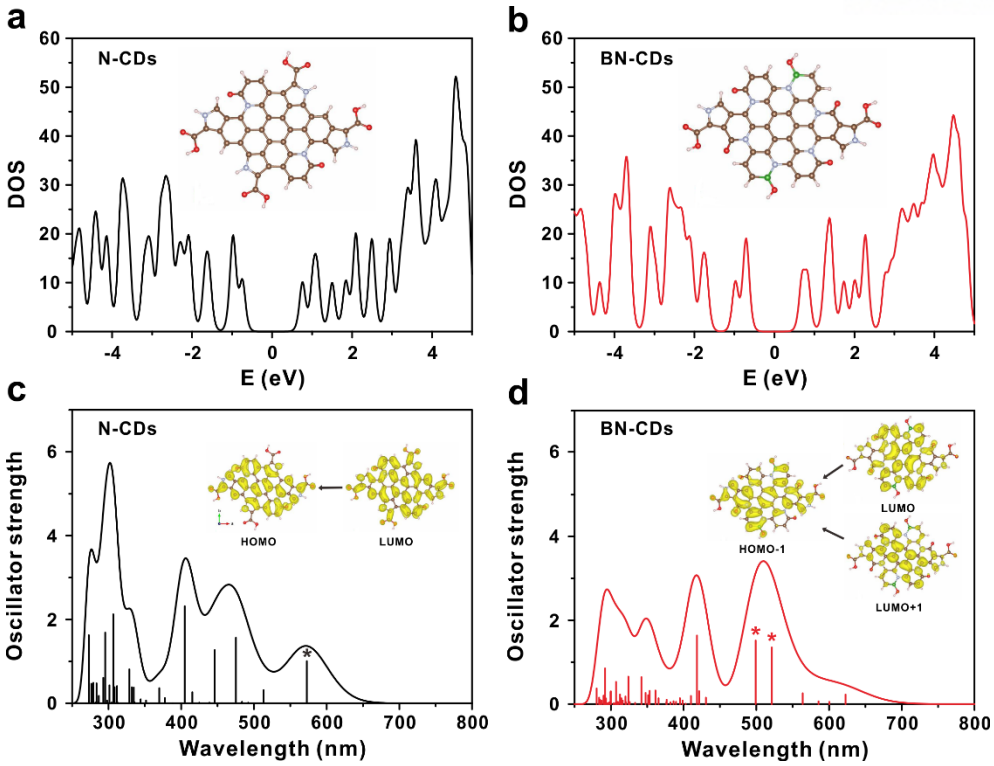

Figure 4.2.15. DFT calculations of N-CD and BN-CD. (a, b) Electronic densities of states (DOSs) and modelled structures for (a) N-CD and (b) BN-CD (brown, C; white, H; red, O; blue, N; and green, B atoms). (c, d) The oscillation strengths and Gaussian functions (FWHM = 0.46 eV) for (c) N-CD and (d) BN-CD. The charge distributions of HOMOs and LUMOs that contribute to the first one (N-CD) or two (BN-CD) main peaks are marked with asterisks in (c) and (d).

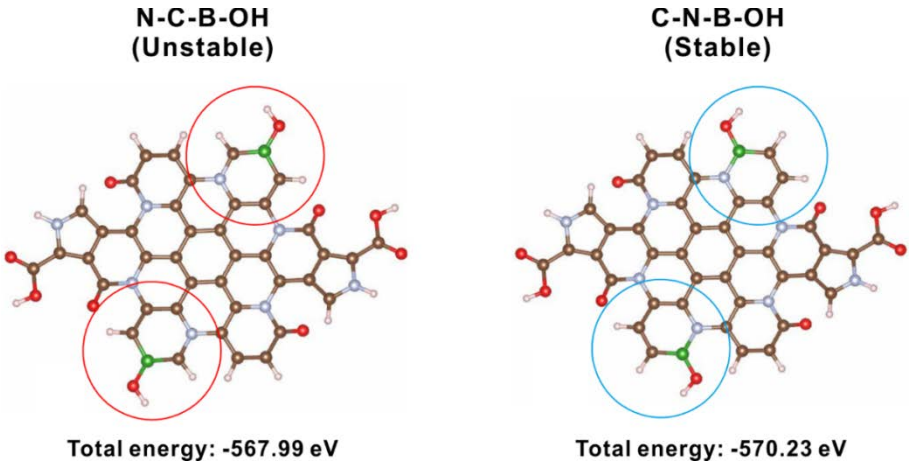

Figure 4.2.16. Chemical structures of BN-CD determined from DFT calculation. When B-OH group is located away from graphitic N on edge site, high total energy is obtained. Thus, B-OH next to graphitic N is the most stable structure with lower total energy.

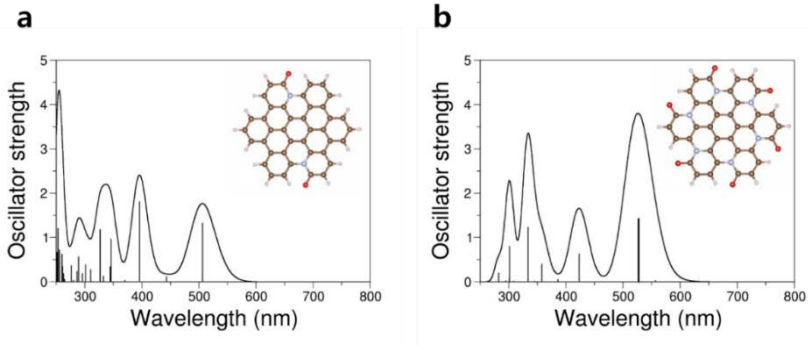

Figure 4.2.17. (a) Two N-C=O groups representing N-CD and (b) six N-C=O groups representing BN-CD. Model calculation results showing that the dipole transition enhancement is mainly caused by enriched edge groups.

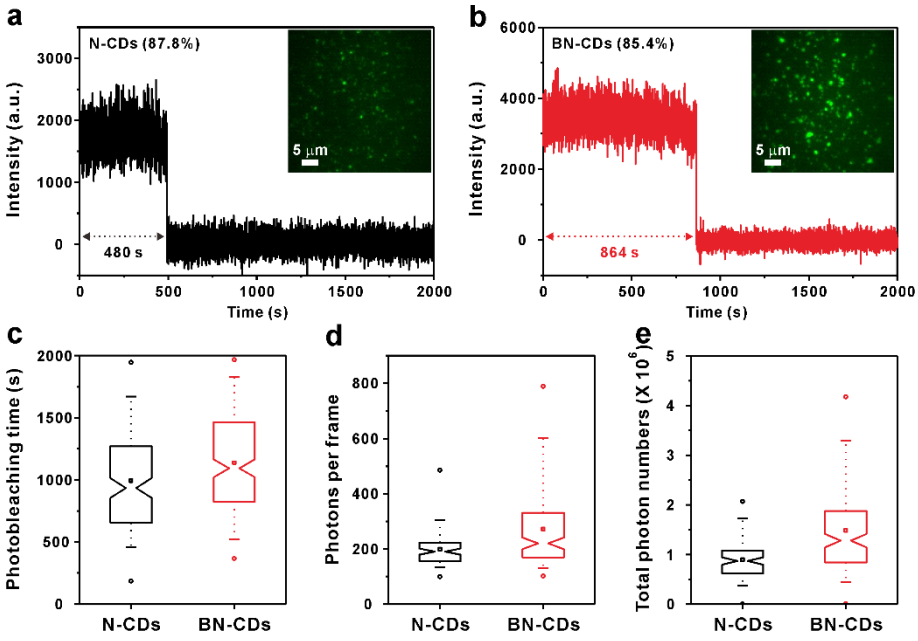

Figure 4.2.18. Single-molecule spectroscopy of N-CD and BN-CD. (a, b) Time-dependent photoluminescence traces of (a) single N-CD and (b) single BN-CD with a single-step photobleaching. The percentages were calculated from collection of N-CD (n = 311) and BN-CD (n = 225). Inset images are single N-CD and BN-CD under 375 nm illumination. (c-e) Box plot comparison of single N-CD and BN-CD bleached in one step. (c) single-step photobleaching time, (d) photons per frame and (e) total photon numbers before photobleaching. The average single-step photobleaching times (τ_{avg}) was 993 ± 397 s and 1138 ± 400 s for N-CD and BN-CD, respectively. The laser power was 50 W/cm^2 and the camera exposure time was 200 ms per frame. Spheres indicate minima and maxima. Squares indicate the average values and notches represent the confidence interval at the confidence level of 95%.

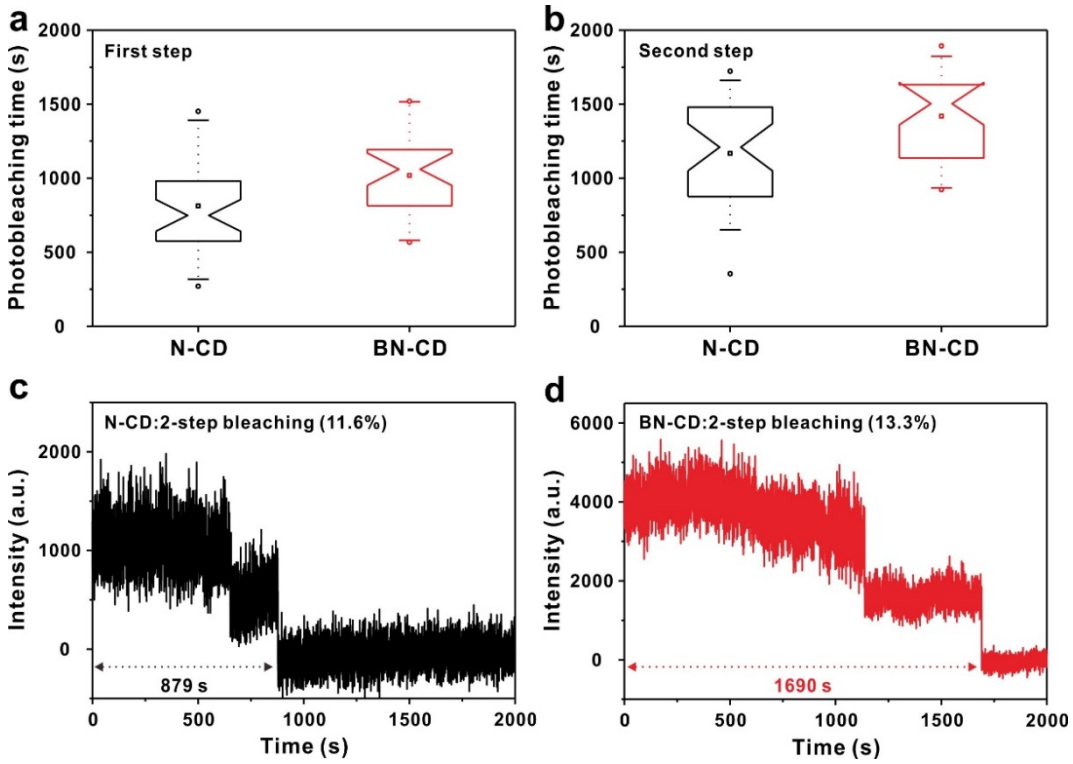

Figure 4.2.19. Comparison of N-CD and BN-CD bleaching in two steps observed in single particle imaging. (a, b) Profiles of photobleaching time at the (a) first and (b) second step. (c, d) Representative time-dependent PL traces with two-step photobleaching (a) N-CD and (b) BN-CD.

Table 4.2.8. Single-particle photoluminescence behaviors of N-CD and BN-CD[a]

Sample	Bleaching (%)		
	One-step	Two-step	Three-step
N-CD	87.8[a]	11.6	0.6
BN-CD	85.4	13.3	1.3

[a]The percentages were calculated from 311 of N-CD and 225 of BN-CD measured individually

Table 4.2.9. Single-particle photoluminescence behaviours with single- and multi-steps of N-CD and BN-CD

Sample	Photobleaching	Time (s)		
		τ_1	τ_2	τ_3
N-CD	1-step	993 ± 397	-	-
	2-step	812 ± 317	1167 ± 353	-
	Multi-step	564 ± 163	762 ± 240	990 ± 320
	τ_{avg}	789 ± 292	964 ± 296	990 ± 320
			818 ± 292	
BN-CD	1-step	1138 ± 400	-	-
	2-step	1018 ± 286	1419 ± 277	-
	Multi-step	832 ± 112	1094 ± 53	1362 ± 189
	τ_{avg}	996 ± 266	1389 ± 281	1362 ± 189
			1053 ± 266	

4.2.5. Conclusion

In summary, we developed a one-step synthesis of BN-CD with superior optical properties via the microwave pyrolysis of simple molecular precursors. BN-CD was characterized by various characterization techniques, including UV/vis, PL, HR-TEM, FT-IR, EA and XPS. All methods conclusively supported the model of a graphitic core structure with more uniform surface states and fewer surface traps in BN-CD, accounting for the observed PL enhancement of BN-CD over that of N-CD. Time-resolved ultrafast spectroscopy and DFT calculations further supported the CD structure involving heteroatom-tailored carbon networks. Furthermore, the single-molecule spectroscopy analysis indicated that high PL of BN-CD originates from the increased number of emitted photons per particle, compared to N-CD. We anticipate that this study will aid in uncovering the full potential of CDs as novel fluorophores for challenging bioimaging applications and optoelectronic devices in the future.

4.2.6. References

1. Georgakilas, V.; Perman, J. A.; Tucek, J.; Zboril, R. Broad Family of Carbon Nanoallotropes: Classification, Chemistry, and Applications of Fullerenes, Carbon Dots, Nanotubes, Graphene, Nanodiamonds, and Combined Superstructures. *Chem. Rev.* **2015,** *115*, 4744-4822.
2. Baker, S. N.; Baker, G. A. Luminescent Carbon Nanodots: Emergent Nanolights. *Angew. Chem. Int. Ed.* **2010,** *49*, 6726-6744.
3. Li, X. M.; Rui, M. C.; Song, J. Z.; Shen, Z. H.; Zeng, H. B. Carbon and Graphene Quantum Dots for Optoelectronic and Energy Devices: A Review. *Adv. Funct. Mater.* **2015,** *25*, 4929-4947.
4. Luo, P. J. G.; Yang, F.; Yang, S. T.; Sonkar, S. K.; Yang, L. J.; Broglie, J. J.; Liu, Y.; Sun, Y. P. Carbon-based Quantum Dots for Fluorescence Imaging of Cells and Tissues. *RSC Adv.* **2014,** *4*, 10791-10807.
5. Song, Y. B.; Zhu, S. J.; Yang, B. Bioimaging based on Fluorescent Carbon Dots. *RSC Adv.* **2014,** *4*, 27184-27200.
6. Zhu, S. J.; Meng, Q. N.; Wang, L.; Zhang, J. H.; Song, Y. B.; Jin, H.; Zhang, K.; Sun, H. C.; Wang, H. Y.; Yang, B. Highly Photoluminescent Carbon Dots for Multicolor Patterning, Sensors, and Bioimaging. *Angew. Chem. Int. Ed.* **2013,** *52*, 3953-3957.
7. Choi, Y.; Kim, S.; Choi, M. H.; Ryoo, S. R.; Park, J.; Min, D. H.; Kim, B. S. Highly Biocompatible Carbon Nanodots for Simultaneous Bioimaging and Targeted Photodynamic Therapy In Vitro and In Vivo. *Adv. Funct. Mater.* **2014,** *24*, 5781-5789.
8. Choi, Y.; Ryu, G. H.; Min, S. H.; Lee, B. R.; Song, M. H.; Lee, Z.; Kim, B. S. Interface-Controlled Synthesis of Heterodimeric Silver-Carbon Nanoparticles Derived from Polysaccharides. *ACS Nano* **2014,** *8*, 11377-11385.
9. Li, H. T.; He, X. D.; Kang, Z. H.; Huang, H.; Liu, Y.; Liu, J. L.; Lian, S. Y.; Tsang, C. H. A.; Yang, X. B.; Lee, S. T. Water-Soluble Fluorescent Carbon Quantum Dots and Photocatalyst Design. *Angew. Chem. Int. Ed.* **2010,** *49*, 4430-4434.
10. Wang, Y.; Kalytchuk, S.; Zhang, Y.; Shi, H. C.; Kershaw, S. V.; Rogach, A. L. Thickness-Dependent Full-Color Emission Tunability in a Flexible Carbon Dot Ionogel. *J. Phys. Chem. Lett.* **2014,** *5*, 1412-1420.
11. Wang, L.; Zhu, S. J.; Wang, H. Y.; Qu, S. N.; Zhang, Y. L.; Zhang, J. H.; Chen, Q. D.; Xu, H. L.; Han, W.; Yang, B.; Sun, H. B. Common Origin of Green Luminescence in Carbon Nanodots and Graphene Quantum Dots. *ACS Nano* **2014,** *8*, 2541-2547.
12. Sun, Y. P.; Zhou, B.; Lin, Y.; Wang, W.; Fernando, K. A. S.; Pathak, P.; Meziani, M. J.; Harruff, B. A.; Wang, X.; Wang, H. F.; Luo, P. J. G.; Yang, H.; Kose, M. E.; Chen, B. L.; Veca, L. M.; Xie, S. Y. Quantum-Sized Carbon Dots for Bright and Colorful

Photoluminescence. *J. Am. Chem. Soc.* **2006,** *128*, 7756-7757.

13. Paraknowitsch, J. P.; Thomas, A. Doping Carbons beyond Nitrogen: An Overview of Advanced Heteroatom doped Carbons with Boron, Sulphur and Phosphorus for Energy Applications. *Energy Environ. Sci.* **2013,** *6*, 2839-2855.
14. Zhang, C. H.; Fu, L.; Liu, N.; Liu, M. H.; Wang, Y. Y.; Liu, Z. F. Synthesis of Nitrogen-Doped Graphene Using Embedded Carbon and Nitrogen Sources. *Adv. Mater.* **2011,** *23*, 1020-1024.
15. Gong, K. P.; Du, F.; Xia, Z. H.; Durstock, M.; Dai, L. Nitrogen-Doped Carbon Nanotube Arrays with High Electrocatalytic Activity for Oxygen Reduction. *Science* **2009,** *323*, 760-764.
16. Li, Y.; Zhao, Y.; Cheng, H. H.; Hu, Y.; Shi, G. Q.; Dai, L.; Qu, L. T. Nitrogen-Doped Graphene Quantum Dots with Oxygen-Rich Functional Groups. *J. Am. Chem. Soc.* **2012,** *134*, 15-18.
17. Wang, S. Y.; Zhang, L. P.; Xia, Z. H.; Roy, A.; Chang, D. W.; Baek, J. B.; Dai, L. BCN Graphene as Efficient Metal-Free Electrocatalyst for the Oxygen Reduction Reaction. *Angew. Chem. Int. Ed.* **2012,** *51*, 4209-4212.
18. Wang, X. W.; Sun, G. Z.; Routh, P.; Kim, D. H.; Huang, W.; Chen, P. Heteroatom-doped Graphene Materials: Syntheses, Properties and Applications. *Chem. Soc. Rev.* **2014,** *43*, 7067-7098.
19. Dong, Y. Q.; Pang, H. C.; Yang, H. B.; Guo, C. X.; Shao, J. W.; Chi, Y. W.; Li, C. M.; Yu, T. Carbon-Based Dots Co-doped with Nitrogen and Sulfur for High Quantum Yield and Excitation-Independent Emission. *Angew. Chem. Int. Ed.* **2013,** *52*, 7800-7804.
20. Das, S. K.; Liu, Y. Y.; Yeom, S.; Kim, D. Y.; Richards, C. I. Single-Particle Fluorescence Intensity Fluctuations of Carbon Nanodots. *Nano Lett.* **2014,** *14*, 620-625.
21. Choi, C. H.; Park, S. H.; Woo, S. I. Binary and Ternary Doping of Nitrogen, Boron, and Phosphorus into Carbon for Enhancing Electrochemical Oxygen Reduction Activity. *ACS Nano* **2012,** *6*, 7084-7091.
22. Wu, Z. S.; Winter, A.; Chen, L.; Sun, Y.; Turchanin, A.; Feng, X. L.; Mullen, K. Three-Dimensional Nitrogen and Boron Co-Doped Graphene for High-Performance All-Solid-State Supercapacitors. *Adv. Mater.* **2012,** *24*, 5130-5135.
23. Iyyamperumal, E.; Wang, S. Y.; Dai, L. Vertically Aligned BCN Nanotubes with High Capacitance. *ACS Nano* **2012,** *6*, 5259-5265.
24. Wen, J. F.; Zhang, Y.; Tang, N. J.; Wan, X. G.; Xiong, Z. H.; Zhong, W.; Wang, Z. L.; Wu, X. L.; Du, Y. W. Synthesis, Photoluminescence, and Magnetic Properties of Nitrogen-Doping Helical Carbon Nanotubes. *J. Phys. Chem. C* **2011,** *115*, 12329-12334.
25. Chiou, J. W.; Ray, S. C.; Peng, S. I.; Chuang, C. H.; Wang, B. Y.; Tsai, H. M.; Pao, C. W.; Lin, H. J.; Shao, Y. C.; Wang, Y. F.; Chen, S. C.; Pong, W. F.; Yeh, Y. C.; Chen, C. W.;

Chen, L. C.; Chen, K. H.; Tsai, M. H.; Kumar, A.; Ganguly, A.; Papakonstantinou, P.; Yamane, H.; Kosugi, N.; Regier, T.; Liu, L.; Sham, T. K. Nitrogen-Functionalized Graphene Nanoflakes (GNFs:N): Tunable Photoluminescence and Electronic Structures. *J. Phys. Chem. C* **2012,** *116*, 16251-16258.

26. Wen, X. M.; Yu, P.; Toh, Y. R.; Hao, X. T.; Tang, J. Intrinsic and Extrinsic Fluorescence in Carbon Nanodots: Ultrafast Time-Resolved Fluorescence and Carrier Dynamics. *Adv. Opt. Mater.* **2013,** *1*, 173-178.
27. Turro, N. J., *Modern Molecular Photochemistry*; University Science Books: Mill Valley, CA, 1991; p 628.
28. Kaniyankandy, S.; Achary, S. N.; Rawalekar, S.; Ghosh, H. N. Ultrafast Relaxation Dynamics in Graphene Oxide: Evidence of Electron Trapping. *J. Phys. Chem. C* **2011,** *115*, 19110-19116.
29. Das, S. K.; Luk, C. M.; Martin, W. E.; Tang, L. B.; Kim, D. Y.; Lau, S. P.; Richards, C. I. Size and Dopant Dependent Single Particle Fluorescence Properties of Graphene Quantum Dots. *J. Phys. Chem. C* **2015,** *119*, 17988-17994.

Charter 4.3. Shape-Tunable Solvatochromic Hybrid Carbon Nanosheets

4.3.1. Introduction

Photoluminescent carbon nanomaterials have attracted considerable interest due to their unique optical properties and photostability useful for optoelectronic devices, biological labels, and sensors.[1,2] To date, different mechanistic frameworks have been proposed to elucidate of the origin of the photoluminescence (PL) depending on their crystal structure, dimension, and chemical functionalization.[3-5] In many cases, however, the PL emission of such carbon nanomaterials have been broad, mostly with a blue emission with a relatively low quantum yield (QY), which potentially limits their broader implications.[6] To address these critical challenges, there have been active researches to tune their PL behaviors, including synthetic control by using various precursors, surface passivation, heteroatom doping, reduction and post-synthetic approach like separation.[7-10]

Besides the aforementioned synthetic approaches, external stimuli such as solvent polarity can also tune the PL spectra of fluorophores, which is called solvatochromism. Depending on the solvent polarity, the position of the absorbance and PL spectra can be changed that is often found in organic dyes.[11-13] Recently, carbon nanomaterials such as carbon nanotube, graphene oxide (GO), and carbon dot (CD) have also exhibited the shifts of emission wavelength on account of the preferential interaction with solvent molecules or the presence of different surface trap states with varying solvent polarity.[14,15] Despite significant progress in the development of efficient solvent-dependent PL in carbon nanomaterials, the emission has been still limited from blue to green under UV irradiation.[16,17]

For a wider emission range of carbon nanomaterials in different polarity, new types of hybrid carbon nanostructures that combine the advantageous features of each are proposed. In particular, GO, an oxidized analogue of graphene has been suggested for the modulation of carbon molecular configuration because of their surface functional groups together with its high specific surface area.[18] For example, GO can change the spherical morphology of carbonized glucose to a two-dimensional (2D) structure in hydrothermal carbonization.[19] Other large surface area of carbon nanomaterials such as carbon black, carbon nanotubes, and reduced GO are inadequate as a template due to lack of hydrophilic properties which limit the solubility of molecular precursors of carbon precursors.[20]

Herein, we propose a unique design of carbon nanoring clusters on the surface of GO nanosheet to synthesize the solvatochromic hybrid carbon nanosheet (CNS). This hybrid CNS is

synthesized through the hydrothermal reaction of small molecular precursors in the presence of GO nanosheets. Unlike the typical formation of spherical CDs in the absence of GO template, the carbon precursors turned into carbon nanorings with a concentric center through the aid of GO template during the carbonization. To our surprise, the prepared CNS displayed a highly tunable emission covering entire visible ranges with respect to the solvents, which is the first example of this kind. A detailed mechanistic framework was carefully developed by using a series of spectroscopic analyses, including PL, FT-IR, and X-ray photoelectron spectroscopy (XPS) coupled with time-resolved ultrafast spectroscopy. This study revealed the origin of high and tunable PL in solvents of low polarity due to the tunable shape according to polarity. In addition, different solvation relaxation between water and DMF is induced to different radiative recombination as demonstrated in time-resolved spectroscopy. Finally, depending on wide range of polar solvent, full-color emission of carbon nanomaterials have been achieved, which is first time for solvatochromic behavior in visible light.

4.3.2. Experimental

4.3.2.1. Preparation of GO

Graphite oxide (GO) was synthesized from graphite powder (Aldrich) by modified Hummers method and exfoliated to give a brown dispersion of graphene oxide under ultrasonication.

4.3.2.2. Synthesis of CNS

Citric acid, ethylenediamine (99%, EDA), and boric acid was purchased from Sigma-Aldrich. CNS was synthesized by hydrothermal reaction at 180 ^{o}C for 6hr. To prepare CNS, 96 mg of citric acid, 31 mg of boric acid, 34.7 μl of EDA was added to10 ml of 0.5 mg/ml GO. After stirring for 10 min, the aggregated black solution was placed into Teflon-lined, stainless steel autoclave. The dark brown solution (supernatant) and black powder (precipitate) was produced after carbonization. Precipitate was washed with ethanol and chloroform for 5 times, then the solvent of final supernatant was evaporated. Finally, this powder was stocked in 10 ml of ethanol.

4.3.2.3. Characterizations

UV/vis spectrophotometer (UV-2550, Shimadzu) was used to analyze the absorbance of CNS. Photoluminescence (PL) emission was measured on a Varian Cary 5000 spectrophotometer. The structure of the CNS was analyzed by XPS (K-alpha, Thermo Fisher) and FT-IR (Varian, Cray 660). The morphology and size of CNS were measured using transmission electron

microscopy (TEM, JEOL JEM-2100, accelerating voltage of 200 kV). Time-resolved emission spectroscopy were measured using a time-correlated single-photon counting spectrometer (Fluotime 300, Pico Quant).

4.3.3. Results and discussion

4.3.3.1. Synthesis of CNS

CNS was prepared by the hydrothermal decomposition of small organic molecules such as citric acid, boric acid, and ethylenediamine in the presence of GO nanosheet. The composition of the simple organic molecules in the production of CNS has been followed our previous approach in the synthesis of highly photoluminescent CDs with dual heteroatom doping. With the assistance of the graphitic framework of GO nanosheet, the hydrothermal decomposition preferentially occurred on the surface of GO nanosheets. Other carbonaceous residues were successfully removed through the extensive rinsing and precipitation steps using a mixture of chloroform and ethanol to yield nanosheets of yellow emission. The final supernatant recovered was dissolved in different solvents of varying polarity to produce the CNS. As representative solvents, we choose water, ethanol, and DMF and they are denoted as a CNS-Water, CNS-Ethanol, and CNS-DMF, respectively (Figure 4.3.1a). Due to solvent polarity, the morphologies of CNS can be tunable, resulting in the different PL properties in various solvents.

4.3.3.2. Solvatochromic behavior of CNS

CNS was initially prepared by the hydrothermal decomposition of small organic molecules such as citric acid, boric acid, and ethylenediamine in the presence of GO nanosheet (see Experimental for details). The composition of the simple organic molecules in the production of CNS was based on our previous approach in the synthesis of highly photoluminescent boron- and nitrogen-doped CDs both in solution and bulk powder. With the assistance of the graphitic framework of GO nanosheet, the hydrothermal decomposition preferentially occurred on the surface of GO nanosheets. Other carbonaceous residues were successfully removed through the extensive rinsing and precipitation steps using a mixture of chloroform and ethanol to yield CNS of yellow emission. The final supernatant recovered was dissolved in different solvents of varying polarity to produce the CNS. As representative solvents with varying polarity, we chose water, ethanol, and DMF, denoted as a CNS-Water, CNS-Ethanol, and CNS-DMF, respectively (**Figure 1a**).

To observe the unique optical properties of CNS, UV/Vis and PL spectra were observed in the representative solvents. When CNS was dissolved in water, two absorption peaks were

displayed at 230 and 310 nm in UV/vis spectroscopy, indicating π- π^* and n-π^* transitions, respectively (Figure 4.3.1b, 4.3.1c and 4.3.1d). Unlike many other carbon nanomaterials reported, an additional peak approximately at 464 nm was observed in CNS. Moreover, CNS-Water showed another tail at 620 nm, which was related with the abundant oxygen groups.

PL spectra exhibited the changes of emission wavelength according to the solvent polarity. When CNS was dissolved in solvents of different polarity, including water, ethanol, and DMF, the emission color was tuned dynamically from blue to pink to yellow-green under UV irradiation. In specific, emission at 430 nm under 360 nm excitation was found in all solvents; however, CNS-Ethanol and CNS-DMF displayed additional PL emission at 573 and 548 nm, respectively, with considerably increased PL intensity. This phenomena induced that 20.2% of QY in DMF was increased approximately twice compared to that in 8.9% of water under excitation at 480 nm (Table 4.3.1). Furthermore, the peak shift in PL spectrum was observed from red in water to green in DMF. These results clearly indicate that CNS has a highly tunable emission wavelength and intensity by solvent polarity. Furthermore, it is of note that the emission peak position was highly dependent on the excitation in water due to additional energy levels as observed from a shoulder peak in UV/Vis spectrum near 620 nm, whereas the emission peak remained almost constant in both ethanol and DMF (Figure 4.3.2).

We then further examined this interesting solvent-dependent optical property of CNS by dissolving them in a water/DMF mixture with different ratio (Figure 4.3.3). Under excitation at 360 nm, the maximum emission shifted gradually from 430 nm in water to dual peaks at 430 and 538 nm in water/DMF (1:1 mixture) and to 548 nm in pure DMF. In addition, the emission intensity was significantly enhanced upon increasing the ratio of DMF to water as observed in pure solvents (Figure 4.3.3).

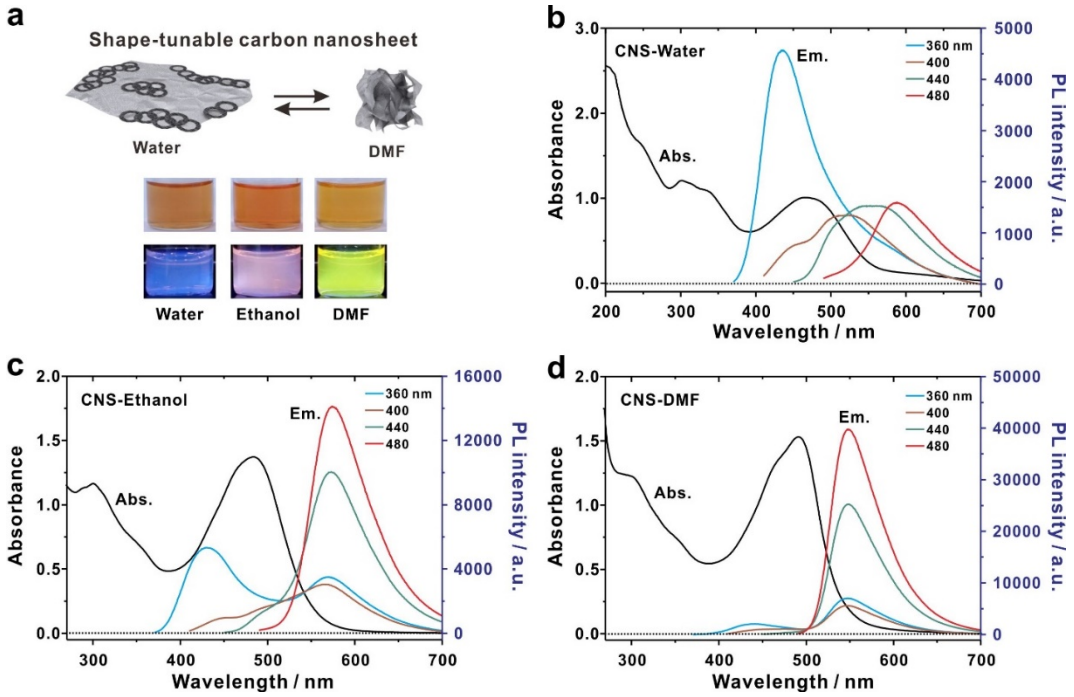

Figure 4.3.1. (a) Schematic representation and optical properties of CNS-Water, CNS-Ethanol, CNS-DMF. The suspension (conc. 0.10 mg/mL) (top) under room light and (bottom) UV illumination at 365 nm. (b-d) UV/Vis and PL spectra of (b) CNS-Water, (c) CNS-Ethanol, and (d) CNS-DMF. PL spectra of CNS under varying excitation wavelengths from 360 to 480 nm with 40-nm increments.

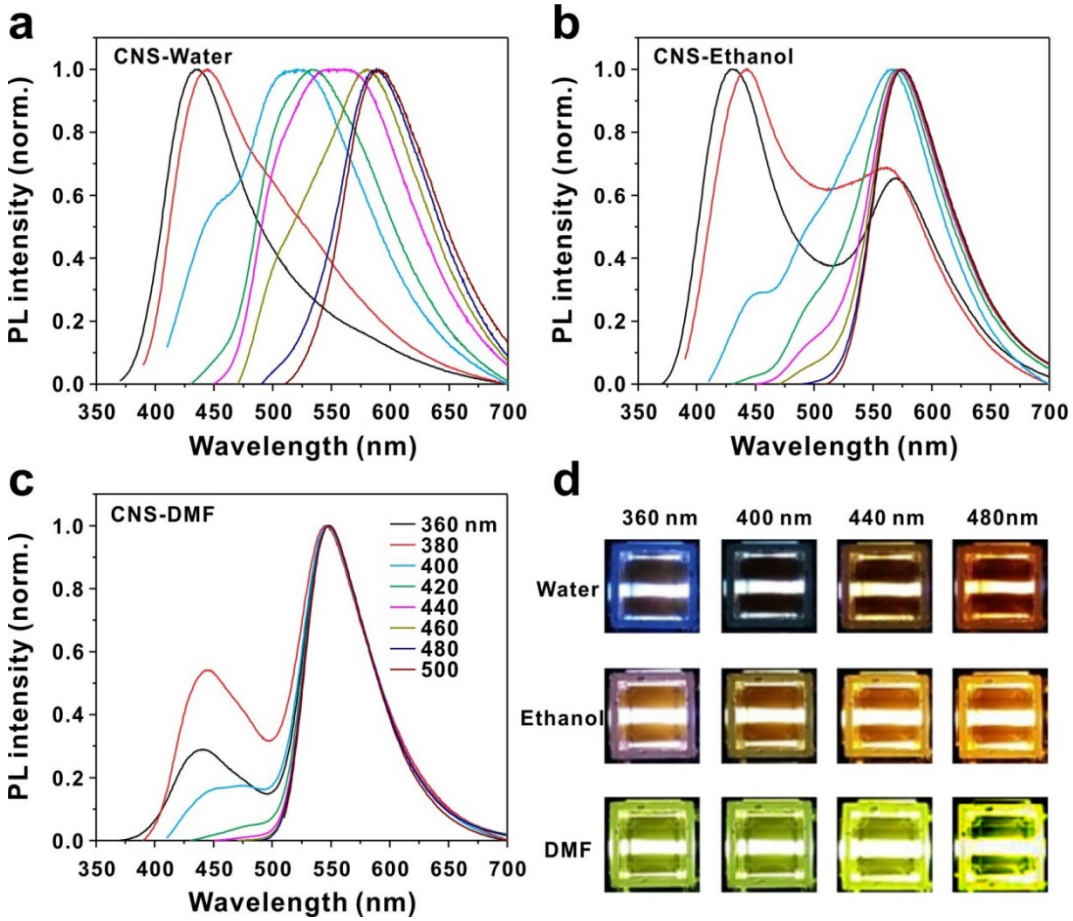

Figure 4.3.2. Normalized PL spectra of (a) CNS-Water, (b) CNS-Ethanol, and (c) CNS-DMF.

Table 4.3.1. Quantum yield (%) of CNS in water, ethanol, and DMF.

Excitation wavelength	Water	Ethanol	DMF
360 nm[a]	23.12	18.03	14.29
480 nm[b]	8.92	16.68	20.23

[a]Reference used was quinine sulfate (QY = 54% in 0.10 M H_2SO_4)

[b]Reference used was rhodamine 6G (QY = 95% in ethanol)

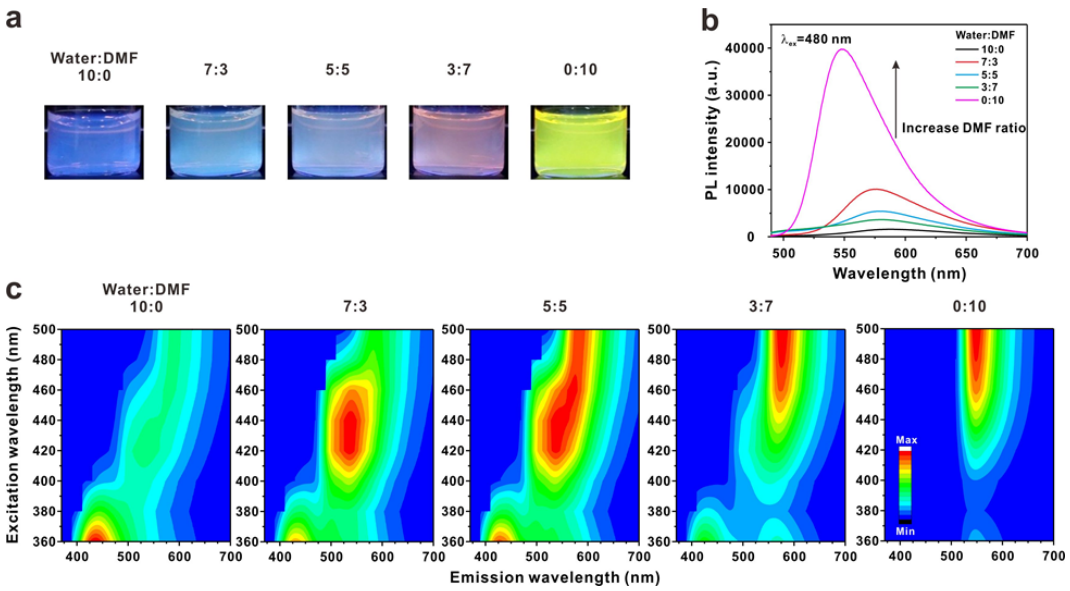

Figure 4.3.3. (a) Optical images, (b) PL spectra at 480 nm excitation , and (c) 2D PL spectra of CNS in a different ratio of water and DMF mixture such as 10:0, 7:3, 5:5, 3:7, and 0:10.

4.3.3.3. Morphologies and structure of CNS

Transmission electron microscopy (TEM) showed the graphene sheets-like structure with occasional appearance of nanorings of 15 nm in diameter on the surface of dried sample of CNS-Water (Figure 4.3.4a). The crystalline carbon nanorings had an interlayer spacing of 0.34 nm, corresponding to the (002) interplanar spacing of graphene in high-resolution TEM image as similarly found other literature (Figure 4.3.4b).[21] These nanorings were postulated to originate from the carbonization of molecular precursors on graphene sheets during hydrothermal reaction. In a stark contrast, we found the CNS-DMF existed in folded and crumpled nanostructures having an average diameter of 106.1 ± 11.8 nm, suggesting their structural tunability between different solvents (Figure 4.3.4c and 4.3.4d). The suspension in DMF was very stable more than several months without any noticeable aggregates. In accordance with this observation, dynamic light scattering (DLS) suggested the presence of folded morphology in DMF with an average hydrodynamic diameter of 212.2 ± 5.4 nm. Although the size was slightly different due to the evaporation of solvent for TEM preparation, homogeneous sized CNS was observed.

To account for the origin of shape-tunable properties of CNS in different solvents, hydrothermal reaction of the small molecular precursors in the absence of GO nanosheet was prepared as a control. The prepared carbon nanoparticles were existed in 20 nm of carbon nanoring-like morphology and displayed a constant blue emission at 430 nm irrespective of the solvent polarity (Figure 4.3.5). Unlike the CNS, this carbon nanoring did not disperse well in less polar solvents such as ethanol or DMF. From these results, we suggest that graphitic carbon nanorings were grown onto graphene nanosheets during carbonization process, resulting in the transformation of a 2D sheet into 3D crumpled morphology from water to DMF due to low solubility of nanoring in less polar solvent. Furthermore, good solubility of GO in various polar solvents as previously reported also contribute to develop the stable and shape-tunable CNS in less polar solvents. This features that different solubility of GO and carbon nanoring plays an important role in inducing the formation of shape-tunable solvatochromic CNS.

To investigate the chemical composition of CNS, FT-IR and X-ray photoelectron spectroscopy (XPS) were performed. In FT-IR spectrum, CNS-Water possessed oxygen functional groups such as 1052 cm^{-1} (C-O stretching), 1677 cm^{-1} (COOH), and a broad peak at approximately 3222 cm^{-1} (O-H and N-H stretching) (Figure 4.3.6). In accordance with FT-IR results, the deconvoluted high-resolution C1s spectrum of CNS-Water displayed high contents of oxygen groups (~22%) such as hydroxyl, carbonyl, and carboxylic groups (Figure 4.3.7). In contrast, upon switching to DMF, the amount of oxygen-related groups was significantly reduced to approximately 5.0% (Table 4.3.2). In addition, the fraction of sp^2-and sp^3-domains in C1s portion was altered from 1.14 to 0.28 upon solvent change from water to DMF. These data also

demonstrated the solvent induced morphological changes, thus eventually leading to changes in the surface energy states of CNS that are responsible for the solvatochromic behavior.

4.3.3.4. Photophysics properties of CNS

As described in PL spectrum, CNS has common emission peak in 430 nm excited at 360 nm, which was associated with core π-conjugated domains of carbon nanorings or graphene nanosheets. However, as different solvent polarity, the emission peak was significantly changed in longer excitation wavelength. To demonstrate different relaxation dynamics of CNS in water and DMF, we performed time-resolved spectroscopy excited at 450 and 510 nm (Figure 4.3.8 and Figure 4.3.9). In time-resolved emission spectrum (TRES), CNS-Water had dual emission wavelengths in 545 and 590 nm, but CNS-DMF exhibited only 545 nm of peak under excitation at 510 nm (Figure 4.3.10). In addition, CNS-Water and CNS-DMF clearly showed different lifetime -decay behaviors in terms of emission wavelength. CNS-Water exhibited fast decay with the increased emission wavelength, suggesting multi-level energy states, whereas CNS-DMF showed no dependence (Figure 4.3.8a and 4.3.8b).

When tri-exponential lifetime was extracted, major lifetime component was significantly different between CNS-Water and CNS-DMF (Table 4.3.3). The origin of τ_1 in both CNS-Water and CNS-DMF was related with oxygen group-related trap states, which confirmed the broad emission at 590 nm and 43% of fraction in CNS-Water in TRES (Figure 4.3.11). Furthermore, due to the abundant oxygen groups in CNS-Water, the fraction of τ_1 was increased in the increased emission wavelength excited at 510 nm. The second fraction, τ_2, was associated with surface state. Different lifetimes between 2.81 ns (CNS-Water) and 5.21 ns (CNS-DMF) were associated with the solvatochromic energy level shifts with respect to polarity. It is generally known that the energy level is changed with polarity due to different solvent relaxation time and DMF has a faster solvation time than water. Moreover, the third fraction, τ_3, of (8 ns component) was attributed to the structural defect states in CNS. Thus, the different solvent relaxation led to different energy levels. Furthermore, shape-tunable nature of solvatochromic CNS can cause distinction of trap and surface states, resulting in different emission upon switching the solvent polarity (Figure 4.3.8c).

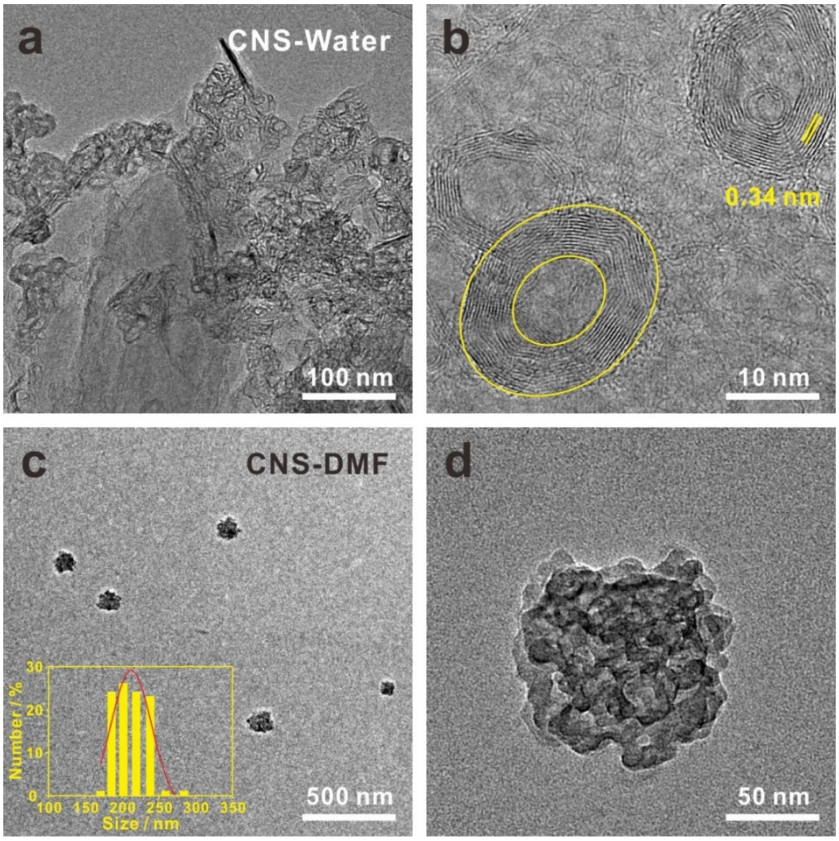

Figure 4.3.4. TEM images of (a, b) CNS-Water and (c, d) CNS-DMF. Note the samples were collected after drying off each solvent. Inset in (c) shows the size distribution histogram measured by dynamic light scattering of CNS-DMF suspension.

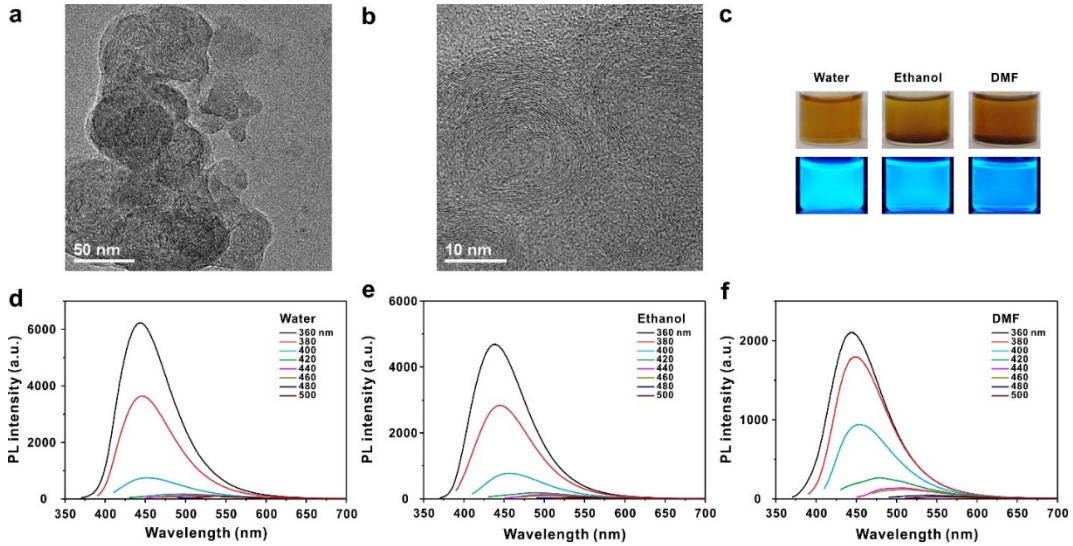

Figure 4.3.5. (a,b) TEM images and (c) optical images of carbon nanorings synthesized from small molecules in the absence of graphene oxide nanosheet. (d-e) PL spectra in (d) water, (e) ethanol, and (f) DMF. After hydrothermal reaction, carbon nanorings were prepared.

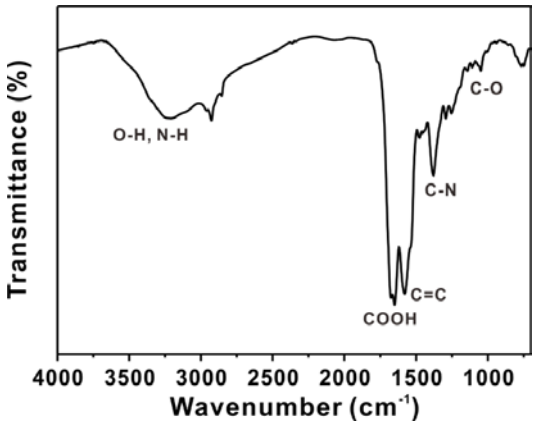

Figure 4.3.6. FT-IR spectra of CNS-Water.

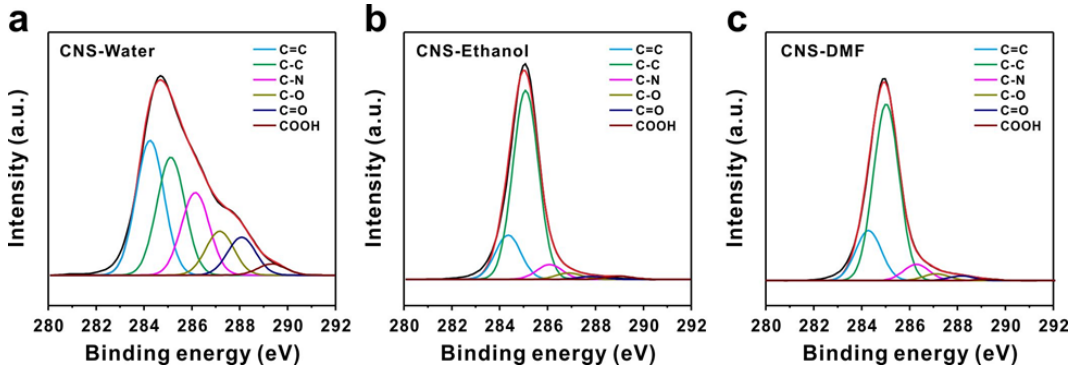

Figure 4.3.7. Deconvoluted high-resolution XPS spectra of (a) CNS-Water, (b) CNS-ethanol, and (c) CNS-DMF.

Table 4.3.2. Chemical compositions of CNS-Water and CNS-DMF determined by XPS.

	CNS-Water		CNS-DMF	
Carbon C 1s	**Position (eV)**	**%**	**Position (eV)**	**%**
C=C	284.25	31.44	284.28	19.56
C-C	285.12	27.54	285.02	69.03
C-N	286.14	19.28	286.28	6.39
C-O	287.16	10.23	287.12	2.64
C=O	288.07	8.85	288.16	1.82
COOH	289.34	2.64	289.22	0.53

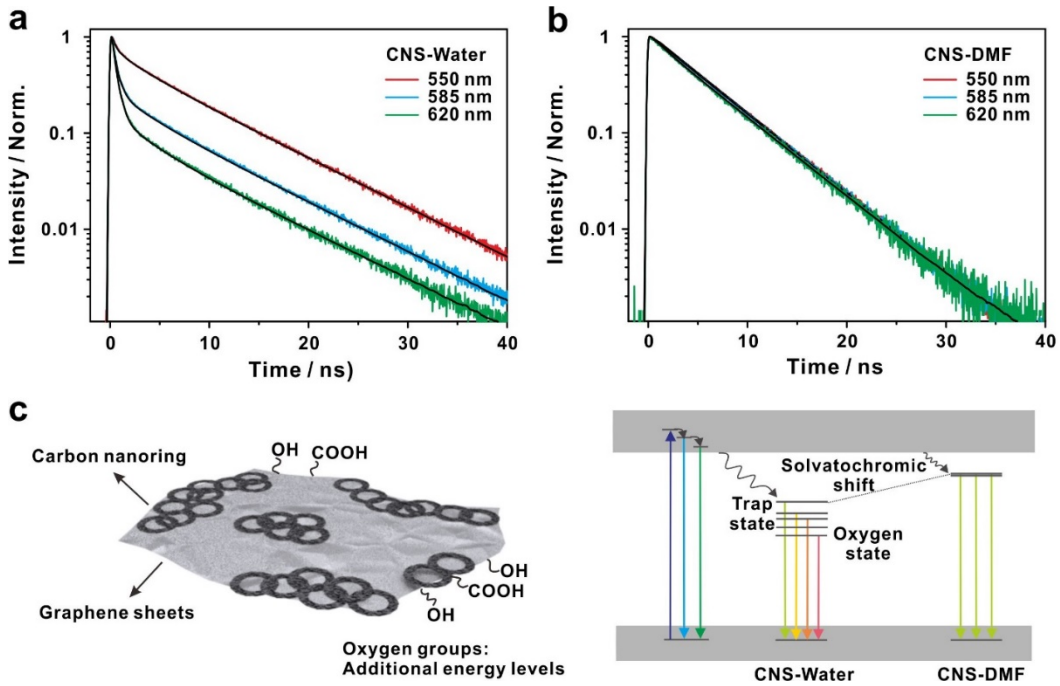

Figure 4.3.8. (a, b) Time-resolved emission spectra of CNS corrected at 550, 585, and 620 nm in different solvents under excitation at 510 nm. (a) CNS-Water and (b) CNS-DMF. (c) Schematic structure and energy level diagrams of CNS.

Table 4.3.3. Fitting parameter for excited-state lifetime (τ) of CNS-Water and CNS-DMF[a]

λ_{ex} (nm)	Sample	λ_{em}[b] (nm)	Time (ns)			
			τ_1 (α_1)[c]	τ_2 (α_2)	τ_3 (α_3)	τ_{avg} (ns)[d]
450	CNS-Water	480	0.41 (28%)	2.74 (26%)	7.94 (46%)	4.48
		550	0.41 (26%)	2.74 (16%)	7.94 (58%)	5.15
		620	0.41 (62%)	2.74 (11%)	7.94 (27%)	2.70
	CNS-DMF	480	1.16 (39%)	5.26 (58%)	10.4 (3%)	3.81
		550	1.16 (8%)	5.26 (90%)	10.4 (2%)	5.03
		620	1.16 (21%)	5.26 (78%)	10.4 (1%)	4.45
510	CNS-Water	550	0.40 (43%)	2.81 (13%)	8.38 (44%)	4.22
		585	0.40 (82%)	2.81 (5%)	8.38 (13%)	1.56
		620	0.40 (90%)	2.81 (4%)	8.38 (3%)	0.72
	CNS-DMF	550	1.18 (2%)	5.21 (96%)	7.68 (2%)	5.18
		585	1.18 (6%)	5.21 (92%)	7.68 (2%)	5.02
		620	1.18 (15%)	5.21 (84%)	7.68 (1%)	4.63

[a] The fluorescence decay curves fitted to the multi-exponential function:

$I(t) = \sum_i^n A_i \, e^{-t/\tau_i}$.

[b] Monitored emission wavelength.

[c] Fractional amplitude.

[d] The average lifetime (τ_{avg}) obtained using the following equation: $\tau_{avg} = \sum_i^n \alpha_i \tau_i$.

Global fitting was performed for all kinetic profiles measured every 5 nm from 460 to 700 nm exciting at 450 nm and from 530 to 700 nm exciting at 510 nm, respectively.

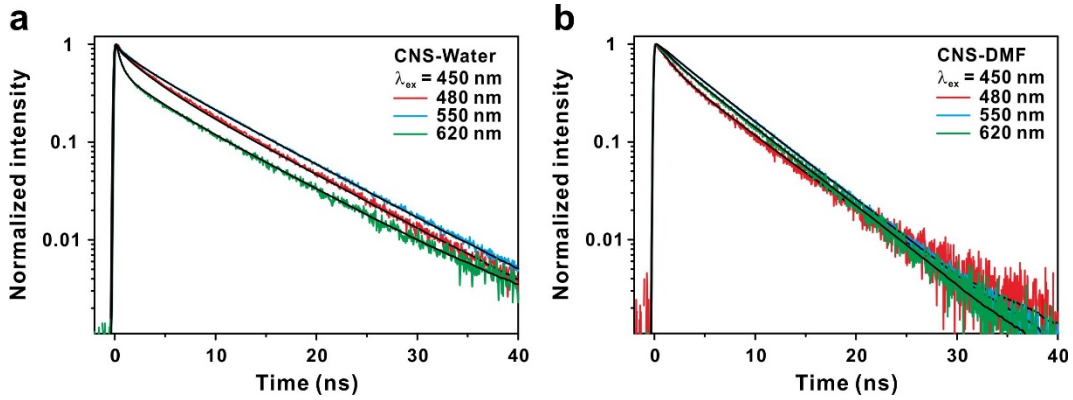

Figure 4.3.9. Normalized PL decay profiles of CNS in different solvents under excitation at 450 nm. (a) CNS-Water and (b) CNS-DMF.

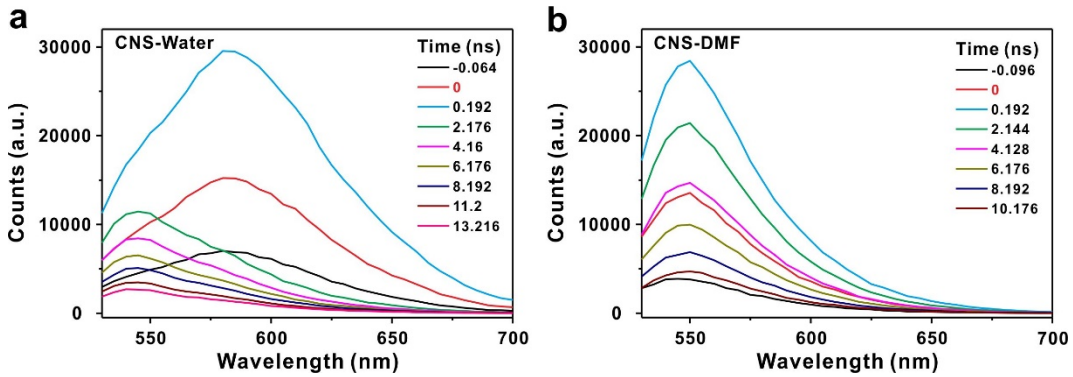

Figure 4.3.10. (a, b) TRES of CNS under excitation at 510 nm. (a) CNS-Water and (b) CNS-DMF.

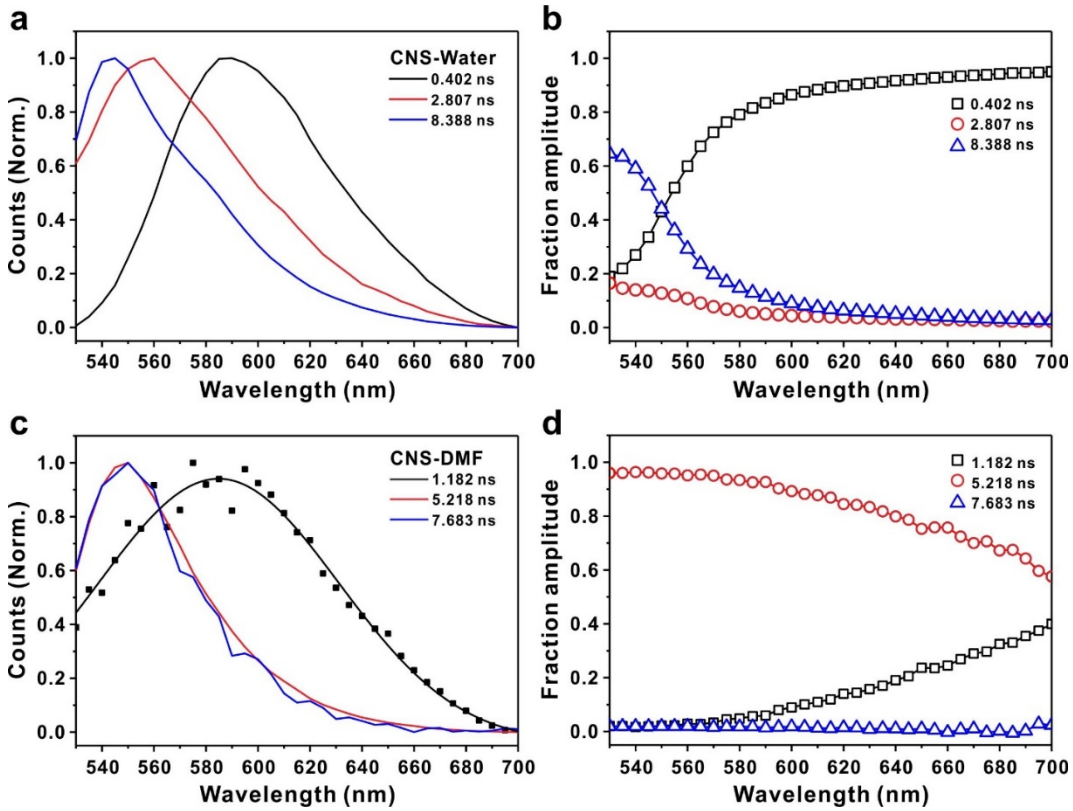

Figure 4.3.11. Time-resolved emission spectra of CNS in different solvents under excitation at 510 nm. (a, b) CNS-Water and (c,d) CNS-DMF.

4.3.3.5. Tunable emission of CNS with respect to polarity

Besides the solvents tested above, CNS exhibited the apparent solvent-dependent optical properties in a wide variety of solvents (Figure 4.3.12). Most interestingly, the PL emission under the excitation of 360 nm was highly tunable with respect to the solvent polarity (Figure 4.3.12a). Additionally, we found that the emission peak is linearly blue-shifted as a function of solvent polarity index, $E_T(30)$, in accordance with the negative solvatochromic factor (Figure 4.3.12c, 4.3.13, and 4.3.14). For instance, changing the solvent from less polar ethylene glycol (EG) to more polar DMSO, the emission peak became blue-shifted to 20 nm and the PL intensity was increased by 490% at 480 nm excitation.

CIE coordinates indicate that the PL emission of CNS is significantly influenced by solvent polarity. Various emission colors that were widely scattered in CIE coordinate were observed at 360 nm excitation according to the solvent polarity due to competitive radiative recombination between carbon nanorings and graphene sheets (Figure 4.3.12b). It is of note that among various solvents tested, the CIE coordinate of CNS dispersed in IPA (0.30, 0.33) is very close to that of white light (0.33, 0.33), implying promise to potential optoelectronic applications. Although the emission range was relatively narrow due to the dominant new energy transition with respect to the polarity in low polar solvents, the points of CIE color was dependent under visible light because of solvatochromic shifts with polarity changes (Figure 4.3.12d and 4.3.15).

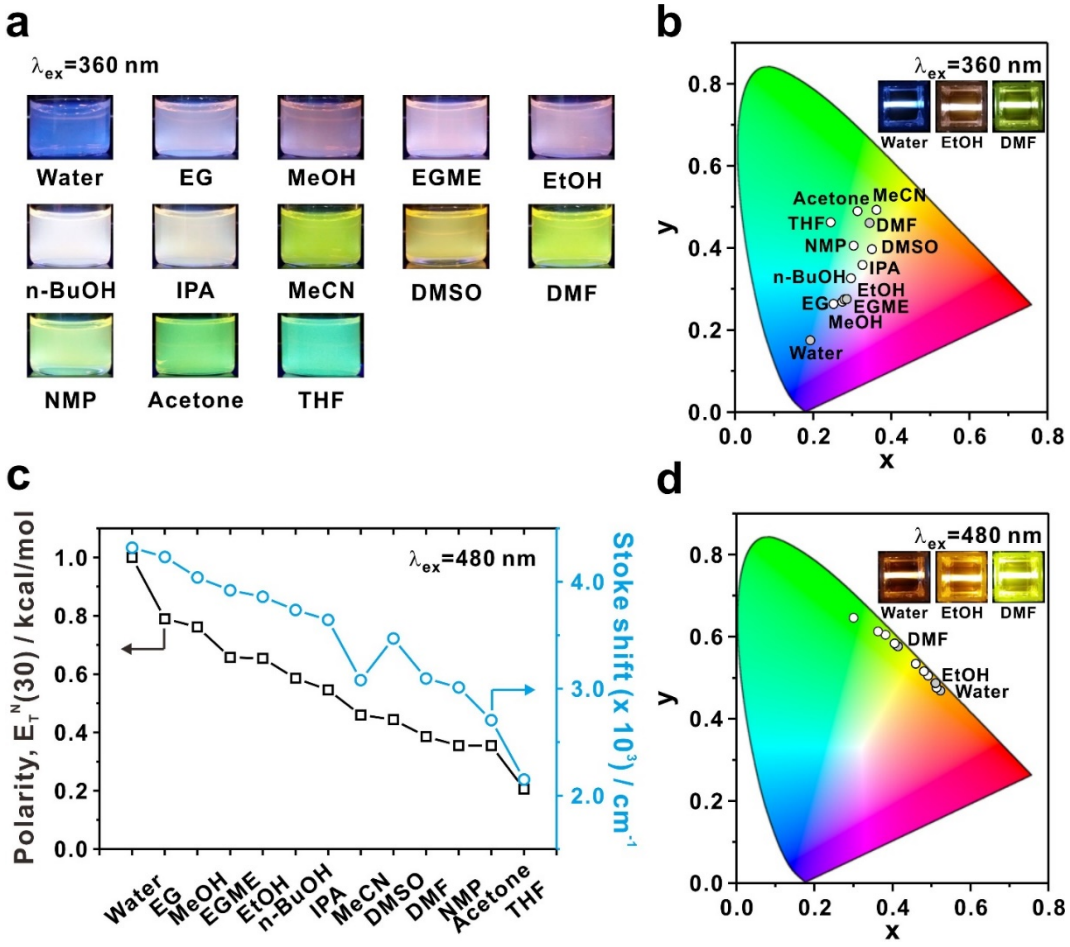

Figure 4.3.12. (a) Optical images of CNS suspension in each solvent under excitation at 360 nm. (b) Calculated CIE coordinates from the PL spectra of solvents with different polarity under excitation at 360 nm. (c) Stoke shifts at 480 nm excitation as a function of solvent polarity factor, $E_T(30)$. (d) Calculated CIE coordinates from the PL spectra of solvents with different polarity under excitation at 480 nm. EG, EGME, and MeCN is ethylene glycol, 2-methoxylethanol, and acetonitrile, respectively. Inset is the optical images excited at 360 and 480 nm.

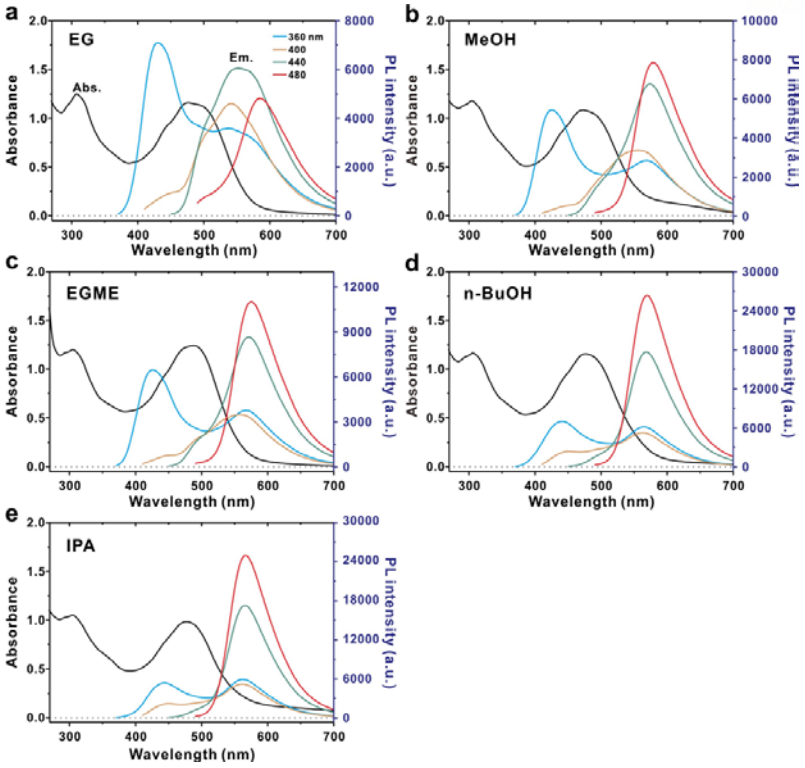

Figure 4.3.13. (a–e) UV/Vis and PL spectra of CNS in (a) ethylene glycol (EG), (b) methanol (MeOH), (c) 2-methoxyethanol (EGME), (d) *n*-butyl alcohol (*n*-BuOH), and (e) isopropyl alcohol.

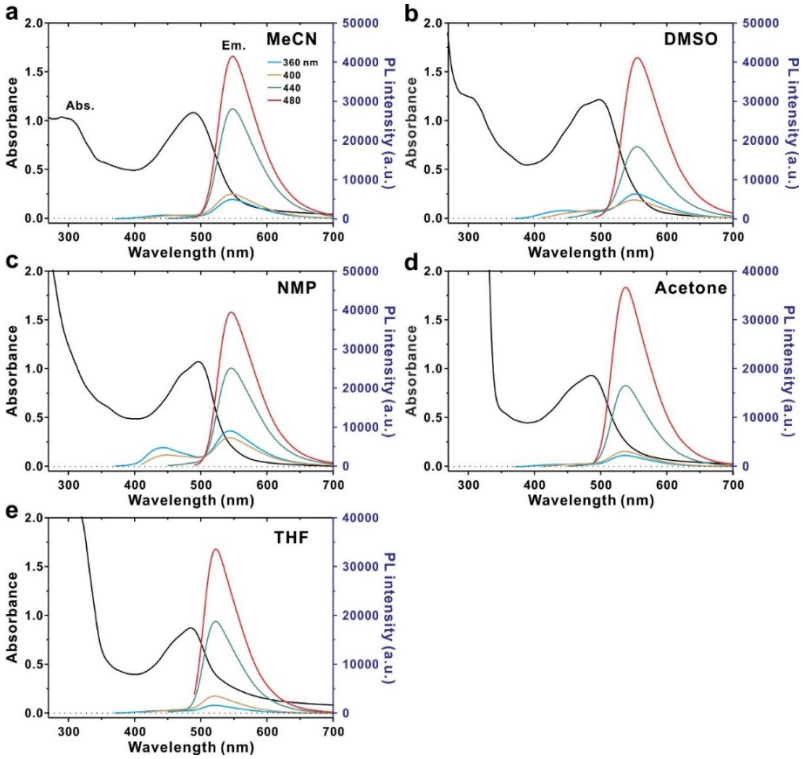

Figure 4.3.14. (a–e) UV/Vis and PL spectra of CNS in (a) acetonitrile (MeCN), (b) dimethyl sulfoxide (DMSO), (c) *N*-methyl-2-pyrrolidone (NMP), (d) acetone, and (e) THF.

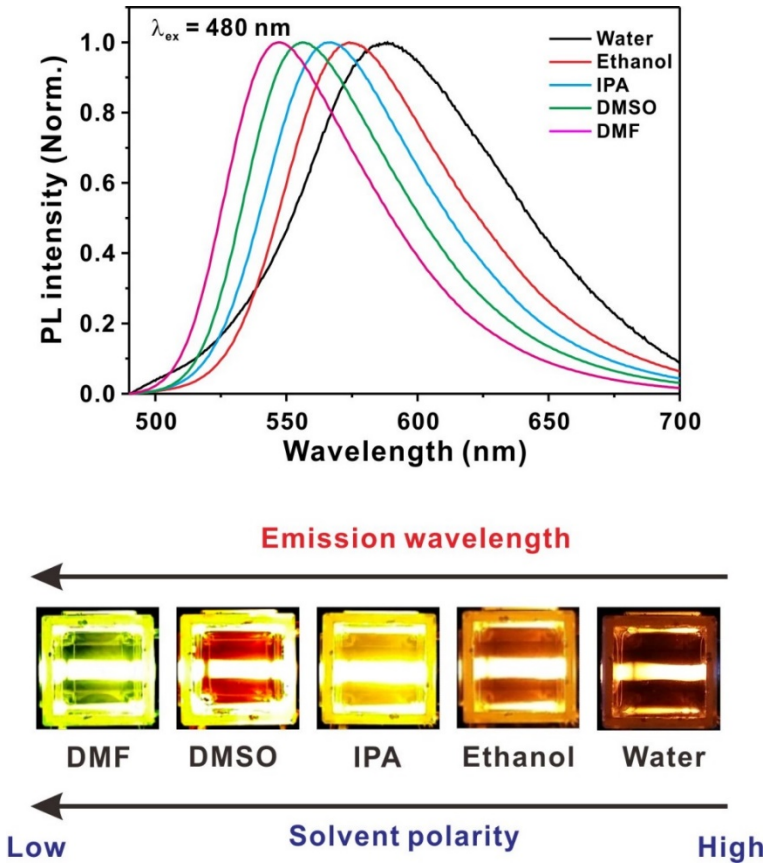

Figure 4.3.15. PL spectra and optical images of CNS in water, ethanol, IPA, DMSO, and DMF excited at 480 nm. As polarity decreased, 589 nm of emission peak in water was blue-shifted to 548 nm in DMF. According to the emission peak shifts, the PL color was also changed from red to green.

4.3.4. Conclusion

In conclusion, we developed a solvatochromic carbon nanosheets using carbonization of small molecular precursors in the presence of GO nanosheet as a template. Due to the abundant surface oxygen groups and carbon nanorings, blue emission and excitation-dependent behavior was observed in CNS-Water. However, the folded and crumpled structure of CNS-DMF was induced to excitation-independent properties and the enhanced green emission. From time-resolved spectroscopy, we demonstrated that different solvatochromic energy level shifts led to different emission according to solvent polarity. Such unique design of hybrid carbon nanostructures are envisioned to synergistically offer unique properties of carbon nanoparticles and crumpled graphene, providing diverse opportunities in tailoring the optical properties of carbon nanomaterials. We anticipate that this CNS poses promising opportunities in optoelectronic devices and sensors.

4.3.5. References

1. Cao, L.; Meziani, M. J.; Sahu, S.; Sun, Y. P. Photoluminescence Properties of Graphene versus Other Carbon Nanomaterials. *Acc. Chem. Res.* **2013,** *46*, 171-180.
2. Kozak, O.; Sudolská, M.; Pramanik, G.; Cigler, P.; Otyepka, M.; Zboril, R. Photoluminescent Carbon Nanostructures. *Chem. Mater.* **2016,** *28*, 4085–4128.
3. Liu, F.; Jang, M. H.; Ha, H. D.; Kim, J. H.; Cho, Y. H.; Seo, T. S. Facile Synthetic Method for Pristine Graphene Quantum Dots and Graphene Oxide Quantum Dots: Origin of Blue and Green Luminescence. *Adv. Mater.* **2013,** *25*, 3657-3662.
4. Chien, C. T.; Li, S. S.; Lai, W. J.; Yeh, Y. C.; Chen, H. A.; Chen, I. S.; Chen, L. C.; Chen, K. H.; Nemoto, T.; Isoda, S.; Chen, M. W.; Fujita, T.; Eda, G.; Yamaguchi, H.; Chhowalla, M.; Chen, C. W. Tunable Photoluminescence from Graphene Oxide. *Angew. Chem. Int. Ed.* **2012,** *51*, 6662-6666.
5. Sun, Y. P.; Zhou, B.; Lin, Y.; Wang, W.; Fernando, K. A. S.; Pathak, P.; Meziani, M. J.; Harruff, B. A.; Wang, X.; Wang, H. F.; Luo, P. J. G.; Yang, H.; Kose, M. E.; Chen, B. L.; Veca, L. M.; Xie, S. Y. Quantum-Sized Carbon Dots for Bright and Colorful Photoluminescence. *J. Am. Chem. Soc.* **2006,** *128*, 7756-7757.
6. Baker, S. N.; Baker, G. A. Luminescent Carbon Nanodots: Emergent Nanolights. *Angew. Chem. Int. Ed.* **2010,** *49*, 6726-6744.
7. Ding, H.; Yu, S. B.; Wei, J. S.; Xiong, H. M. Full-Color Light-Emitting Carbon Dots with a Surface-State-Controlled Luminescence Mechanism. *ACS Nano* **2016,** *10*, 484-491.
8. Hu, S.; Trinchi, A.; Atkin, P.; Cole, I. Tunable Photoluminescence across the Entire Visible Spectrum from Carbon Dots Excited by White Light. *Angew. Chem. Int. Ed*. **2015,** *54*, 2970-2974.
9. Jiang, K.; Sun, S.; Zhang, L.; Lu, Y.; Wu, A.; Cai, C.; Lin, H. Red, Green, and Blue Luminescence by Carbon Dots: Full-Color Emission Tuning and Multicolor Cellular Imaging. *Angew. Chem. Int. Ed*. **2015,** *54*, 5360-5363.
10. Tetsuka, H.; Nagoya, A.; Fukusumi, T.; Matsui, T. Molecularly Designed, Nitrogen-Functionalized Graphene Quantum Dots for Optoelectronic Devices. *Adv. Mater.* **2016,** 4632–4638
11. Lu, Z.-Z.; Zhang, R.; Li, Y.-Z.; Guo, Z.-J.; Zheng, H.-G. Solvatochromic Behavior of a Nanotubular Metal− Organic Framework for Sensing Small Molecules. *J. Am. Chem. Soc.* **2011,** *133*, 4172-4174.
12. Yan, X.; Cook, T. R.; Wang, P.; Huang, F.; Stang, P. J. Highly Emissive Platinum (II) Metallacages. *Nat. Chem.* **2015,** *7*, 342-348.
13. Lee, J.; Chang, H. T.; An, H.; Ahn, S.; Shim, J.; Kim, J.-M. A Protective Layer Approach to Solvatochromic Sensors. *Nat. Commun.* **2013,** *4*, 2641.

14. Zhu, S. J.; Zhang, J. H.; Qiao, C. Y.; Tang, S. J.; Li, Y. F.; Yuan, W. J.; Li, B.; Tian, L.; Liu, F.; Hu, R.; Gao, H. N.; Wei, H. T.; Zhang, H.; Sun, H. C.; Yang, B. Strongly Green-Photoluminescent Graphene Quantum Dots for Bioimaging Applications. *Chem. Commun.* **2011,** *47*, 6858-6860.
15. Cushing, S. K.; Li, M.; Huang, F. Q.; Wu, N. Q. Origin of Strong Excitation Wavelength Dependent Fluorescence of Graphene Oxide. *ACS Nano* **2014,** *8*, 1002-1013.
16. Chen, Y.; Zheng, M.; Xiao, Y.; Dong, H.; Zhang, H.; Zhuang, J.; Hu, H.; Lei, B.; Liu, Y. A Self-Quenching-Resistant Carbon-Dot Powder with Tunable Solid-State Fluorescence and Construction of Dual-Fluorescence Morphologies for White Light-Emission. *Adv. Mater.* **2016,** *28*, 312-318.
17. Kozák, O. e.; Datta, K. K. R.; Greplová, M.; Ranc, V. c.; Kašlík, J.; Zbořil, R. Surfactant-Derived Amphiphilic Carbon Dots with Tunable Photoluminescence. *J. Phys. Chem. C* **2013,** *117*, 24991-24996.
18. Zheng, X.; Luo, J.; Lv, W.; Wang, D. W.; Yang, Q. H. Two-Dimensional Porous Carbon: Synthesis and Ion-Transport Properties. *Adv. Mater.* **2015,** *27*, 5388-5395.
19. Krishnan, D.; Raidongia, K.; Shao, J.; Huang, J. Graphene Oxide Assisted Hydrothermal Carbonization of Carbon Hydrates. *ACS Nano* **2013,** *8*, 449-457.
20. Paredes, J.; Villar-Rodil, S.; Martínez-Alonso, A.; Tascon, J. Graphene oxide dispersions in organic solvents. *Langmuir* **2008,** *24*, 10560-10564.
21. Li, X.; Liu, Y.; Song, X.; Wang, H.; Gu, H.; Zeng, H. Intercrossed Carbon Nanorings with Pure Surface States as Low-Cost and Environment-Friendly Phosphors for White-Light-Emitting Diodes. *Angew. Chem. Int. Ed.* **2015,** *54*, 1759-1764.

Chapter 5. Summary

There are various hybrid nanomaterials based on nanocarbons; however, the development of the controlled and homogeneous structure of hybrid nanomaterials is still challenging for the high efficiency in a wide range of applications.

This thesis describes the development of hybrid nanomaterials based on nanocarbons and their applications. The uniform and controlled structure of hybrid materials can be successfully synthesized by unique approaches.

First, the abundant of oxygen groups and large surface area in nanocarbons such as graphene oxide and carbon nanoparticles provide the covalent bonding sites for metal nanoparticles, small molecules, and polymers. The chemically surface-modified nanocarbons have induced homogeneous and well-organized hybrid nanomaterials. Second, the outstanding properties of nanocarbons can be tuned by controlling the electron density and surface states by heteroatom doping. Especially, dual heteroatom doping give synergetic effect to nanocarbons, resulting in the enhanced optical properties. Third, the photoreduction properties of nanocarbons lead to heterodimeric nanoparticles without the reductant within a few minutes. Finally, by combining the advantages of each nanocarbons, shape-tunable hybrid carbon nanomaterials have been proposed. We expect that this new kinds of hybrid nanomaterials will be extended the synthetic approach to enhance the characteristics of nanocarbons.

This homogenous hybrid nanomaterials show the excellent ability and high efficiency in bio and energy applications such as bioimaging, therapy, electrocatalyst, solar cell, and light-emitting diodes. Besides these applications, we anticipate that new types of hybrid nanomaterials based on nanocarbons can be applied for a wide range of field.

List of Publications

1. **Yuri Choi,** Sunghu Kim, Youngkyu Choi, Tae-Hyuk Kwon, Oh-Hoon Kwon, Byeong-Su Kim "**Shape-Tunable Solvatochromic Hybrid Carbon Nanosheets**" **2016**, *near to submit*

2. Seongchan Kim,[1] **Yuri Choi,**[1] Ginam Park, Cheolhee Won, Byeong-Su Kim, Dal-Hee Min "**Functional siRNA Delivery and Bioimaging Based on Fluorescent Carbon Dot**" **2016,** *Submitted*

3. **Yuri Choi,** Byungkyun Kang, Jooyong Lee, Sunghu Kim, Gyeong Tae Kim, Hyunju Kang, Bo Ram Lee, Hajin Kim, Sang-Hee Shim, Geunsik Lee, Oh-Hoon Kwon, Byeong-Su Kim "**Integrative Approach toward Uncovering the Origin of Photoluminescence in Dual Heteroatom-Doped Carbon Nanodot**" *Chemistry of Materials* **2016**, *Under revision*

4. Byungkyun Kang, **Yuri Choi**, Byeong-Su Kim, Seung Youn and Geunsik Lee* "**Orbital Hybridization Mechanism for the Enhanced Photoluminescence in Edge-Functionalized sp^2 Carbon Clusters**" *Carbon* **2016**, DOI: 10.1016/j.carbon.2016.06.007

5. **Yuri Choi,** Gyeong Hee Ryu, Sa Hoon Min, Bo Ram Lee, Myoung Hoon Song, Zonghoon Lee, and Byeong-Su Kim* "**Interface Controlled Synthesis of Heterodimeric Silver–Carbon Nanoparticles Derived from Polysaccharides**" *ACS Nano* **2014**, *8*, 11377-11385

6. **Yuri Choi**,[1] Sihyuk Choi,[1] Hu Young Jeong, Meilin Liu, Byeong-Su Kim,* and Guntae Kim* "**Highly Efficient Layer-by-Layer-Assisted Infiltration for High-Performance and Cost-Effective Fabrication of Nanoelectrodes**" *ACS Applied Materials & Interfaces* **2014**, *6*, 17352-17357

7. **Yuri Choi**,[1] Seongchan Kim,[1] Myung-Ho Choi, Soo-Ryoon Ryoo, Jongnam Park, Dal-Hee Min, Byeong-Su Kim "**Highly Biocompatible Carbon Nanodots for Simultaneous Bioimaging and Targeted Photodynamic Therapy in Vitro and in Vivo**" *Advanced Functional Materials* **2014**, 24, 5781-5789

8. **Yuri Choi**, Teresa Brugarolas, Sung-Min Kang, Bum Jun Park, Byeong-Su Kim, Chang-Soo Lee, Daeyeon Lee "**Beauty of Lotus is More than Skin Deep: Highly Buoyant Superhydrophobic Films**" *ACS Applied Materials & Interfaces* **2014**, 6, 7009-7013

9. Daeun Kim, **Yuri Choi**, Eeseul Shin, Yun Kyung Jung, Byeong-Su Kim "**Sweet Nanodot for Biomedical Imaging: Carbon Dot derived from Xylitol**" *RSC Advances* **2014**, 4, 23210-23213

10. Hyosung Choi, Seo-Jin Ko, **Yuri Choi**, Piljae Joo, Taehyo Kim, Bo Ram Lee, Jae-Woo Jung, Hee Joo Choi, Myoungsik Cha, Jong-Ryul Jeong, In-Wook Hwang, Myoung Hoon Song, Byeong-Su Kim, Jin Young Kim "**Versatile Surface Plasmon Resonance of Carbon-Dot-Supported Silver Nanoparticles in Polymer Optoelectronic Devices**" *Nature Photonics* **2013**, 7, 732-738

11. **Yuri Choi**, Minsu Gu, Jongnam Park, Hyun-Kon Song, Byeong-Su Kim "**Graphene Multilayer Supported Gold Nanoparticles for Efficient Electrocatalysts toward Methanol Oxidation**" *Advanced Energy Materials* **2012**, 2, 1510-1518

12. **Yuri Choi**, Hee Son Bae, Eunyong Seo, Seonwan Jang, Kang Hyun Park, Byeong-Su Kim "**Hybrid Gold Nanoparticle-reduced Graphene Oxide Nanosheets as Active Catalysts for Highly Efficient Reduction of Nitroarenes**" *Journal of Materials Chemistry* **2011**, 2, 15431-15436

Acknowledgement

I would like to thank many people who help me complete my Ph.D thesis.

First of all, I truly grateful to my advisor Prof. Byeong-Su Kim for his support and excellent guidance in my Ph.D study and research. He always give me the scientific knowledge and interests to enhance my independent research ability.

I also would like to thank to my committee professors, Prof. Jin Young Kim, Prof. Tae-Hyuk Kwon, Prof. Oh-Hoon Kwon, and Prof. Wonoh Lee, for their encouragement and insightful comments. In addition, I thank to Prof. Geunsik Lee, Prof. Guntae Kim, Prof. Daeyeon Lee, Prof. Kang Hyun Park, and Prof. Dal-Hee Min, for the experimental suggestion and collaboration.

I also appreciate to my members in KBS groups, for a valuable help and cooperation during my studies. Especially, I am grateful to Eunyong Seo and Taemin Lee who give me assistance and help whenever I want.

Finally, I would like to express my love and gratitude to my parents and brother. They always trust, support, and encourage me to accomplish this thesis.

Moreover, I also thankful to my husband, Yongji Park for his unstinting encouragement and unwavering love.

I would like to thank everyone once more.

감사의 글

설렘과 두려움 반으로 시작했던 학위 과정 동안 여러 방면에서 저에게 큰 힘이 되어 주신 많은 분들께 감사 드립니다. UNIST에 처음 와서 건물을 헤매고 있을 때 한 걸음에 마중 나오셨던 김병수 교수님, 그 때가 아직 생생한데 6년이란 시간 동안 교수님께 많은 가르침을 받았습니다. 부족한 점도 많고 실수투성이였던 저를 이끌어 주시고 성장할 수 있도록 지도해주셔서 진심으로 감사 드립니다. 그리고 소중한 시간 내주셔서 논문 심사 해주신 김진영 교수님, 권태혁 교수님, 권오훈 교수님, 전북대 이원오 교수님께도 감사의 인사를 드립니다. 공동 연구를 통해 많은 도움을 주신 이근식 교수님, 김건태 교수님, UPENN 이대연 교수님, 부산대 박강현 교수님, 서울대 민달희 교수님께도 감사 드립니다.

6년 동안 같이 공부하면서 저에게 큰 버팀목이 되어준 은용 오빠 그리고 태민 오빠, 오빠들 덕분에 재미있었고 힘이 났습니다. 그리고 언제나 곁에 있어 힘이 되어준 고맙고 소중한 친구들, 은경이, 은희, 수은이. 대학원 생활 같이 해서 든든했던 필재 오빠도 고마워요.

연구뿐만 아니라 미래에 대한 조언을 아낌없이 해주신 민사훈 박사님, 정윤경 박사님, 송수희 박사님 감사합니다. 부족하지만 그 동안 잘 따라와줘서 너무 고마운 연구실 식구들, 응진이, 민수, 이슬이, 민주, 병호, 준희. 그리고 기영이, 수현이. 실험실에 적응하느라 고생인 우리 새내기들, 영규, 균혁이, 재은이, 해리, 송아. 너희들 덕분에 웃으면서 연구할 수 있었어. 그 동안 많은 추억을 함께 한 연구실 멤버들에게 고마움을 전합니다.

5층에서 같이 공부하면서 알게 모르게 힘이 되었고, 각자 다른 곳에서 연구 중인 정인 언니, 지은 언니, 선이 언니, 형민 오빠, 신호 오빠, 효진 오빠, 이정수 교수님 감사합니다. 내 친구 선영이, 잘 연락 안 해도 내 얘기 들어줘서 고마워.

마지막으로, 저를 끝까지 믿어주시고 지원해 주신 엄마, 아빠, 감사합니다. 부모님께 효도하고 자랑스러운 딸이 될게요. 정말 사랑하고 존경합니다. 누나의 빈자리를 잘 채워주고 있는 현우, 고맙습니다. 이제 한 가족이 된 시부모님, 믿고 기다려 주셔서 감사합니다. 그리고 앞으로 나의 든든한 지원군이 될 용지 오빠, 내가 가는 길을 지켜봐 주고 힘들 때마다 다독여 줘서 고맙습니다. 가족들의 믿음으로 여기까지 올 수 있었습니다. 고맙고 사랑합니다.

다시 한번, 학위를 잘 마칠 수 있도록 도와주신 많은 분들께 진심으로 감사 드립니다